QUANTIFYING 3D CELLULAR ORGANISATION TO UNCOVER THE STRUCTURE-FUNCTION RELATIONSHIPS IN MULTICELLULAR TISSUES

by

MATTHEW DAVID BRUCE JACKSON

A thesis submitted to the University of Birmingham for the degree of

DOCTOR OF PHILOSOPHY



School of Biosciences

University of Birmingham

September 2018

UNIVERSITY OF
BIRMINGHAM

University of Birmingham Research Archive

e-theses repository

This unpublished thesis/dissertation is copyright of the author and/or third parties. The intellectual property rights of the author or third parties in respect of this work are as defined by The Copyright Designs and Patents Act 1988 or as modified by any successor legislation.

Any use made of information contained in this thesis/dissertation must be in accordance with that legislation and must be properly acknowledged. Further distribution or reproduction in any format is prohibited without the permission of the copyright holder.

ABSTRACT

A wide range of multicellular forms are observed throughout biology, constructed using tightly regulated developmental processes. Cell communication occurs across these cellular architectures, and loss of normal cell organisation is often deleterious to an organism, suggesting that these cellular structures themselves perform a functional role. Despite this, organisational features of multicellular tissues that support these functions are poorly understood, due to low availability of appropriate datasets, and the lack of a quantitative framework to explore them.

To quantify cell patterning in 3D tissues, organ-wide cellular interactions are converted into a network, and network science algorithms are employed to uncover both local and organ-wide organisational principles of cells in 3D space. Models were used to understand how cellular architecture affects the potential flow of information throughout an organ. Topological analysis of cells in the embryonic plant stem revealed a previously unknown molecular transport conduit, while quantification of cellular organisation in the plant shoot apical meristem revealed mechanisms for the maintenance of the stem cell population.

This work enables the discrete comparison of diverse 3D multicellular tissues, and the identification of structure-function relationships in organs. Understanding the organ-wide design principles that have emerged through evolution will provide guidance for future organ design.

ACKNOWLEDGEMENTS

Firstly, sincere thanks are due to Prof. George Bassel and Dr. Iain Johnston for their continued supervision and support throughout my PhD, and for providing a fascinating scientific journey for myself and everyone involved in this project. I would like to thank Dr. Salva Duran-Nebreda for his willingness and ability to explain even the most complex topics at a level that I could engage with and 'nerd-out' over. Thanks are also due to Jack Mitchell, who for the last three years has been a beacon of positivity for everyone. To every member of the lab, past and present, I would like to say thank you for making my experience a productive and enjoyable one.

I would like to thank the BBSRC for funding my research and training through the MIBTP. Particular thanks are due to my MIBTP cohort for being there to have a drink and a chat throughout.

Finally, I would like to thank my wife Lori, who supported me the whole way, including (unfortunately for her) spending the first two months of our married lives getting me through the completion of this thesis.

PUBLICATIONS AND CONTRIBUTIONS

JACKSON, M. D. B., DURAN-NEBREDA, S., KIERZKOWSKI, D., STRAUSS, S., XU, H., LANDREIN, B., HAMANT, O., SMITH, R. S., JOHNSTON, I. G. & BASSEL, G., W. 2018. Global Topological Order Emerges through Local Mechanical Control of Cell Divisions in the *Arabidopsis* Shoot Apical Meristem. *Cell Systems*, 8, 1-13. (Incorporated into thesis, see Appendix 3)

JACKSON, M. D. B., DURAN-NEBREDA, S. & BASSEL, G. W. 2017. Network-based approaches to quantify multicellular development. *Journal of The Royal Society Interface,* 14**,** 20170484. (Incorporated into thesis, see Appendix 1)

JACKSON, M. D. B., XU, H., DURAN-NEBREDA, S., STAMM, P. & BASSEL, G. W. 2017. Topological analysis of multicellular complexity in the plant hypocotyl. *Elife,* 6**,** e26023. (Incorporated into thesis, see Appendix 2)

STAMM, P., TOPHAM, A. T., MUKHTAR, N. K., JACKSON, M. D. B., TOMÉ, D. F. A., BEYNON, J. L. & BASSEL, G. W. 2017. The Transcription Factor ATHB5 Affects GA-Mediated Plasticity in Hypocotyl Cell Growth during Seed Germination. *Plant Physiology,* 173**,** 907-917.

TABLE OF CONTENTS

CHAPTER ONE: INTRODUCTION 1

1.1 Biological systems 2

1.1.1 Tissue-level systems 3

1.2 Multicellularity 5

1.2.1 Barriers to multicellularity 6

1.2.2 Advantages of multicellularity 8

1.2.3 Organisation of cells in a multicellular context 9

1.3 Relating structure to function 10

1.4 Plant tissues 13

1.4.1 Plant cell communication through the apoplastic pathway 17

1.4.2 Plant cell communication through the symplastic pathway 17

1.4.3 Plant cell communication through transport proteins 19

1.4.4 Long range plant cell signalling 20

1.4.5 Consequences of cell organisation in plant tissues 22

1.5 Aims 24

CHAPTER TWO: METHODS AND MATERIALS 26

2.1 Sample preparation and imaging 27

2.1.1 Plant growth conditions 27

2.1.2 Sample preparation 28

2.1.3 Imaging 29

2.2 Image processing and network extraction 29

2.2.1 Importing confocal images into MorphoGraphX 30
2.2.2 Appling Gaussian blur 30
2.2.3 Image segmentation 30
2.2.4 Generating a mesh of a segmented image 31
2.2.5 Extracting the cell connectivity network 31
2.2.6 Cell type annotation 33
2.2.7 Network curation 33
2.2.8 Co-segmentation 34
2.3 Model generation 35
2.3.1 Ordered lattices 36
2.3.2 Voronoi meshes 36
2.4 Network analysis 37
2.4.1 Node centralities 37
2.4.2 Edge centrality 38
2.4.3 Centrality normalisation 39
2.4.4 Logarithm of node betweenness centrality 40
2.4.5 Weighted centralities 41
2.4.6 Local and global efficiency 42
2.4.7 Topological buffering 43
2.5 Geometric analysis 46
2.5.1 Area and volume 46
2.5.2 Cell growth 46
2.5.3 Anisotropy 46
2.6 Statistical analysis 47

2.6.1 Comparing means and medians 47
2.6.2 Comparing distributions 49
2.6.3 Corrections for multiple comparisons 49
2.6.4 Correlations 50
2.6.5 Clustering 50
2.6.6 Logistic regression 51
2.6.7 Coefficient of variation 51
2.7 Visualisation 52
2.7.1 Topological property visualisation 52
2.7.2 Network visualisation 53
2.8 Cell division simulation 54
2.8.1 Cell fusion 54
2.8.2 Rules for simulating division 54
2.8.3 Division order permutations 55
2.8.4 Comparing division planes 56

CHAPTER THREE: CELLULAR ORGANISATION IN 3D ORGAN MODELS 57

3.1 Introduction 58
3.1.1 Qualitative assessment of cellular patterning 59
3.1.2 Abstracting cell connectivity into networks 60
3.1.3 Quantifying tissue organisation in neuroscience 63
3.1.4 Quantifying organisation in other tissues 65
3.1.5 Advances in 3D image acquisition and processing 67
3.1.6 Structure and function in networks 68
3.1.7 Measuring organisation in 3D cell interaction networks 71

3.2 Results 75
3.2.1 Topological effects of increasing the number of cells in an organ 76
3.2.2 Topological effects of increasingly random cell positions 89
3.2.3 Topological effects of biased cell positioning 94
3.2.4 Topological effects of vascularisation 100
3.3 Discussion 110

CHAPTER FOUR: TOPOLOGICAL ANALYSIS OF THE PLANT HYPOCOTYL.. 115

4.1 Introduction 116
4.2 Results 120
4.2.1 Hypocotyl cellular connectivity networks 120
4.2.2 Topological analysis of the Arabidopsis thaliana (Col) hypocotyl 124
4.2.3 Comparison of topology in three A. thaliana ecotypes 128
4.2.4 Geometric considerations in topological measurements 130
4.2.5 Quantifying molecular movement in the hypocotyl epidermis 133
4.2.6 Topological analysis of hypocotyls in other plant species 136
4.2.7 Topological analysis of mutant A. thaliana hypocotyls 140
4.2.8 Relationship between topology and geometry in hypocotyl cells 147
4.2.9 Variability in topological properties 150
4.2.10 Comparison of organisational features in diverse hypocotyls 151
4.3 Discussion 158

CHAPTER FIVE: TOPOLOGICAL ORDER IN THE SHOOT APICAL MERISTEM 161

5.1 Introduction 162

5.2 Results 168
5.2.1 Topological buffering of the SAM 169
5.2.2 Geometry and topology of the SAM 171
5.2.3 Dynamics of geometric and topological cell properties in the SAM 178
5.2.4 Predicting division plane orientation in the A. thaliana SAM 188
5.2.5 Organisational consequences of cell divisions in the A. thaliana SAM 196
5.2.6 Influences of cell shape and topology on the emergence of organisation . 200
5.2.7 The effect of mechanical cell interactions on SAM organisation 211
5.3 Discussion 214

CHAPTER SIX: GENERAL DISCUSSION 219
6.1 Overview 220
6.2 Organisational optimisation in the hypocotyl and SAM 220
6.3 Exploring cellular organisation in other plant tissues 221
6.4 Functional annotation of cellular connectivity networks 223
6.5 Normalisation of topological measurements of cellular connectivity 226
6.6 Inspirations for further cellular network analysis 227
6.7 Applications to animal tissues 231
6.8 Potential for optimal organ design 232
6.9 Concluding remarks 234

APPENDICIES 235

LIST OF REFERENCES 241

LIST OF FIGURES

Figure 1.1. Maintenance of stem cells in the shoot apical meristem. 15

Figure 1.2. Control of root hair development by neighbouring cell signalling. 24

Figure 2.1. Processing pipeline to extract cell connectivity networks from 3D confocal images. 32

Figure 2.2. Cosegmentation of the shoot apical meristem in *Arabidopsis thaliana*. . 35

Figure 2.3. Using $\log_{10}$ betweenness centrality. 41

Figure 2.4. Topological buffering in hypocotyl and meristem samples. 45

Figure 3.1. Abstraction of cellular assemblies into cellular connectivity networks. ... 62

Figure 3.2. Structural and functional network representations of the Birmingham (UK) rail system. 71

Figure 3.3. Topological measurements of cellular connectivity networks. 73

Figure 3.4. Construction of random 3D voronoi organ models with increasing size. 77

Figure 3.5. Spatial distribution of topological properties in randomly generated voronoi models with increasing numbers of cells. 80

Figure 3.6. Distribution of topological properties in a 3D Voronoi model. 81

Figure 3.7. Spatial distribution of topological properties in staggered lattice models with increasing numbers of cells. 82

Figure 3.8. Average topological properties of models with increasing numbers of cells. 88

Figure 3.9. Construction of 3D Voronoi organ models with increasingly random cell positions. 90

Figure 3.10. Spatial distribution of topological properties in randomly generated Voronoi models with increasingly random cell positions. 92

Figure 3.11. Average topological properties of models with increasingly random cell positions. 93

Figure 3.12. Construction of 3D voronoi organ models with increasingly biased cell positions. 95

Figure 3.13 Spatial distribution of topological properties in voronoi models with increasingly biased cell positions. 98

Figure 3.14. Average topological properties of models with increasingly biased cell positions. 99

Figure 3.15. Construction of 3D organ models with vascularisation. 101

Figure 3.16 Spatial distribution of topological properties in random Voronoi models with increasing vascularisation. 102

Figure 3.17 Spatial distribution of topological properties in random Voronoi models with an increasing amount of cell fusion. 103

Figure 3.18. Average topological properties of models with increasing vascularisation. 106

Figure 3.19. Average topological properties of models with increasing vascularisation, where the vasculature itself is not reported on 107

Figure 3.20. Average topological properties of models with an increasing amount of cell fusion. 108

Figure 3.21. Local and global efficiency of models with varying numbers of cells and increasing amounts of vasculature. 109

Figure 3.22. Topological properties of models with varying dimensionality. 111

Figure 3.23. Efficiency of cellular connectivity networks extracted from a range of models. 113

Figure 4.1. Schematic of hypocotyl structure..... 117

Figure 4.2. Shared wall area of physically interacting cells in different cell layers of *Arabidopsis thaliana* Col. hypocotyls..... 121

Figure 4.3. Topological buffering of the hypocotyl. 122

Figure 4.4. An annotated cellular interaction network extracted from an *Arabidopsis thaliana* hypocotyl of the colombia ecotype..... 123

Figure 4.5. Topological analyses of three *A. thaliana* ecotypes, Col, L*er* and Cvi.. 127

Figure 4.6. Degree and betweenness centrality in different *Arabidopsis* hypocotyl cell types. 128

Figure 4.7. Interface sizes between adjacent cell types in in *A. thaliana* ecotypes, Col, L*er* and Cvi..... 132

Figure 4.8. Weighted betweenness centrality in *A. thaliana* ecotypes, Col, L*er* and Cvi 133

Figure 4.9. Movement of fluorescein through the hypocotyl. 135

Figure 4.10. Topological analyses of the poppy and foxglove hypocotyls. 139

Figure 4.11. Degree and betweenness centrality in hypocotyl cell types of different species. 140

Figure 4.12. Topological analyses of three mutant *A. thaliana* hypocotyls. 145

Figure 4.13. Degree and betweenness centrality in hypocotyl cell types of different *A. thaliana* mutants. 146

Figure 4.14. Relationships between geometric and topological measurements in the hypocotyl. 149

Figure 4.15. Variability in betweenness centrality across the hypocotyl. 151

Figure 4.16. Average topological measurements in cell types of each hypocotyl sample. 153

Figure 4.17. Similarities between degree distributions in diverse hypocotyls. 155

Figure 4.18. Similarities in betweenness centrality distributions in diverse hypocotyls. 157

Figure 5.1. Structure of the shoot apical meristem. 164

Figure 5.2. Classical meristem cell division observations. 166

Figure 5.3. Topological buffering of the shoot apical meristem. 170

Figure 5.4. Distribution of geometric and topological properties in the *Arabidopsis* and tomato T0 sams. 172

Figure 5.5. Spatial distribution of geometric and topological properties in the *Arabidopsis* SAM. 175

Figure 5.6. Spatial distribution of geometric and topological properties in the tomato SAM. 176

Figure 5.7. Dynamics of geometric and topological properties in the *Arabidopsis thaliana* SAM 182

Figure 5.8. Dynamics of geometric and topological properties in the tomato SAM. 186

Figure 5.9. Prediction of division plane placement in *A. thaliana* using geometric and topological features. 193

Figure 5.10. Closest plane predictions in individual *A. thaliana* SAM layers. 195

Figure 5.11. Spatial distribution of divisions predicted by different rules. 196

Figure 5.12. Simulating repeated divisions across the entire *Arabidopsis* SAM..... 199

Figure 5.13. Random walk centrality before and after simulated divisions in individual *Arabidopsis* meristem samples. 200

Figure 5.14. SAM models constructed using the Centroidal Voronoi Tessellation path. 203

Figure 5.15. SAM models constructed using equidistant centroids, with the addition of random noise before Voronoi tessellation. 205

Figure 5.16. SAM models constructed using anisotropic Voronoi tessellation. 208

Figure 5.17. Pairwise linear regressions between cell measurements in the anisotropic Voronoi tessellation models with magnitudes 1-3. 209

Figure 5.18. The effect of simulating repeated divisions in a model SAM. 210

Figure 5.19. Geometric and topological properties of the *ktn1* mutant SAM. 213

Figure 5.20. Pairwise linear regressions between measurements in the *ktn1* SAM. 214

LIST OF TABLES

Table 2.1. Statistical analyses and statistical software packages used. 48

Table 5.1. Cell division rates in the *Arabidopsis* SAM..... 177

Table 5.2. Cell division rates in the tomato SAM. 177

Table 5.3. Type II ANOVA test on a logistic regression model with geometric and topological measurements in *Arabidopsis thaliana*. 183

Table 5.4. Type II ANOVA test on a logistic regression model with geometric and topological measurements in tomato..... 187

CHAPTER ONE: INTRODUCTION

1.1 Biological systems

Historically, the discovery of DNA as the unit of heredity (Watson and Crick, 1953), and the subsequent advent of molecular biology has encouraged a reductionist approach to understanding life (Rosenberg, 2008). Using increasingly complex methods to address the fundamental workings of biological processes at increasingly smaller scales, from individual cells, to genetics, to the behaviour of molecules, many questions about the nature of life have been answered (Van Regenmortel, 2004). As these methods have become more high-throughput, the fields of genomics, proteomics and transcriptomics have emerged, generating vast amounts of data concerning every gene, protein and metabolite within a given organism (Simó et al., 2014). Previously, these approaches were widely regarded as having the potential to revolutionise our understanding of biology (Duncan, 2007).

Yet, despite increasing rates of biological data collection (Bell et al., 2009), we are still far from understanding how individual, small-scale biological processes work together to contribute to growth, development and maintenance of an entire organism (Witten and Tibshirani, 2012) (Gomez-Cabrero et al., 2014). The relatively new field of systems biology uses more holistic approaches, seeking to understand how individual parts of biological systems interact, to give rise to emergent properties of the whole (Kitano, 2002). Now, data collected from ‘omics’ is starting to be integrated into computational models, in attempts to bridge this scale-wide gap in our understanding of biological systems (Chuang et al., 2010) (Yurkovich and Palsson, 2018). For example, using large proteomic datasets, interactions between proteins, rather than individual defective proteins, were identified to contribute to the onset of

carcinogenesis in cells (Chuang et al., 2007). In plants, interactions between metabolites through chemical reactions within compartments of the cell have been shown to predict the flux of carbon during stresses, identifying targets for increasing stress resistance through genetic engineering (Williams et al., 2010).

1.1.1 Tissue-level systems

Systems biology has produced many examples of modelling of metabolic pathways, along with gene and protein interactions, and these models are often built to reflect the workings of a processes within a single cell (Libault et al., 2017) (Nielsen, 2017) (Becker and Wittmann, 2018). However, many scales of interactions are present within a single organism, from molecular processes, to the functioning of entire organs (Qu et al., 2011). In multicellular organisms, while much is understood about individual cells, less research has been devoted to how cells interact to give rise to organ function (Moor and Itzkovitz, 2017) (Duran-Nebreda and Bassel, 2017a). Though a huge amount of data from 'omics' studies is now widely available for use in modelling intracellular processes (Perez-Riverol et al., 2017) (Martens and Vizcaíno, 2017), there is a comparative a lack of data available to develop an understanding of cell interactions at the tissue and organ scale (Moor and Itzkovitz, 2017) (Duran-Nebreda and Bassel, 2017a).

Early examples of linking tissue form to function can be found in *On growth and Form*, published by D'arcy Thompson in 1942. The book is widely regarded to be one of the first examples of using mathematics to understand biology, detailing diverse

examples such as the fractal properties of antlers, the geometric features of honeycombs and the mechanically constrained shapes of cells (Thompson, 1942) (Ball, 2013). Thompson famously observed that simple mathematical laws often governed the forms of seemingly complex structures throughout biology, and paved the way for the mathematical modelling of organ composition.

While there are few datasets available to explore the organisation of cells that make up tissues, it is clear that in multicellular systems, perturbation of normal cell organisation can be deleterious to normal organ function. Through experiments using cell patterning mutants, insight has been gained into the importance of proper tissue and organ construction at the cellular level. Many studies show that the organisation of cells within organs is tightly regulated by a host of genetic factors, for example epidermal cell patterning in the roots and shoots of *Arabidopsis thaliana* (Schiefelbein, 2003), or the spatial distribution of stem cells within the *Mus musculus* small intestine (Buske et al., 2011). Mutations in particular genes result in the loss of normal cell organisation or patterning. The loss of function of in three individual ERECTOR family genes causes abnormal, clustered, stomata to develop in *A. thaliana* (Shpak et al., 2005), affecting the regulation of gas exchange in the leaf (Bergmann and Sack, 2007). In addition, it is thought that disorganisation in tissues is related, and can lead, to carcinogenesis in animals (Soto and Sonnenschein, 2011). These examples, amongst others, clearly show that the positioning of cells in a multicellular context is an important feature of a tissue, and is fundamental to the normal function of an organ. Understanding the organisation within tissues and

organs may provide further insights into the relationship between the structural organisation of cells, and the functions of these multicellular assemblies.

1.2 Multicellularity

Multicellular organisms, and in more complex forms of life, the organs within them, consist of many cells, often referred to as the basic building blocks of life (Marth, 2008). It is thought that in many cases, multicellularity originated via transitions from independent to colonial behaviour in single-celled organisms, leading to increases in fitness in specific environments (Hochberg et al., 2008). Through subsequent evolutionary processes, cells in colonies formed sustained cell-cell connections, and signalling processes arose to allow communication between cells (Niklas and Newman, 2013).

Multicellularity has evolved at least 25 independent times across living organisms (Solé et al., 2018). Whole hosts of genes responsible for cell adhesion and cell communication, of key importance to a successful multicellular organism, have arisen separately across the animal, plant and fungi kingdoms, allowing the formation of cohesive multicellular tissues and organs (Rokas, 2008) (Cock et al., 2010) (Sebé-Pedrós et al., 2017).

Aggregative multicellularity is a common evolutionary transition from a single celled to multicellular life strategy (Du et al., 2015). A common model used to illustrate the emergence of aggregative multicellularity is the life cycle of the social amoeba

Dictyostelium discoideum (Marée and Hogeweg, 2001). In *D. discoideum*, cells spend parts of their life cycle foraging for food as unicellular organisms, only coming together to form multicellular structures to migrate and reproduce (Raper, 1940). Though temporary, this type of multicellularity represents an early form of cellular cooperation.

Multicellularity can evolve when single celled organisms are subjected to environmental stress. *In vitro*, the single celled yeast *Saccharomyces cerevisiae* will evolve multicellularity under certain environmental constraints (Ratcliff et al., 2012). Using gravity to artificially select for heavier individuals consisting of more cells, Ratcliff et al. showed that the yeast cells evolve a proclivity for post-division adhesion. Models suggest that though increases in organism size in the multicellular yeast were linked to changing adhesion rates amongst cells, the number of cells in each organism was limited through toxicity-related localised cell death (Duran-Nebreda and Solé, 2015)

Given the repeated evolution of multicellularity in many diverse clades (Niklas and Newman, 2013), there must be significant benefits to cooperation amongst cells in certain circumstances.

1.2.1 Barriers to multicellularity

It is not immediately apparent what the fitness benefits of being multicellular are, for an individual cell. For a cell, there are risks inherent to aggregation. For example,

cooperation can encourage individual cells to become become cheaters, contributing little to their cellular community for great individual gain, like in *Dictyostelium discoideum* (Buttery et al., 2009). The reproductive fruiting body of *D. discoideum* contains a stalk necessary for reproduction, made up of non-viable cells that will never pass on their genes to the next generation (Raper, 1940). Competition between individual cells can favour genotypes that rarely contribute to the stalk, and always migrate to the fruiting body (Strassmann et al., 2000). This results in a net loss of fitness for cells in the stalk, that provide more to the cellular collective than the cheating cells. Within multicellular organisms, there is often reproductive specialisation of cells (Simpson, 2011), which by its very nature results in cells that will never reproduce, the somatic cells. Because of a lack of ability to produce a next generation, the effective fitness of somatic cells is zero, making somatic specialisation seem like a huge risk for the individual cell (Willensdorfer, 2009).

It is clear however, due to its repeated emergence (Solé et al., 2018), that the benefits of multicellularity can clearly outweigh the associated costs. In many cases, problems with individual ‘cheater’ cells have been overcome with a host of genes exist that encourage synergistic and altruistic behaviours in cells within multicellular systems (Michod and Roze, 2001). Mechanisms have also been described for purging cheating cells from cooperating populations (Hammerschmidt et al., 2014). The issues with somatic specialisation for the individual cell can be overcome, when each individual cell in a multicellular aggregate is genetically identical (Buss, 2014). With this strategy, ensuring the success of the germ-line cells also ensures that an individual cell’s genes are passed onto the next generation.

1.2.2 Advantages of multicellularity

At points in the repeated emergence of multicellularity, fitness at the individual cell level is relinquished in favour of fitness of the organism as a whole (Michod, 2005). There are multiple fitness advantages to being multicellular, depending largely on the environment that an organism must survive in. There can be simple size-related advantages to being multicellular, where a cohesive group of cells is less likely to be predated, thus increasing the fitness of an individual (Lürling and Van Donk, 2000).

Importantly, multicellularity also allows increased organism complexity, increasing organism fitness through the division of labour amongst cells (West and Cooper, 2016). As stated previously, one of the most common forms of division of labour across many kingdoms of life is reproductive specialisation of cells (Simpson, 2011). Even with this simple division of cell roles, this represents a system with extreme specialisation, where the non-reproductive somatic cell's sole purpose is to ensure reproduction of the germ-line cells (Cooper and West, 2018).

A mathematical model has shown that multicellularity, driven by the fitness advantages of the division of labour, can theoretically arise spontaneously from homogenous populations of single cells (Ispolatov et al., 2011). In this model, incompatibility between simulated biochemical processes in individual cells was overcome by the compartmentalisation of specific processes to specific cells, in an emergent multicellular aggregate.

The evolution of division of labour amongst cells in multicellular organs has enabled incredibly complex assemblies of specialised cells. For example, it is proposed that the animal eye evolved from an ancient single multi-purpose metazoan ancestor cell type, recently resulting in cell types with diverse functions, including pigment cells, photoreceptor cells and neurons to relay visual information to the brain (Arendt et al., 2009).

1.2.3 Organisation of cells in a multicellular context

The transitions to and subsequent evolution of multicellular life has resulted in an enormous variety of organism shapes and forms (Flagel and Wendel, 2009) (Carroll, 2000). Whilst unicellular organisms can compartmentalise specific processes to organelles within the cell (Winzeler and Davis, 1997) (Lindsay et al., 2001), it is thought that the evolution of multicellularity allows the potential for greater flexibility in compartmentalisation of processes within tissues, a precursor for the development of specialised organs (Ispolatov et al., 2011). An increase in cell number, along with increased diversity in cell types, allows the construction of increasingly complex organs and tissues with specific cell organisations and patterning (Carroll, 2001).

As the complexity of a multicellular system becomes greater, the need for organisation of cells within organs and tissues during developmental processes becomes greater (Müller, 2007). To use again the example of the animal eye, the genetic control of cell proliferation and differentiation is fundamental to the

organisation of retinal cells (Del Bene et al., 2004). Without proper control of cell arrangement and development in the eye, in any given species, the organ cannot perform its function.

There is evidence to suggest that the development of cancerous tissue is due to a breakdown in cell cooperation, named the tissue organisation field theory (Rubin, 1985) (Satgé, 2001). It has been suggested that tumour development is driven by failure of cellular mechanisms that coordinate each individual cell to contribute to normal growth, reaching a target morphology (Levin, 2012). This breakdown in cellular organisation resulting in cancer has catastrophic, often fatal, consequences for a host organism.

These examples suggest a link between the cellular organisation within a tissue or complex organ and the function that it performs. When cellular organisation is perturbed, the result is loss of function or disease. The associated reduction in fitness accounts for the conservation of organ structures throughout evolution, whose development is tightly controlled by hosts of morphogenetic and other signalling genes (Lai, 2004)

1.3 Relating structure to function

Cell organisation in multicellular organisms is highly constrained by a host of genetic components throughout organ development (Loh et al., 2016). It stands to reason

that if particular biological structures are observed time and time again, within and across diverse species, that these structures serve a biological function.

Relationships between structure and function in biology have been studied across various scales. At the molecular level, protein structure determination and prediction is an active area of research (Baker and Sali, 2001) (Yang et al., 2015). Along with its current environment, the amino acid sequence of a protein contributes to its tertiary, folded structure, which has implications for its function within a biological system (Zaidi and Smith, 1996). Identification of protein structure has been used to identify how receptor proteins function to identify wide ranges of ligands (Katritch et al., 2013), and identification of different structural proteoforms of the cancer repressing p53 protein have been shown to have various functional properties (Uversky, 2016). Protein structure is linked to function in such a way, that functional insight into a protein can be gained from an amino acid sequence, due to the recycled nature of protein domains across biology (Yachdav et al., 2014) (Yang et al., 2015)

Structure-function relationships also exist at the single cell scale. A huge variety of cell shapes can be found within prokaryotes, each tailored to improve survival in particular environments that these single celled organisms face (Young, 2006). The highly specialised archaea *Haloquadratum walsbyi* has a peculiar, square, flat structure, contributing to buoyancy and efficient light collection in its aquatic environment (Walsby, 2005). Cells can also distribute structures within themselves in order to perform their function efficiently. In animal systems, pancreatic cells that must react quickly to signals from the intestine compartmentalise enzymes in

specialised vesicular structures close to the cell membrane, for rapid secretion when required (Gorelick et al., 2018).

At the tissue scale, the same repeated use of structures occurs. Using the example of neural systems, in 1888 Ramon y Cajal showed using simple light microscopy and staining that the animal nervous system is made up of many neurons, highly elongated cells that make many cell-cell connections (y Cajal, 1888). Later, he proposed that it is through interaction of individual neuron cells that the nervous system functions (y Cajal, 1888). This neuronal architecture is conserved throughout the nervous systems of diverse species (Kandel et al., 2000) (Brodal, 2004).

The full cellular resolution map of the nematode worm (*Caenorhabditis elegans*) nervous system has been pieced together used serial sections and electron microscopy (White et al., 1986). Analysis of the structure of this map was used to predict neurons involved in the function of touch sensitivity (Chalfie et al., 1985). This provides an example of a direct link between cellular organisation and function.

Although imaging constraints currently prevent cellular resolution mapping of neuronal connections in more complex nervous system components like the human brain, connectivity between coarse-grained parts of brain tissue have been mapped (Lori et al., 2002) (Hagmann et al., 2003) (Hagmann et al., 2008). Statistical analyses of structural links between human neocortex regions show that organisation of brain tissue is highly organised, with particular regions having many more connections to other parts of the neocortex than would be expected at random (Mišić et al., 2016).

Structure-function relationships also exist at this level, where functional magnetic resonance imaging (fMRI) has been used to identify functional connections between brain regions, which exist within the brain structure (Smith et al., 2013). Comparisons of the fMRI patterns in healthy and diseased individuals have been used to identify functional differences in brain activity resulting from particular neurological dysfunctions, like epilepsy (Filippi et al., 2013) (Engel Jr et al., 2013) (Matthews and Hampshire, 2016).

In brains, and all multicellular tissues and organs, both short and long-range signals must travel throughout cellular arrangements in order to coordinate growth, development and function (Loh et al., 2016) (Choi et al., 2017) (Naganathan and Oates, 2017), and a hypothesis can be made that particular tissue architectures would be favourable for the propagation of these signals.

1.4 Plant tissues

There is huge diversity among the shape and forms of multicellular plants, and the organs that form them. In plant species, the diversity of leaf shape alone is enormous, yet the same core developmental programmes are thought to create every design of leaf that we see in nature (Runions et al., 2017). In fact, all plant organs and tissues are constructed primarily through a combination of cell division and cell growth. These two processes are responsible for the many and varied cell organisations are found in different plant organs.

All above ground plant tissue originates from the shoot apical meristem (Bowman and Eshed, 2000). In the model plant *Arabidopsis thaliana*, symmetric cell divisions maintain a relatively uniform, isotropic, population of cell shapes at the centre of the meristem, the central zone (Errera, 1886) (Gibson et al., 2011) (Shapiro et al., 2015), which is the site of pluripotent stem cells (Figure 1.1).

Cells within the central zone undergo continuous growth, and large cells are more likely to divide, restricting the range of cell sizes observed in the tissue (Willis et al., 2016). The WUSCHEL/CLAVATA3 genetic feedback loop maintains the size of the stem cell population, where the mobile protein WUSCHEL is expressed deep within the meristem, moving towards the surface into the central zone to promote cell differentiation (Schoof et al., 2000). CLAVATA3 is expressed in the top-most layers of the meristem, within the central zone, acting in an antagonistic manner to repress the activity of WUSCHEL and maintain a population of stem cells (Brand et al., 2000). Cell growth and division in the central zone pushes cells to the boundary of the meristem dome, outside of the WUSCHEL/CLAVATA3 expression zone, where auxin accumulation induces the development of primordial organs and cell differentiation (Jönsson et al., 2006).

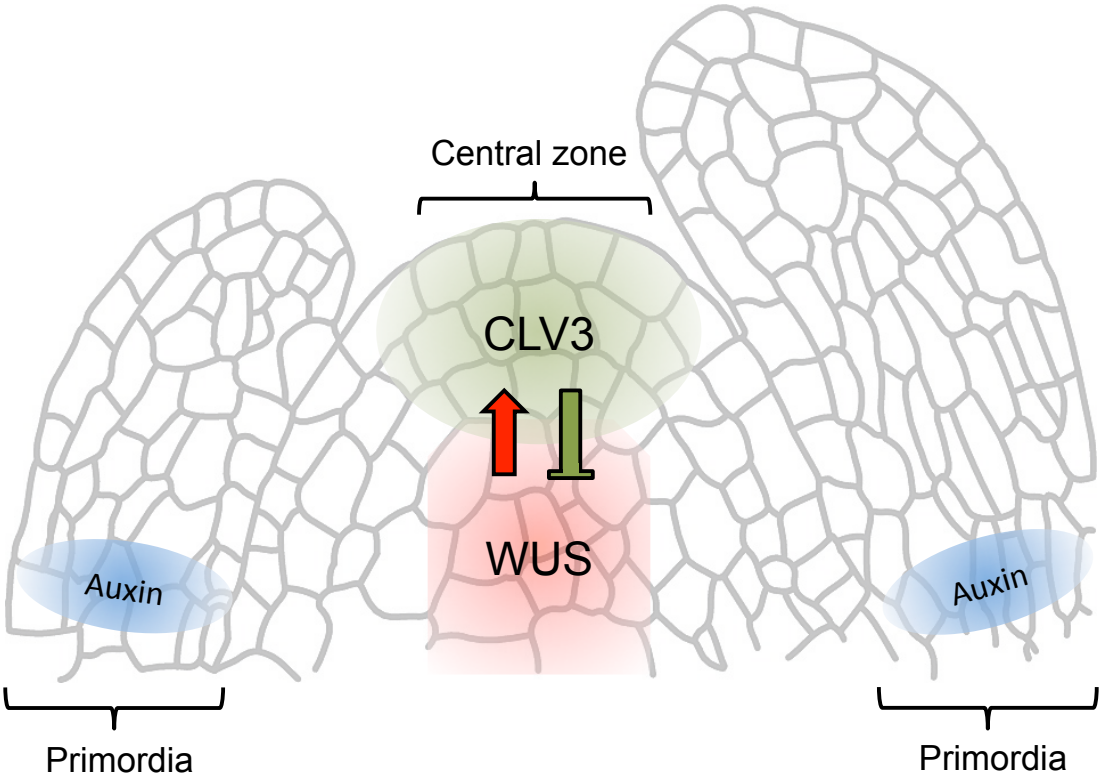


Figure 1.1. Maintenance of stem cells in the shoot apical meristem.
WUSCHEL (WUS) promotes cell differentiation and is expressed deep below the epidermis of the meristem. CLAVATA3 (CLV3) promotes the maintenance of stem cell identity, acting antagonistically to WUS, and is expressed in the uppermost three layers of the meristem dome, known as the central zone. As cells in the central zone grow and divide, cells are pushed outside of the WUS/CLV3 expression zone, where auxin maxima induce the development of organ primordia. Figure adapted from https://figshare.com/articles/Vegetative_shoot_apical_meristem/4786366, attributed to Alexis Maizel.

In contrast, organisation in the *Arabidopsis* root is developed by tightly regulated asymmetric cell divisions, essential to create its radial symmetry (Di Laurenzio et al., 1996). The SHORT-ROOT gene controls both asymmetry in the division plane, as well as cell type specification in the radial direction (Helariutta et al., 2000). In the

root meristem, growth is driven by continuous cell division in the stem cell niche, close to the root tip. Growth of the new cells causes them to enter the division zone, where cells continue to divide (van den Berg et al., 1997), pushing them into the elongation zone. Here they rapidly expand and differentiate, losing the ability to divide further (Dolan and Davies, 2004). Balance between the rate of division and expansion rate of cells maintains the size of the root meristem, as well as controlling overall root development (Di Mambro and Sabatini, 2018).

In each of these structures, and all other plant organs, plant cells cannot move. Due to their immotile nature, most signals between different parts of the plant must occur by passing through a series of cells to reach their destinations. These signals are crucial for responding to the environment and controlling development (McLean et al., 1997).

The primary means of communication throughout plant tissues is through neighbouring, physically connected cells (De Rybel et al., 2014), known as non-autonomous cell signalling, mediated by many different molecules (Long et al., 2015). Molecules can travel through two primary routes, the apoplastic and symplastic pathways. The transport of specific molecules between cells can occur through transport proteins.

1.4.1 Plant cell communication through the apoplastic pathway

The apoplastic pathway refers to the space between plant cell membranes occupied by cell walls, through which water and water-soluble molecules can be transported across an organ, driven by hydraulic pressure (Steudle and Peterson, 1998). This property makes the apoplastic pathway suitable for the uptake and subsequent transport of water from the root epidermis to further within the root tissue. The apoplastic pathway has also been shown to play a role in the response to various stresses, acting as a conduit for alkalinisation of entire organs, resulting in pH-driven responses to the environmental stressor (Felle et al., 2005) (Geilfus and Mühling, 2011). The transfer of electrical signals has been demonstrated to take place through the apoplast, as a rapid response to leaf wounding that takes place before chemical ion transport (Zimmermann et al., 2009).

1.4.2 Plant cell communication through the symplastic pathway

In contrast to the apoplastic pathway, the symplastic pathway refers to the intercellular transport of molecules through the cell cytoplasm, bypassing the need for movement through the plant cell wall (Erickson, 1986). This movement is enabled by plasmodesmata, which are cytoplasmic bridges connecting the cytoplasm of adjacent cells, and allowing the free exchange of molecules (Lucas et al., 1993). Formation of plasmodesmata occurs both during cell division, preserving connections between daughter cells, and post-cell division, to connect existing cell lineages together (Burch-Smith et al., 2011), resulting in two separate types of

plasmodesmata, referred to respectively as primary and secondary plasmodesmata (Ehlers and Kollmann, 2001).

Primary plasmodesmata are formed during cell division, where random strands of endoplasmic reticulum cross the site of new cell wall deposition (Hepler, 1982). Small areas of cytoplasm near the endoplasmic reticulum are trapped during formation of the new cell plate, forming continuous junctions between the daughter cells (Staehelin and Hepler, 1996). As such, primary plasmodesmata are only found between cells from the same lineage. Less is known about the biogenesis of secondary plasmodesmata, but rather than during cytokinesis, secondary plasmodesmata are formed between neighbouring cells during cell growth, as the cell wall is extended (Maule, 2008). New secondary plasmodesmata have been observed to form between trichomes and epidermal leaf cells during cell expansion, through the fission of primary plasmodesmata, and are co-localised in plasmodesmata-rich regions known as pit fields (Faulkner et al., 2008).

Plasmodesmata allow the movement of small molecules, RNAs and even entire organelles between cells (Brunkard et al., 2015). The intercellular movement of these biological agents can be controlled by the plant, through the deposition of callose (β-1,3-glucan) at the plasmodesmata junction, blocking the cytosolic connection (Vatén et al., 2011). Callose accumulation is controlled by callose synthases, enzymes that synthesise callose, whilst degradation is controlled by hydrolytic enzymes specific to callose (Zavaliev et al., 2011).

These features result in plasmodesmata having a high capacity for intercellular communication throughout the plant, along with effective control of this information transfer through callose deposition. Environmental changes and stresses can induce modifications in plasmodesmata permeability, controlled by the up- and down-regulation of callose synthases and hydrolases. For example, during development of the birch shoot apical meristem (*Betula pubescens*), short days encourage the synthesis of callose, blocking symplastic transport (Rinne et al., 2001). When the photoperiod becomes longer, plasmodesmata once again become open, restoring the capacity for cell communication in the shoot apex.

Because of their role in molecular transport throughout plant tissues, plasmodesmata also provide a gateway for microbial pathogens from a site of an infection, to the rest of the plant (Lee and Lu, 2011). The cucumber mosaic virus, amongst other plant viruses, can exploit the symplastic pathway using a specialised 'movement protein', which localises to plasmodesmata and aids in intercellular viral transfer (Sasaki et al., 2006). However, in *Arabidopsis thaliana*, there is evidence to suggest that viral infection can trigger excessive callose synthesis at the site of infection, which inhibits the spread of viral infection across plant tissue (Zavaliev et al., 2009).

1.4.3 Plant cell communication through transport proteins

As well as plasmodesmata, proteins and protein complexes transport specific molecules between plant cells, often in a directed manner (Kierzkowski et al., 2013). For example, the PIN family of membrane-localised transport proteins (named after

the isolation of the first protein in the family, *pin-formed1* in *A. thaliana*) control developmental processes in the shoot apical meristem, the developing lateral root and the developing embryo, amongst others (Okada et al., 1991) (Adamowski and Friml, 2015). PIN family proteins are often positioned in a polar manner within the cell, to facilitate movement of auxin in specific directions, to a particular cellular neighbour, representing a tightly controlled cell signalling process (Reinhardt et al., 2003).

In another example of specific directed cell communication, when a plant experiences drought, the plant hormone abscisic acid is synthesized by and exported from vascular parenchymal cells in the leaf, through the specific ABA transporters ABCG25 and DTX50 (Kuromori et al., 2014). This is imported into stomatal guard cells, through the ABA importer ABCG40 (Kang et al., 2010), which induces stomatal closure, reducing the loss of water through the leaf epidermis (Park et al., 2017). Here, communication between cells with specialised roles allows the plant to respond to the environmental stress of drought, perceived in the roots and acted upon in the leaves.

1.4.4 Long range plant cell signalling

In order to react to external stresses, and ensure coordination of growth and development across different plant tissues in a changing environment, there is a need to transmit long-range signals between distal parts of a plant. For example, when nitrogen availability becomes low in plant tissue above the ground, signals from

the shoot are transmitted to roots to increase nitrogen uptake through increased expression of the *AtNrt2.1* gene (Gansel et al., 2001) (Krouk et al., 2010).

To fine-tune the expression of genes post-transcription, plant cells can produce silencing RNAs that bind to specific messenger RNAs to prevent translation, functionally disabling a gene (Ghildiyal and Zamore, 2009). Silencing RNAs have previously been shown to move in a short-range, intercellular fashion, using the symplastic pathway to regulate embryogenesis (Kobayashi and Zambryski, 2007), and have more recently been established as long-range signalling agents (Brosnan and Voinnet, 2011). The expression of endogenous silencing RNAs in *Arabidopsis* are capable of inducing DNA methylation, through silencing of regulatory genes, in distal plant tissues (Molnar et al., 2010).

It is thought that plants can induce plant-wide responses to external stimuli using the transport of calcium ions and reactive oxygen species, although the mechanism of their propagation through plant tissues is currently unknown (Choi et al., 2017). In response to salt stress, a wave of calcium (Ca^{2+}) and reactive oxygen species was observed, where their cytoplasmic concentrations increased in the first in the cortical and endodermal root cell files, before spreading through the stem and into the leaves (Choi et al., 2014) (Evans et al., 2016).

As well as chemical signals, there has recently been increasing evidence that plants also transmit long-range electrical signals across plant tissues and between organs (Vodeneev et al., 2018) (Hilleary and Gilroy, 2018). These electrical signals are

mediated through cellular architecture within the plant, though exactly how they are propagated is at present poorly understood (Canales et al., 2018).

1.4.5 Consequences of cell organisation in plant tissues

The intercellular manner in which these signals are transported across a plant, coupled with the immotile nature of plant cells, means that the cellular organisation making up plant tissues benefits from being arranged in a way that allows for efficient information transfer.

One clear example of this is the presence of vasculature systems in land plants, allowing resources from the air and soil to be transported throughout the plant (Cho et al., 2017). Within the vasculature, the xylem, responsible for transporting water, is comprised of a series of long, interconnected tubes with low resistance to the flow of water (De Boer and Volkov, 2003). The phloem performs a similar function, forming a microfluidic network for carbohydrate transport throughout the plant (Jensen, 2018). Overall, the vasculature system has a fractal, branching structure, allowing efficient delivery of resources to all parts of the plant (West et al., 1999). Loss of normal vasculature patterning through mutation in *OBERON1* and *OBERON2* in *A. thaliana* has negative consequences for plant growth and development (Thomas et al., 2009), showing that there are severe fitness costs associated with abnormal vascular structure.

Cell fate can also be affected by cellular arrangement. In the root, epidermal cell specialisation is determined by local cell-cell signalling between the cortical and epidermal cell layers (Schiefelbein et al., 2014). Newly formed epidermal cells physically connected to two underlying cortical cells differentiate into trichoblasts (root-hair cells), due to high amounts of SCRAMBLED (SCM) receptor-like kinase signalling from the root cortex. This leads to reduced transcription of WEREWOLF (WER), a gene that normally represses the formation of root hairs, through a series of downstream gene interactions, controlled by the now elevated expression of ROOT HAIR DEFECTIVE6 (Lee and Schiefelbein, 1999) (Kwak and Schiefelbein, 2007) (Bruex et al., 2012), Contrastingly, epidermal cells neighbouring only one cortical cell do not receive enough SCM signalling, allowing WER to be transcribed, blocking the activation of ROOT HAIR DEFECTIVE6 and downstream signalling, which represses the development of root hairs and results in epidermal cell differentiation into the atrichoblast (non-hair) cell type. Here, local positional cell arrangement is responsible for gene dosage effects that influence neighbouring cells, leading to developmental changes.

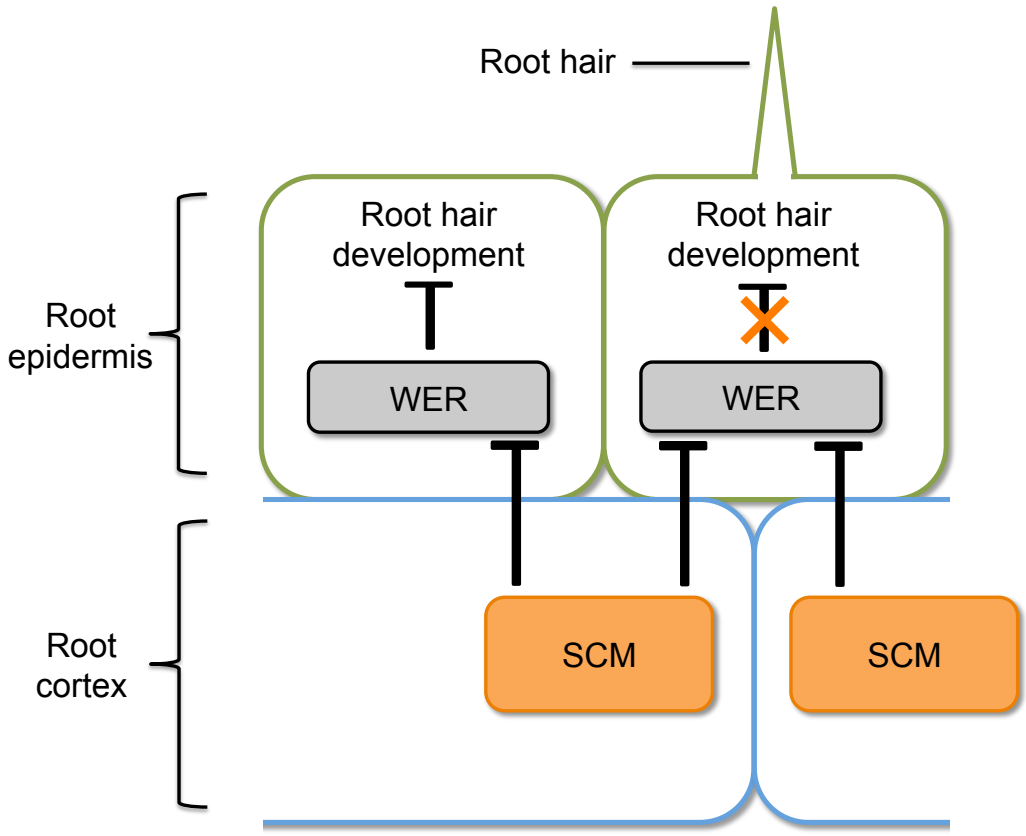


Figure 1.2. Control of root hair development by neighbouring cell signalling. SCRAMBLED (SCM) is expressed in the cortical cell layer, and is transported to cells in the epidermis. SCM interacts with the expression of WEREWOLF (WER) in epidermal cells, and represses its activity. SCM from one underlying cortical cells is insufficient to repress activity of WER, whilst SCM from two underlying cortical cells blocks WER activity. Blocking WER activity allows the development of root hair cells, following activation of a downstream signalling cascade.

1.5 Aims

To explore the organisation of cells in tissues in detail, and how different organisations affect the functional properties of organs, a method for quantifying aspects of cellular patterning is required. To address the capacity for both short and long-range cell communication, the contributions of 3D cellular arrangement to

possible local and global signalling must be addressed. With a suitable framework for quantifying organisational properties and high-resolution 3D imaging of plant organs at cellular resolution, the gap in understanding between organ structure and organ function at the tissue level can start to be bridged.

In this thesis, the abstraction of cellular connectivity in plant organs and their subsequent analysis using network science algorithms is proposed as a method to quantify tissue organisation. In Chapter 2, algorithms to quantify the capacity a tissue has for local and long-distance transport are introduced. These proposed algorithms are evaluated for their ability to capture and highlight interesting organisational features using model 3D organ systems in Chapter 3. Their relevance to plant tissues is explored in Chapters 4 and 5, where through the extraction and analysis of cellular networks, novel mechanisms for organ-wide transport and the generation of tissue architecture are elucidated.

CHAPTER TWO: METHODS AND MATERIALS

2.1 Sample preparation and imaging

2.1.1 Plant growth conditions

To generate samples for hypocotyl imaging, the *Arabidopsis thaliana* ecotypes Colombia (Col), Cape Verdi Islands (Cvi) and Landsberg *erecta* (L*er*), along with the associated mutants *cdka1;1* (ProCDKA;1::CDKA;1-T14D;Y15E) (Dissmeyer et al., 2009), *monopteros* (*mp* B4149) (Schlereth et al., 2010) and *laterne* (Treml et al., 2005) were grown in environmentally controlled cabinets, with a 16 hour light cycle (light: intensity 150-175 µmol m^2s^{-1}, 23°C dark: 18°C).

Dry siliques from the plants were harvested and the seeds were cleaned through a 500µm mesh. Of the other species imaged, poppy (*Papaver rhoeas*) was grown by the Noni Franklin group (University of Birmingham, UK), and foxglove (*Digitalis purpurea*) was harvested from Birmingham Botanical Gardens (Birmingham, UK).

To generate samples for live meristem imaging, wild-type tomato as well as wild-type *Arabidopsis thaliana* and *katanin1* mutants (Uyttewaal et al., 2012), each with YFP markers for the plasma membrane, were also grown in environmentally controlled cabinets with a 16 hour light cycle (light: intensity 110 µEm^2s^{-1}, 20°C dark: 16°C) as done previous in previous work (Kierzkowski et al., 2012).

2.1.2 Sample preparation

For hypocotyl samples, embryos were dissected 3 hours after imbibition, before preparation for confocal microscopy. Samples were prepared using the same protocol as in previous studies (Truernit et al., 2008) (Bassel et al., 2014).

Following this protocol, samples were fixed in fixative comprising of 50% methanol and 10% acetic acid, at 4°C for 4 to 12 hours, depending on sample thickness. Each hypocotyl was then washed with water, before incubation in 1% periodic acid at room temperature for 40 minutes. Again, the tissue was washed with water and subsequently incubated in Schiff's reagent, containing propidium iodide (100 mM sodium metabisulphite, 0.15 N HCl and propidium iodide to a concentration of 100 mg/mL) for 1 to 2 hours until staining was visible. From here, each hypocotyl was transferred to a microscope slide and covered with chloral hydrate (4 g chloral hydrate, 1 mL glycerol and 2 mL water). Slides were left overnight at room temperature. After this, excess chloral hydrate solution was removed and drops of Hoyer's solution (30 g gum arabic, 200 g chloral hydrate, 20 g glycerol and 50mL water) were added directly to the tissue, before a cover slip was placed on top.

For shoot apical meristems, shoot apices were dissected from 11 day old plants under a light microscope and washed in 50 mM sodium phosphate buffer (pH 7.2), before being mounted under cover slips (Fleming et al., 1996). The YFP marker present at the plasma membrane prevented the need for tissue fixation and propidium iodide staining which kills cells, allowing time course images to be collected.

2.1.3 Imaging

3D images of plant tissues were obtained using confocal microscopy, using a Zeiss LSM 710 or Leica SP8 upright confocal microscope. For each image, a 25x oil immersion objective was used. Images were taken with a bit depth of 16. The pinhole slice thickness used was typically 1.9 µm, with a slice interval width of 0.7 µm. Scan speed was typically set to 9, while intensities of each slice were taken from 4-8 averages. These standard settings were tweaked depending on sample quality and clarity, to capture images with appropriate quality for subsequent 3D segmentation.

Hypocotyl z-stacks were taken using the Zeiss LSM 710 confocal microscope. Excitation of the propidium iodide stained samples was at a wavelength of 488 nm, and images were collected at 520-720 nm.

Shoot apical meristems were imaged at 3 separate time points, 0 hours 11 hours and 22 hours, using the Leica SP8 upright confocal microscope. Excitation of YFP at the plasma membrane was carried out with an argon laser, at a wavelength of 514 nm. 3D stacks were taken at 529-545 nm using a HyD detector, ensuring that sufficient signal was present in the uppermost four layers of the imaged meristems.

2.2 Image processing and network extraction

Several steps are needed to convert an original confocal microscope z-stack image (around 400 MB to 1 GB) into a mesh (200 – 400 MB), with which geometric properties can be measured, and from a mesh into a cellular connectivity network (50

– 800 kB), from which topological properties can be extracted (Figure 2.1). Each step taken to convert an original z-stack to a connectivity network results in a further abstraction of the original image data, making additional analyses possible.

2.2.1 Importing confocal images into MorphoGraphX

Images from confocal microscopy in the Zeiss (lsm) and Leica (lif) formats were imported into the open source image platform FIJI (Schindelin et al., 2012). The Bio-Formats plugin for FIJI (Linkert et al., 2010) was used to convert these proprietary file formats into the more compatible bitmap tiff format stacks. 3D tiff stacks were then imported into the open-source software package MorphoGraphX (de Reuille et al., 2015).

2.2.2 Applying Gaussian blur

These stacks were modified in preparation for segmentation using the ‘Gaussian Blur’ process, with a radius of 0.3 µm. This step lowers the original quality of the images by averaging the intensity of pixels over a small radius, ensuring that cell boundaries are properly resolved and smoothing over artefacts from the imaging process (de Reuille et al., 2015). This blurring step is essential for good subsequent automatic segmentation.

2.2.3 Image segmentation

The ‘ITK Watershed Auto Seeded’ process (Ibanez et al., 2005) was then used to automatically assign a label to each individual cell (Figure 2.1). The quality of the

original captured 3D image greatly affects the accuracy and effectiveness of the automatic segmentation. After the original segmentation, when images were under segmented, with the same labels assigned to more than one cell, the ‘Threshold’ parameter was lowered to find a more suitable segmentation threshold value. If the image was over segmented, either the ‘Threshold’ parameter was raised, or manual corrections were made. Manual corrections to segmentations were made by using the ‘Pick Label’ and ‘Fill Label’ buttons on the MorphoGraphX toolbar. Through a combination of threshold manipulation and manual corrections, efforts were made to ensure 100% accuracy of organ segmentations. Segmentations were saved as the MorphoGraphX Stack (mgxs) file format.

2.2.4 Generating a mesh of a segmented image

Segmented stacks were then converted into a mesh format using the ‘3D Marching Cubes’ process in MorphoGraphX, with the ‘Cube Size’ parameter set to 1 μm. This resulted in the average, roughly isotropic cell being represented by around 3000 vertices. The 1 μm cube size was chosen as a balance between realistic representations of cell surfaces, and the speed at which meshes could be created, rendered and analysed. The generated MorphoGraphX mesh (mgxm) format describes the surface of every cell with vertices in 3D space (Figure 2.1).

2.2.5 Extracting the cell connectivity network

The mesh format contains the necessary information to isolate physical cell connectivity and connecting cell wall area between every pair of physically connected cells, which can be extracted as a network using the MorphoGraphX plugin

3DCellAtlas (Montenegro-Johnson et al., 2015). Each extracted cell connectivity network was saved as a csv file, as a list of all existing pairwise cell interactions in the mesh, along with the size of the connecting cell wall in μm^2.

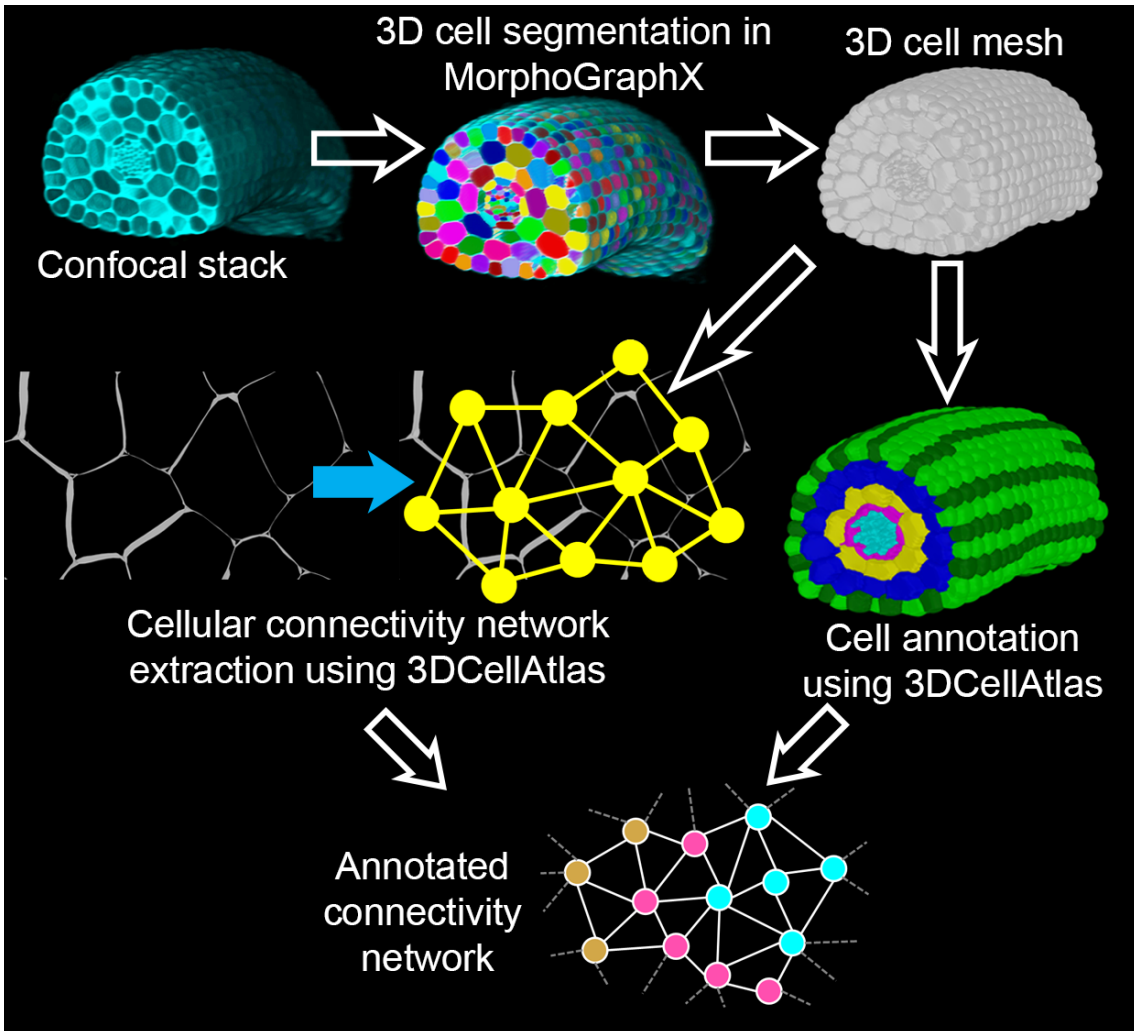


Figure 2.1. Processing pipeline to extract cell connectivity networks from 3D confocal images.
The example shown here is an *Arabidopsis thaliana* Col. hypocotyl.

2.2.6 Cell type annotation

To generate cell-type-annotated cellular connectivity networks, ‘Parent Labels’ were used in MorphoGraphX. These labels can be used to add metadata labels to each cell. Different cell types were computationally identified, based on size, shape and radial position, using the 3DCellAtlas plugin for MorphoGraphX (Montenegro-Johnson et al., 2015) in the case of the radially symmetric hypocotyl. For the meristem, cell types were identified manually by stripping away layers of the meristem mesh successively. The ‘Save Parents’ process was then used to generate a csv file containing each cell label and it’s associated cell type. Manual corrections to cell type annotations were then applied by modifying the csv file in line with observations of the original 3D image, to ensure 100% annotation accuracy. In combination with the cellular connectivity network file generated with the 3DCellAtlas tool, the curated cell type lists were used to generate annotated cell connectivity networks with a Python script.

Additionally, the 3DCellAtlas tool can also be used to identify segments of mesh representing air spaces in tissues. Since these segments are not representative of cells, they introduce artificial edges in cellular connectivity networks. Where air spaces were identified by 3DCellAtlas, they were deleted.

2.2.7 Network curation

In some meshes, artefacts from imaging and image processing resulted in cell meshes that would protrude between adjacent cells from different cell layers. This resulted in edges in the extracted cellular connectivity network that were not

representative of real cellular interactions. Where artefacts were present, manual corrections were made to the extracted cellular connectivity networks, by removing edges in the previously generated csv file detailing all physical cell-cell interactions.

2.2.8 Co-segmentation

Co-segmentation was performed in MorphoGraphX to identify cell divisions across time course images, and track cell lineages (Figure 2.2). Meshes generated from both earlier and later shoot apical meristem time point images were overlaid, and rendered transparently (Figure 2.2A). Using parent labelling, within the 'Lineage Tracking' processes in MorphoGraphX, cells in both time points were assigned the same parent labels (Figure 2.2B). Where cells had divided in the later time point, the same parent label from the previous time point was assigned to both. This allowed the measurement of cell growth and division over the intermediate time. After lineage tracking, the 'Heat Map Proliferation' process in MorphoGraphX was used to visualise cell divisions (Figure 2.2C).

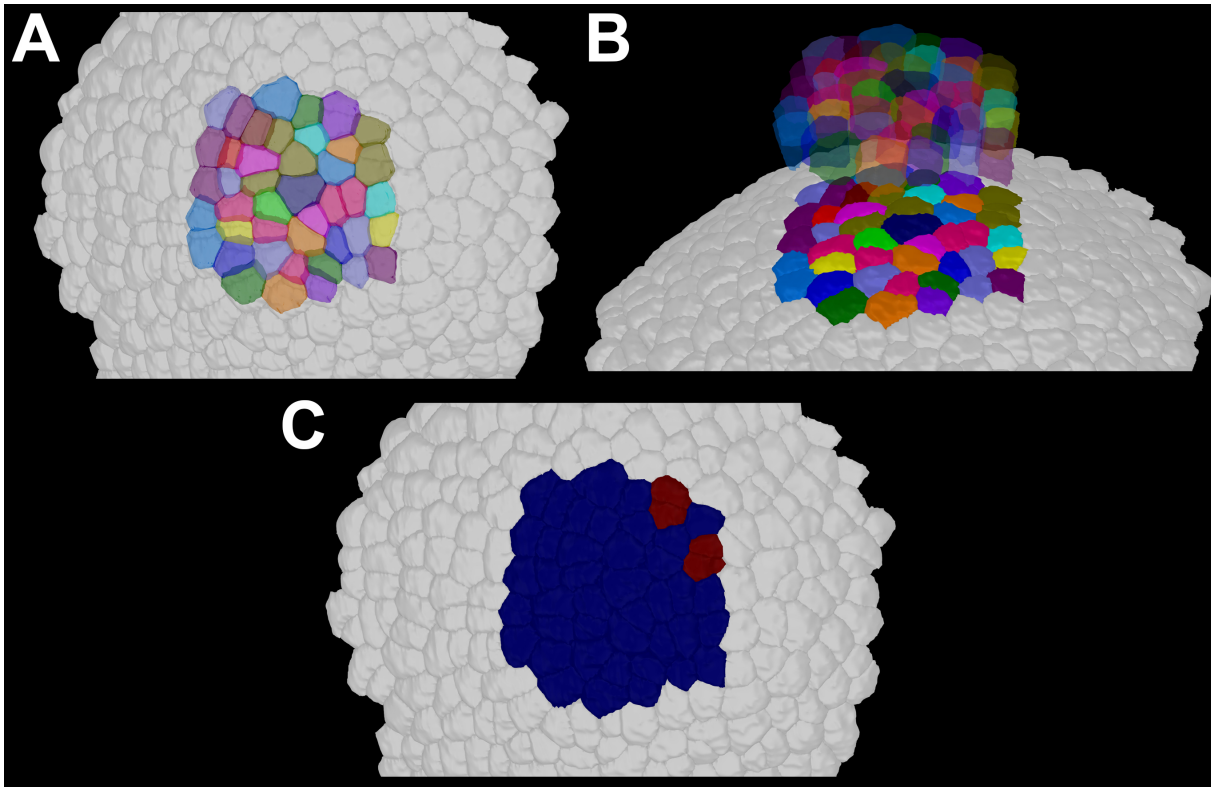


Figure 2.2. Cosegmentation of the shoot apical meristem in *Arabidopsis thaliana*. (A) A subset of cells from an earlier time point (in colour) overlaid on top of cells from an image taken 11 hours later (white). (B) Labels from cells in the earlier time point (transparent), transferred onto the later time point using parent labelling (newly labelled cells in solid colour). Where cells have divided, daughter cells have been assigned the same label. (C) A proliferation heat map of divisions that occurred in the 11 hours between time point images, showing non-divided (blue) and divided (red) cells.

2.3 Model generation

3D models of tissues and organs were generated with the as yet unpublished CellMaker add-on in MorphoGraphX (Richard Smith group, Max Planck Institute, Germany). Their cellular connectivity networks could then be extracted in the same manner as with the real sample meshes, using 3DCellAtlas (Montenegro-Johnson et al., 2015).

2.3.1 Ordered lattices

Ordered lattices of cells, resembling stacked cubes, were created using various CellMaker processes. In all lattices, cells were staggered to more accurately model the brick-like pattern of cells observed in the hypocotyls and shoot apical meristems analysed.

2.3.2 Voronoi meshes

Voronoi models were generated using 3D centroid positions, which were used in Voronoi tessellation with a bounding mesh (Du and Wang, 2003). Centroid positions were pre-generated with a Python script. Centroids were then imported into MorphoGraphX using the 'Load Point Cloud' process in CellMaker. Surface meshes were created using various CellMaker processes, depending on the gross morphology of the desired organ. The surface mesh prevented centroids on the surface of the model from growing infinitely in Voronoi tessellation, due to lack of any boundary. With both centroids and a surface mesh loaded, 3D Voronoi tessellation of points was then carried out using the 'Voronoi Cells from Point Cloud' process (relevant parameters: cage points = 1000, minimum distance cage points = 1.0, threshold merging = 0.01).

To generate series of models for analysis, various centroid parameters, for example the number or position of centroids, were adjusted before tessellation. Centroid point clouds were generated with a Python script.

2.4 Network analysis

Network analyses were performed using Python 2.7. Prior to analyses, cellular connectivity networks extracted in MorphoGraphX, listing pairwise interactions, were imported into Python as a undirected graph object using the NetworkX library (version 1.10) (Hagberg et al., 2008). On import into NetworkX, duplicate edges present in the original lists of pairwise interactions were automatically converted into a single cell-cell interaction. Graph objects in NetworkX are stored as adjacency dictionaries for fast lookup and data manipulation.

The biological relevance of each of these network analysis measures is discussed in Section 3.1.7.

2.4.1 Node centralities

For the calculation of degree, betweenness centrality and random walk centrality, NetworkX was used.

Degree is calculated in NetworkX by simply counting the number of edges that a given node has. This equates to the number of neighbours for each node.

Betweenness centrality (log and normalised, see Sections 2.4.3 and 2.4.4) of a node v is calculated using Brandes' algorithm:

$$c_B(v) = log_{10}\left(\sum_{i,j \in V} \frac{\sigma(i,j|v)}{\sigma(i,j)} \times \frac{2}{(n-1)(n-2)}\right)$$

where V is all nodes, $\sigma(i,j)$ is the number of shortest (i,j)-paths, and $\sigma(i,j|v)$ is the number of (i,j)-paths that pass through the node v other than i,j themselves (Brandes, 2001).

Random walk centrality, also known as current flow centrality, is calculated in NetworkX by not only counting shortest paths through a given node, but also all possible paths between pairs of nodes that could cross it (Newman, 2005). To calculate this, random walkers are instantiated that randomly move between all pairs of nodes, until all possible paths between all possible pairs of nodes are traversed.

The formal definition of random walk centrality (normalised) of a node v is:

$$c_{RW}(v) = \sum_{i \neq v \neq j} r_{ij} \times \frac{2}{(n-1)(n-2)}$$

where r_{ij} is the probability of a random walk starting at node i and ending at node j passing through node v.

2.4.2 Edge centrality

As well as assessing the topological properties of individual cells, the contribution of individual cell interfaces can be measured. To determine the number of shortest paths that pass through a cell connectivity network edge e, edge betweenness centrality (normalised) was calculated using:

$$c_B(e) = \sum_{i,j \in V} \frac{\sigma(i,j|e)}{\sigma(i,j)} \times \frac{2}{n(n-1)}$$

where V represents all nodes in the network, $\sigma(i,j)$ is the number of shortest paths, and $\sigma(i,j|e)$ is the number of shortest paths that pass through edge e.

2.4.3 Centrality normalisation

To enable comparisons between networks representing different amounts of cells possible, the global measurements of betweenness centrality and random walk centrality were normalised by the number of possible node pairs across the network, multiplying each value by:

$$\frac{2}{(n-1)(n-2)}$$

where n is the number of nodes.

For comparison of edge betweenness centrality in different networks, the value for each edge was normalised by multiplying by:

$$\frac{2}{n(n-1)}$$

where n is the number of nodes in the network.

As opposed to other types of networks, such as 'small world' networks (Watts and Strogatz, 1998), or classes of random Erdös-Rényi networks where nodes are randomly connected together with different probabilities (Erdos and Rényi, 1960), all networks analysed are essentially 3D lattices (Van Wijk et al., 2010). Due to inherent physical constraints of a 3D lattice, network density is largely consistent over all networks analysed, so no normalisation was applied for density.

2.4.4 Logarithm of node betweenness centrality

In most cases, the betweenness centrality distribution of 3D cellular connectivity networks analysed was long-tailed (Figure 2.3A). To ensure that statistical tests carried out between different measurements were valid and comparable, in many cases $\log_{10}$ betweenness centrality was used, which has a more normal distribution (Figure 2.3B) (Seguin et al., 2018).

Log_{10} betweenness centrality was also used when visual discrimination between cells with relatively low betweenness centrality was required, such as in cells at the surface of the model in Figure 2.3C. After the logarithm of betweenness centrality is taken, higher and lower values of betweenness centrality in cells at the surface are more easily distinguished (Figure 2.3D).

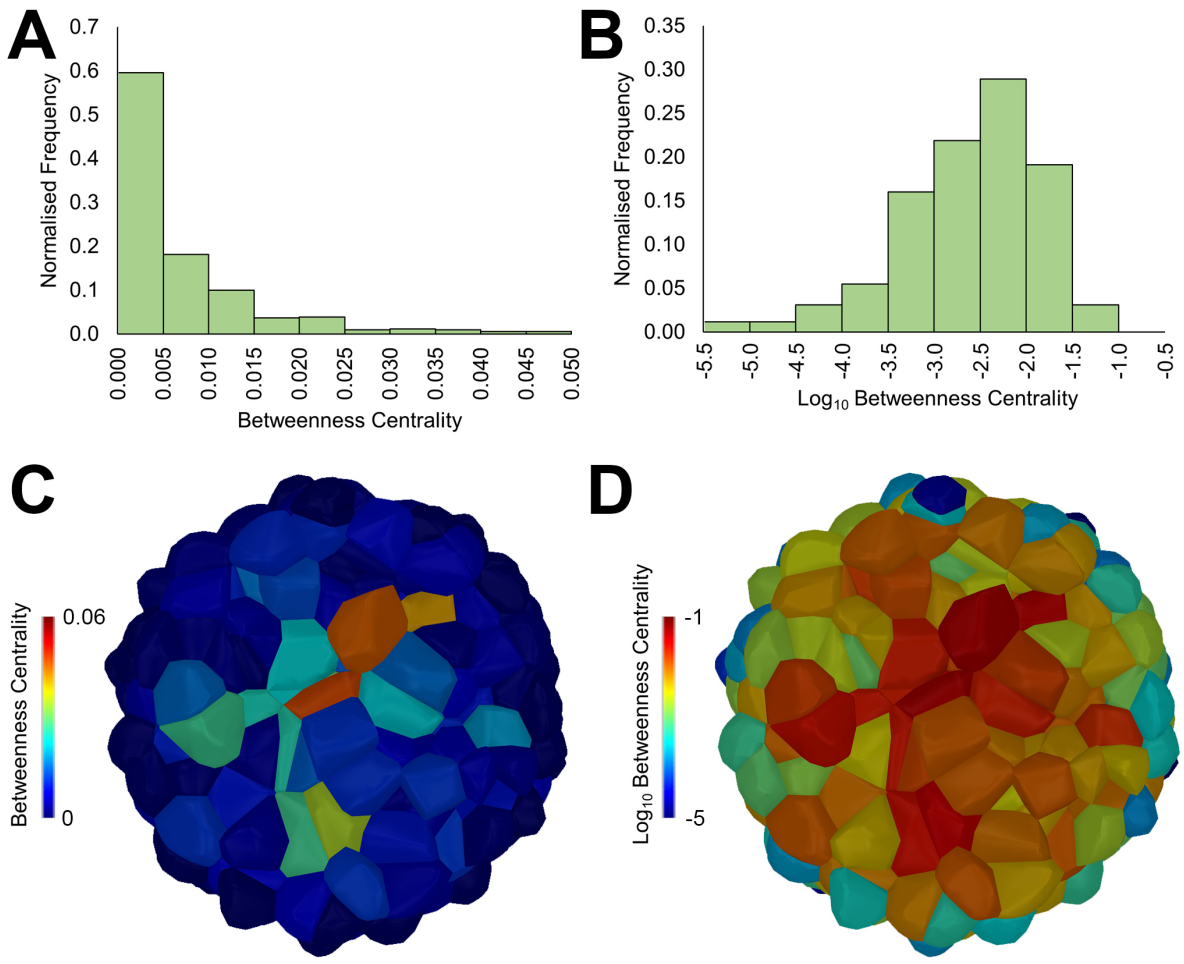


Figure 2.3. Using $\log_{10}$ betweenness centrality.
(A) Distribution of betweenness centrality in the cellular connectivity network of a simple spherical Voronoi model with 512 cells. (B) Distribution of $\log_{10}$ betweenness centrality in the same model. (C) A cross-section of the model, false coloured with betweenness centrality. (D) A cross-section of the model, false coloured with $\log_{10}$ betweenness centrality.

2.4.5 Weighted centralities

In network science, rather than every edge having the same contribution to a network, weighting can be added to edges to assign value to connections between particular nodes (Newman, 2018). In cellular connectivity networks, the interface size between cells in μm^2 can be used as a weighting. With this weighting, algorithms that

navigate paths between nodes, like betweenness centrality and random walk centrality, more readily use larger cell interfaces.

By default in NetworkX, random walk centrality weighting is defined as a measure of connectivity between nodes, so edges representing a large connecting surface area are preferentially traversed by random walkers. In contrast, in NetworkX the weighting of betweenness centrality is defined as a resistance to traversal between nodes. Therefore, for consistency between the centrality measurements, the inverse of the size of the physical cell interaction was used as a weighting in weighted betweenness centrality calculations.

2.4.6 Local and global efficiency

Local and global efficiency were used to measure how efficiently graphs exchange information. Local efficiency measures how robust a graph is to damage, and is related to the clustering coefficient of a graph. Global efficiency is a measure of the suitability of a network for exchanging information between all nodes concurrently, and is related to the average shortest path length. Both local efficiency and global efficiency were calculated using the algorithms in the Brain Connectivity Toolbox for MATLAB (Rubinov and Sporns, 2010), translated into a Python script.

For the calculation of either local or global efficiency, it is necessary to calculate the average efficiency of a graph. For any given graph G, the average efficiency is:

$$E(G) = \frac{1}{n(n-1)} \sum_{i \neq j \in G} \frac{1}{d(i,j)}$$

where n represents the number of nodes in the network, and $d(i,j)$ is the shortest path between nodes i and j.

On a graph G, local efficiency is defined as:

$$E_{loc}(G) = \frac{1}{n} \sum_{i \in G} E(G_i)$$

where n is the number of nodes in the whole network, and G_i is a local subgraph comprising only the nodes connected to node i (neighbouring nodes), but not node i itself.

For a given graph G, global efficiency is calculated using:

$$E_{glob}(G) = \frac{E(G)}{E(G^{ideal})}$$

where G^{ideal} is a graph consisting of all nodes in G, where all possible edges between these nodes exist.

2.4.7 Topological buffering

Because of limitations of the confocal microscope field of view, and clarity of signal, only sections of entire organs can be imaged at high enough resolution for correct segmentation, resulting in cells in the image that are not within their normal multicellular context. When cells at image boundary regions do not have their correct local interactions represented in the 3D image, they do not have the correct cell connections in the associated cellular connectivity network, after the image

processing and network extraction steps. These cells bias the topological measurements of other cells in the network, both locally and globally. To reduce the effects of this on subsequent network analysis, topological buffering was used in both the hypocotyl and meristem.

Topological buffering refers to including all imaged cells and cell interactions in a cellular connectivity network for the purposes of topological analysis, but not reporting on the measurements of every cell. Cells near artificial imaging boundaries were excluded from further analysis (Fig 2.4). To do this, cells that were to be included in further analysis were selected in MorphoGraphX, and their labels were exported using the ‘Heat Map’ function. After topological analysis was carried out on the entire cellular connectivity network, a subset of the selected cells to include was taken from the analysis results, effectively removing the buffer region cells.

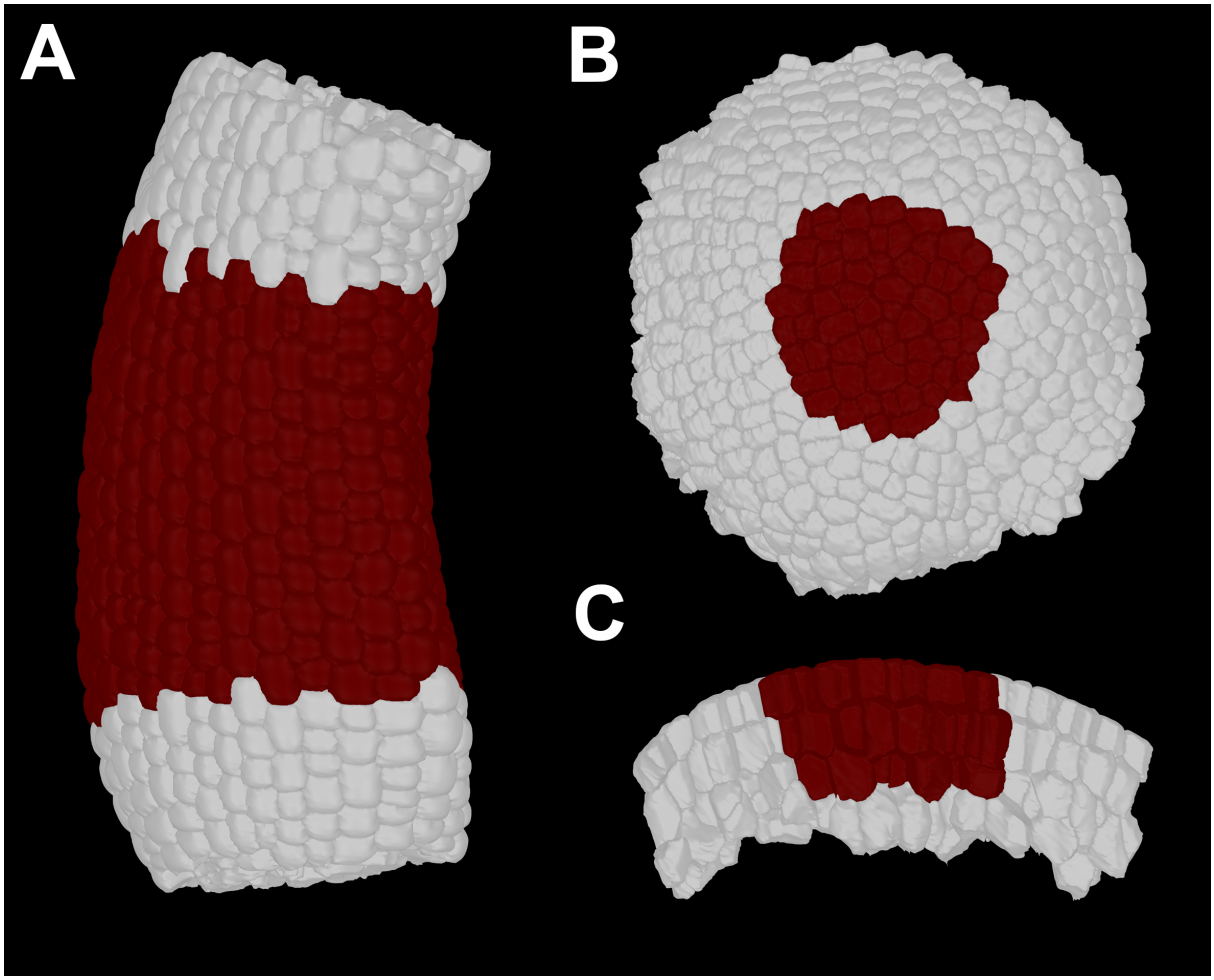


Figure 2.4. Topological buffering in hypocotyl and meristem samples.
(A) Analysed regions (red) and topological buffer cells (white) in an *A. thaliana* Col. hypocotyl. (B) Top down image of topological buffering in the *A. thaliana* shoot apical meristem. (C) Cross-section of topological buffering in the *A. thaliana* shoot apical meristem.

In the hypocotyl, ends of the samples connected to the radicle and rest of the embryo, around five cells from the artificial imaging boundary, were treated as topological buffer (Figure 2.4A). In the shoot apical meristem, only cells in the centre of the meristem dome, at least five cells from the artificial imaging boundary, were used in further analysis, while the rest of the meristem dome was treated as topological buffer (Figure 2.4B). In addition, only the top three layers of the meristem,

L1 to L3, were reported on, while the L4 was treated as topological buffer (Figure 2.4C).

2.5 Geometric analysis

2.5.1 Area and volume

To measure the size of cells, both cell area and volume were used. The calculation of cell area and volume was performed in MorphoGraphX, using the 'Heat Map' function with a sample mesh.

2.5.2 Cell growth

Time course meristem images were used to calculate cell growth over the intermediate time of 11 hours. Lineage tracking and co-segmentation was used in MorphoGraphX to track individual cells in both time points. Cell growth was calculated by dividing the volume of the cell at a later time point, by the volume of the cell at the earlier time point, resulting in a fold change in size over the 11-hour period.

2.5.3 Anisotropy

To capture the anisotropy of individual cell shape, the MorphoGraphX process 'PCAnalysis' (relevant parameters: span correction = Ellipsoid, threshold = 100, shape details = 3) was used with a fully segmented stack. This generated a mesh of ellipsoids representing the three principal directions of cell elongation, along with a

csv file containing the magnitudes of these directions. A Python script was used to convert these magnitudes into a measure of anisotropy, by dividing the largest magnitude by the sum of all three magnitudes extracted. In this way, highly elongated cells have an anisotropy score closer to 1, while isotropic cells score lower, where the minimum anisotropy is 0.33 in completely isotropic cells.

2.6 Statistical analysis

All statistical analyses performed can be found in Table 2.1, with more details in individual sections.

2.6.1 Comparing means and medians

Two-sample *t*-tests were performed without assuming equal variances (also known as Welch's *t*-test). *t*-tests were carried out in Python using the scipy library (Jones et al., 2001), using the 'ttest_ind' function (revelvant parameters: equal_var=False).

One-way analysis of variance (ANOVA) was used to simultaneously compare means of three or more groups. Post-hoc Tukey's tests were used in conjunction with ANOVA to determine groups of measurements that shared similar means (Tukey, 1949). One-way ANOVA and associated post-hoc Tukey tests were performed in SPSS.

The Mann-Whitney U test was used to compare medians of independent variables, without assuming that they are normally distributed (Kruskal, 1957). Mann-Whitney U tests were performed using a Python script, with the scipy function 'mannwhitneyu' (default parameters) (Jones et al., 2001).

Table 2.1. Statistical analyses and statistical software packages used.

Statistical Analysis	**Software**	**Additional Packages/Libraries**
t-test	Python	scipy (Jones et al., 2001)
Mann-Whitney U test	Python	scipy (Jones et al., 2001)
One-way ANOVA	SPSS	-
Tukey's test	SPSS	-
χ^2 test	Python	scipy (Jones et al., 2001)
Kolmogorov-Smirnov test	Python	scipy (Jones et al., 2001)
Linear Coefficient of Determination (R^2)	Python	scipy (Jones et al., 2001)
Hierarchical Clustering	Python	scikit-learn (Pedregosa et al., 2011)
Logistic Regression	R	*glm2* (Marschner, 2011), *car* (Fox et al., 2012) and *ROCR* (Sing et al., 2005)

2.6.2 Comparing distributions

χ^2 tests (for discrete variables) (Pearson, 1900) and two-sample Kolmogorov-Smirnov tests (for continuous variables) (Kolmogorov, 1933), to test for significant differences in distributions, were performed in Python using the scipy library, using the 'chisquare' and 'ks_2samp' functions.

Earth-mover's distance (Rubner et al., 1998), also known as Wasserstein distance, was used to quantify the extent of difference between distributions. Considering two probability distributions, the calculation of earth-mover's distance essentially involves finding the minimum amount of one probability distribution that can be 'moved around' to match another probability distribution. Earth-mover's distance was carried out using scipy, using the 'wasserstein_distance' function.

2.6.3 Corrections for multiple comparisons

In statistical analysis of hypocotyl topological distributions, a total of 3200 individual statistical tests were carried out. To compensate for the likely introduction of false positive results of statistical significance, the Bonferroni correction for multiple comparisons was used (Dunn, 1961). This reduced the *p*-value threshold for significance throughout hypocotyl distribution comparisons, resulting in more stringent statistical tests.

A new *p*-value, subject to Bonferroni correction for multiple comparisons, is calculated using:

$$p_{corrected} = \frac{p_{original}}{m}$$

where $p_{original}$ is the original *p*-value to denote significance before correction, and m is the number of comparisons made.

2.6.4 Correlations

The coefficient of determination, R^2, was used to determine the degree of linear correlation between variables. The R^2 value represents how much variance in one variable can be explained using another variable, which is an indication of the relatedness of two measurements. This can take any value from 0 (no relationship between variables) to 1 (a perfect relationship between variables).

The correlation coefficient *R* was calculated using the scipy Python library, using the 'linregress' function to calculate a simple linear regression line. The value for *r* was then squared, resulting in the coefficient of determination, R^2.

2.6.5 Clustering

Clustering was used to classify hypocotyl cell types, using test statistics from pairwise χ^2 tests and Kolmogorov-Smirnov tests carried out with degree and betweenness centrality distributions, respectively, as a measure of distance. The Ward method for hierarchical clustering was used, which progressively merges data points into clusters, attempting to minimise the variance within each cluster. The Ward method was used due to the unsupervised nature of the algorithm, which reduces bias, and it's tendency to result in reasonably regular cluster sizes (Ward Jr, 1963). Three clear clusters were chosen using a clustering dendrogram, to group a

minimum of 90% of the data points into specific clusters (Hastie et al., 2009). The most dissimilar data points were not grouped into any cluster.

Hierarchical clustering was carried out using the scikit-learn machine-learning package for Python (Pedregosa et al., 2011), using the 'AgglomerativeClustering' function (relevant parameters: n_clusters = 3, linkage = 'ward').

2.6.6 Logistic regression

Logistic regression was used to classify non-dividing and dividing cells with factors influencing cell division in the shoot apical meristem. This was performed using R and the *glm2* (Marschner, 2011), *car* (Fox et al., 2012) and *ROCR* (Sing et al., 2005) packages. Data used was merged from all meristem samples to ensure a large enough sample size for logistic regression modelling. A high likelihood ratio, LR χ^2, for a particular measurement, indicates its usefulness in classifying cells that would and would not divide (Lemeshow and Hosmer Jr, 1982).

2.6.7 Coefficient of variation

The coefficient of variation was used to determine the normalised amount of variability in a measurement (Searls, 1964). Unlike comparing standard deviations, the coefficient of variation allows direct comparisons of variability between measurements that have vastly different scales.

The coefficient of determination c_v was calculated using:

$$c_v = \frac{\sigma}{|\mu|}$$

where σ is the standard deviation of a set of measurements, and $|\mu|$ is the absolute value of the mean.

The coefficient of variation was calculated using a Python script.

2.7 Visualisation

2.7.1 Topological property visualisation

To visualise topological properties of cells in tissues *in situ*, degree, betweenness centrality and random walk centrality values from topological analysis of the cellular connectivity networks were first saved as csv files, with associated cell labels. The mgxm mesh that the network was originally extracted from was then loaded into MorphoGraphX. The related topological analysis csv file was then imported into MorphoGraphX using the 'Import Heatmap' process, where the choice of measure to visualise could then be selected from a drop down menu.

Scales were adjusted for better discrimination between high and low values using the 'Heat Map Rescale' and 'Heat Map Scale' processes. The 'Heat Map Rescale' process was used to specify high and low limits of the heat map. The 'Heat Map Scale' process was used to switch between linear and logarithmic heat map scales where appropriate.

2.7.2 Network visualisation

To visualise parts of networks in 2D, subgraphs representing cross-sections of cellular connectivity networks were first extracted in MorphoGraphX, by selectively deleting cells in all but the region of interest before extracting the node labels to be visualised using the 'Heat Map' function. The original full cellular connectivity network was then imported in NetworkX, and all nodes except those listed in the extracted labels from MorphoGraphX were removed using a Python script. The remaining subgraph was visualised in 2D using the Python package NetworkX and the associated visualisation package Graphviz (Ellson et al., 2001). Edge properties were visualised using a heat map, displaying either physical cell interface size, or edge betweenness centrality.

Graphs were visualised and rendered in 3D using BioLayout3D/Miru (Theocharidis et al., 2009). To preserve node position in 3D network visualisation, a Python script was used to generate a native BioLayout3D file, a layout file. The layout file is a text file specifying nodes and edges in the cellular connectivity network, along with relevant metadata. Node metadata was used to specify each cell's position in 3D space, as well as the cell type. Edge metadata was used to specify the edge betweenness centrality of each edge, which could then be visualised in BioLayout3D/Miru as a heat map.

2.8 Cell division simulation

The 'DivisionAnalysis' MorphoGraphX plugin (Richard Smith group, Max Planck Institute, Germany, unpublished) was used to simulate cell divisions in the shoot apical meristem *in silico*. Cell divisions were simulated using information from earlier time points to predict the orientation of division plane in later time points.

2.8.1 Cell fusion

In the shoot apical meristem samples, as well as division, cell growth occurred during the 11 hours between both the T0 and T1, and T1 and T2 time point images. To make it possible to compare division plane predictions and real division planes, cells that divided between time points were fused in the T1 images to represent cell topology and geometry in the T0 time point, and likewise cells in the T2 images were fused to represent cell topology and geometry in the T1 time point. Cells were computationally fused in shoot apical meristem meshes, using the 'Fuse Cells' process in DivisionAnalysis.

2.8.2 Rules for simulating division

Four different rules were used to simulate cell division, using both geometric and topological features of the undivided cell. Irrespective of the rule used, divisions were restricted to being positioned no further than 0.2 μm from the cell centre. This was to correctly simulate the positioning of the majority of observed division planes in the shoot apical meristem, in line with previous geometric observations (Shapiro et al., 2015). All simulated division planes were also restricted to being perpendicular to the

surface of the meristem dome, replicating previous observations of exclusively anticlinal cell divisions (Bowman and Eshed, 2000).

Errera's rule for cell division (Errera, 1886), also referred to as the shortest wall rule, was simulated by finding the wall with the smallest surface area that bisected the cell. The degree minimisation rule found the division plane that minimised the degree of the daughter cells after division. Similarly, the random walk minimisation rule identified the division plane that minimised the random walk centrality of the daughter cells post-division. The Gibson rule identified the plane that bisected the neighbouring cell with the lowest degree, according to previous observations (Gibson et al., 2011).

In the case where multiple planes in the same cell satisfied the minimisation of degree, random walk centrality, or criteria for the Gibson rule, the wall with the smallest surface area was chosen.

2.8.3 Division order permutations

The order of divisions between each time point was unknown. Each cell division has topological consequences for both neighbouring cells, and cells distal to the newly divided cell. To compensate for the unknown orders of cell division and the effects on division predictions that incorporated topology, three permutations of division order were carried out for the degree minimisation rule, the random walk centrality minimisation rule, and the Gibson rule.

2.8.4 Comparing division planes

To make comparisons between the real and simulated division planes, each plane was manually isolated in MorphoGraphX, and saved as a txt file containing the 3D position of every vertex within the plane mesh. Each simulated and real division plane was imported into Python and converted into an infinite mathematical plane best representing the vertices, by minimising the sum of squares of the distance from each vertex to a mathematical plane using the SymPy package (Meurer et al., 2017). The normals of each mathematical plane were then calculated, and the angle between plane normals of the real and simulated planes was found using the 'angle_between' function in SymPy. This angle represented the degrees deviation between the simulated division plane and the real division plane.

CHAPTER THREE: CELLULAR ORGANISATION IN 3D ORGAN MODELS

3.1 Introduction

An enormous variety of forms of multicellular tissues and organs exist throughout living organisms. Plants utilise diverse growth strategies across different species, from the filamentous chains of cells in some algae (McCourt et al., 2004), to planar, ground-covering thallus development in *Marchantia* (Shimamura, 2015), to building up complex body plans of flowering land plants with intricate tissue structures (Harrison, 2017). This abundance of shapes and forms is also present in the animal kingdom, where multicellular metazoan forms range from the simple symmetrical body plans of the starfish, to the vast complexity of the human body (De Robertis, 2008).

Within both animals and plants, there is division of labour across an organism, compartmentalising processes and splitting tasks between organs, which are in turn made up of highly specialised tissues with specific functions. Within tissues, cells are arranged in particular patterns, formed by variation in cell size, position and shape (Koch and Meinhardt, 1994).

Cell organisation is conserved both within individuals of similar species, and often across diverse evolutionary clades (Lohmann and Weigel, 2002) (Arnold and Robertson, 2009). Where cell patterning is perturbed, loss of the normal function of an organ is often observed (Couso et al., 1994) (Byrne et al., 2000) (Helariutta et al., 2000), and in an extreme example, normal cell patterning is lost in cancerous tissues (Moore et al., 2017). It is therefore of biological relevance to study cell patterning and organisation, and to link these structural features to tissue and organ function.

3.1.1 Qualitative assessment of cellular patterning

Many efforts have been made to elucidate the underlying mechanisms of how cellular patterns and organisation are formed in tissues through cell division (Besson and Dumais, 2011), migration (Forgacs and Newman, 2005) and programmed death (Gunawardena, 2007). However, the way in which cell organisation affects the function of an organism, and the emergent properties of cell patterning, are poorly understood due to limited qualitative descriptions (Jackson et al., 2017a).

Because there are consequences of cell arrangement in tissues, it is of biological relevance to have a quantitative framework with which to measure organisation, and compare tissues. In the developmental biology field, it is common to qualitatively compare the cell organisation or patterning in tissues. For example, qualitative comparison is used to compare the organisation of cells in mutant fruit fly (*Drosophila melanogaster*) imaginal discs (Tabata and Kornberg, 1994), and patterning in the *Arabidopsis thaliana* root meristem (Aida et al., 2004) to characterise the phenotypic effects of various mutations. More recently, cells in various mutant mouse corneal epithelial tissues were qualitatively referred to as ‘disorganised cells’ (Panzica et al., 2017). While in each of these cases (and many more), the identification of binary ‘order’ or ‘disorder’ in cell patterning is a relevant feature of a mutant phenotype, cell patterning mutants would be directly comparable using a quantitative measure of organisation. A quantitative method for measuring cell organisation would also allow deeper insight into exactly how the cell patterning in a particular system was disrupted.

With a quantitative measurement of cell patterning, it may also be possible to gain insights into why cellular structure is arranged in certain configurations. Identifying cells that make unintuitive physical links between other cells, or parts of a tissue, would be possible using a non-biased quantitative approach. This would represent a first step in understanding how the structure of a tissue contributes to the function it performs (Jackson et al., 2017a).

3.1.2 Abstracting cell connectivity into networks

Networks are used to represent complex systems with many interacting components. For example, they are often used in the representation of protein-protein interactions, in the field of proteomics (De Las Rivas and Fontanillo, 2010) (Szklarczyk et al., 2014) (Rajagopala et al., 2014). In protein-protein interaction networks, nodes represent the interacting agents, proteins. The interactions between proteins are represented by edges, connecting two nodes (Xia et al., 2014). These networks can be used to make predictions about which proteins form complexes (Brohee and Van Helden, 2006), as well as to isolate families of proteins that are characterised poorly in order to direct further research (Huttlin et al., 2015), and even to predict the onset of cancer (Taylor et al., 2009) using simple graph theory analyses.

At a much larger scale, networks are also used to model a wide range of ecological interactions between species (Jordán and Scheuring, 2004). In ecological networks, nodes can be used to represent an entire species, while edges are representative of antagonistic or synergistic interactions between different species in a given

environment (Bascompte, 2007). The use of networks in ecology predated their use in the field of protein-protein interactions (Paine, 1966), and contributed to the now widely accepted view that most pairwise interactions between species do not occur in isolation, but rather as part of a greater ecosystem (Proulx et al., 2005). Ecological networks have been used to show that in there are an increased number of generalist pollinators in ecosystems where plant species richness is high (Olesen and Jordano, 2002), as well as to model the cascading effects of individual species extinctions on the wider ecosystem (Dunne et al., 2002)

In between these scales, at the organ level, the same network abstraction can be made with physically interacting cells. Here, a cell can be represented as a node, while the physical interactions between them are represented by an edge (Figure 3.1). This results in the generation of a cellular interaction network.

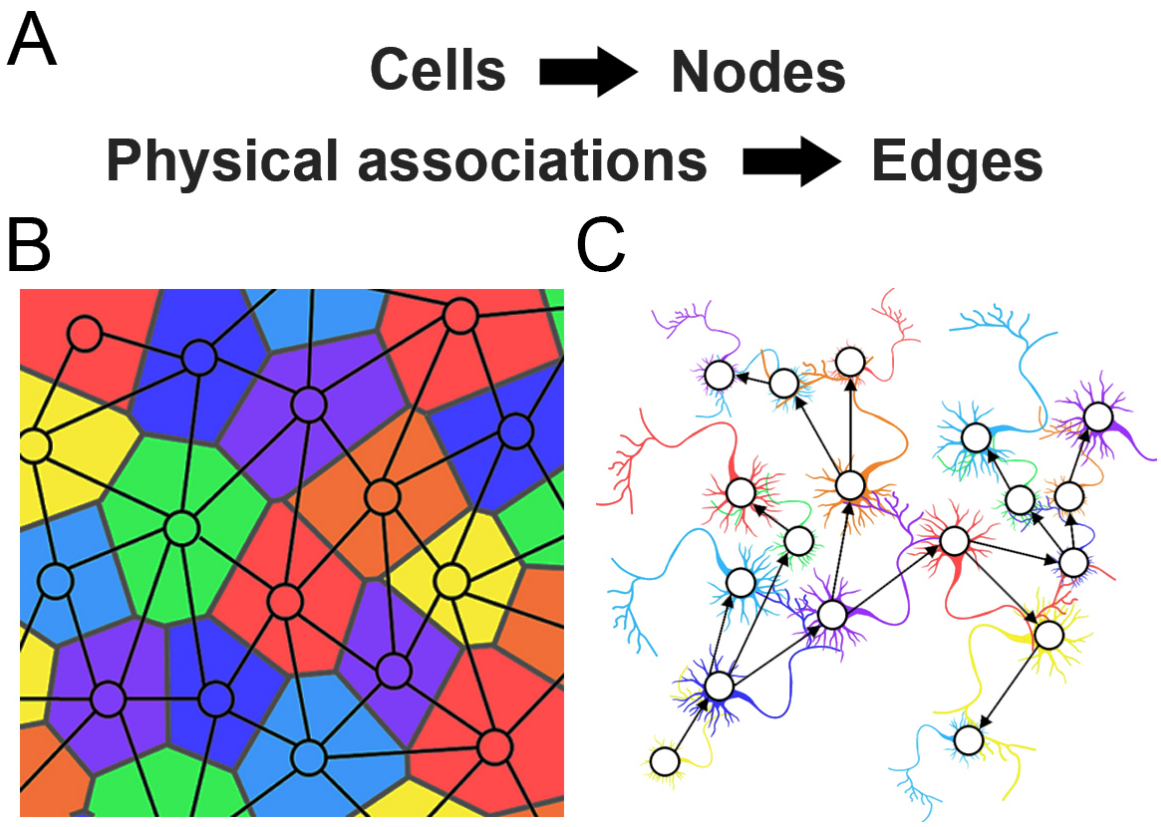


Figure 3.1. Abstraction of cellular assemblies into cellular connectivity networks. (A) Making a map of cellular interactions involves representing cells as nodes, and representing the physical interactions between cells as edges. (B) An example diagram of a cellular connectivity network in plant or animal epithelia. (C) An example diagram of a cellular connectivity network of interactions between neurons, where information flows directionally from axons to dendrites. Figure reproduced from Jackson et al. (2017), *Journal of the Royal Society Interface*.

Building on hand drawn diagrams of nervous system cell connectivity (y Cajal, 1894), an early example of a cellular interaction network is the full mapping of all neuronal cell connections in the nematode worm, *Caenorhabditis elegans*, using electron microscopy of serial sections (White et al., 1986) as previously mentioned in Section 1.4. The nervous system map, consisting of 302 neurons, could be represented as a directed network, where signals are passed from axons to dendrites, which through synapses deliver signals to other axons (Figure 3.1C). This work allowed hypotheses

to be made about the function of certain neurons, such as those related in touch sensitivity, using information solely from the network structure (Chalfie et al., 1985).

3.1.3 Quantifying tissue organisation in neuroscience

The complete map of the *C. elegans* nervous system paved the way for studies of nervous system connectivity in other systems, as better imaging techniques and more powerful computers become available (Emmons, 2015). Often referred to as 'connectomics', the study of how different regions of the brain interact, and how this relates to brain function, is now a rapidly expanding field of research (Morgan and Lichtman, 2013) (Sporns and Bassett, 2018). In the connectomics field, network science is used to quantify the organisational properties of regions of the brain.

Using fMRI scanning, regions of the brain that are activated simultaneously, or in quick succession, can be identified (Smith et al., 2013). Using this information, maps of associated brain regions can be inferred and drawn, represented by a network. From these kinds of networks, ways in which interacting regions of the human brain dynamically change during the performance of different tasks have been shown (Bullmore and Bassett, 2011). The structures of brain networks have also been used to suggest regions of the human brain that have high control capacity through the identification of 'hubs', regions of the brain that share more connections with other brain regions than average (van den Heuvel and Sporns, 2013). Hubs were identified in the cerebral cortex, meaning that damage to these regions is likely to have drastic consequences for overall brain function.

There are however clear limitations to this technique for building network maps of brain activity. Networks built through fMRI scanning, often referred to as ‘mesoscale’ networks (Zeng, 2018), lack cellular resolution, despite our knowledge that individual neurons are the units that transmit information throughout the brain (y Cajal, 1888) (López-Muñoz et al., 2006). While it has been suggested that interactions between neuron ensembles operate at a multi-neuron level (Alivisatos et al., 2012), the image resolution possible with fMRI scanning is far more coarse-grained than even this level of detail (Van Essen and Ugurbil, 2012). This means that potential complex interactions between neurons, or groups of neurons, are likely overlooked using this method. While conclusions about how whole regions of the brain interact can be drawn with mesoscale networks, coarse-graining of actual brain network structure prevents cellular-scale insights into the structure-function relationships within the brain.

Though collection of cellular resolution data is currently limited by image acquisition and image reconstruction methods (Helmstaedter, 2013), some data of this nature has been successfully collected. Outside of studies into the human brain or *C. elegans*, parts of the *Drosophila melanogaster* brain have been successfully imaged at cellular resolution (Chiang et al., 2011). The *Drosophila* brain is estimated to contain around 100,000 neurons (Schröter et al., 2017). About 16,000 neurons in the *D. melanogaster* brain were imaged using multicoloured cell labeling and light microscopy, and a network of cellular connectivity was constructed (Chiang et al., 2011). Analysis of the network revealed hierarchical modular structure in brain regions associated with sensory processing, along with ‘small-world’ properties,

where a few select neurons are connected to thousands of others, while most have connections to a far smaller number (Shih et al., 2015).

Although detailed, this cellular connectivity map is incomplete. Because of limitations of the imaging method as well as the limited power in computational identification of individual neurons (Chiang et al., 2011), the imaged part of the *D. melanogaster* brain is taken out of the whole-tissue context. This could have consequences for analyses performed on the extracted neuronal map, as there is no knowledge of whether parts of the network are, in reality, connected to important parts of the *Drosophila* brain. Therefore, interesting features present in the true cellular connectivity of the tissue could easily be missed. Additionally, there is no guarantee that the imaged portion of the brain is representative of other regions, as different brain regions are reported to have very different coarse-grained neural structures (Finlay et al., 2001) (Waskom and Wagner, 2017).

3.1.4 Quantifying organisation in other tissues

Outside of the network neuroscience field, the study of cell connectivity is largely focused on epithelial organisation. It was observed in the 19th century using simple light microscopy that cells in many epithelial tissues pack in a honey-comb like structure (Schwann, 1847). More recently, by tracking the local cell-cell connections in the epithelia of the freshwater cnidarian *Hydra*, *Drosophila* imaginal wing disks and the *Xenopus* tail, this hexagonal cell patterning was found to be an emergent property of cell proliferation and the constraints of cell adhesion (Gibson et al., 2006).

The organisation of cells in epithelia of different tissues in both chick and *Drosophila* were later characterised more thoroughly, using standard network science measurements to compare cellular patterning (Escudero et al., 2011). After abstraction into a network, the number of neighbours each cell had, known as the degree, was calculated for each cell, along with the average degree of a cell's neighbours and the clustering coefficient of each cell, a measure of the local cell packing. This revealed that different types of epithelia had distinct, reproducible, cell patterning features.

Voronoi diagrams have been used to capture the subtly different organisational properties of diverse epithelia (Sánchez‐Gutiérrez et al., 2015). Voronoi diagrams are constructed by placing seed points in space, then allowing each point to expand and claim as much space as possible, until all expanded points are tessellated (Fortune, 1995). It was observed that epithelia from many diverse species and tissues had similar polygonal class, or degree, distributions to sets of Voronoi diagrams with increasingly ordered seed points. Interestingly however, degree distributions measured in epithelial cell patterns, from mutant backgrounds and diseased tissue, could not be approximated by any Voronoi diagram. This suggests that quantitative measurement of cellular organisation has applications in diagnosis of diseases causing tissue abnormalities.

There are however drawbacks to the study of epithelia in isolation, and the statements that can be made by measuring their cellular connectivity. In many cases, where tissue is not completely two-dimensional in nature, epithelial cells are taken

out of context in terms of their physical relationships with cells below them. Imaging constraints in the outlined studies prevent the acquisition of cellular-resolution tissue structure below the epithelia, so conclusions must be made with no knowledge of how 3D cellular interactions may affect both the structural aspects and functional properties of epithelia imaged in isolation.

3.1.5 Advances in 3D image acquisition and processing

The argument can be made that without whole, representative structures of cellular connectivity, or with coarse-graining of organisation in networks, it is difficult to link tissue and organ structure to function.

Recent advances in imaging have allowed three-dimensional imaging of entire plant tissues and organs. Using tissue fixation, fluorescent staining, and high-resolution confocal microscopy, the structure of the entire *Arabidopsis* embryo has been captured at cellular resolution, at multiple stages of development (Yoshida et al., 2014), as well as enabling the capture of cellular resolution images of the entire hypocotyl, the embryonic stem (Stamm et al., 2017). Technological improvements in semi-automated image segmentation and registration technology allow the conversion of these images into digital formats, from which every physical cell interaction can be extracted (de Reuille et al., 2015) (Montenegro-Johnson et al., 2015). Using this information, fully accurate, cellular resolution, cell connectivity networks can be constructed (Jackson et al., 2017a). The structure of these networks can then be quantitatively analysed, to try to understand the functional relevance of 3D cell organisation.

3.1.6 Structure and function in networks

Structural networks are often rich in information by their very nature, and a wide range of network science, or graph theory, algorithms exist to measure their organisational properties (Rubinov and Sporns, 2010) (Barabási, 2016).

Exploring the structure of a network can give us insights into its function. To illustrate, the rail system of the Birmingham area can be represented as a structural network where stations are nodes, and direct routes between stations are edges (Figure 3.2A) (Jackson et al., 2017a). New Street Station is a hub node, a node that has a high number of connections to other nodes.

Overlaying additional information onto edges, such as the number of trains running between stations, or the average speed of trains, results in the generation of a functional network (Figure 3.2B and C). From visual inspection, there are higher numbers of trains running between the New Street Station hub node and other stations, than on average between other pairs of stations (Figure 3.2B). Lastly, the speed of trains running near New Street Station is slower than on average (Figure 3.2C). Here, the structure of the Birmingham rail network has a large influence over its function.

Importantly, the structural nature of New Street Station and its many surrounding stations is purposefully designed to make rail transport around Birmingham more efficient. It is therefore no surprise that this designed structural property leads to a

high number of trains passing through the station, allowing an increased number of passengers to travel to their destinations in a given time period. Additionally, the low speed of trains running through New Street Station is possibly an emergent property of high traffic through the station, as well as a feature of the short train lines linking this station and others nearby.

While we can assume that the Birmingham rail system structure was designed to be as efficient as possible, evolution has driven the design of cellular organisation, and we do not strictly know the design principles that have been selected for. Therefore, an approach to measuring cellular patterning and organisation that uses multiple measures than degree alone is appropriate.

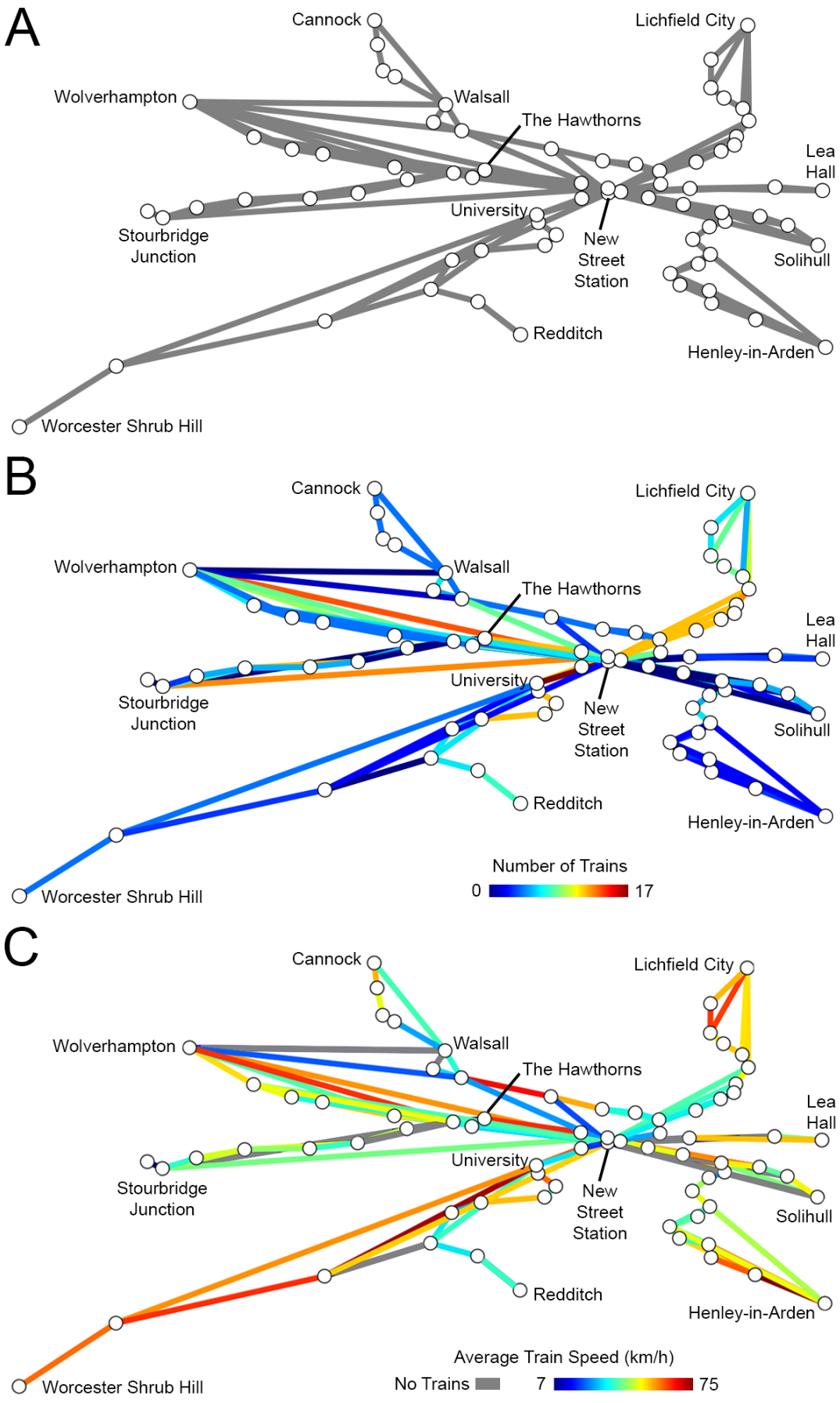

A
Cannock
Lichfield City
Wolverhampton
Walsall
The Hawthorns
Lea Hall
University
Stourbridge Junction
New Street Station
Solihull
Redditch
Henley-in-Arden
Worcester Shrub Hill
B
Cannock
Lichfield City
Wolverhampton
Walsall
The Hawthorns
Lea Hall
University
Stourbridge Junction
New Street Station
Solihull
Redditch
Henley-in-Arden
Worcester Shrub Hill
Number of Trains
0
17
C
Cannock
Lichfield City
Wolverhampton
Walsall
The Hawthorns
Lea Hall
University
Stourbridge Junction
New Street Station
Solihull
Redditch
Henley-in-Arden
Worcester Shrub Hill
Average Train Speed (km/h)
No Trains
7
75

Figure 3.2. Structural and functional network representations of the Birmingham (UK) rail system.
(A) The structure of the Birmingham rail network, where nodes (circles) represent individual stations, and edges (lines connecting circles) represent direct rail routes that can be taken between stations. (B) A functional annotation of the Birmingham rail network, overlaid with a heat map showing the number of trains over the period 8.00 to 10.00 A.M. on a weekday. (C) A functional annotation of the Birmingham rail network, overlaid with a heat map showing the average speed of trains over the period 8.00 to 10.00 A.M. on a weekday. Figure reproduced from Jackson et al. (2017), *Journal of the Royal Society Interface*.

3.1.7 Measuring organisation in 3D cell interaction networks

Like in rail networks, the structural organisation of cells may influence the functional properties of a tissue as a whole. The organisation, or the topology, of cellular networks can be measured at both local and global scales. At the local scale, we can gain insight into the immediate neighbourhood of a cell, the physical interactions that one cell makes. At the global scale, the contribution of individual cells to overall connectivity throughout the system can be measured. Standard network science measurements can be used to analyse the local and global connectivity of cells in cellular connectivity networks (Jackson et al., 2017a).

The degree of a cell is a simple measure of local connectivity, identical to the number of neighbours a node in a network has (Figure 3.3A). In terms of a cellular connectivity network, this is the number of cells that are physically connected to each cell. In the epithelial work discussed earlier, this is equivalent to the polygonal class of a cell, and was used to classify two-dimensional epithelial patterning (Escudero et al., 2011), as well as to inform general principles of cell proliferation driving cellular organisation (Gibson et al., 2006).

Another commonly used measure of connectivity in a network is betweenness centrality (Freeman, 1977) (Brandes, 2001) (Figure 3.3B). This differs from degree in that it is a global measurement, and its calculation takes into account the entire network. The betweenness centrality of a node is measured by finding the shortest path between all pairs of nodes in a network, and counting how many times any particular node lies on a shortest path. Betweenness centrality identifies optimal routes of transport throughout the cellular network, using knowledge of the position of every cell in the system. Where betweenness centrality is particularly high, the measure also has the ability to identify cells that have an increased capacity to control movement of information due to the cellular connections that they make. In network science, these types of nodes are commonly referred to as 'information brokers' (Haythornthwaite, 1996).

Random walk centrality is another global measure of connectivity in a network (Newman, 2005) (Figure 3.3C). Similarly to betweenness centrality, random walk centrality also finds paths between all pairs of nodes, though the shortest paths do not have to be taken. Its calculation involves agents, 'random walkers' (Noh and Rieger, 2004), that randomly move between connected nodes until they find a complete path from a starting node to their destination. This is performed for every possible path between each pair of nodes with no knowledge of the network layout, making it more similar to a diffusion process across a network. In terms of a cellular network, random walk centrality captures how the passive movement of a mobile

signal might traverse a tissue, similar to the movement of morphogens in development (Gurdon and Bourillot, 2001).

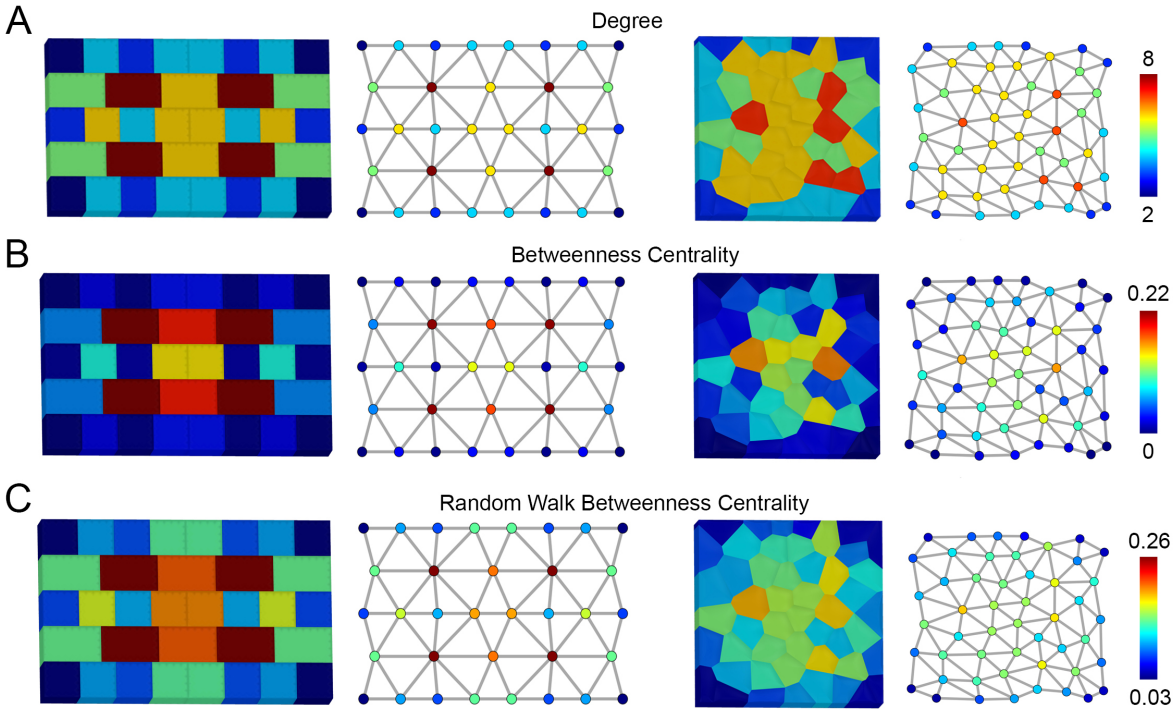


Figure 3.3. Topological measurements of cellular connectivity networks.
(A) Example model tissues and their associated cellular networks, false coloured with degree. (B) Cellular networks, false coloured with betweenness centrality. (C) Cellular networks, false coloured with degree random walk centrality. Figure reproduced from Jackson et al. (2017), *Journal of the Royal Society Interface*.

As well as measuring properties of individual cells within a cellular connectivity network, the concept of network efficiency can be used to describe the network as a whole. Efficiency of a network can be measured at both local and global scales (Bullmore and Sporns, 2009).

Global efficiency is related to the average length of paths between pairs of nodes (Latora and Marchiori, 2001). A high global efficiency represents a high capacity for transport between all nodes, where a graph containing connections between every pair of nodes has the highest possible global efficiency. The measurement of global efficiency shares features with global centrality measurements across a system, where a cellular connectivity network containing long cells that spanned large regions of the tissue connecting many cells, like the vasculature in land plants (Cho et al., 2017), would have a high global efficiency, as well as a high betweenness and random walk centrality in the highly connected vascular cells.

In contrast, local efficiency is a measure of how robust a network is to perturbation or damage (Latora and Marchiori, 2001). High local efficiency in a cellular connectivity network would indicate a cellular structure that could still properly operate in terms of information transport throughout the tissue, if cells were removed. Because of this, local efficiency is a good measure of the resilience, or robustness, of a system (Boccaletti et al., 2006). This is a particularly relevant feature in cellular connectivity networks, as many tissues are susceptible to localised damage and cell death, for example through infection (Takizawa et al., 1993), or in the case of plants, herbivory (Goggin, 2007).

In many real world networks, local efficiency is often inversely related to global efficiency (Latora and Marchiori, 2001). The presence of a very short path connecting many distant cells in a network makes a network highly susceptible to damage along that particular path, resulting in high global, but low local efficiency. Measuring local

and global efficiency in cellular connectivity networks can give us insight into the role that cellular organisation might play in a tissue, where evolution has promoted the construction of either highly transport efficient, or highly robust networks (Jackson et al., 2017a).

In each case, these topological measurements allow quantification of cellular patterning and organisation, enabling topological phenotyping of tissues, and comparison of tissue structure between different organs and species. Importantly, these measures cannot necessarily be used to model specific biological process, but rather inform us about the possible routes that information in biological processes can take. It is through identification of these non-intuitive patterns present in cellular organisation, that insight into possible structure-function relationships is gained.

To better understand how the cellular structure of 3D organs affects cell connectivity at both local and global scales, simple model organs with varying properties were constructed and analysed. Topological measurement of these organs will give insight into design principles used in the development of 3D tissues, leading to the understanding of how cellular structure might provide different organ-wide functional properties.

3.2 Results

Models for topological analysis were constructed using MorphoGraphX and the CellMaker plugin (Section 2.3), made with varying parameters. 30 replicate models

were created for each set of parameters used. To measure cellular organisation within these models in a quantitative manner, the cellular connectivity network of each model was extracted (Section 2.2.5) and topological analysis was used to examine the structure of each network (Section 2.4). Degree, betweenness centrality (BC) and random walk centrality (RWC) were calculated for each cell in each model, to determine the contribution of each cell to both local and global organisation (Section 2.4.1). The average degree, BC and RWC was determined for each model, in addition to the variability of these measurements amongst cells in an individual model, the coefficient of variation (Section 2.6.7). To further characterise the structure of a network, the local and global efficiency of each cellular configuration was measured (Section 2.4.6).

3.2.1 Topological effects of increasing the number of cells in an organ

A series of models was constructed with increasing numbers of cells, from 4 to 512 (Figure 3.4). Different numbers of uniformly distributed random centroid positions were Voronoi tessellated to produce different configurations of connected cells (Figure 3.4C).

In extracted networks of cellular connectivity, there was a strong relationship between the number of nodes, and number of edges, as the size of models increased (Figure 3.4B). The linear correlation observed in a log-log plot suggests that this relationship is scale invariant, and the existence of a power law relating the number of nodes and edges in these models, a common property in many randomly generated networks (Barabási and Albert, 1999).

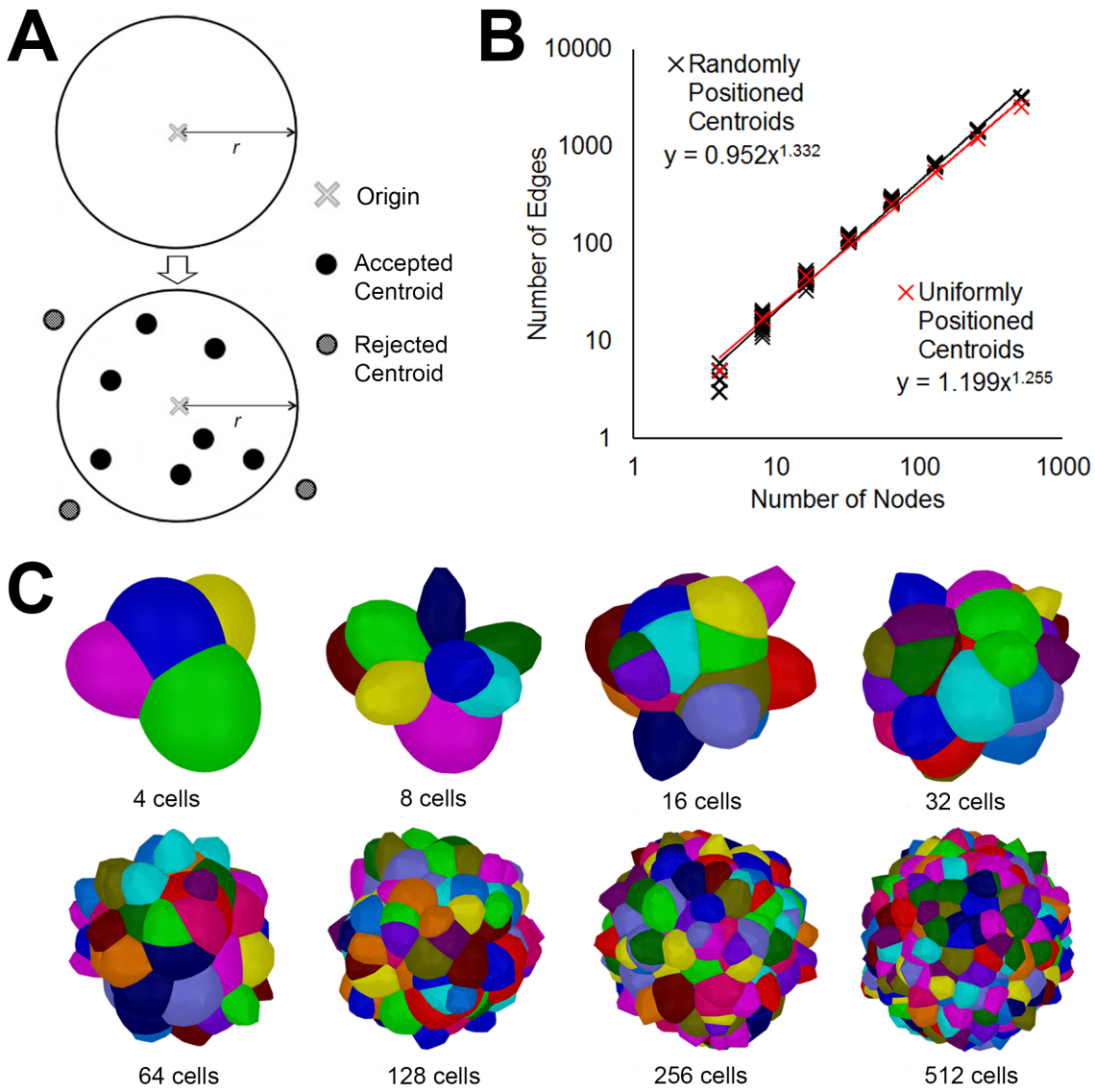


Figure 3.4. Construction of random 3D Voronoi organ models with increasing size. (A) Schematic of determining the position of centroids within a sphere. Centroids were generated in a cube, double the length, width and height of the sphere radius. Centroids falling outside of the sphere were rejected, while centroids inside of the sphere were accepted, until the desired number of centroids was reached. (B) Numbers of nodes and edges in extracted 3D Voronoi organ model cellular connectivity networks, in a $\log_{10}$-$\log_{10}$ plot. (C) 3D Voronoi organ model meshes with different numbers of cells, rendered in MorphoGraphX.

To begin to examine the topological properties of these cellular configurations, network analysis measurements of each cell in models were overlaid onto organ meshes as a heat map (Figure 3.6). The heat maps provide an indication of the spatial distribution of graph measurements in models.

The range of the degree of cells increased around 4-fold as the number of cells in a model increased (Figure 3.5A). Organ models containing very low numbers of cells are limited strongly in the number of cell-cell connections they can make. As the number of cells increases, an increasingly clear distinction between the degree of cells on the surface and in the centre of models can be made.

While the degree and RWC of cells is fairly normally distributed in most models, the distribution of BC was non-normal and long-tailed (Figure 3.6). To enable the comparison of BC between cells in these models, BC was transformed to $\log_{10}$ BC (Figure 3.6B and C) (Section 2.4.4). This resulted in a more normal distribution in $\log_{10}$ BC, also allowing the calculation of mean averages later on in this section.

In models with few cells, log BC is consistently high across all cells, while in models with large numbers of cells there is qualitatively more variability (Figure 3.5B). This is due to how BC is normalised across networks. In the calculation of BC, the shortest paths are found between all pairs of cells, and then subsequently normalised by the number of possible paths in the graph (Section 2.4.3). As a consequence, in cellular interaction networks between small numbers of cells, a minority of cells are located in most paths between nodes, resulting in very high log BC.

Because BC finds the absolute shortest paths between pairs of nodes, in models with just 4 cells there are cells that are never traversed, resulting in a BC of 0 (and therefore an incalculable log BC) (Figure 3.5B). In a biological system optimised for transport efficiency, of this size, these cells would not be involved in the transduction of signals between other pairs of cells.

In the global topological measurement of BC, there are also signs of a distinction between the core and periphery of the cellular connectivity network in some models (Figure 3.5B). As with degree, a difference between BC in the model surface and core becomes apparent in models with 64 or more cells.

The calculation of RWC shares features with BC, in that paths between cells are determined, and cells that lie on short paths have a higher RWC (Newman, 2018). There are qualitative similarities between the two global topological measurements across this set of models (Figure 3.5C). However, as RWC does not always locate the shortest paths between nodes, but rather identifies all paths between nodes, cells in the 4 cell model that have a BC of 0 have a value for RWC. Here, RWC is high in cells that lie on shorter paths, and longer valid paths are penalised according to their length, resulting in lower RWC.

The maximum values of RWC are lower in models with higher numbers of cells. This is due to the same weighting effect as discussed in the calculation of BC (Figure

3.5C). The same topologically distinct core and peripheral cell layer are present in heat maps of RWC, though qualitatively not as obvious as those in degree and BC.

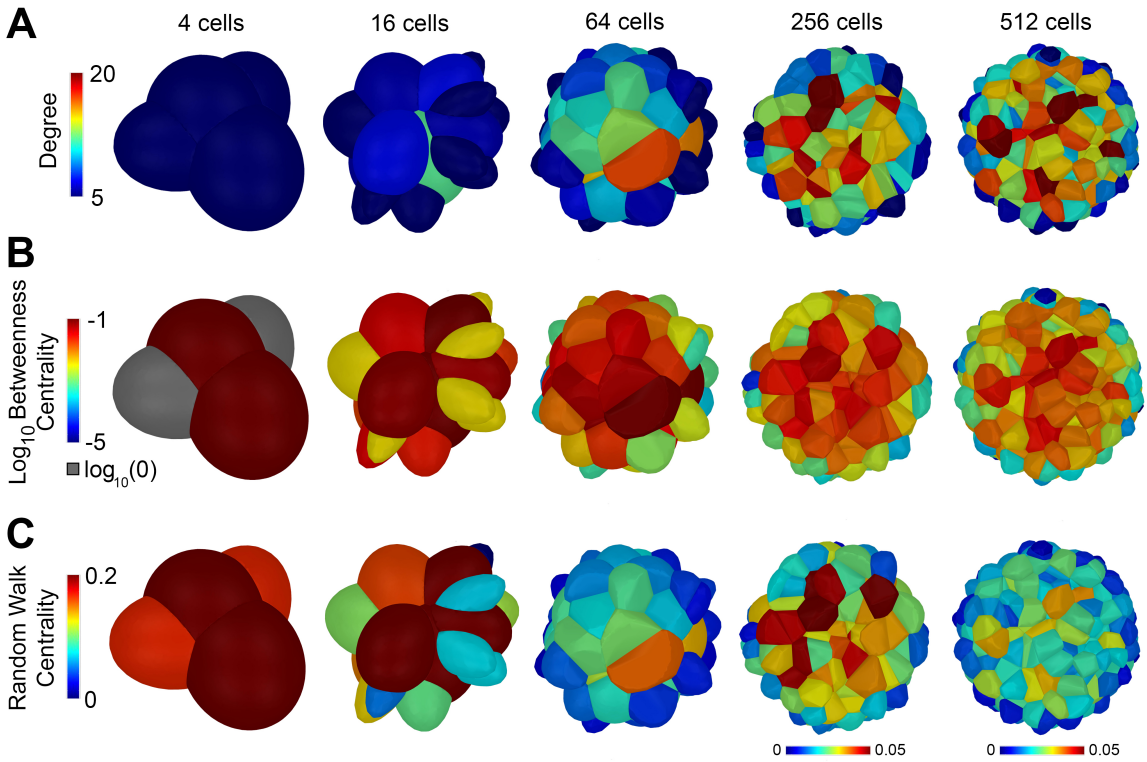


Figure 3.5. Spatial distribution of topological properties in randomly generated Voronoi models with increasing numbers of cells.
(A) Models false coloured with a heat map of degree. (B) Models false coloured with $\log_{10}$ betweenness centrality. Grey cells represent nodes with a betweenness centrality of 0, making it impossible to calculate the $\log_{10}$ betweenness centrality in those cells. (C) Models false coloured with random walk centrality. The surface is displayed of models with 4 and 16 cells, while cross-sections are shown in models with 64, 256 and 512 cells.

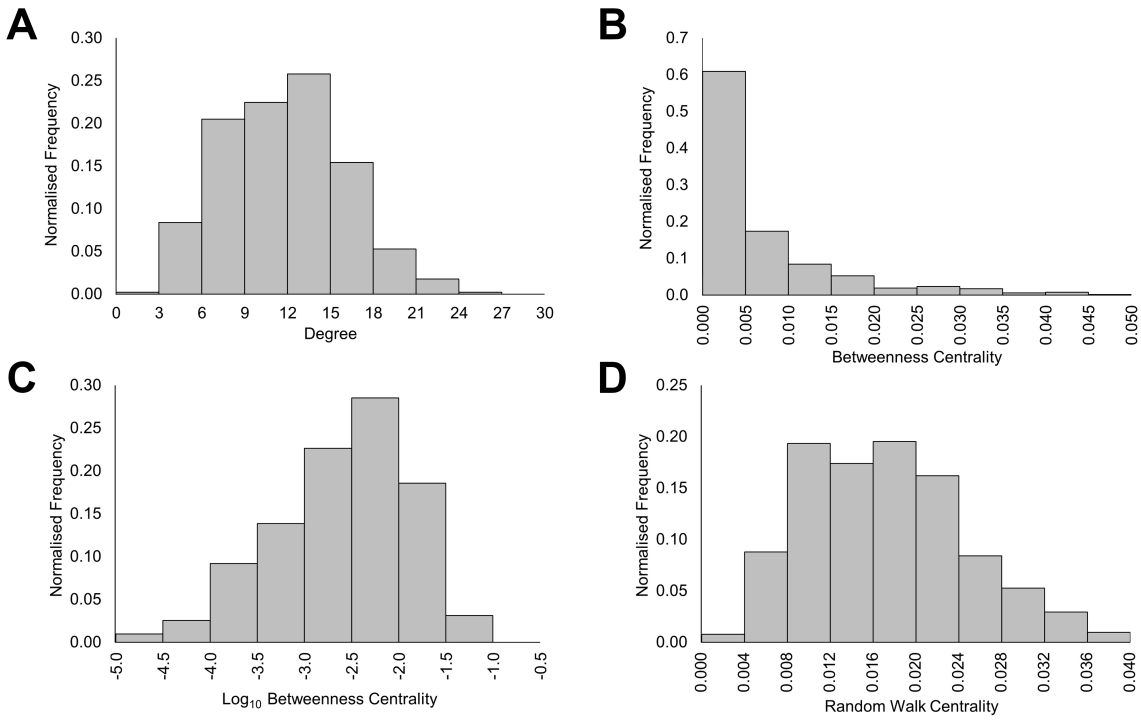


Figure 3.6. Distribution of topological properties in a 3D Voronoi model.
(A) Normalised frequency of cell degree in a model with 512 cells. (B) Normalised frequency of betweenness centrality. (C) Normalised frequency of $\log_{10}$ betweenness centrality. (D) Normalised frequency of random walk centrality.

To fully isolate the nature of patterning quantification in models with increasing numbers of cells, a separate set of models of increasing size were created where there was no random positioning of nodes, and no Voronoi tessellation used (Figure 3.7). Instead, uniformly shaped polyhedrons were stacked in staggered lattices, so that any individual cell completely surrounded by other cells on all sides would have exactly 12 immediate neighbours Indeed, the maximum degree of any cell within these lattice models was 12 (Figure 3.7A).

Analysis of the spatial distributions of topological properties in the lattice models reveals both similarities and differences to the random centroid Voronoi models. The

existence of topologically distinct epithelia is clearer in the lattice models, where degree, log BC and RWC are all considerably lower in the periphery of structures with 16 or more cells (Figure 3.7). However, the distribution of each cell connectivity network measurement within the core of the lattice models has far less variation, particular in the local measurement of degree, which is completely invariant (Figure 3.7A). In models with at least 64 cells, there is a subtle bias in both log BC and RWC for cells in the centre of the lattice models, a feature that is not apparent in the random Voronoi models (Figure 3.5).

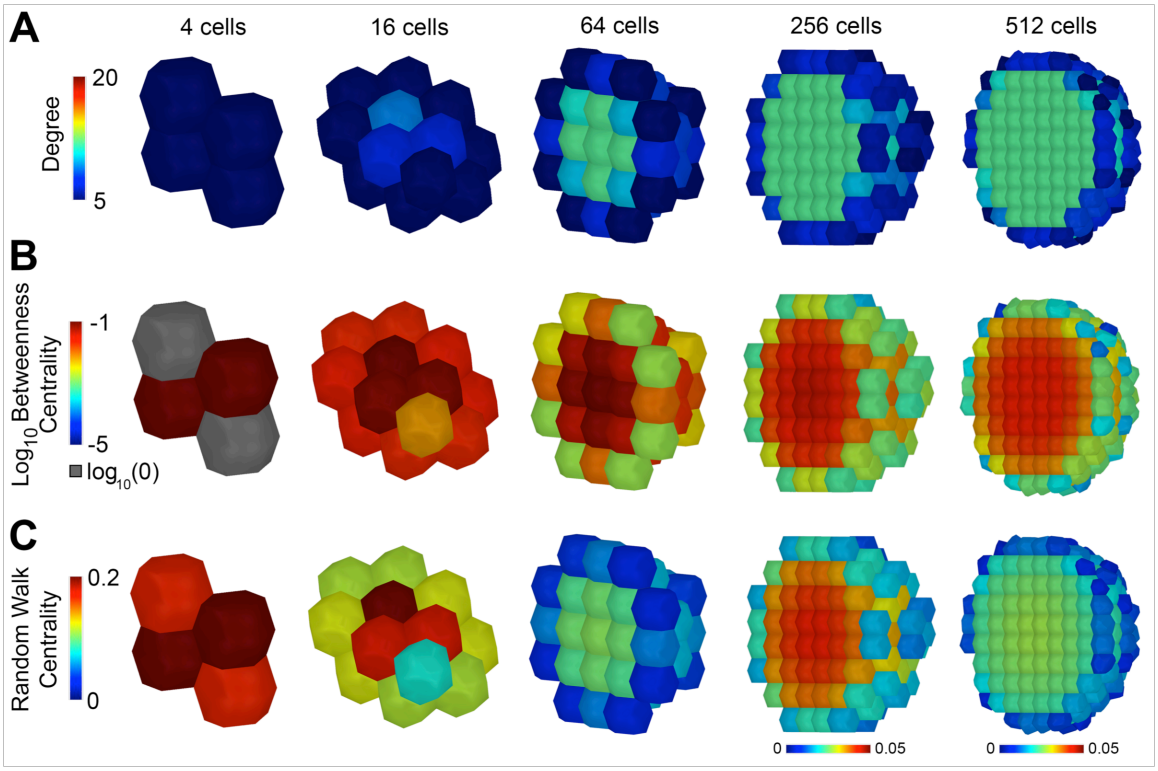


Figure 3.7. Spatial distribution of topological properties in staggered lattice models with increasing numbers of cells.
(A) Models false coloured with a heat map of degree. (B) Models false coloured with $\log_{10}$ betweenness centrality. Grey cells represent nodes with a betweenness centrality of 0, making it impossible to calculate the $\log_{10}$ betweenness centrality in those cells. (C) Models false coloured with random walk centrality. The surface is displayed of models with 4 and 16 cells, while cross-sections are shown in models with 64, 256 and 512 cells.

Further insights can be made about how the structure of models relates to topological properties using data from replicate models. Kernel density estimate plots were used to visualise summary statistics of topological measurements across 30 models for each parameter set (Figure 3.8). Both the mean average measurement, and the coefficient of variation (CV) (Section 2.6.7) of a measurement are used to characterise organ models. The coefficient of variation is a normalised measure of variability of a measurement within a property of a model. For example, the CV of degree in the 512-cell random Voronoi model (Figure 3.5A) would be higher than the CV of degree in the 512-cell lattice model (Figure 3.7A). This is because out of these two models, a higher overall variation in cell degree is observed in the Voronoi model.

As the number of cells in models increases, the average degree increases (Figure 3.8A). This is likely a consequence of larger models having fewer surface cells, with more cells surrounded by others on all sides in the centre of the organ (Figure 3.5A). The CV of degree increases with the number of cells in models up to around 32 to 64 cells, and then begins to decrease as models become larger still (Figure 3.8A). It is possible that this is due to the establishment of the core-periphery distinction in models with more cells, as variability within the centre of the models, containing more and more of the total model cells, becomes lower (Figure 3.5A).

In this analysis of log BC, the 4-cell models were excluded due to inability to calculate averages with measurements of $\log_{10}(0)$. Average log BC fell steadily as the number of cells in models increased, as individual cells lay upon a decreasing amount of paths between other cell pairs (Figure 3.8B). Cells in smaller models bear a heavier load in terms of the fraction of information transport possible throughout the cellular connectivity network. Like the trend observed in the CV of degree across cells in different models, the CV of log BC increases as cell number is raised from 4 to around 32, then begins to decline as the surface becomes topologically distinguished from the centre of the Voronoi models (Figure 3.5B).

Similar to observations of log BC, the average RWC falls steadily each time the number of cells in models is doubled (Figure 3.8C). Individual cells in larger model models fall on fewer paths between other cell pairs, because in a cellular connectivity network with more cells, there are more options of paths to take. In contrast to the CV of degree and log BC, the CV of RWC decreases as the number of cells in random Voronoi models increases.

In addition to summary statistics of topological measurements across the models, the whole-network local and global efficiencies were calculated in models with different cell numbers (Figure 3.8D). Aside from the difference in 4-cell and 8-cell models, increasing the number of cells in Voronoi models had very little effect on the local efficiency of the cellular networks they formed, meaning there was no large increase in network robustness as more nodes were introduced. This is likely due to the constraints of 3D space in the creation of these models, where models are unlikely to

form structures that can be easily perturbed by the elimination of some cells in the calculation of local efficiency (Section 2.4.6). Instead, similar to patterning in many biological tissues (Sánchez‐Gutiérrez et al., 2015), Voronoi tessellation produces cells that grow to fill all available space, producing enough connections to withstand random damage. In contrast, some 4-cell models had a filamentous structure, resulting in a one-dimensional extracted cellular network. Local efficiency in these networks is very poor, as the elimination of cells in the centre of the filamentous chain results in a complete fragmentation of the organ, eliminating cellular communication throughout the system. The low local efficiency of these models can be observed at the left of the 4-cell kernel-density estimate (Figure 3.8D).

Contrastingly, global efficiency decreased steadily as the number of cells was increased (Figure 3.8D). Global efficiency is related to the average length of paths between pairs of nodes. As an organ increases in cell number, the distances between cells become larger and the number of cells that must be traversed to pass information between the most distal parts of the system increases, with a potential cost to transport efficiency. However, at smaller model sizes of 4 to 8 cells, without random cell positioning, there is a clear optimisation choice between robustness of a cellular connectivity network (local efficiency), and the speed of transport across the system (global efficiency). Tight control of cell positioning, often observed throughout real biological tissues (Lecuit and Lenne, 2007) (Fisher and Sozzani, 2016), could ensure suitable optimisations of either local or global efficiency in cell communities, depending on the functions a tissue must perform.

Throughout all topological measurements, a reduction in the spread of the average and CV is observed within the replicates, as the number of cells in models is increased from 4 to 512 (Figure 3.8). The same is true for the variability in local and global efficiency across models. Randomly placing centroids for each cell and performing 3D Voronoi tessellation with low numbers of points means that 'extreme' topologies such as filaments and fully connected networks, where all cells are connected to all other cells, are much more common (Brede, 2010). With more cells, the probability of observing these types of arrangements becomes increasingly unlikely. However, it is possible that in systems where neither growth or cell placement is well controlled, like the onset of some cancers (Moore et al., 2017), a more robust topological phenotype can be constructed if a large number of cells are created.

Individual points representing the topological properties of lattices of increasing size were plotted along side kernel-density estimates for the random Voronoi models for direct comparison (Figure 3.8). In all cases, the CV of degree, BC and RWC was lower in lattices than in random Voronoi models. This is in agreement with previous qualitative comparisons of topology (Figures 3.5 and 3.7). A higher average degree can be reached without an ordered cell lattice structure (Figure 3.8A), while in contrast average log BC is lower in identically sized random Voronoi models (Figure 3.8B). This is due to certain 'hub-like' cells having many local connections in the Voronoi models due to their position, which create shortcuts through the organ and direct information flow away from other cells, decreasing the average log BC. In lattices, no such 'hub-like' cells exist, as degree is uniform throughout the core of the

models. Therefore, short paths are shared more evenly amongst the lattice model cells, increasing average log BC. Average RWC is similar in both lattice and random Voronoi cell connectivity networks (Figure 3.8C). Both local and global efficiencies are noticeably lower in cell lattices than in Voronoi models, above 32 cells (Figure 3.8D). This is related to the limited degree observed in the lattice structures, where cells make fewer connections. Fewer network edges means both a reduction in robustness of the cellular network, and an increase in average distances between cells.

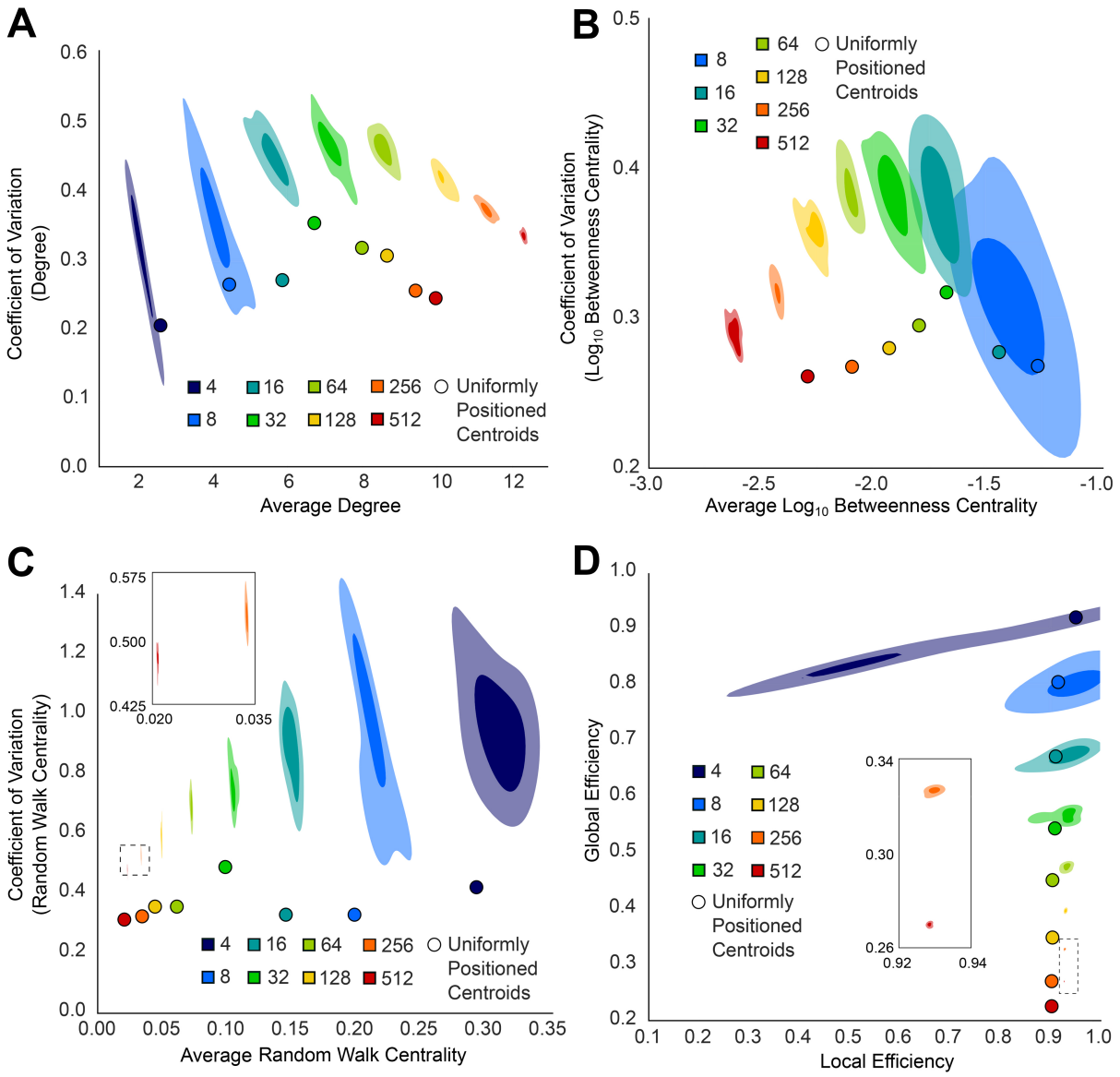


Figure 3.8. Average topological properties of models with increasing numbers of cells.
(A) A kernel-density estimate of the average degree and the coefficient of variation of degree in each random Voronoi model. Each kernel density estimate represents 30 individual models. The averages of each lattice model are shown as single points on the same chart for comparison. The legend refers to numbers of cells in the models. (B) Average and coefficient of variance of $\log_{10}$ betweenness centrality. (C) Average and coefficient of variance of random walk centrality. (D) The local efficiency and global efficiency of models.

3.2.2 Topological effects of increasingly random cell positions

Whilst the number of cells in organs has clear effects on tissue topology, the differences between ordered lattices of cells and organs with random cell positions highlights that cell position also plays a role in both local and global cell organisation. Epithelia in animal tissues have been shown to have archetypal, non-random organisation resulting from cell positioning, while departures from this cell arrangement are associated with disease (Sánchez‐Gutiérrez et al., 2015). This indicates that on tissue surfaces, cell positioning is likely to be an organisational feature with consequences for organ function.

To further explore the topological effects of cell positioning on cellular connectivity in 3D organs, another set of models was generated (Figure 3.9). 512 deterministically spaced centroids, 10 μm apart in the X- and Y- directions, and staggered in the Z-direction, within a sphere were used in Voronoi tessellation, creating an ordered 3D lattice. Further models were created by randomly perturbing the location of these centroids in Euclidean space, before Voronoi tessellation (Figure 3.9A). Each centroid was moved in the X-, Y- and Z-directions by a random number, between a minimum value of 0 movement, and a varying maximum movement value. This method was used to generate increasingly ‘noisy’ centroids, resulting in increased divergence from ordered cell positions seen in an ordered lattice (Figure 3.9B).

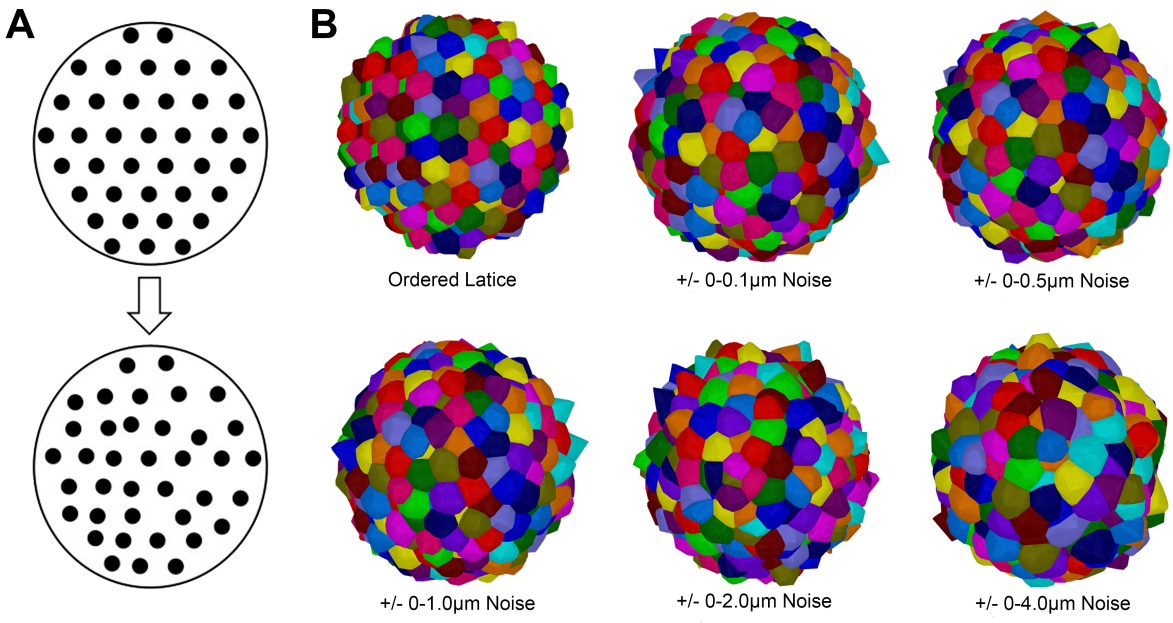


Figure 3.9. Construction of 3D Voronoi organ models with increasingly random cell positions.
(A) Schematic of centroid perturbation, from equally spaced centroids (top) to centroids shifted in 3D space with a given amount of noise (bottom). (B) An ordered lattice created from Voronoi tessellation of equally spaced centroids, and 3D Voronoi organs created from these lattice centroids shifted in space with increasing noise.

From qualitative inspection of topological properties, it is clear that cell degree is initially limited by uniformity in cell centroid positions, and can increase as centroid position is gradually perturbed (Figures 3.10A and 3.11A). The variation across the whole model originally drops as 0 – 0.001 µm centroid noise is added, though the CV of degree in just the model centre is initially 0 (Figure 3.11A). From here, as cell position becomes increasingly disordered the CV of degree increases and reaches a maximum at around 0 – 0.2 µm centroid noise.

In contrast to degree, log BC across cells in the model seems to become spatially redistributed, rather then noticeably increasing or decreasing (Figure 3.10B).

Originally log BC is distributed evenly from the centre of the lattice, but with increasing noise added to cell position, cells with high log BC become less biased towards the centre.

Kernel density estimate plots show that the average log BC decreases slightly as cell centroids become increasingly random (Figure 3.11B). There is an initial drop in the CV of BC as 0 – 0.001 μm centroid noise is applied to ordered lattice centroids, which as observed in degree, increases as cell position becomes less ordered, again reaching a maximum variance at 0 – 0.2 μm centroid noise. The reason for the particularly high variance across models with 0 – 0.2 μm centroid noise is not clear, though it may be due to interaction between the initial centroid spacing at 10 μm apart and this specific amount of noise, and represent a transition point in the generation of random organ topologies.

Random walk centrality is less biased towards the centre initially in the lattice than log BC, though increasing noise in centroid position seems to result in the same redistribution in both global topological measurements (Figure 3.10C). Quantitatively, a similar trend is observed in the average RWC and CV of RWC, similar to log BC, as cell position is increasingly perturbed from the original lattice (Figure 3.11C).

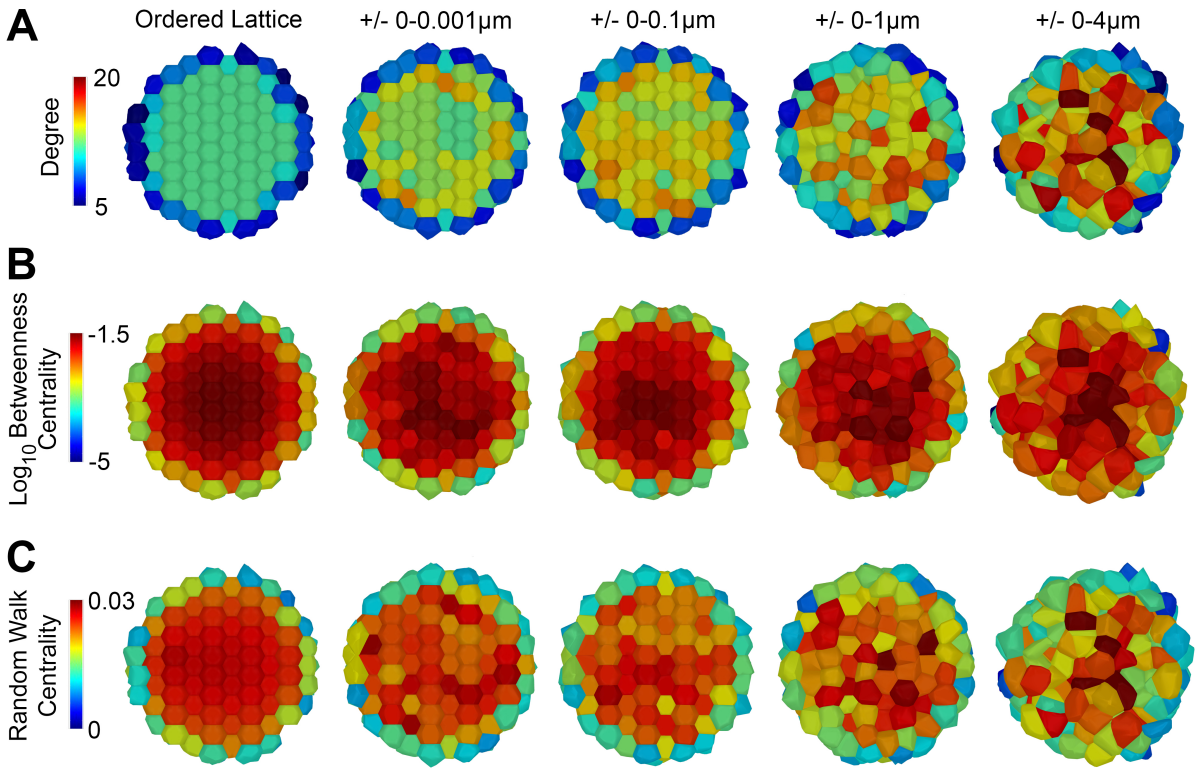


Figure 3.10. Spatial distribution of topological properties in randomly generated Voronoi models with increasingly random cell positions.
(A) Cross-sections of models false coloured with a heat map of degree. (B) Models false coloured with $\log_{10}$ betweenness centrality. (C) Models false coloured with random walk centrality.

Local and global efficiency both increase drastically as the lowest amount of 0 - 0.001 µm noise is added to ordered centroids before Voronoi tessellation (Figure 3.11D). From this point, further increasing the amount of centroid noise introduced results in increases in global efficiency.

Across all topological measurements used, adding 0 - 0.001 µm random noise to lattice centroids causes a dramatic change in both the average and the CV (Figure 3.11). Even the smallest change in cell position is sufficient to allow deviation from strict local and global patterning observed in the ordered lattice (Figure 3.10). This

allows the development of variation in local cell patterning, leading to the establishment of short paths across organs, which provide conduits for efficient global information transfer. These results show that cell positioning is a relevant feature of a tissue in terms of both local and global cell organisation, and the communication capacity throughout an organ.

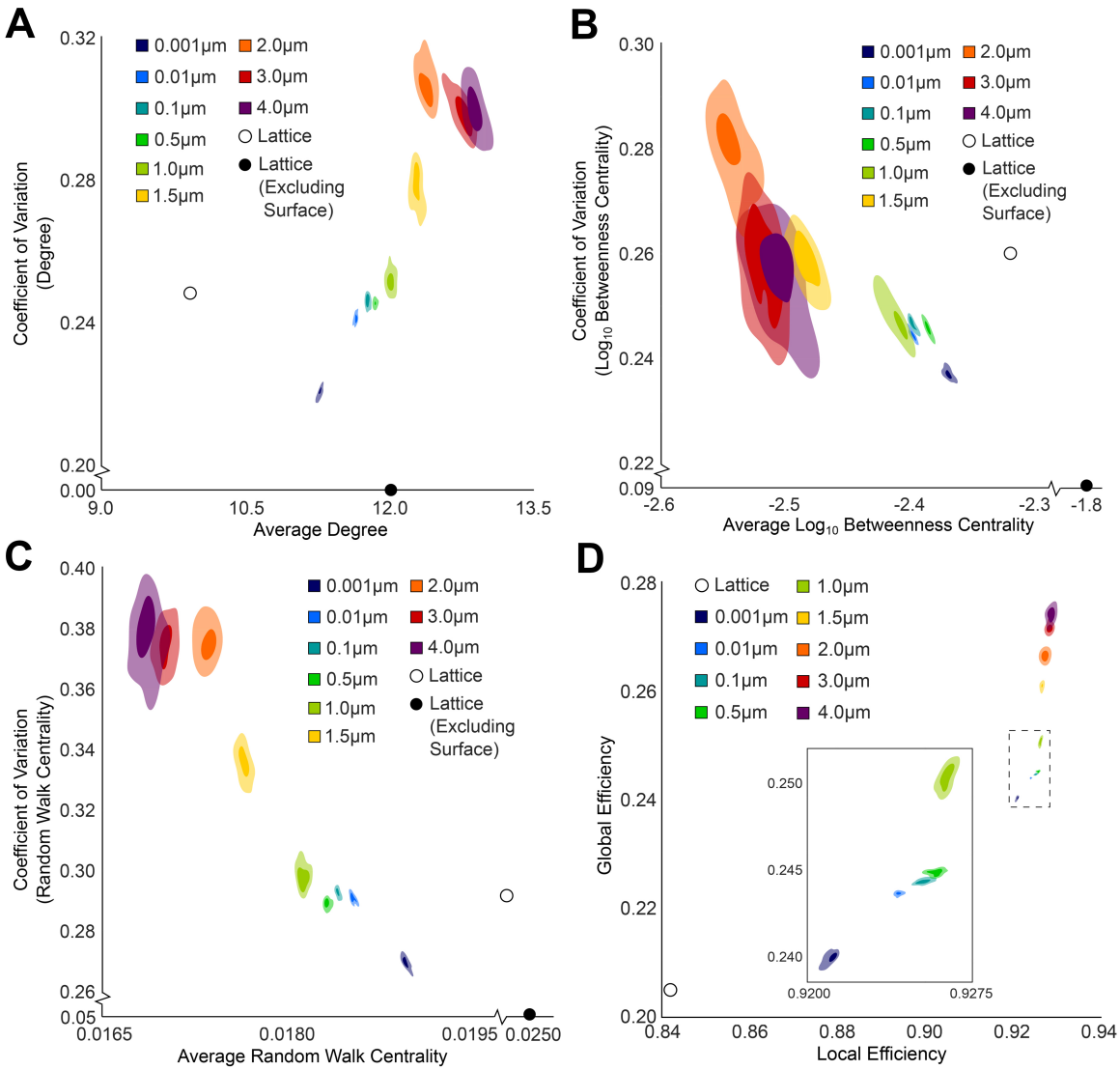


Figure 3.11. Average topological properties of models with increasingly random cell positions.

(A) A kernel-density estimate of the average degree and the coefficient of variation of degree in each random Voronoi model. Each kernel density estimate represents 30 individual models. The legends refer to the amount of centroid noise that was applied to ordered lattice centroids before Voronoi tessellation was carried out to generate models. (B) Average and coefficient of variance of $\log_{10}$ betweenness centrality. (C) Average and coefficient of variance of random walk centrality. (D) The local efficiency and global efficiency of models.

3.2.3 Topological effects of biased cell positioning

Cell position in tissues varies greatly, and adding noise to ordered centroids before Voronoi tessellation cannot capture the diversity of cell positioning observed in organs. For example, cells in different layers of the radially symmetrical *Arabidopsis thaliana* root are not spaced evenly, but are regularly spaced within each layer (Dolan et al., 1993). In the early stages of the developing *Drosophila melanogaster* embryo, polarity is established and cells are asymmetrically distributed, with few large nurse cells at one pole and many smaller follicle cells at the opposite side of the organism (St Johnston and Nüsslein-Volhard, 1992). To explore the effects of this asymmetric cell positioning on local and global cellular connectivity, a new set of models was constructed.

Using completely random cell positions as a baseline, organ model cell centres were increasingly biased towards one point on the sphere that constrained the gross morphology of the model organs (Figure 3.12). This set of models was first generated by choosing X, Y and Z centroid positions from a Gaussian distribution, with the mean located at a point on the sphere surface, representing a point of attraction (Figure 3.12A). Centroids that fell outside of the sphere were discounted, as in the

creation of earlier models with varying cell number (Figure 3.4). Here however, centroids were sampled until 512 valid centroids were found, for every model. Different values of σ were used to generate Gaussian distributions for centroid sampling around an identical mean (Figure 3.12A), resulting in 3D Voronoi tessellated models with increasingly biased cell position towards one pole of the organ (Figure 3.12B).

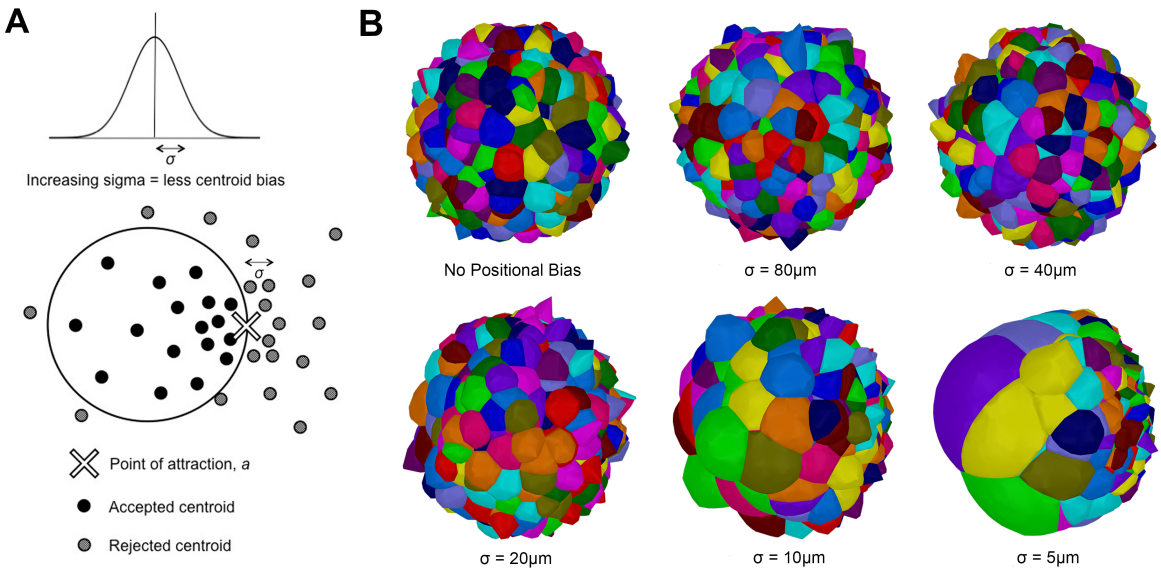


Figure 3.12. Construction of 3D Voronoi organ models with increasingly biased cell positions.
(A) Schematic of spatially biased centroid sampling using Gaussian distributions to designate a centroid 'point of attraction' on the surface of a spherical boundary mesh. (B) A 3D Voronoi tessellation model generated using random centroids with no positional bias, and models created with increasing biased centroid sampling from Gaussian distributions with decreasing values of σ.

Increasing the positional bias of cells resulted in a greater range of cell sizes across the model. Whilst in other models cells on the surface tend to have low local and global connectivity (Figures 3.5 and 3.10), changes in cell positioning can change

this trend (Figure 3.13). As cell centroids are increasingly biased, the degree, log BC and RWC of large surface cells become higher, particularly in models where centroids were generated using Gaussian distributions with σ = 10 μm or σ = 5 μm.

Average degree increases in models with increasing positional bias (Figure 3.14A), when centroids are sampled from Gaussian distributions of σ = 20 μm or higher. This suggests that a transition in local topology of the Voronoi models occurs only with sufficiently biased centroids. As the cell positions become increasingly ordered, clustering around a position on the surface of the organ, the variance in degree, measured using the CV, decreases.

A similar trend is observed in the global property of log BC as cell positions become more constrained (Figure 3.14B). The average log BC increases, whilst the variability is reduced, as cell position becomes increasingly biased towards one pole of the organs. Here, changes in the number of local interactions that cells make are linked strongly to the global topological property of BC.

However, a different trajectory is observed using RWC, highlighting important distinctions in the two global topological measurements used (Figure 3.14C).
The average RWC decreases as cells are increasingly biased in their positioning (Figure 3.14C), and the initial decrease in RWC with a small amount of centroid bias is large, in comparison with the subsequent changes. A small number of large cells, directly opposite the area with the highest cell concentration on the surface of the organ, are travelled through by a disproportional amount of random walkers in the

calculation of RWC (Figure 3.13C). This division of labour in transport capacity reduces the RWC of all other cells, thereby reducing the mean average RWC (Figure 3.14C). Variability in RWC is reduced as cells are positioned increasingly closer to one pole of the models, similar to observations in degree and log BC.

Small changes are observed in the measurement of local and global efficiency, compared to other classes of models examined (Figure 3.14D). Both local and global efficiency of the cellular connectivity networks are subtly increased when the value of σ used in centroid sampling was lower than 40 μm. This transition in organisational properties, when cell centres are drawn from sufficiently biased distributions, reflects observations of changes in degree (Figure 3.14A) and log BC (Figure 3.14B).

Whilst biased cell positioning has an effect on both local and global cellular organisation, this effect is small compared to changes in topology mediated by varying the number of cells (Figure 3.8), or by perturbing the positions of equidistant cells (Figure 3.11).

In biological terms, it is unlikely that investing resources into the control of cell positioning and growth required for this kind of biased cell position would be worth the incremental increases or decreases in intercellular transport capacity of a multicellular system. In addition, with these biased cell arrangements resulting in vastly different sizes of cells, it is possible that there would be consequences for the mechanical stability of the tissue (Brezny and Green, 1990) (Ingber, 1998) that are not captured by topological analysis.

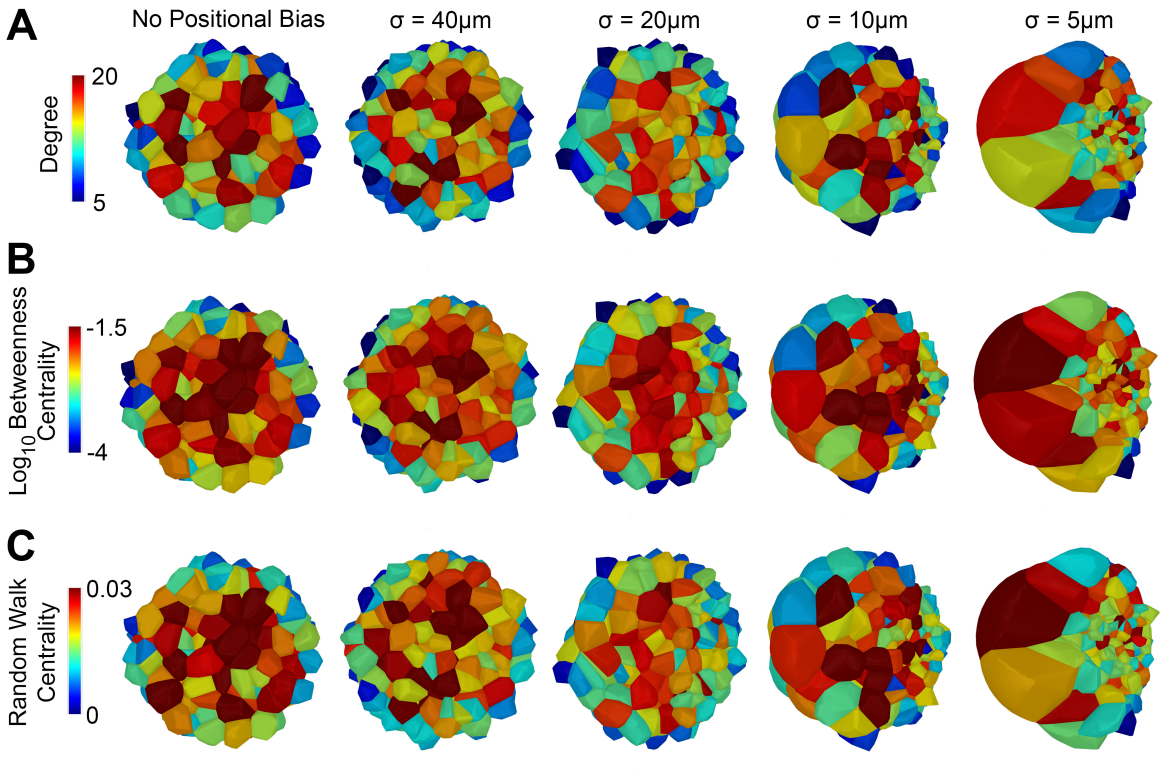


Figure 3.13 Spatial distribution of topological properties in Voronoi models with increasingly biased cell positions.
(A) Cross-sections of models false coloured with a heat map of degree. (B) Models false coloured with $\log_{10}$ betweenness centrality. (C) Models false coloured with random walk centrality.

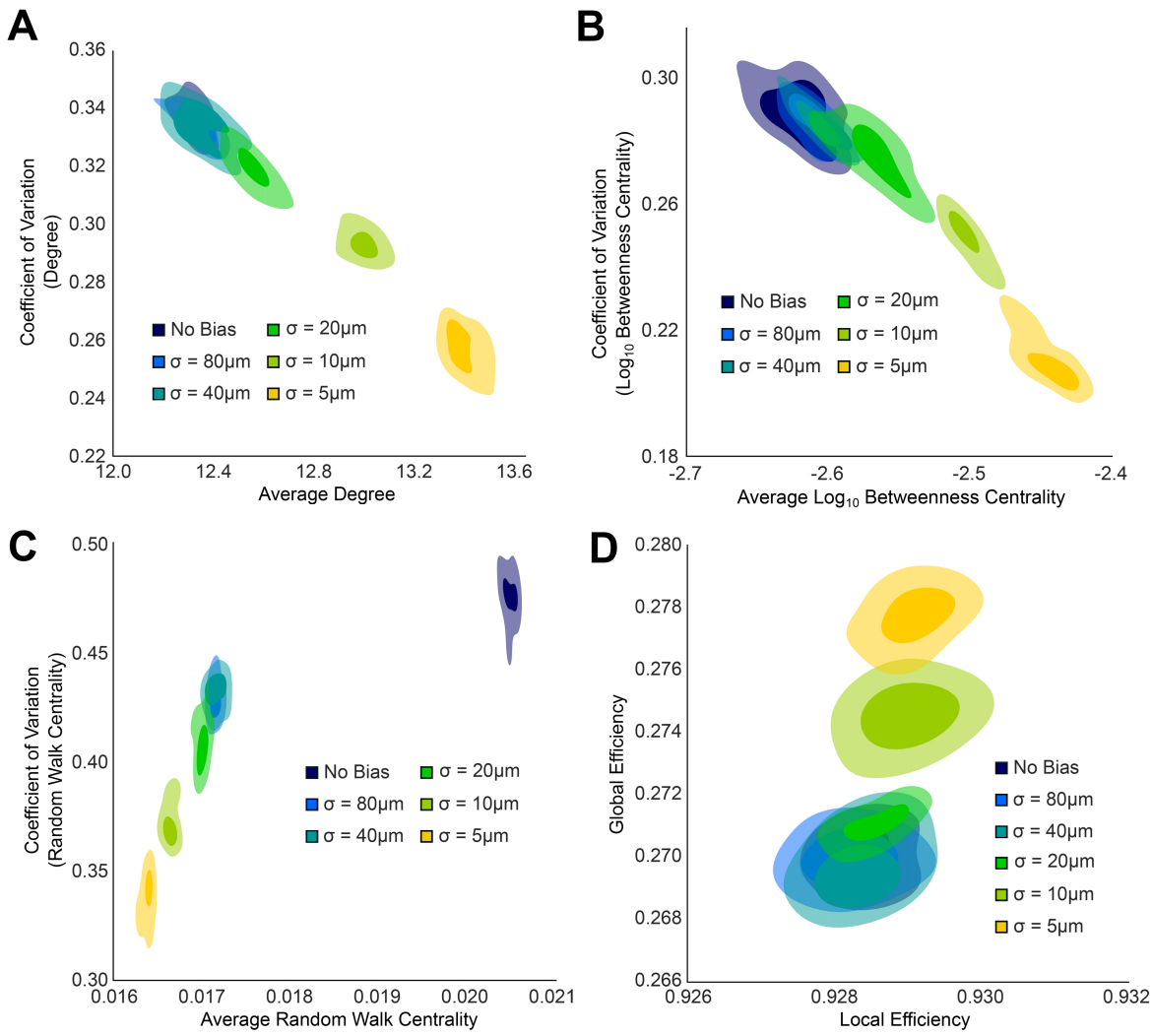


Figure 3.14. Average topological properties of models with increasingly biased cell positions.
(A) A kernel-density estimate of the average degree and the coefficient of variation of degree in each random Voronoi model. Each kernel density estimate represents 30 individual models. The legends refer to the value of σ in the Gaussian distributions centred around one point on the surface of a boundary mesh during model creation. (B) Average and coefficient of variance of $\log_{10}$ betweenness centrality. (C) Average and coefficient of variance of random walk centrality. (D) The local efficiency and global efficiency of models.

3.2.4 Topological effects of vascularisation

Vasculature is observed in organs throughout multicellular life (West et al., 1999) (Jain, 2005) (Martínez‐Vilalta et al., 2012), and has a role in providing transport routes for substances between distant regions of an organ or organism.

To generate organ models with vasculature, cells in 3D Voronoi models with 512 cells in random positions were selectively and progressively fused (Figure 3.15A). To create vasculature-like systems, cells were fused based on their BC, a measure that represents their capacity to act as a 'shortcut' between other pairs of cells in the system, a known feature of vasculature in biological systems (West et al., 1999). The cell with the highest BC was fused to its highest-BC neighbour iteratively, until a desired percentage of cells were fused in each model. Using this method, a set of models was generated with between 0% and 40% of cells fused into connected vasculature systems (Figure 3.15B).

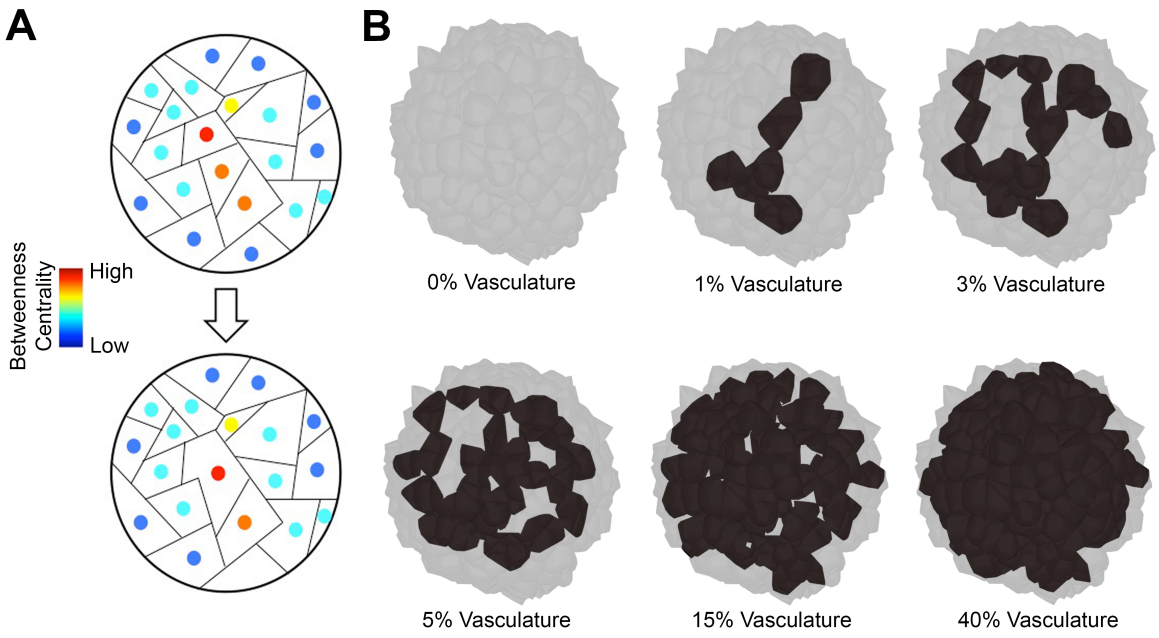


Figure 3.15. Construction of 3D organ models with vascularisation.
(A) Schematic of how vascularisation is carried out in 3D Voronoi organ models. The cell with highest betweenness centrality is identified (top), and subsequently fused to the neighbouring cell with highest betweenness centrality (bottom). (B) Models with increasing amounts of vascularisation, measured as a percentage of all cells in the organ.

In all topological measurements carried out, both local and global, the vasculature system itself has the highest values (Figure 3.16). This is unsurprising, as cells are selected for their highest BC during model construction (Figure 3.15A), and previous results in other model classes have shown relationships between the measurements of degree, log BC and RWC (Figures 3.5, 3.10 and 3.13). As the percentage of vasculature in a model increases, the degree, log BC and RWC of other cells drops dramatically, and can be more easily observed with a $\log_{10}$ scale (Figure 3.16).

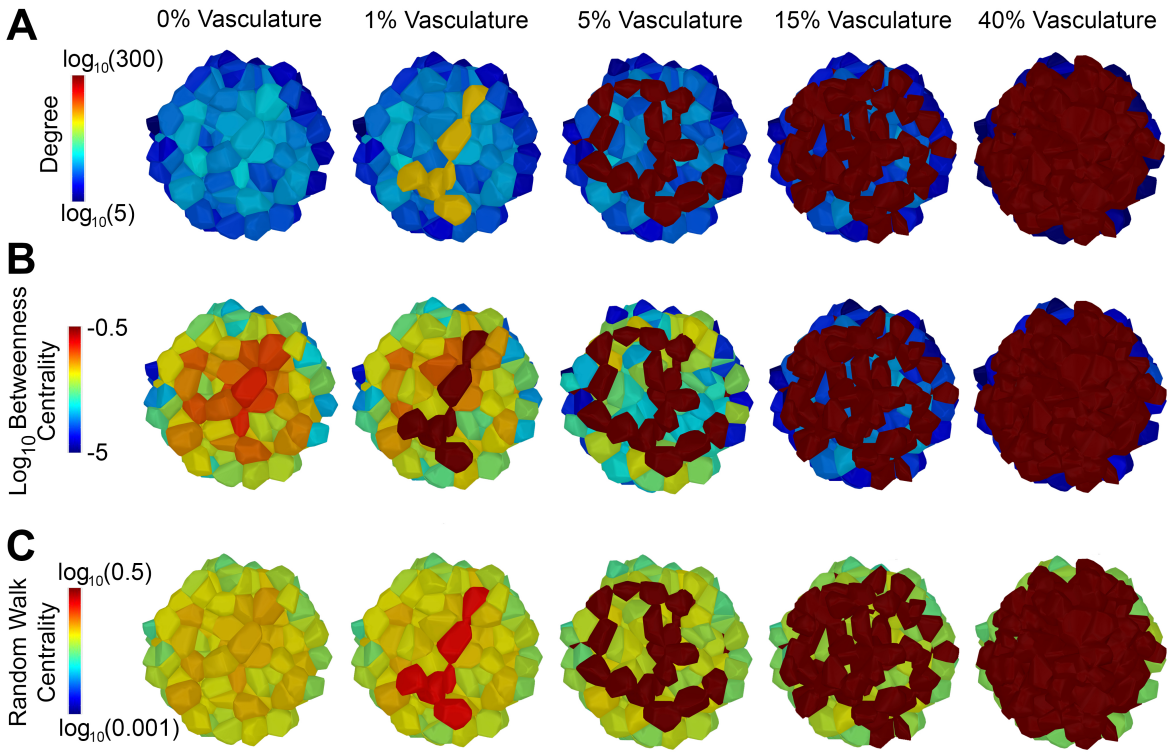


Figure 3.16 Spatial distribution of topological properties in random Voronoi models with increasing vascularisation.
(A) Cross-sections of models false coloured with a heat map of degree. A $\log_{10}$ scale is used for more clear comparison between high and low values. (B) Models false coloured with $\log_{10}$ betweenness centrality. (C) Models false coloured with random walk centrality. A $\log_{10}$ scale is used for more clear comparison between high and low values.

Fusing cells in a model reduces the overall number of nodes in the cellular connectivity network, shown earlier to have a measureable impact on topological properties (Figures 3.5 and 3.8). To examine the more general effects on topology of fusing cells in a model organ, a set of models was constructed where neighbouring cells were fused at random (Figure 3.17). These models act as a control for cell number, so that differences between randomly fused cell models and vascularised models can be attributed to the existence of a vascular element in the system. The change in spatial properties of both local and global measurements of organisation is

much less severe when cells are fused randomly, than when cells are fused into vascular-like systems (Figures 3.16 and 3.17).

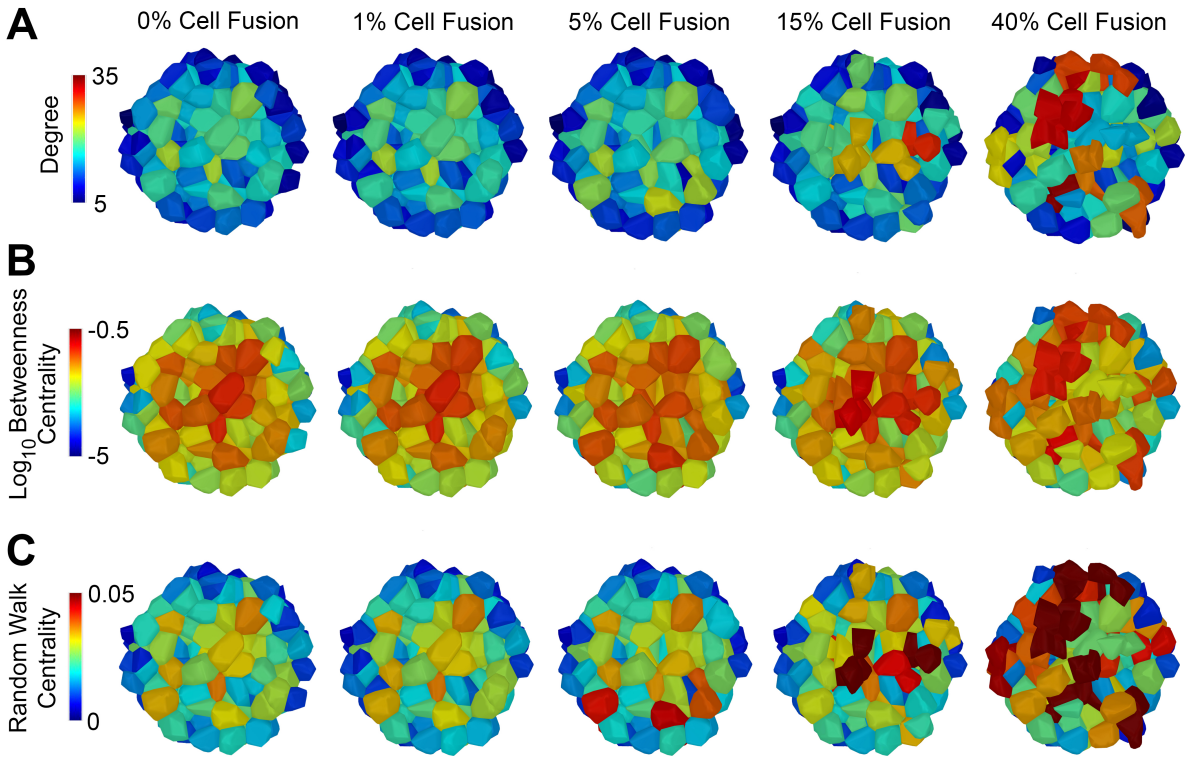


Figure 3.17 Spatial distribution of topological properties in random Voronoi models with an increasing amount of cell fusion.
(A) Cross-sections of models false coloured with a heat map of degree. (B) Models false coloured with $\log_{10}$ betweenness centrality. (C) Models false coloured with random walk centrality.

Looking more closely at the quantification of patterning in the vascularised models, the local property of cell degree has a relatively stable average of around 12 until 10% vascularisation is reached (Figure 3.18A). The average degree then falls at 15% vascularisation and above, as cells become increasingly surrounded by the vasculature itself, which is treated as just one neighbouring cell in these models. The CV of degree increases steadily with the introduction of more vascularised tissue in the models. This increase in variance can be attributed to the disparity between the

high number of neighbours of the vascular element itself, and the low degree observed in all other cells as the size of the vasculature grows (Figure 3.16).

In both global measurements, BC and RWC, the averages decrease as more vasculature is introduced, up to around 15% vascularisation (Figure 3.18B and C). Above this, averages begin to increase, driven by the disproportionally high value of BC and RWC in the vascular-like cell. This effect is also responsible for the large CVs across the global patterning measurements as vascularisation increases, which are substantially larger than in any other class of models examined (Figures 3.8, 3.11 and 3.14).

To further clarify the effects of the presence of a highly connected vascular-like node in a cellular connectivity network, the average and CV of degree, log BC and RWC were calculated again, excluding the vasculature cell from the summary statistic calculations (Figure 3.19). Here, in both local and global measurements, the average and CV falls as the vasculature becomes larger. Cells that have not been fused into the vascular element have fewer neighbours, and become steadily less involved in theoretical transport paths across the system. This may represent a viable strategy for the division of labour among cells, between cells that form transport conduits, and cells that are free to perform separate tasks.

Randomly fusing cells does not result in similar changes to vascularisation in terms of local and global cell organisation (Figure 3.20A, B and C). The overall changes in

degree, log BC and RWC as cells are fused randomly are much more subtle than when high BC cells are fused together.

The effect of vascularisation in random 3D Voronoi models on the transport efficiency of the organ is of particular interest (Figure 3.18D). As vasculature is added to 3D Voronoi models, both local and global efficiency of the cellular connectivity networks increase, up to 15% vascularisation. Beyond this point, the fusing of more cells into vasculature no longer increases global efficiency, and substantially reduces the local efficiency of the system. At 15% vasculature, almost all pairs of cells can communicate via just two steps, passing information first through the vasculature, then to the target cell. With this cellular organisation, there are no additional benefits to transport if the vasculature is larger, meaning there is a maximum possible global efficiency. Every cell fusion reduces the number of cells in the organ models, meaning that random removal of nodes is increasingly likely to affect the vascular system, as more cells are incorporated in to it. This effect is responsible for the loss of local efficiency observed at over 15% vascularisation, and can be interpreted as a loss of transport robustness. These trends are not observed when randomly fusing cells together (Figure 3.20), and are a specific consequence of using BC-mediated vascularisation to generate an efficient topology. The identification of 15% vasculature being optimum for both transport efficiency and robustness to damage in these 3D models may represent a core design principle in the evolutionary design of optimum transport systems in multicellular tissues.

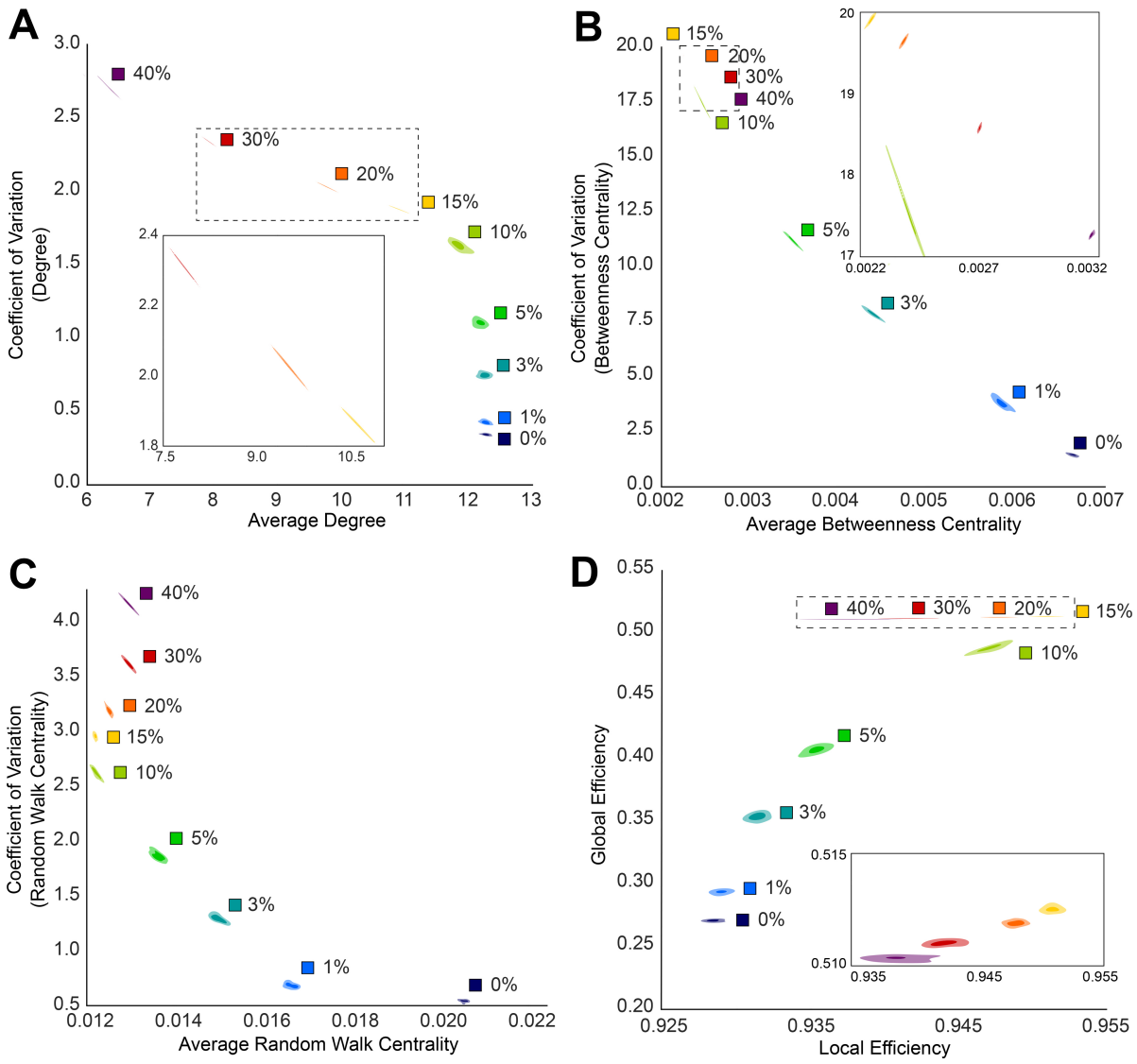


Figure 3.18. Average topological properties of models with increasing vascularisation.
(A) A kernel-density estimate of the average degree and the coefficient of variation of degree in each random Voronoi model. Each kernel density estimate represents 30 individual models. The legends refer to the percentage of cells in models that are fused into vasculature. Legends are placed next to density fields to allow better visualisation of their position in the chart. (B) Average and coefficient of variance of betweenness centrality. (C) Average and coefficient of variance of random walk centrality. (D) The local efficiency and global efficiency of models.

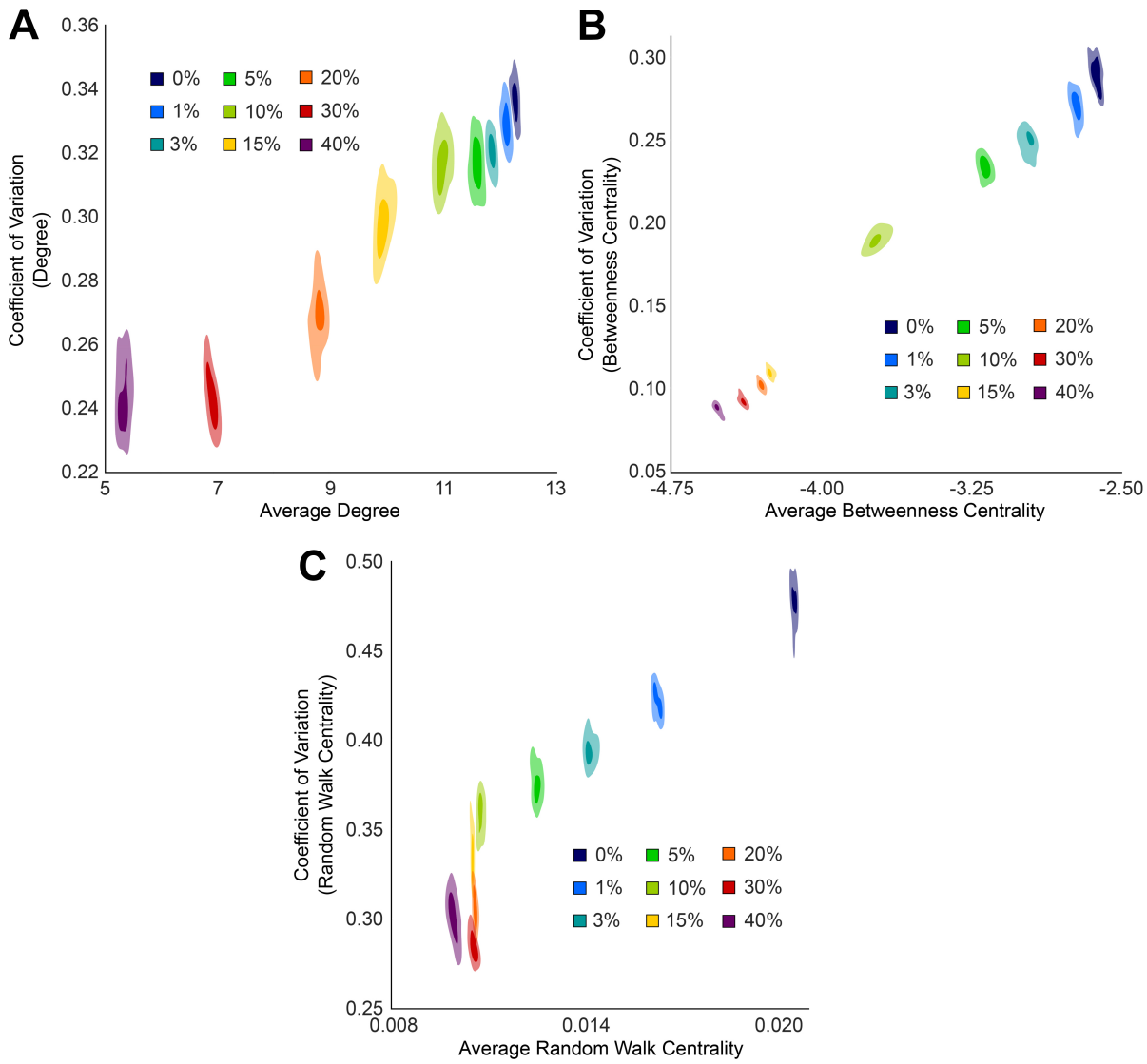


Figure 3.19. Average topological properties of models with increasing vascularisation, where the vasculature itself is not reported on.
(A) A kernel-density estimate of the average degree and the coefficient of variation of degree in each random Voronoi model. Each kernel density estimate represents 30 individual models. The legends refer to the percentage of cells in models that are fused into vasculature. (B) Average and coefficient of variance of $\log_{10}$ betweenness centrality. (C) Average and coefficient of variance of random walk centrality.

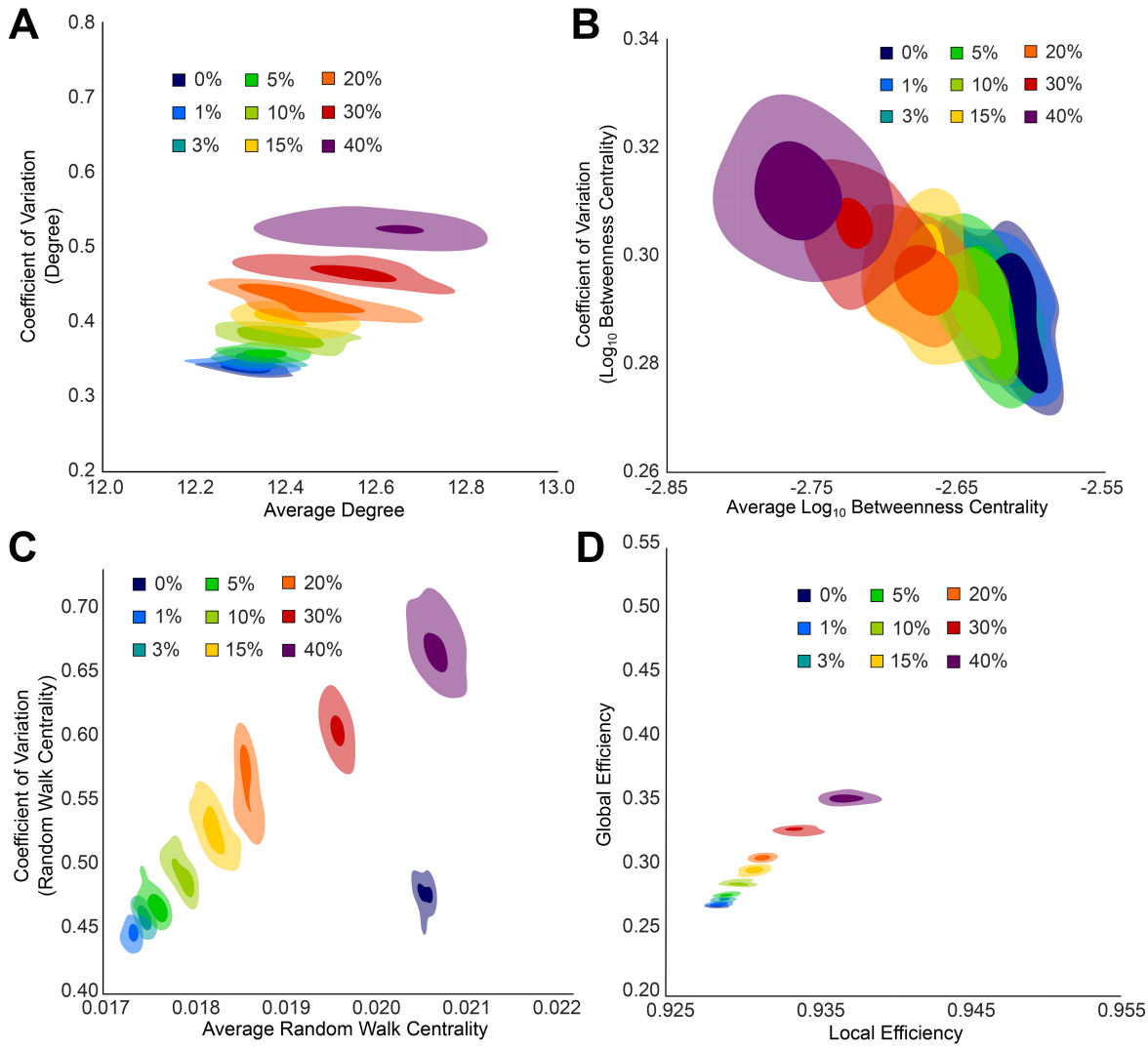


Figure 3.20. Average topological properties of models with an increasing amount of cell fusion.
(A) A kernel-density estimate of the average degree and the coefficient of variation of degree in each random Voronoi model. Each kernel density estimate represents 30 individual models. The legends refer to the percentage of fused cells in models. (B) Average and coefficient of variance of $\log_{10}$ betweenness centrality. (C) Average and coefficient of variance of random walk centrality. (D) The local efficiency and global efficiency of models.

The observation of a critical transition in the topology of models at around 15% vascularisation is independent of the number of cells in the model (Figure 3.21). Irrespective of cellular connectivity network size, global and local efficiency of a multicellular system can only be improved by vascularisation up to a point, after which networks become less robust. This result is indicative of a general property of organs in 3D space, and the cellular connectivity networks they form.

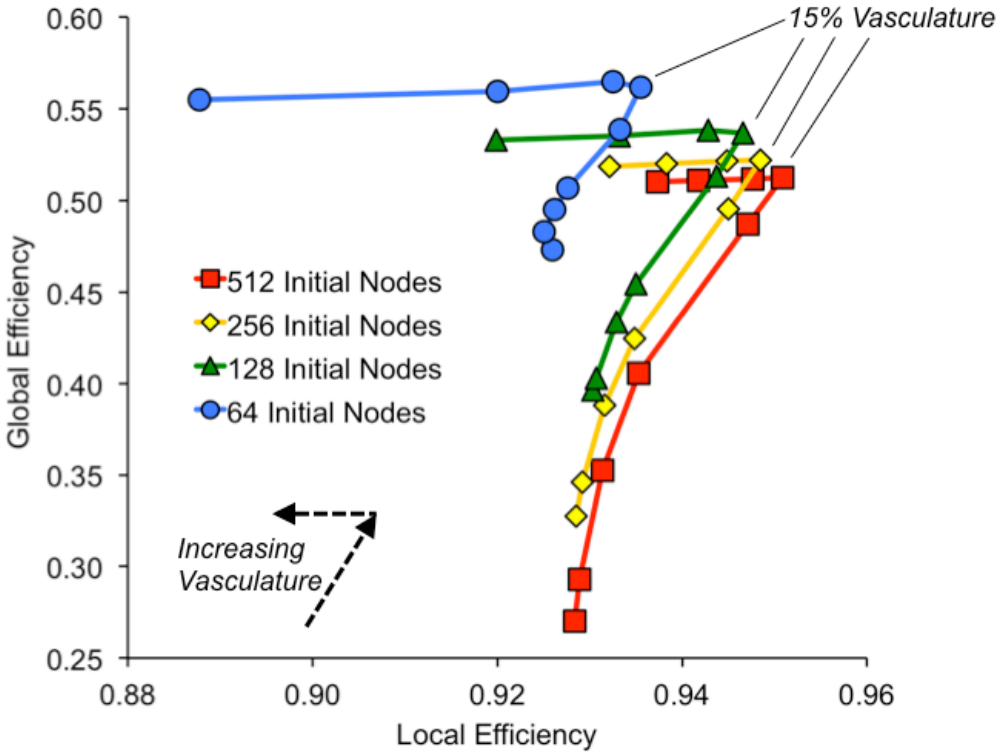


Figure 3.21. Local and global efficiency of models with varying numbers of cells and increasing amounts of vasculature.
Each point represents the average of 30 models, while lines connecting points represent the trajectories taken as the percentage of vascularisation is increased.

3.3 Discussion

Using tools from network science, diverse patterns and organisations of cells in 3D organ models can be quantified. Extracting a cell connectivity network from a tissue allows the exploration of local cell connectivity, as well as the emergent organ-wide properties of global connectivity and transport efficiency. This approach could be used to quantify differences in organisation between 3D tissues, assuming that considerations are made about the cellular connectivity networks that are being compared.

The number of cells in a model had a large effect on the global measurements of cellular patterning used, BC and RWC (Figure 3.8). This suggests that despite the normalisation applied (Section 2.4.3), in order to make comparisons between different samples valid, it is therefore important to constrain the number of cells included in a network, perhaps using subsampling methods to ensure that network size is as similar as possible.

Many previous studies have used connectivity properties of epithelia to explore tissue organisation (Escudero et al., 2011) (Sánchez‐Gutiérrez et al., 2015), while 3D connectivity networks at cellular resolution have been studied comparatively less (Jackson et al., 2017a). There are notable differences in topological properties between networks with different dimensionality, with transitions in both local and global organisation as networks are extracted from 1- to 3- dimensional systems (Figure 3.22). This highlights the importance of making comparisons only between same-dimensional networks, to avoid topological measurement bias. As more 3D

cellular resolution datasets become available due to advances in imaging and image analysis (Power and Huisken, 2017) (McQuin et al., 2018), more meaningful comparisons of organisation in 3D tissues will become possible.

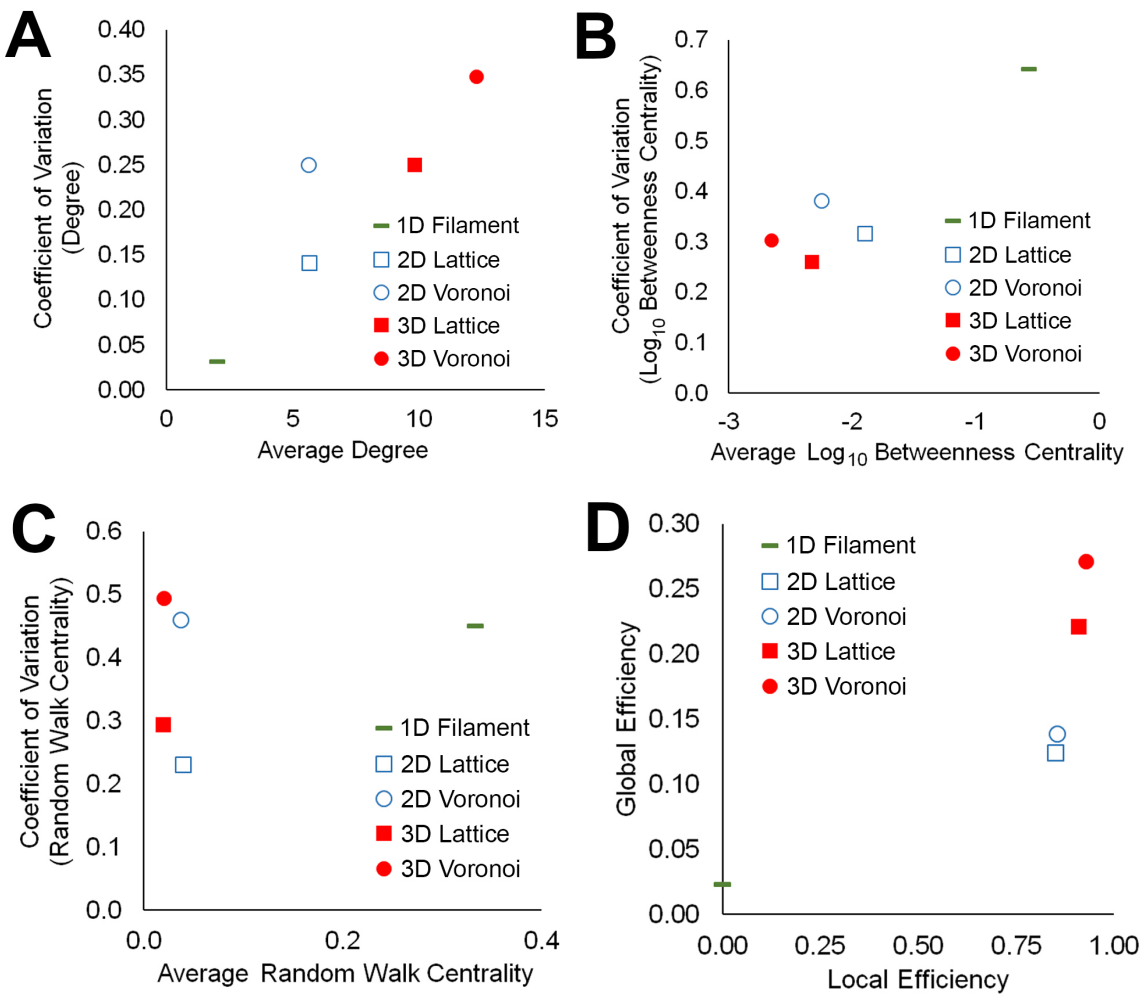


Figure 3.22. Topological properties of models with varying dimensionality.
(A) Mean average and CV of degree in model cellular networks with different dimensionality. (B) Average and CV of $\log_{10}$ betweenness centrality. (C) Average and CV of random walk centrality. (D) Local and global efficiency.

The effect of tissue-level properties on cell organisation was explored with the generation of Voronoi-tessellated 3D models. Voronoi tessellation is a suitable method for creating models where cells have a ‘greedy’ type of growth, where by the nature of the Voronoi algorithm each cell simultaneously attempts to fill as much 3D space as possible. In biological systems, cell growth is often controlled much more tightly, for example by cell signalling or chemical gradients (Aplin et al., 1999) (Grieneisen et al., 2007). While more complex, 3D tissue models could be created that are constrained by further features, allowing the control of additional cell features such as cell shape and variable growth.

The creation of vascular ‘shortcuts’ for the transport of information throughout the model organs resulted in vast reductions in path length between distal cells in the model tissues (Figure 3.18). Reserving roughly 15% of tissue cells and space for a vascular system within a spherical 3D organ results in the maximum level of efficiency and robustness (Figure 3.18D and 3.21). Whilst the number of cells and the arrangement of cells in a tissue changed topological properties of model organs, these changes did not have as large an influence on cell organisation as the introduction of vasculature (Figure 3.21). Vasculature within an organ, in a sense, allows a tissue to transcend the dimensionality of a system, as the inclusion of short paths drastically increases the global efficiency of a cellular connectivity network, in a similar trend to the increase of efficiency between 2D and 3D systems (Figure 3.22 and 3.23). Systems with vasculature have ‘hubs’, sharing topological properties with ‘small-world networks’ that are usually unconstrained by Euclidean 3D space (Barabási, 2016).

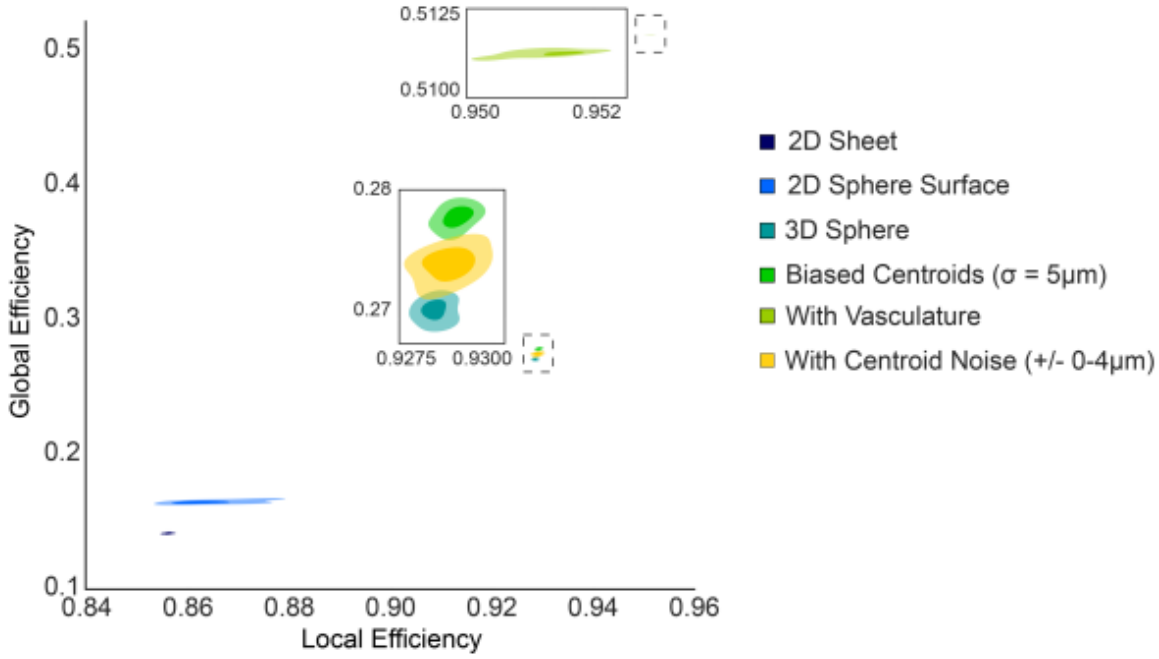


Figure 3.23. Efficiency of cellular connectivity networks extracted from a range of models.
Each kernel density estimate represents 30 individual models. Each model has 512 cells.

The insights into the effects of vascular systems may have implications for vascularity in tumours, where increased amounts of vasculature within cancerous tissue are associated with tumour proliferation (Weidner, 1999) (Miles and Williams, 2008). When transport efficiency of the tissue is high, increased proliferation likely results from increased nutrient delivery to cancerous cells. Targeting vascular systems in tumour treatment may reduce tumour viability, and with cellular level imaging the direct effects on tissue efficiency could be quantified using a cellular network analysis approach.

This analysis of 3D cellular organisation has allowed the identification of optimal cellular arrangements for both local and global intercellular information transport. Recent advances in synthetic biology have allowed the assembly of 3D organs using computer aided 3D printing and design (Mironov et al., 2003) (Murphy and Atala, 2014). Combining this with the understanding of emergent properties of cell organisation in tissues has the potential to inform organ designs that maximise, or minimise, global information transport throughout a system, depending on the desired biological function.

CHAPTER FOUR: TOPOLOGICAL ANALYSIS OF THE PLANT HYPOCOTYL

4.1 Introduction

The hypocotyl is a multicellular plant organ, the embryonic plant stem. In the embryo, the hypocotyl is connected to the radicle, which pushes downwards through the soil during germination and develops into the root (Figure 1A). The other end of the hypocotyl is connected to the cotyledons, which during germination, are pushed through the surface of the soil purely by hypocotyl cell expansion. The function of the hypocotyl post-germination is to develop into the stem, which, primarily through the vasculature, provides a conduit for transport of molecules and communication between the below-ground and above-ground organs in the plant (Felle et al., 2005) (Krouk et al., 2010) (Hilleary and Gilroy, 2018).

In the hypocotyl, cells are positioned in a radial arrangement, with clearly defined layers (Figure 1B) (Dolan et al., 1993). In the model plant *Arabidopsis thaliana*, the hypocotyl has a vasculature running longitudinally through the axis, made up of many long, thin xylem and phloem elements. A single layer of larger cells, the endodermis, surrounds the vasculature. Two separate layers of cortical cells in turn enclose the endodermis, which lastly are surrounded by the epidermis, which is exposed to the environment. The hypocotyl shares a similar structure with the mature root and stem, both responsible for the transport of water and nutrients around the plant (Dolan et al., 1993).

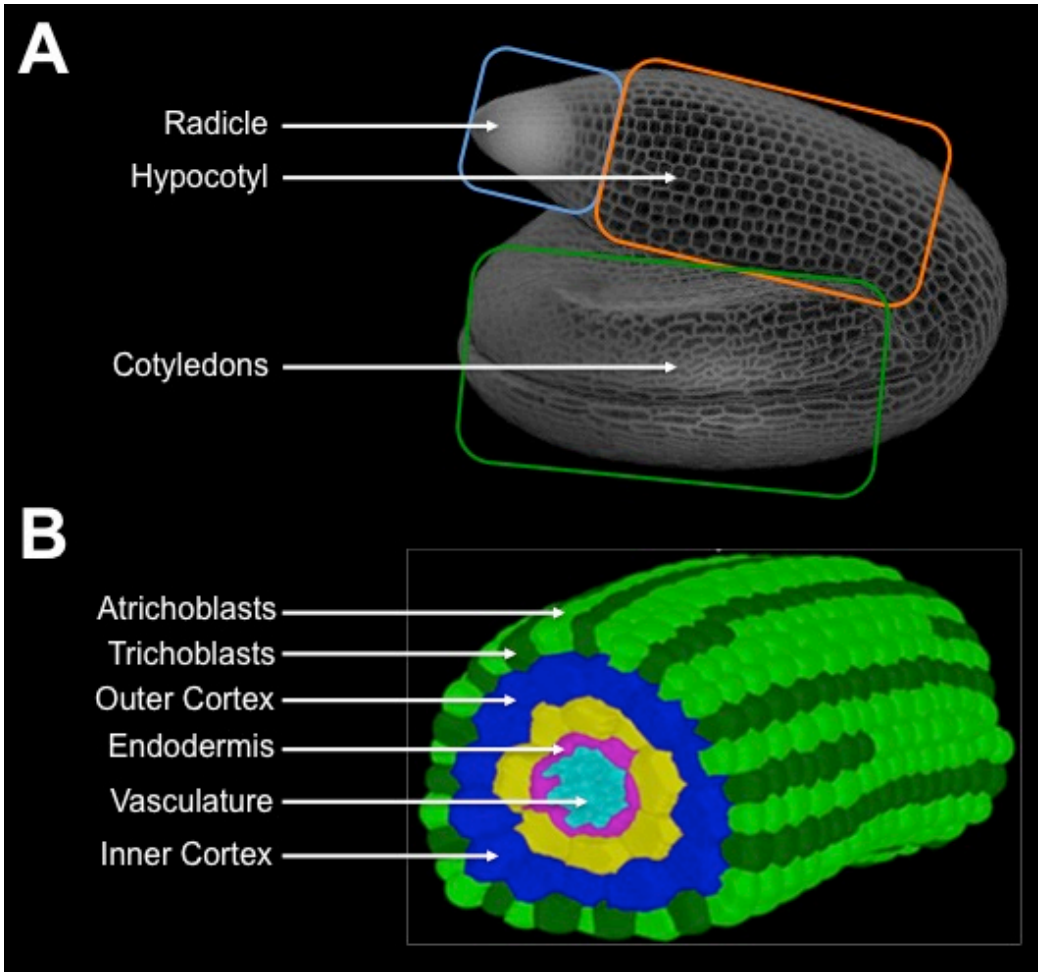


Figure 4.1. Schematic of hypocotyl structure.
(A) Position of the hypocotyl in the mature *Arabidopsis thaliana* embryo. (B) Cell types in the *A. thaliana* hypocotyl. Figure adapted from Jackson et al., 2017, *eLife.*

Further cell specialisation occurs in the epidermis of the hypocotyl, where two different cell types are present, the atrichoblasts and the trichoblasts. These cell types are determined by local cell-cell interactions between the epidermal and cortical layers (Schiefelbein et al., 2014). Epidermal cells adjacent to only one cortical cell in the radial direction develop into atrichoblasts, while epidermal cells adjacent to two cortical cells in the radial direction develop into trichoblasts. This process is

mediated by gene dosage effects from neighbouring cells, previously described in detail (Section 1.4.5). In the root, epidermal trichoblasts have the capacity to develop root hairs, which absorb nutrients and water from the soil (Gilroy and Jones, 2000). This cell specialisation is a well-understood example of the role of local cell interactions in plant development. However, though the same hypocotyl and stem patterns and structures are seen repeatedly throughout different plant species (Speck and Burgert, 2011), less is known about how this organ-wide cell patterning has been shaped by evolution (Ollé-Vila et al., 2016).

In certain cell types, much is known about how the local features of cells in the stem, and by extension the hypocotyl, contribute to their function. For example, the structure of connected xylem elements within the vascular system of the stem is specialised for the efficient transport of water from the roots to the leaves, using energetically efficient cohesion-tension driven by their thin shape, which is specialised for capillary action (Hacke and Sperry, 2001). Less is known about the arrangements of cells in the organ-wide multicellular context of the hypocotyl, and how this contributes to hypocotyl and stem function (Jackson et al., 2017a). The position of the vasculature at the centre of the hypocotyl and stem is speculated to be due to mechanical stability provided by the layers of surrounding cells (Sperry, 2003) (Speck and Burgert, 2011). The separation of the vasculature from the environment through the use of cortical cell layers may simply provide a physical barrier to pathogens that seek to gain access to the primary transport conduit of the plant (Rahme et al., 1995) (Faulkner and Robatzek, 2012), which plays such an important role in plant development and growth (Lucas et al., 2013).

Due to advancements in 3D imaging and computational methods for image segmentation, it is now possible to capture every cell within the hypocotyl at high resolution, in the native context of the whole organ (Yoshida et al., 2014) (de Reuille et al., 2015). Cell interactions within the hypocotyl are also invariant during germination-triggered cell expansion and further development, making the hypocotyl a particularly appropriate model to study the connectivity of cells (Jensen et al., 1998). The hypocotyl has been shown to provide a conduit for the transport of molecules and long range signalling between the radicle and the embryonic leaves (Bishopp et al., 2011). Given that signals primarily travel through cell-cell interactions in plants (Section 1.3), this means that cellular connectivity in the hypocotyl has a functional role.

Functional roles for cellular connectivity can be explored and quantified by extracting the cellular network of the organ, and using the network analysis algorithms detailed in Section 2.4.1, namely degree and betweenness centrality. In the context of the hypocotyl, where molecular transport is a primary role of the organ, using degree to measure the number of cells neighbouring a given cell may indicate the importance of cells in local cell-cell transport or other local interactions. In contrast, cells with high betweenness centrality (BC) are poised to coordinate long distance information transport throughout the hypocotyl, and may highlight particular cell's role in such processes.

With the ability to abstract cellular connectivity into networks, allowing quantitative analysis of cellular organisation (Section 3), the hypocotyl represents a system in which both cellular structure and organ function can be captured. This enables relationships between structure and function to be determined, and allows the design principles that are employed in the construction of this organ to be explored.

4.2 Results

4.2.1 Hypocotyl cellular connectivity networks

Hypocotyl samples were prepared and imaged at high-resolution as in Section 2.1. Images were processed and cell connectivity networks were extracted as in Section 2.2. Additional steps were taken to ensure the accuracy of the extracted hypocotyl cell interaction networks, and to ensure that topological analyses carried out were representative of cell organisation in the tissue.

Due to artefacts from image processing resulting in artificial mesh protrusions (Section 2.2.7), some extracted hypocotyl cellular connectivity networks contained edges that were not representative of real cell-cell interactions. To counteract this, edges in the annotated cellular connectivity network that could not exist, for example an epidermal to vasculature cell connection, were removed from the networks. In addition, edges representing less than 2 μm^2, which due to their size were unlikely to be of biological relevance, or unlikely to represent real cellular interactions, were

removed from the final annotated cell networks before network analysis was carried out (Figure 4.2).

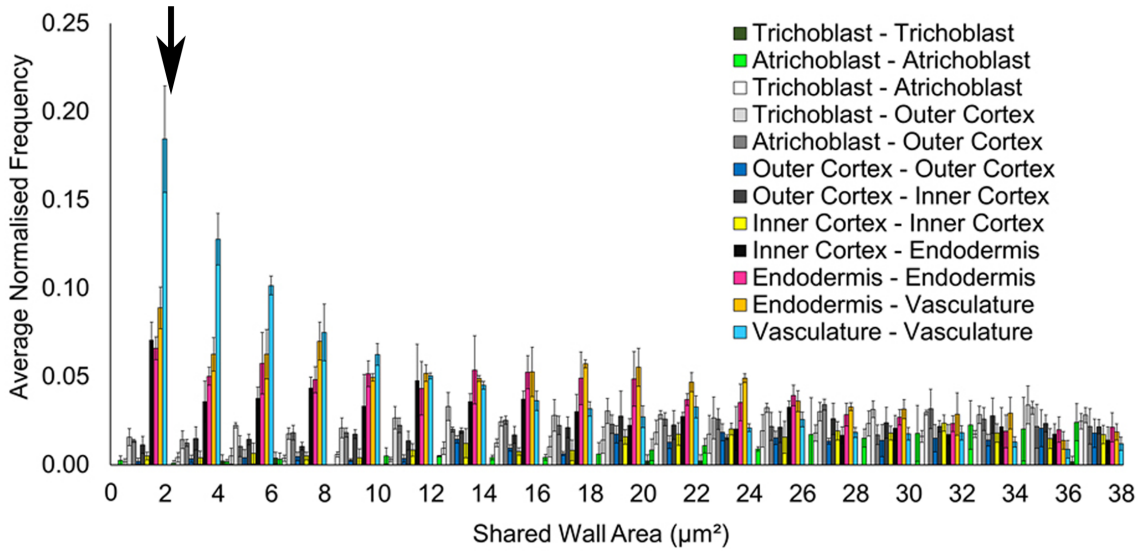


Figure 4.2. Shared wall area of physically interacting cells in different cell layers of *Arabidopsis thaliana* Col. hypocotyls.
Edges representing a cell wall interaction of less than 2µm^2 (left of the arrow) were removed from the final annotated cell networks. Figure reproduced from Jackson et al., 2017, *eLife.*

Additionally, in the original 3D hypocotyl images, as much of the hypocotyl as could be imaged was collected in z-stacks, but this still resulted in both ends of the hypocotyl image being artificially disconnected from the rest of the plant. To prevent this artefact from affecting topological analyses, cells close to the image boundaries were included in topological analyses, but not reported on (Figure 4.3).

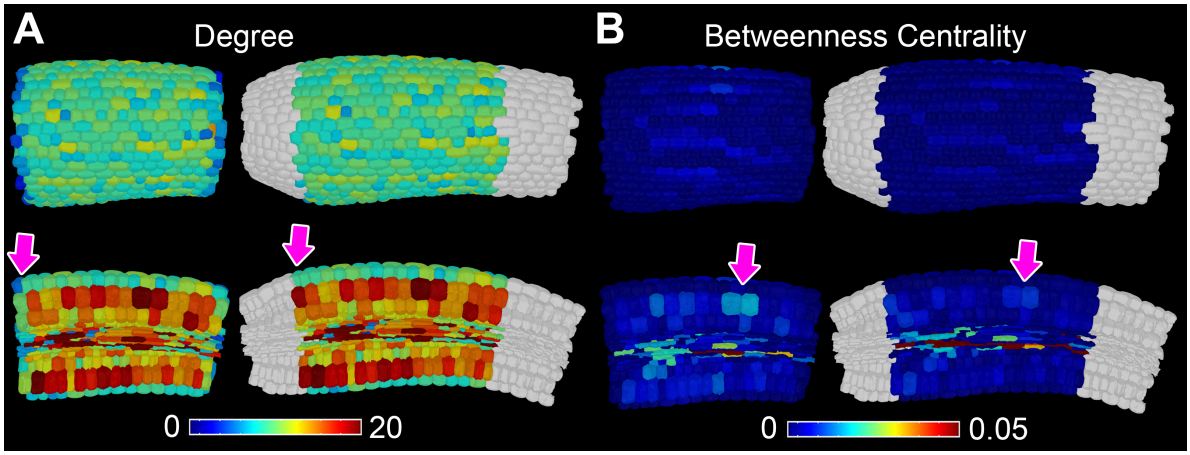


Figure 4.3. Topological buffering of the hypocotyl.
(A) Surface (top) and cross-section (bottom) of the non-buffered (left) and buffered (right) *A. thaliana* mesh, false coloured with degree. (B) The *A. thaliana* mesh false coloured with betweenness centrality. White cells represent the topological buffer. Pink arrows point to cells that are significantly different in degree or betweenness centrality before and after buffering. Figure reproduced from Jackson et al., 2017, *eLife.*

Lastly, the hypocotyl vasculature was included in the cell networks, but subsequently excluded from analyses due to difficulties with vasculature segmentation in the image-processing step. Though it was not possible to ensure 100% accuracy in the vasculature segmentation, manual attempts were made to ensure it was as close to representing the real cell connectivity as possible. These three additional steps resulted in highly accurate cell interaction networks (Figure 4.4), ensuring that interpretation of structural network analysis results was justified.

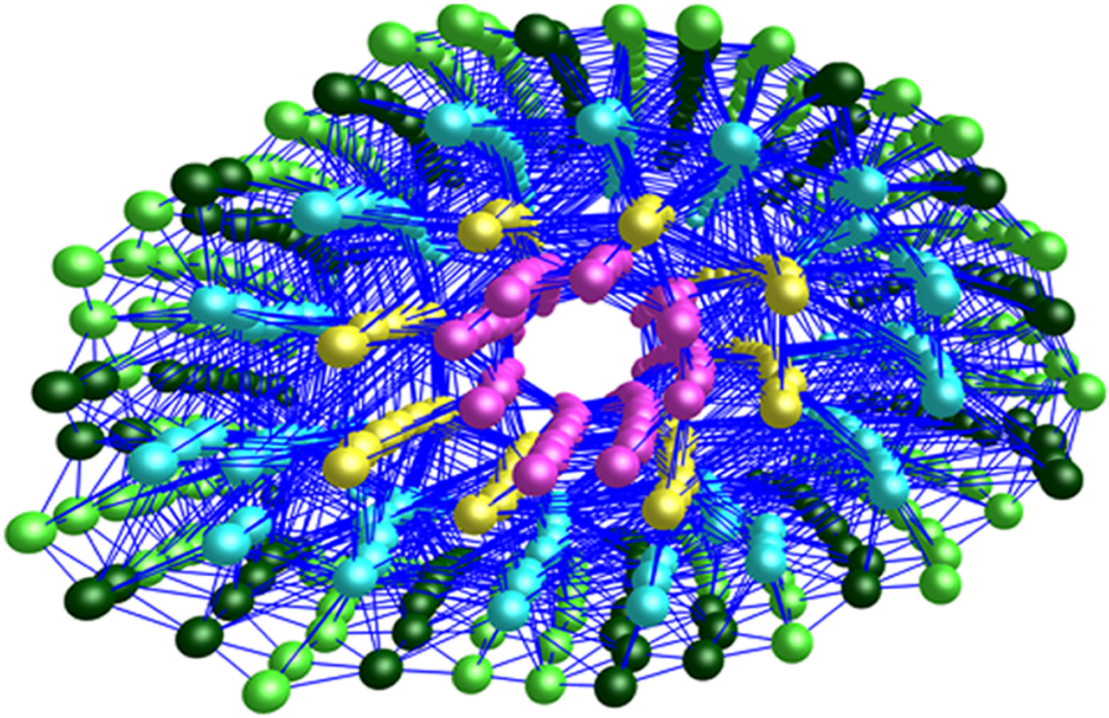


Figure 4.4. An annotated cellular interaction network extracted from an *Arabidopsis thaliana* hypocotyl of the Colombia ecotype.
Each node represents a cell, while each blue edge connecting the nodes represents a physical connection between cells. Nodes are coloured by cell type. Cell types shown are trichoblasts (dark green), atrichoblasts (light green), outer cortex (blue), inner cortex (yellow) and endodermis (pink). Vasculature cells, and cell-cell interfaces that they make, have been omitted in this image for clarity. Figure reproduced from Jackson et al., 2017, *eLife.*

In each network, the degree and BC of each cell was calculated (Section 2.4.1). Degree is measured by counting the number of physically connected neighbours each cell has, and can be used to identify 'hubs', cells with high degree (van den Heuvel and Sporns, 2013).

BC is a measure of global connectivity that can identify highways of information transport. Due to the known function of the hypocotyl in transport between the

developing root and embryonic leaves, betweenness centrality (BC) was used to measure the global connectivity of each cell. Measuring BC in the hypocotyl connectivity networks highlights cells that lie on many short paths between other pairs of cells, suggesting that efficient transport routes may incorporate high BC cells.

4.2.2 Topological analysis of the *Arabidopsis thaliana* (Col) hypocotyl

Three biological replicate *Arabidopsis thaliana* hypocotyls of Colombia ecotype were analysed (Figure 4.5A). Using false colouring, the degree of each cell can be examined *in situ* (Figure 4.5B). Degree was lower in epidermal cells than in cortical cells, due to their position at the periphery of the cellular network (Figure 4.5B and 4.6A). The vasculature cells representing xylem vessels also had high degree (Figure 4.5B), as their elongated shape causes them to be adjacent to many cells in the endodermis. Within cell types, distribution of degree values did not appear to have any specific patterning.

BC was also visualised as a heat map in *A. thaliana* (Col) hypocotyls (Figure 4.5C). As well as high degree, the hypocotyl vasculature contained cells that had higher BC than all other cell types. In terms of BC calculation, these vasculature cells create short paths between cells in the longitudinal direction through the hypocotyl. This is in agreement with their known biological role in transport throughout the system. Notably, an additional region of high BC values is present along particular cell files in the epidermis, representing another potential conduit for information transport in the hypocotyl cellular network.

When comparing distributions of topological properties, there are noticeable differences between the two epidermal cell types, atrichoblasts and trichoblasts (Figure 4.5D and E). In the Colombia ecotype, trichoblast cells have a significantly higher degree (Figure 4.5D). This is due to their position in relation to underlying cortical cells, where trichoblasts have two neighbouring cortical cells in the radial direction (Schiefelbein, 2003). Atrichoblasts are positioned next to only one cortical cell in the radial direction, lowering their average degree.

Distributions of BC also differ between atrichoblasts and trichoblasts in *A. thaliana* (Col) (Figure 4.5E). Trichoblasts tended to have the lowest BC of all cell types (Figure 4.6B). Despite their lower degree, atrichoblasts tend to have higher BC than trichoblasts, shown by the longer tail in the BC distribution (Figure 4.5E). This suggests that higher order organisational properties in the hypocotyl are not necessarily dictated by local cell-cell interactions.

As well as topological analysis of cell properties, the BC of cell interfaces was also examined by calculating edge betweenness centrality (Figure 4.5F and G) (Section 2.4.2). Edge betweenness centrality assesses the contribution of edges towards short paths throughout the hypocotyl. In the Colombia ecotype of *A. thaliana*, false coloured cross sections of the cellular network layout show a higher edge BC in cell interfaces close to the vasculature (which is omitted for clarity due to the large number of network edges), as well as high edge BC in edges connecting some files of epidermal cells (Figure 4.5F). This result mirrors the observations when using global topological measurement of node properties.

Plotting the distribution of edge BC shows that there tends to be much higher edge BC in Colombia ecotype atrichoblast-atrichoblast cell interfaces, than in trichoblast-trichoblast, or atrichoblast-trichoblast connections, again reflecting results from node BC measurements (Figure 4.5G). Again, this indicates a difference in global organisational properties between the epidermal cell types.

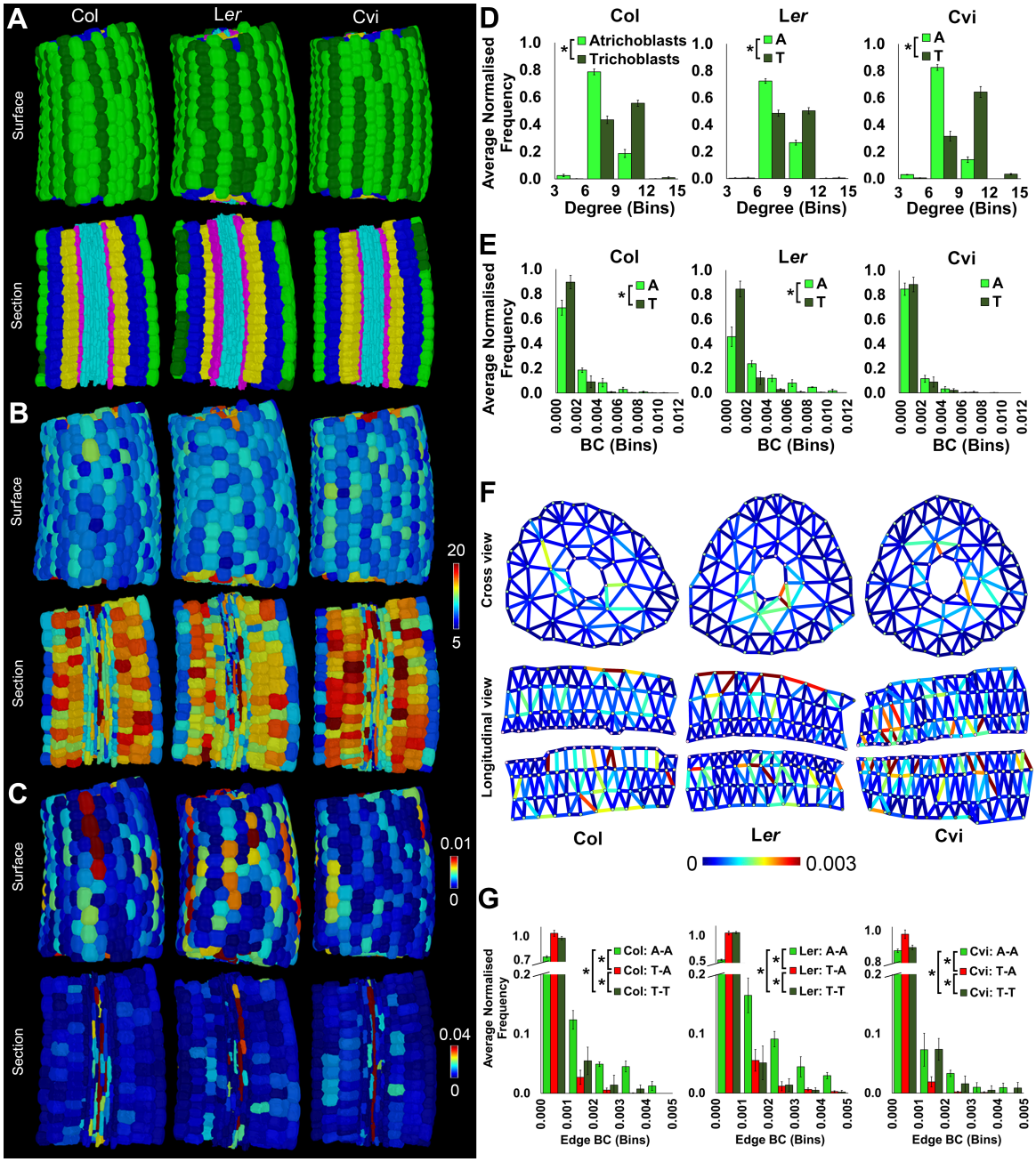


Figure 4.5. Topological analyses of three *A. thaliana* ecotypes, Col, L*er* and Cvi. (A) Hypocotyl meshes false coloured by cell type in both the surface and the cross section of three *A. thaliana* ecotypes. Cell types shown are trichoblasts (dark green), atrichoblasts (light green), outer cortex (dark blue), inner cortex (yellow), endodermis (pink) and vasculature (light blue). (B) Hypocotyl meshes false coloured with cell degree. (C) Hypocotyl meshes false coloured with cell betweenness centrality. (D) Degree of epidermal cells in all ecotypes. (E) Betweenness centrality of epidermal cells in all ecotypes. (F) Cross sections of the cell connectivity networks in all three ecotypes, false coloured with edge betweenness centrality. (G) Edge betweenness centrality in epidermal cell interfaces. Data in charts represent the average

normalised frequency from triplicate biological replicates. Error bars are +/- one standard deviation in a frequency bin. A * indicates a significant difference between distributions using the chi-squared test (degree) or the Kolmogorov–Smirnov test (betweenness centrality), at the $p \leq 0.05$ level ($p \leq 1.56\times10^{-5}$ after Bonferroni correction for 3200 distribution comparisons in the study). Figure reproduced from Jackson et al., 2017, *eLife.*

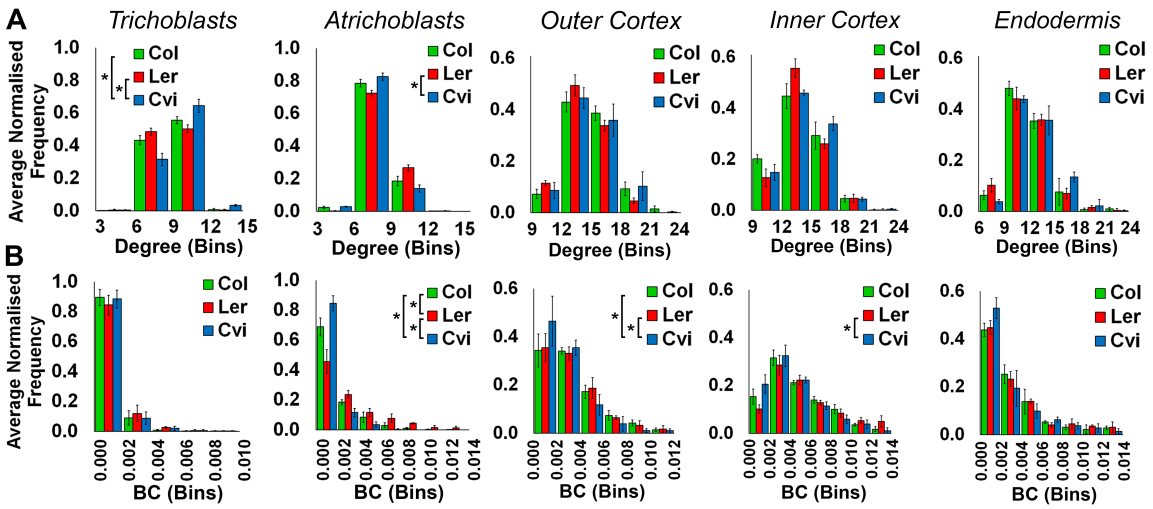


Figure 4.6. Degree and betweenness centrality in different *Arabidopsis* hypocotyl cell types.
(A) Degree in three *A. thaliana* ecotypes, Col, L*er* and Cvi. (B) Betweenness centrality. Data shown represents the average normalised frequency from triplicate biological replicates. Error bars are +/- one standard deviation in a frequency bin. A * indicates a significant difference between distributions using the chi-squared test (degree) or the Kolmogorov–Smirnov test (betweenness centrality), at the $p \leq 0.05$ level ($p \leq 1.56\times10^{-5}$ after Bonferroni correction for 3200 distribution comparisons in the study). Figure reproduced from Jackson et al., 2017, *eLife.*

4.2.3 Comparison of topology in three *A. thaliana* ecotypes

To establish whether differences in cell-type specific organisation are present in genetically similar hypocotyls, ecotypes of *A. thaliana* were collected from different locations with different climates and challenges for plant growth. Each *Arabidopsis*

ecotype has genomic and phenotypic differences (Gan et al., 2011). Cell organisation in the Lansberg *erecta* (L*er*) and Cape Verdi Islands (Cvi) ecotypes was compared with organisation in the Colombia ecotype to examine the variation in cellular patterning across different genotypes.

The *in situ* distribution of degree across the hypocotyl was qualitatively similar in all three ecotypes examined (Figure 4.5B). The same high BC was observed in the vasculature of each ecotype, though high BC epidermal cell files were more striking in the Col and L*er* hypocotyls than in the epidermis of Cvi (Figure 4.5C).

In all three genetic backgrounds, trichoblasts had more neighbouring cells than atrichoblasts, again due to adjacent cortical cell positioning (Figure 4.5D). Comparing cell type degree across ecotypes, degree was highest in the trichoblasts of Cvi, and lowest in L*er* (Figure 4.6A). Atrichoblast cells in L*er* had more physically connected neighbours than other ecotypes. The degree of cells in both cortical layers and the endodermis was fairly consistent across each *A. thaliana* ecotype.

Like in the *A. thaliana* Col ecotype, atrichoblast cells had higher BC than trichoblast cells in L*er* (Figure 4.5E). However, this trend was not present in Cvi, where the distribution of BC in both trichoblasts and atrichoblasts was similar. Across all three ecotypes, the BC of trichoblasts did not differ, while the distribution of BC in atrichoblasts of the L*er* ecotype had the longest tail, followed by Col, then Cvi (Figure 4.6B). Differences in global connectivity in the outer cortex of Cvi were also identified, where BC was lower than in other ecotypes.

These topological analyses in different *A. thaliana* ecotypes suggest the presence of phenotypic plasticity in the cellular organisation of the hypocotyl. Large variation in epidermal path lengths in different cell types, driven by unintuitive global topological features, was observed in the Col and L*er* ecotypes, but not Cvi.

4.2.4 Geometric considerations in topological measurements

The size of the physical connection between cells is not the same for each cell-cell interaction in the hypocotyl (Figure 4.7). In *A. thaliana* ecotypes, interactions between different cell layers, as well as interactions between endodermal cells, are the smallest in terms of shared cell wall area in μm^2 (Figure 4.7C and D). Interactions between cells in the epidermis tend to be slightly larger (Figure 4.7A), while the size of interfaces between cells in cortical layers are the largest in the hypocotyl (Figure 4.7B). These differences in interface size are largely accounted for by overall cell sizes (Figure 4.8A).

To examine whether interface size could be a useful feature to incorporate into analysis of a cellular network, the physical cell interaction size was added to each edge as metadata. The inverse of this additional value for each edge can be used as a weighting to calculate betweenness centrality (Section 2.4.5). The inclusion of interface size into this calculation assumes that connecting cell wall area is a feature relevant to global information transfer across the network.

In situ examination showed that cells in both the inner and outer cortex had the highest weighted BC in all three *A. thaliana* ecotypes (Figure 4.8B). The vasculature, which previously in networks without weighting had the highest BC values, did not stand out as a high weighted BC cell type. The size of cells and the interactions they make was the key factor in geometrically determined path length throughout a cell type, which was very short in cortical cells compared to all other cell types (Figure 4.8C).

Interface size is a biologically relevant feature for potential information transport between cells, which could relate to the capacity for the movement of molecules through high numbers of plasmodesmata or transport proteins (Jackson et al., 2017a). However, due to the calculation of weighted betweenness centrality being dominated by geometric features, this approach does not seem appropriate for the identification of topologically interesting features in the cellular organisation of the hypocotyl.

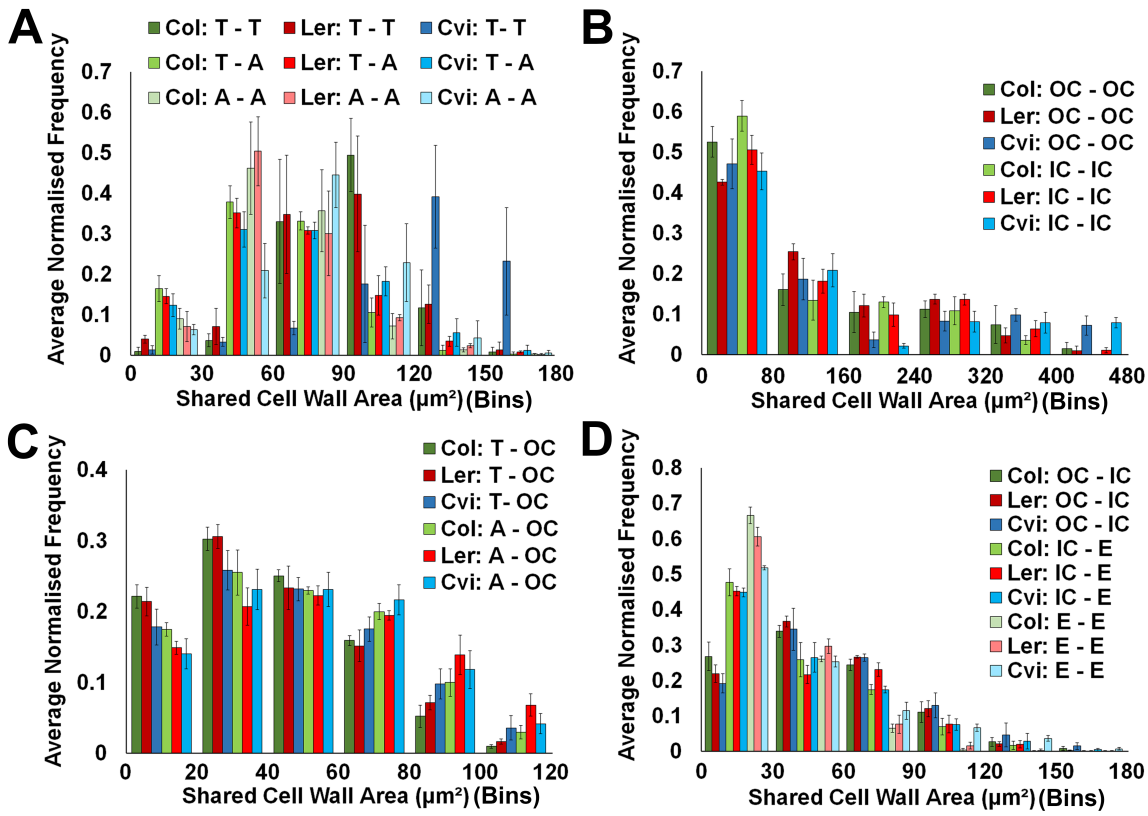


Figure 4.7. Interface sizes between adjacent cell types in in *A. thaliana* ecotypes, Col, L*er* and Cvi.
(A) Shared cell wall area between epidermal cell types, the trichoblasts and atrichoblasts. (B) Shared cell wall area between cells within the outer cortex and inner cortex. (C) Shared cell wall area between trichoblast, atrichoblast and outer cortical cells. (D) Shared cell wall area between cells in the outer and inner cortex, the inner cortex and endodermis, and within the endodermis. Error bars are +/- one standard deviation in a frequency bin. Figure reproduced from Jackson et al., 2017, *eLife.*

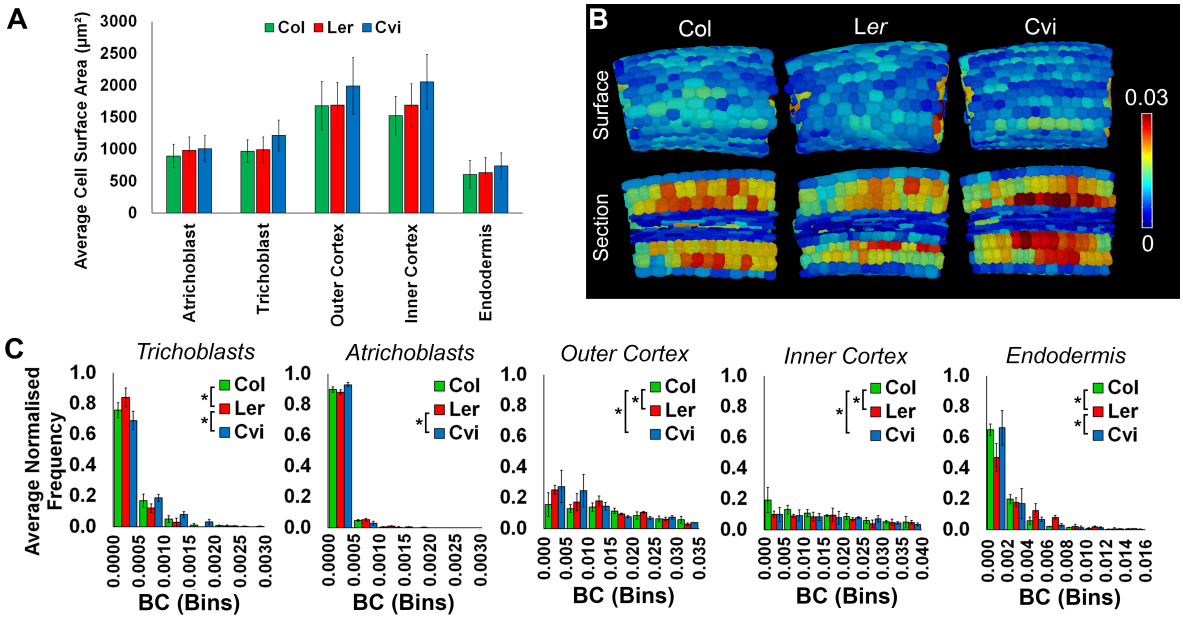


Figure 4.8. Weighted betweenness centrality in *A. thaliana* ecotypes, Col, L*er* and Cvi.
(A) Cell surface area in *A. thaliana.* (B) The surface and cross-sections of hypocotyl meshes, false coloured with weighted betweenness centrality. (C) Weighted betweenness centrality in different hypocotyl cell types. Data in charts represent the average normalised frequency from triplicate biological replicates. Error bars are +/- one standard deviation in a frequency bin. A * indicates a significant difference between distributions using the Kolmogorov–Smirnov test (betweenness centrality), at the $p \leq 0.05$ level ($p \leq 1.56 \times 10^{-5}$ after Bonferroni correction for 3200 distribution comparisons in the study). Figure reproduced from Jackson et al., 2017, *eLife.*

4.2.5 Quantifying molecular movement in the hypocotyl epidermis

The optimum route for information to take between two nodes in a network is the shortest path (Barabási, 2016). In *A. thaliana* Col and L*er* ecotypes, atrichoblast cells were identified as lying on many short paths, in contrast to the trichoblast cells, using betweenness centrality (Figure 4.9A). In the Cvi ecotype, there were no differences in BC in both epidermal cell types.

Using data from Jackson et al. (2017b) (see Appendix 2), BC was assessed for its capacity to predict cell-type specific transport in the hypocotyl epidermis. Data were collected using a fluorescein transport assay (Duran-Nebreda and Bassel, 2017b) (Jackson et al., 2017b). In a normal developing plant molecules would be absorbed by hair cells in the root, and would subsequently be transported through the hypocotyl, the embryonic stem, to the rest of the plant. In this assay, cut hypocotyl sections were dipped into fluorescein, representing transport after root uptake, and fluorescein was allowed to move through the tissue. There is no biological role for fluorescein in plants, so its movement is representative of the movement of non-specific molecules throughout the hypocotyl.

Fluorescence, representing fluorescein concentration, was measured in the epidermis, away from the site of original uptake, in the L*er*, Col and Cvi ecotypes of *Arabidopsis thaliana* (Figure 4.9B, C and D). Transport of the fluorescent molecule occurred in all *A. thaliana* ecotypes examined. Upon qualitative inspection, the concentration of fluorescein indicated by fluorescence was not equal in each epidermal cell.

Fluorescence in the epidermal cells of each ecotype was quantified (Figure 4.9E, F and G). Atrichoblast cells in L*er* and Col hypocotyls had higher levels of fluorescence in atrichoblast cells than in trichoblast cells, while there was no significant difference between the epidermal cell types in the Cvi ecotype (Figure 4.9H), where the distribution of fluorescence was spread more evenly across all epidermal cells.

These results show that topological analysis at a global scale can be used to predict the bulk transport of molecules. Fluorescein preferentially moves along short paths, located primarily in atrichoblasts in the epidermis, which were identified using only the hypocotyl structural networks to calculate BC. A difference in cell organisation in Cvi, compared to cell arrangements in the Col and Ler ecotypes, directly translates to a difference in observed tissue function.

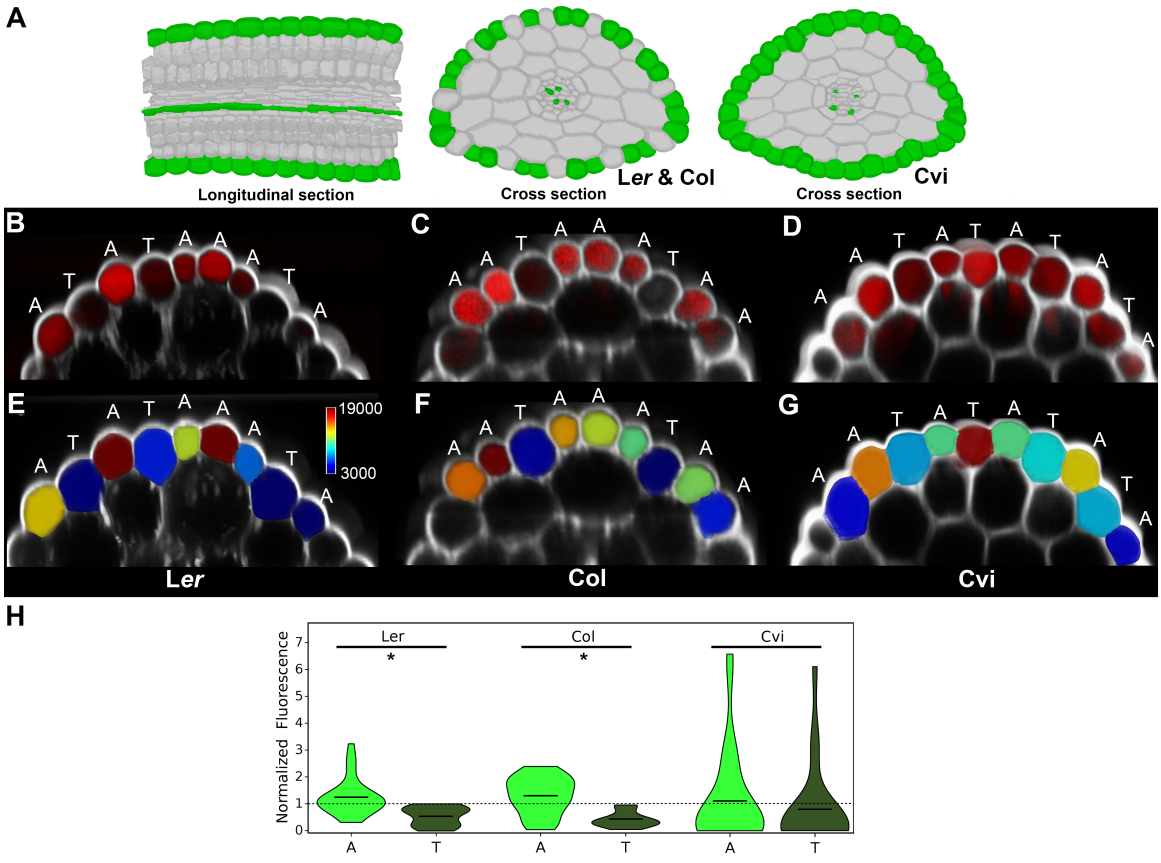


Figure 4.9. Movement of fluorescein through the hypocotyl.
(A) A model of molecular movement through the hypocotyl, predicted by betweenness centrality. (B) Confocal microscope image of the L*er* hypocotyl epidermis (white) and fluorescein concentration (red). (C) Image of the Col hypocotyl.

(D) Image of the Cvi hypocotyl. (E) False-coloured individual cell quantification of fluorescein concentration in the L*er* hypocotyl epidermis. (F) Fluorescein concentration in the Col epidermis. (G) Fluorescein concentration in the Cvi epidermis. (H) Violin plot of normalised fluorescence in atrichoblasts and trichoblasts in *A*. *thaliana* ecotypes. A black bar in each violin represents the mean. A * indicates a significant difference between fluorescence in atrichoblasts and trichoblasts. Data are from three biological replicates for each ecotype. Cells in each sample were pooled and mean normalised for comparison. Figure reproduced from Jackson et al., 2017, *eLife.*

4.2.6 Topological analysis of hypocotyls in other plant species

In addition to *A. thaliana* ecotypes, hypocotyls from different plant species, poppy (*Papaver rhoeas*) and foxglove (*Digitalis purpurea*) were topologically analysed, to determine whether there is plasticity in cell patterning across diverse plant lineages. Though each species is evolutionarily distant from each other, they are all present throughout Western Europe, enabling the comparison of cell organisation in plants that experience similar environmental challenges. Three hypocotyls from each species were imaged and converted into annotated cellular connectivity networks. In terms of structure, the poppy hypocotyl is larger than in *Arabidopsis thaliana*, and has larger cells. The foxglove hypocotyl is also larger than in *A. thaliana*, as well has having an additional layer of cortical cells (Figure 4.10A).

As in *A. thaliana*, degree is lower in epidermal cells than in all other cell types in both poppy and foxglove, again due to the position of the cells at the edge of the cellular connectivity network (Figure 4.10B and Figure 4.11A). Upon *in situ* examination, BC is highest in the vasculature in both species, again reflecting features of the *A. thaliana* hypocotyls (Figure 4.10C).

Comparing local topological properties of epidermal cell types, degree was higher in trichoblasts than in atrichoblasts in both poppy and foxglove (Figure 4.10D). Again, as in *A. thaliana*, this is due to the trichoblast positions adjacent to two cortical cells in the radial direction. Degree distributions in the *A. thaliana* Col, poppy and foxglove endodermis were also all significantly different from each other. In contrast to any observations in *Arabidopsis* ecotypes, the BC of trichoblast cells in poppy was higher than in atrichoblast cells, indicating that more short paths through the hypocotyl are present in the poppy epidermis (Figure 4.10E). This difference in path lengths however is much more subtle than in *A. thaliana* Col, where the distribution of BC in atrichoblasts has a much longer tail (Figure 4.11B). In foxglove, there was no difference between BC in the epidermal cell types, similar to observations in the *A. thaliana* Cvi ecotype.

While the additional layer of cortical cells in foxglove was similar to other cortical layers in terms of degree (Figure 4.11A), it was topologically distinct in its BC from other inner cortical cell layers examined (Figure 4.11B). This means that more short paths run through the additional layer of cells than in other cortical layers, possibly suggesting a role for these extra cortical cells in organ-wide cellular communication or transport.

Cross sections of the poppy and foxglove hypocotyl cellular network, overlaid with a heat map for edge BC, show that edge BC tends to be higher the closer an edge is to the radial centre of the network, where the vasculature is present (Figure 4.10F). This

is a different pattern of edge BC than observed in *A. thaliana*, where edge BC was high in some epidermal cells (Figure 4.5F). Quantitative comparison of edge BC in the epidermis is in agreement with this observation, where distributions of edge BC in *A. thaliana* Col are significantly longer-tailed in all epidermal cell-cell interfaces (Figure 4.10G).

Together, these results show that there is plasticity in epidermal cell patterning between genetically diverse plant species, as well as between *A. thaliana* ecotypes. BC identified that path length in atrichoblasts is shorter in *A*. *thaliana* than in poppy or foxglove, particularly in the L*er* ecotype. The presence of different cellular organisation, irrespective of the similar growing environments for each species, may suggest that the conduits of information transport in the epidermis may be a recent evolutionary innovation in *A. thaliana* that has not been adopted in other plants.

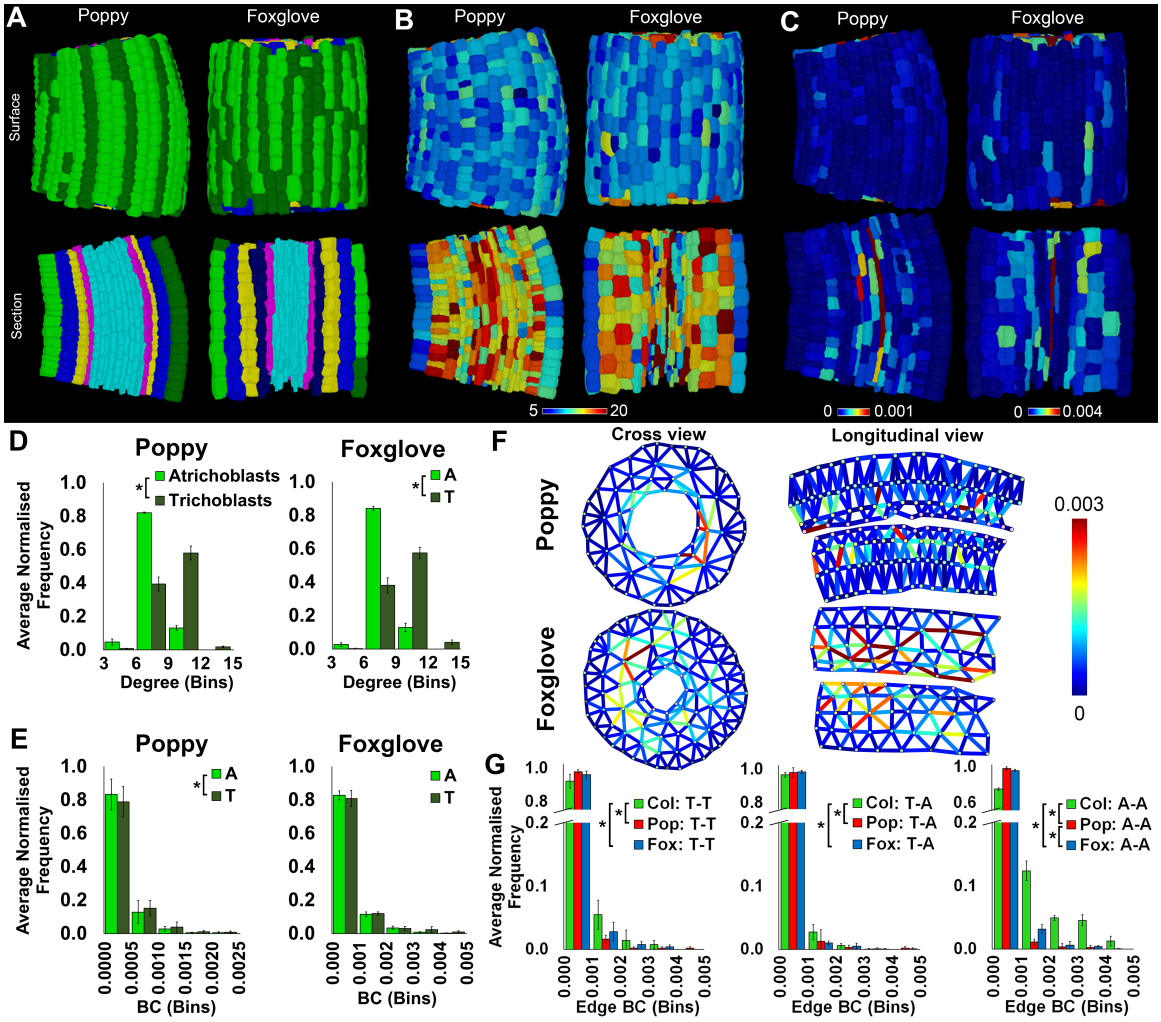


Figure 4.10. Topological analyses of the poppy and foxglove hypocotyls.
(A) Hypocotyl meshes false coloured by cell type in both the surface and the cross section of poppy and foxglove. Cell types shown are trichoblasts (dark green), atrichoblasts (light green), outer cortex (dark blue), inner cortex (yellow), endodermis (pink) and vasculature (light blue). (B) Hypocotyl meshes false coloured with cell degree. (C) Hypocotyl meshes false coloured with cell betweenness centrality. (D) Degree of epidermal cells both species. (E) Betweenness centrality of epidermal cells in both species. (F) Cross sections of the cell connectivity networks in both species, false coloured with edge betweenness centrality. (G) Edge betweenness centrality in epidermal cell interfaces. Data in charts represent the average normalised frequency from triplicate biological replicates. Error bars are +/- one standard deviation in a frequency bin. A * indicates a significant difference between distributions using the chi-squared test (degree) or the Kolmogorov–Smirnov test (betweenness centrality), at the $p \leq 0.05$ level ($p \leq 1.56 \times 10^{-5}$ after Bonferroni correction for 3200 distribution comparisons in the study). Figure reproduced from Jackson et al., 2017, *eLife*.

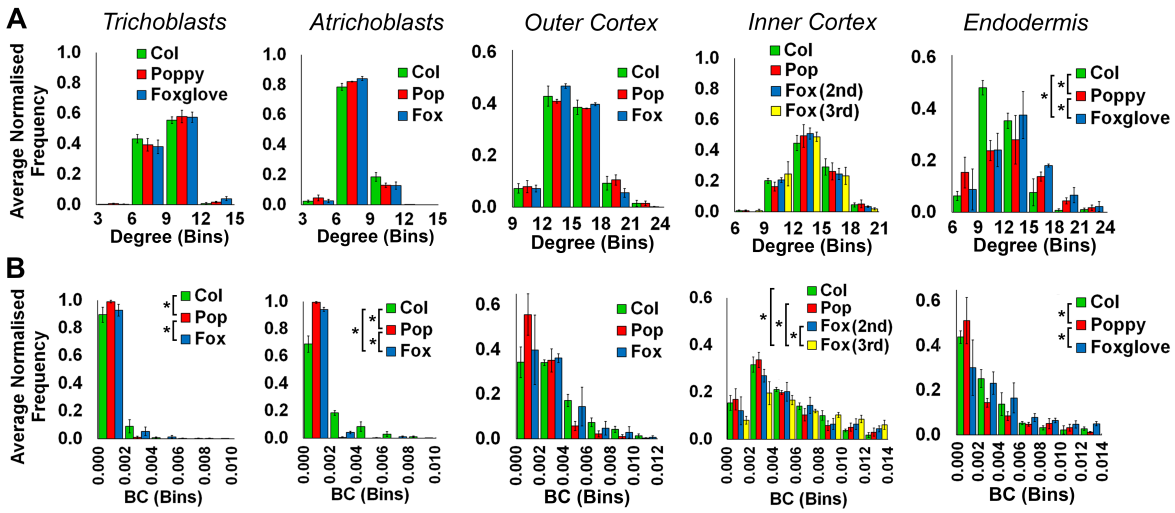


Figure 4.11. Degree and betweenness centrality in hypocotyl cell types of different species.
(A) Degree in hypocotyls of three species, *Arabidopsis thaliana* (Col), poppy and foxglove. (B) Betweenness centrality. Data shown represents the average normalised frequency from triplicate biological replicates. Error bars are +/- one standard deviation in a frequency bin. A * indicates a significant difference between distributions using the chi-squared test (degree) or the Kolmogorov–Smirnov test (betweenness centrality), at the $p \leq 0.05$ level ($p \leq 1.56\times10^{-5}$ after Bonferroni correction for 3200 distribution comparisons in the study). Figure reproduced from Jackson et al., 2017, *eLife.*

4.2.7 Topological analysis of mutant *A. thaliana* hypocotyls

The cellular organisation that we observe in different tissues results from the evolutionary selection of functional cellular configurations. These configurations are constrained however, by the limitations imposed on their geometry and topology in Euclidean space, as well as limitations due to the mechanical and functional roles

tissues must carry out (Thompson, 1942) (Niklas, 2009). The quantitative comparison of cellular patterning between ecotypes and species reveals differences in cellular organisation, suggesting a possible role for genetic elements in the arrangement of the hypocotyl.

When genes contributing to cellular organisation are lost, alternative cell arrangements can arise in tissues, which are often sub-optimal in fitness and function (Lin and Schiefelbein, 2001) (Bean et al., 2002). By quantitatively measuring patterning in mutant hypocotyls, where the gene responsible for loss of normal cell arrangement is known, allows the quantitative contribution of a gene to normal pattering to be determined. To achieve this, the topologies of three different mutants with altered hypocotyl cell patterning were each compared to their wild-type equivalent.

CDKA1;1 (*CYCLIN-DEPENDENT KINASE A1;1*) regulates the cell cycle, as well as having a role in asymmetric cell division which affects patterning (Nowack et al., 2012). On qualitative inspection, though cell shape is slightly different, the arrangement of cells in the *ckda1;1* mutant *Arabidopsis* hypocotyl seems similar to cellular organisation of the wild-type *A. thaliana* Col (Figure 4.5A and 4.12A).

The spatial distribution of degree across the *cdka1;1* hypocotyl is also similar to that of the wild-type (Figure 4.12B), though comparison of degree distributions in the both the inner cortex and endodermis with wild-type *A. thaliana* Col reveals that cells in these layers tend to have a higher degree in *cdka1;1* (Figure 4.13A). The relationship

between the degree distributions of atrichoblasts and trichoblasts in *cdka1;1* is unchanged from this wild-type hypocotyl, but differences are observed in higher-order organisational properties (Figure 4.12D). Whilst BC in the vasculature is high, reflecting that of *A. thaliana* Col, the epidermal BC patterning observed in the wild-type is less obvious upon visualisation of the property as a heat map in the *cdka1;1* mutant hypocotyl (Figure 4.12C). The long tail in atrichoblast BC distribution is lost in *cdka1;1* (Figure 4.12D), and no difference is observed between the existence of short paths in either epidermal cell type. This result suggests that the *CDKA1;1* gene contributes to the reduction in path length in atrichoblast cells through the mediation of cellular patterning, providing a shortcut for transportation along the hypocotyl epidermis. The local activity of *CDKA1;1* in controlling cell divisions may therefore be responsible for a global change in cellular organisation.

The second patterning mutant that was topologically analysed was *monopteros* (*mp*). In *Arabidopsis thaliana,* the *MONOPTEROS* gene controls auxin-mediated cell patterning through its activity as a transcription factor (Hardtke and Berleth, 1998).

The *mp* mutant does not develop vasculature during growth, resulting in qualitatively highly perturbed cellular organisation, consisting of only of an epidermal layer and cortical cells (Figure 4.12A). The distribution of degree in the epidermis is qualitatively similar to wild-type *A. thaliana* Col (Figure 4.12B), and the difference between the degree of trichoblasts and atrichoblasts is maintained in the *mp* mutant. However, compared to in the wild-type, degree in *mp* atrichoblast cells is higher (Figure 4.13A). Cells in the inner cortex of *mp* tend to have fewer neighbours than in

the wild-type control, due to the lack of thin vasculature cells that are usually adjacent to this cell type.

The distribution of BC across the *mp* hypocotyl was drastically different to that of *A. thaliana* (Figure 4.13B). Whilst the difference between atrichoblast and trichoblast BC was still present in the *mp* hypocotyl epidermis (Figure 4.12E), both cell types had significantly higher BC than in the wild-type control. Path lengths were also considerably shorter through the outer cortex in the *mp* mutant (Figure 4.13B). These results suggest that the *MONOPTEROS* transcription factor has a role in reducing path length along the hypocotyl epidermis through the control of cellular organisation, but is not necessary for the distinction between transport capacity in the atrichoblast and trichoblast cell types. The lack of vasculature in the *mp* mutant has consequences for the way in which information can theoretically travel through the tissue. Visualising edge BC in the mutant cellular connectivity network shows that short paths are present in the radial direction, in contrast to all other networks examined (Figure 4.12G).

The final mutant examined was *laterne* in the *A. thaliana* L*er* genetic background, which lacks cotyledons, the embryonic leaves (Treml et al., 2005). Cotyledons do not develop in mature *laterne* mutant embryos, as the auxin signalling required for development is defective. The *laterne* phenotype had few differences in local cell arrangement, as all degree distributions were similar to the wild-type control L*er* ecotype, with the exception of the endodermis (Figure 4.13C). In contrast, path length in the *laterne* hypocotyl measured with BC was significantly longer in

atrichoblasts, trichoblasts and the outer cortex (Figure 4.13D), though the distinction between BC distributions across epidermal cell types was maintained (Figure 4.12F). The *laterne* phenotype therefore limits path lengths in the hypocotyl. This suggests that signalling from the cotyledons is required for normal organ-wide cell patterning in the embryonic stem, or that gene products absent in the *laterne* mutant are required for normal cell organisation, coordinated through local cell signalling activity (Treml et al., 2005).

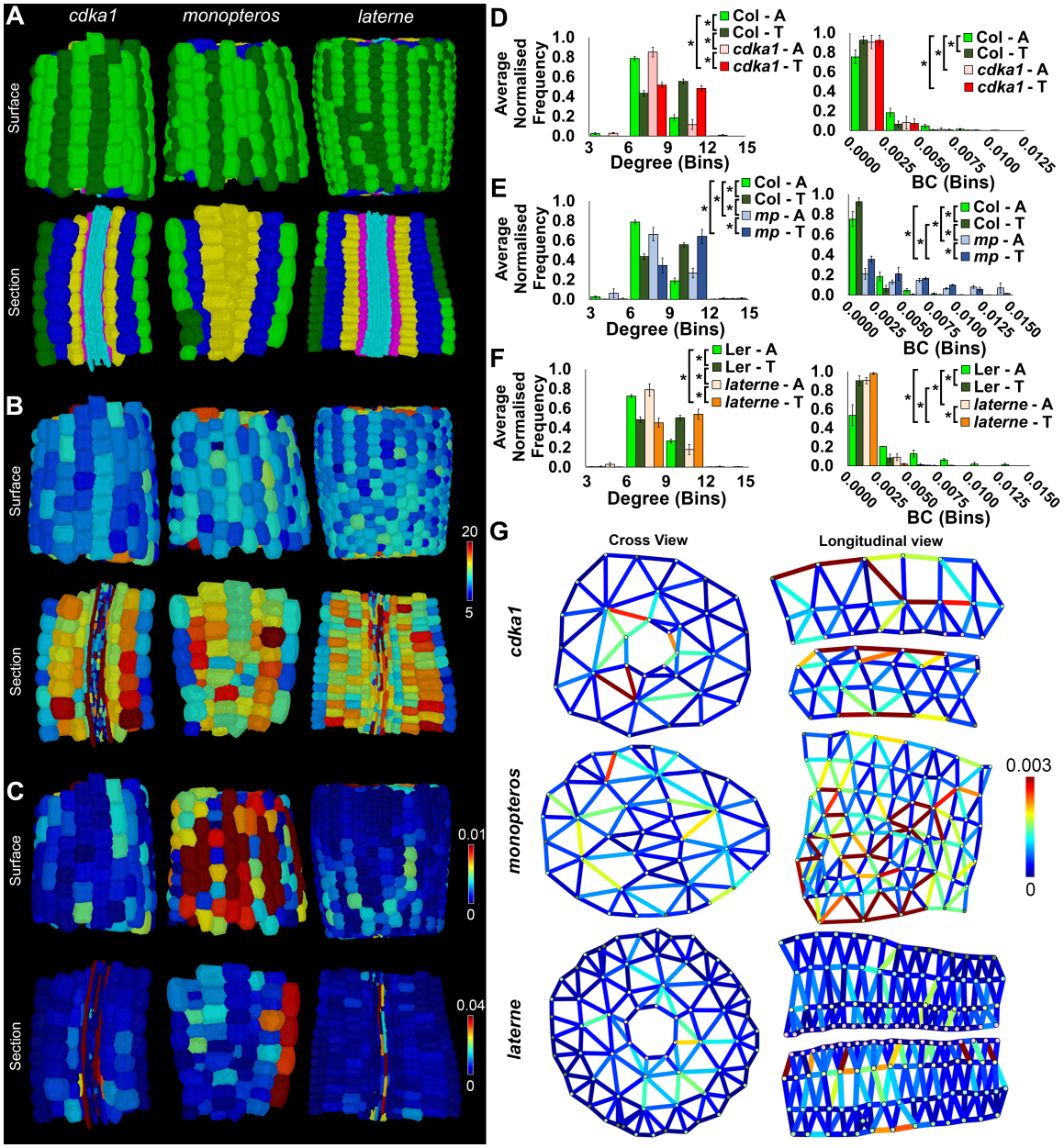


Figure 4.12. Topological analyses of three mutant *A. thaliana* hypocotyls.
(A) Hypocotyl meshes false coloured by cell type in both the surface and the cross section of the *A. thaliana* mutants, *cdka1;1*, *monopteros*, and *laterne*. Cell types shown are trichoblasts (dark green), atrichoblasts (light green), outer cortex (dark blue), inner cortex (yellow), endodermis (pink) and vasculature (light blue). (B) Hypocotyl meshes false coloured with cell degree. (C) Hypocotyl meshes false coloured with cell betweenness centrality. (D) Degree and betweenness centrality of epidermal cells (T – trichoblasts, A – atrichoblasts) in wild type *A. thaliana* (Col) and the *cdka1;1* mutant. (E) Degree and betweenness centrality of epidermal cells in wild type *A. thaliana* (Col) and the *monopteros* mutant. (F) Degree and betweenness centrality of epidermal cells in wild type *A. thaliana* (L*er*) and the *laterne* mutant, from the L*er* background. (G) Cross sections of the cell connectivity networks in all three mutants, false coloured with edge betweenness centrality. Data in charts represent

the average normalised frequency from triplicate biological replicates. Error bars are +/- one standard deviation in a frequency bin. A * indicates a significant difference between distributions using the chi-squared test (degree) or the Kolmogorov–Smirnov test (betweenness centrality), at the $p \leq 0.05$ level ($p \leq 1.56 \times 10^{-5}$ after Bonferroni correction for 3200 distribution comparisons in the study). Figure reproduced from Jackson et al., 2017, *eLife.*

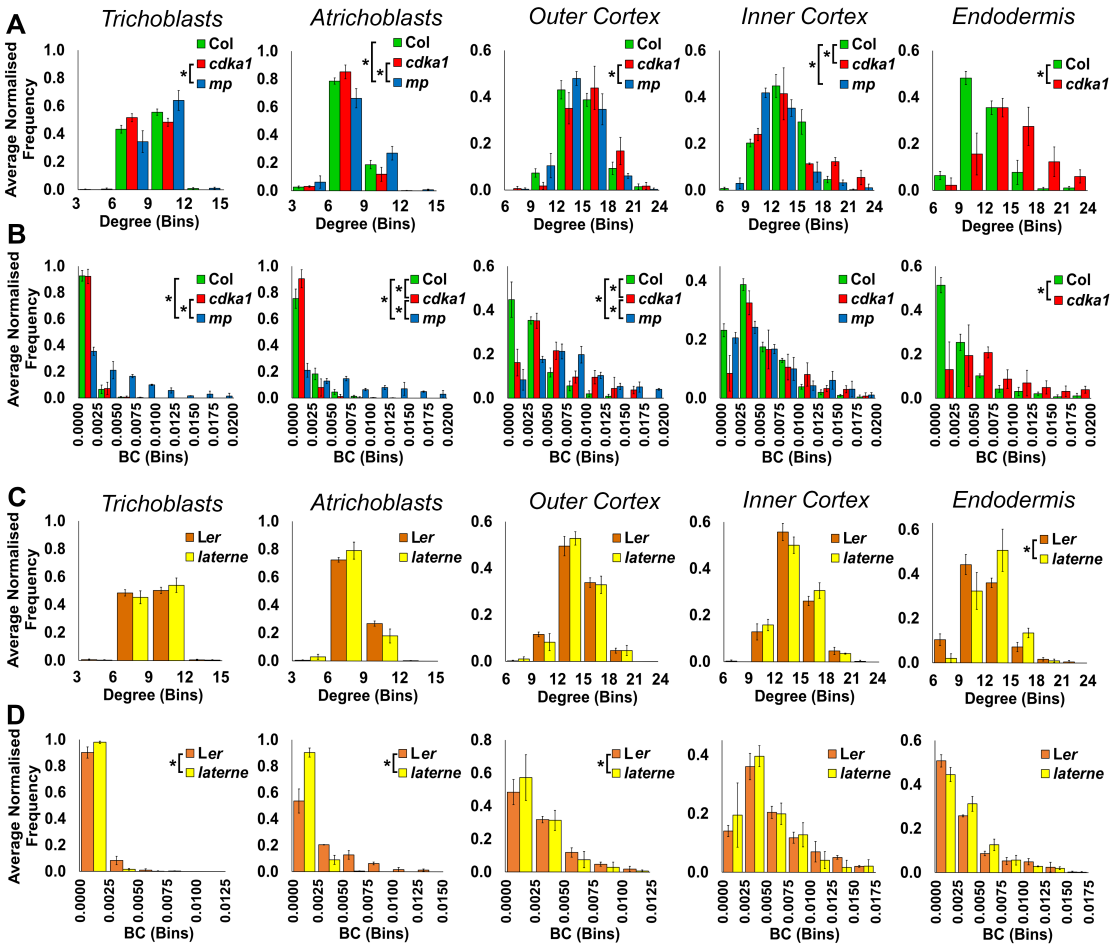


Figure 4.13. Degree and betweenness centrality in hypocotyl cell types of different *A. thaliana* mutants.
(A) Degree in hypocotyls of wild-type *A. thaliana* (Col), and both the *cdka1;1* and *monopteros* mutants, in the Col background. (B) Betweenness centrality in the same genetic backgrounds. (C) Degree in hypocotyls of wild-type *A. thaliana* (L*er*), and the *laterne* mutant, in the L*er* background. (D) Betweenness centrality in the same genetic backgrounds. Data shown represents the average normalised frequency from triplicate biological replicates. Error bars are +/- one standard deviation in a frequency bin. A * indicates a significant difference between distributions using the

chi-squared test (degree) or the Kolmogorov–Smirnov test (betweenness centrality), at the $p \leq 0.05$ level ($p \leq 1.56\times10^{-5}$ after Bonferroni correction for 3200 distribution comparisons in the study). Figure reproduced from Jackson et al., 2017, *eLife*.

4.2.8 Relationship between topology and geometry in hypocotyl cells

To examine the relationship between topological and geometric properties in cells within the hypocotyl, the linear coefficient of determination was used, R^2 (Wright, 1921) (Section 2.6.4). This gives an estimation of the correlation between two measured features, and indicates the ability of one measurement to predict another using a simple linear model.

Acting as a benchmark, there was an almost perfect correlation (R^2 ranging from 0.95 to 1.00) between the geometric measurements of cell area and volume in all hypocotyls analysed (Figure 4.14). There was a much more subtle relationship between both local and global topological measurements, degree and BC, and geometric features in most hypocotyls examined (R^2 ranging from 0.05 to 0.40). This indicates that local and global topology are not a simple linear readout of the geometry of cells. There was a considerable correlation between degree and BC in most hypocotyls (R^2 ranging from 0.60 to 0.80), showing that in this tissue, local topology has a fair amount of influence over path length. Still, the degree of cells is not sufficient to capture global patterning features in the hypocotyl, shown by lack of significant differences between degree distributions, while BC distributions reveal significant differences in path lengths (Figure 4.5 and 4.10).

Relationships between topology and geometry were stronger in cells within *monopteros* mutant hypocotyls (Figure 4.14C) (R^2 ranging from 0.35 to 0.70). This is perhaps due to the loss of typical cell type structure driven by the lack of a vasculature. There was also a noticeable weakening of the linear relationship between degree and BC in the *monopteros* hypocotyl (R^2 = 0.29) compared to the relationship in other hypocotyls, indicating a decoupling of local and global topological properties in the mutant.

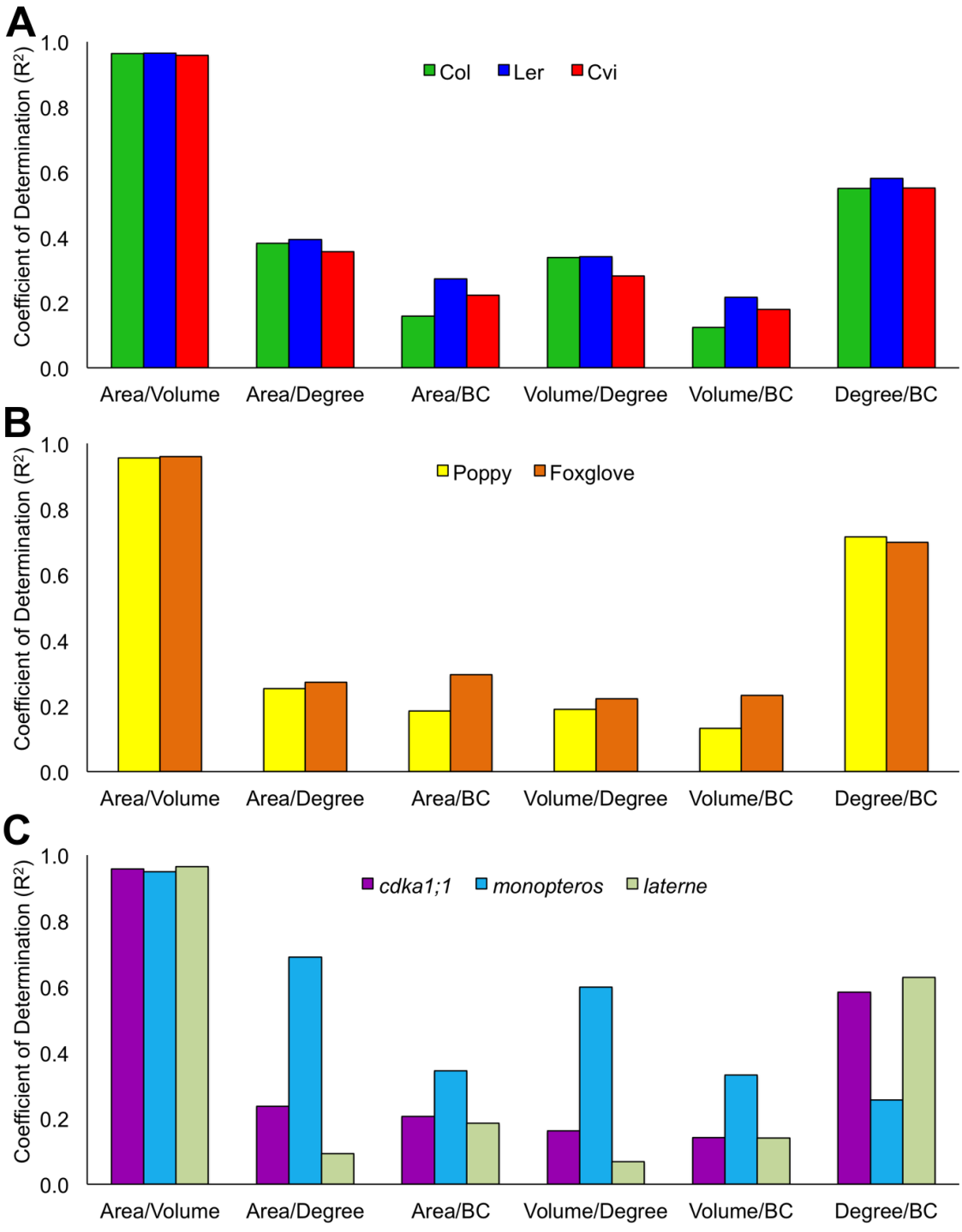


Figure 4.14. Relationships between geometric and topological measurements in the hypocotyl.
(A) The coefficient of determination (R^2), a measure of relatedness, between both geometric and topological measurements of hypocotyl cells in three *A. thaliana* ecotypes. (B) The coefficient of determination between measurements of cells in poppy and foxglove. (C) The coefficient of determination between measurements of cells the *A. thaliana* mutants *cdka1;1*, *monopteros* and *laterne*. All measurements

from every cell across three biological replicates are used to determine the coefficient of determination for two features.

4.2.9 Variability in topological properties

There is variability in the spatial distributions of BC measurements between cells of the same type in all hypocotyls examined (Figures 4.5C, 4.10C and 4.12C). This shows that cellular organisation varies not just across, but also within cell types. The magnitude of variation within a specific cell type was measured using the coefficient of variation (CV), a normalised measure of variability in a feature (Section 2.6.7).

In epidermal cell types, most hypocotyls showed no difference in their ability to generate global patterning with consistent levels of variation, with the exception of the *monopteros* mutant, where BC variability was significantly higher than in all other hypocotyls (Figure 4.15A and B). A similar trend was observed in cortical cells, where *monopteros* had greater variability in BC than most other hypocotyls topologically analysed (Figure 4.15C and D). This may represent a loss of the ability to organise cells correctly in the *monopteros* mutant at this early developmental stage, resulting in highly variable path lengths in some cell types. This suggests that the *MP* gene product may have a role in maintaining consistent path lengths in the hypocotyl.

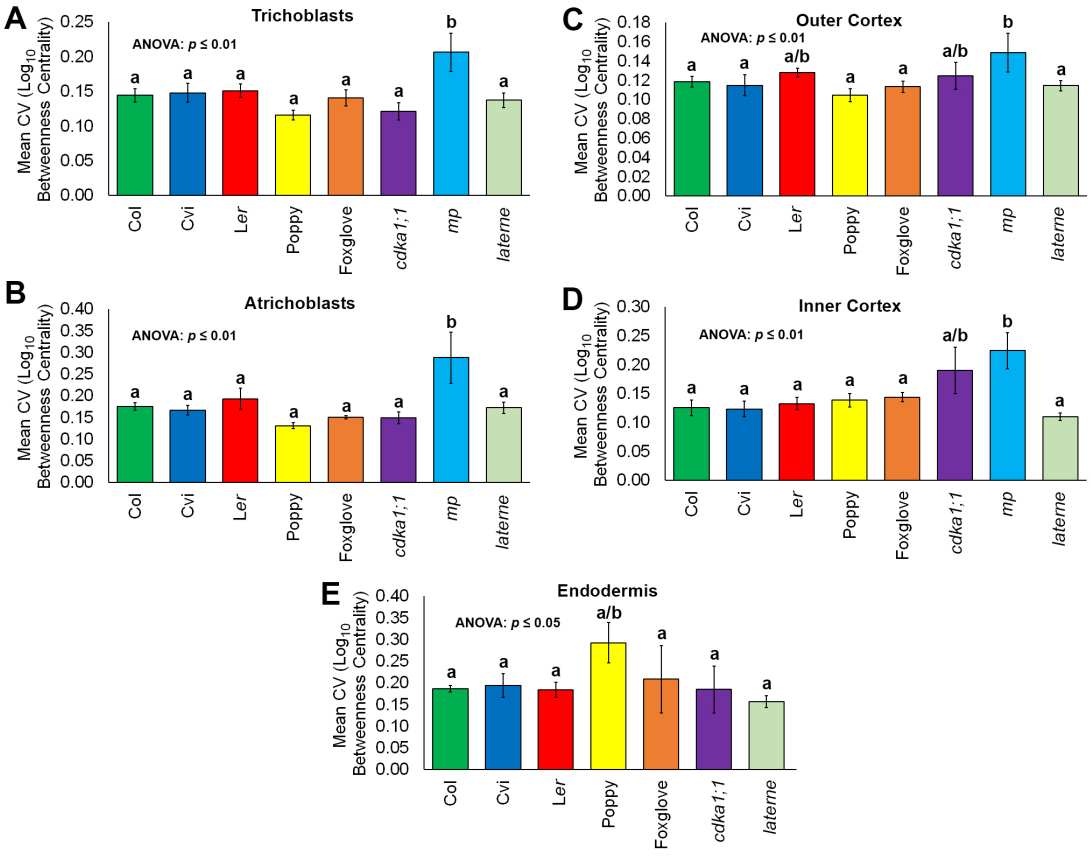


Figure 4.15. Variability in betweenness centrality across the hypocotyl.
(A) The average coefficient of variation of betweenness centrality within trichoblast cells of one biological replicate, in *A. thaliana* ecotypes (Col, L*er* and Cvi), mutants (*cdka1;1*, *monopteros* and *laterne*) and other plant species (poppy and foxglove). (B) The average coefficient of variation of betweenness centrality in atrichoblast cells. (C) The average coefficient of variation of betweenness centrality in outer cortex cells. (D) The average coefficient of variation of betweenness centrality in inner cortex cells. (E) The average coefficient of variation of betweenness centrality in endodermal cells. Error bars represent the standard deviation of the mean coefficient of variation. ANOVA tests suggested significant differences in means of a cell-type group (endodermis: $p \leq 0.05$, other cell types $p \leq 0.01$). Different letters above bars represent groupings using Tukey's tests ($p \leq 0.01$). Figure reproduced from Jackson et al., 2017, *eLife.*

4.2.10 Comparison of organisational features in diverse hypocotyls

Varied cellular patterning was observed at both local and global scales, in hypocotyls from different ecotypes and species, as well as from cell patterning mutant lines. To

further explore the diverse nature of each of these cellular organisations, scatterplots of the average degree and BC in each cell type of each biological replicate hypocotyl were drawn (Figure 4.16). Mean degree was plotted due to its relatively normal distribution within each sample. In contrast, median BC was plotted, as the distribution of BC across cells is consistently non-normal and long-tailed. The global property of BC is relatively constant across the epidermis of most hypocotyls, while the average degree in atrichoblasts and trichoblasts varies considerably more (Figure 4.16A and B). Both average degree and BC in individual hypocotyls show increase variation in the outer cortex (Figure 4.16C), while in contrast degree is relatively consistent in the inner cortex, compared to a more variable BC across different genetic backgrounds and species (Figure 4.16D).

In the epidermis and cortex, *monopteros* stands out as being both more variable than, and more dissimilar, to all other hypocotyls examined. This shows that the *monopteros* mutant has not only high variation in BC at the individual cell level (Figure 4.16) but also large organisational variation between hypocotyl samples (Figure 4.15), indicating a loss of organisational control in *monopteros* mutant individuals.

There is a strong relationship between average degree and average BC in the endodermis, where both local and global property averages are more variable across diverse hypocotyl samples than any other cell type examined (Figure 4.16E). The endodermis of *cdka1;1* has cells with considerably more local neighbours and shorter

paths than the endodermis of any other hypocotyl topologically analysed, as well as high between-sample variation.

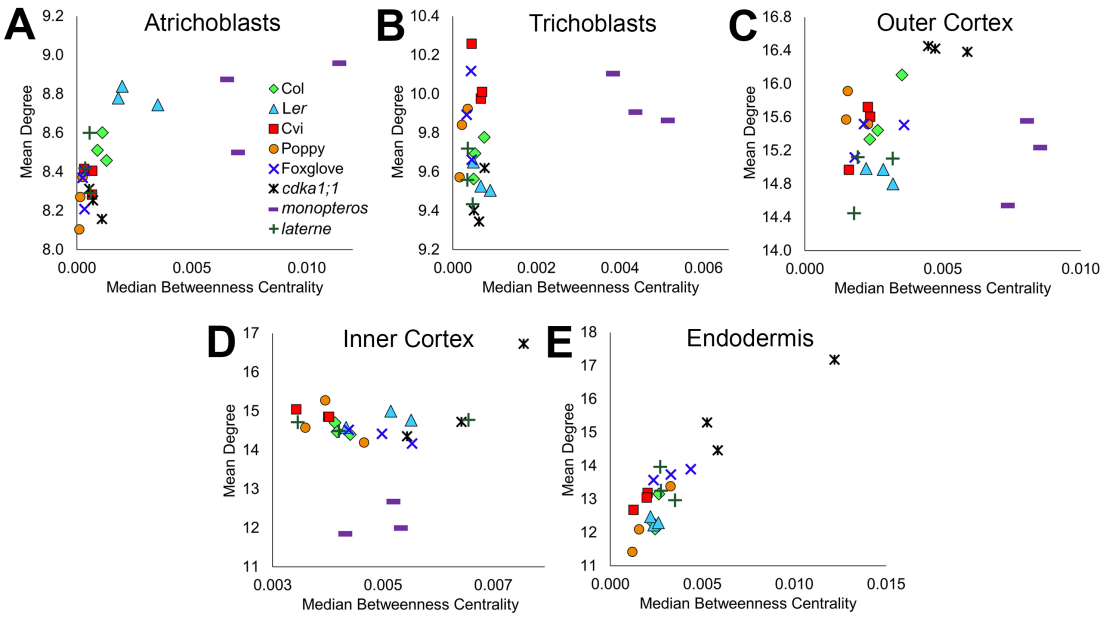


Figure 4.16. Average topological measurements in cell types of each hypocotyl sample.
(A) Mean degree and median betweenness centrality in atrichoblast cells within the hypocotyls of *A. thaliana* ecotypes (Col, L*er* and Cvi), mutants (*cdka1;1*, *monopteros* and *laterne*) and other plant species (poppy and foxglove). (B) Average degree and betweenness centrality in trichoblast cells. (C) Average degree and betweenness centrality in cells in the outer cortex. (D) Average degree and betweenness centrality in cells in the inner cortex. (E) Average degree and betweenness centrality in cells in the endodermis. Each data point represents the cell type averages of one biological replicate. Figure reproduced from Jackson et al., 2017, *eLife.*

Using mean and median values to summarise the local and global patterning properties in the hypocotyl results in a compression of information from the original distribution. Instead, comparing distributions of these organisational properties preserves more features of the measurements in comparisons, such as the long tail in many BC distributions, representing the presence of short paths through a cell type. To compare distributions, the χ^2-test can be used with discrete data such as cell degree (Pearson, 1900), while the Kolmogorov-Smirnov test can be used with continuous variables like BC (Kolmogorov, 1933) (Section 2.6.2). By using the test statistics obtained from these tests as a measure of distance, or the lack of similarity, between both degree and BC distributions, matrices of distances were constructed using pairwise comparisons between all cell types in all hypocotyls examined (Figure 4.17 and 4.18).

Distances between degree distributions were calculated, and similar distributions were grouped into three clusters (Figure 4.17A) (Section 2.6.5). All trichoblast and atrichoblast degree distributions, from all ecotype, species and mutant hypocotyls, were separated into cell type specific clusters, due to their highly constrained distributions (4.17B). Their position on the epidermis of the hypocotyl, and therefore the edge of the cellular connectivity networks, results in both atrichoblasts and trichoblasts having distinct local patterning properties, independent from all other cell types. Additionally, as mentioned previously, trichoblasts have two underlying cortical cells in the radial direction of the hypocotyl, whereas atrichoblasts have just one. This is sufficient for the distributions of local neighbourhood properties in trichoblast and atrichoblast cell types to be significantly different, resulting in a clear separate cluster

for each. All other cell types were placed into a third cluster, with the exception of the *monopteros* inner cortex and the poppy endodermis, which were each sufficiently different to all other groups to remain outside all clusters. Together, these results show that epidermal cells have distinct local connectivity properties from all other cells, and suggest that degree is able to classify atrichoblast, trichoblast and internal hypocotyl cells.

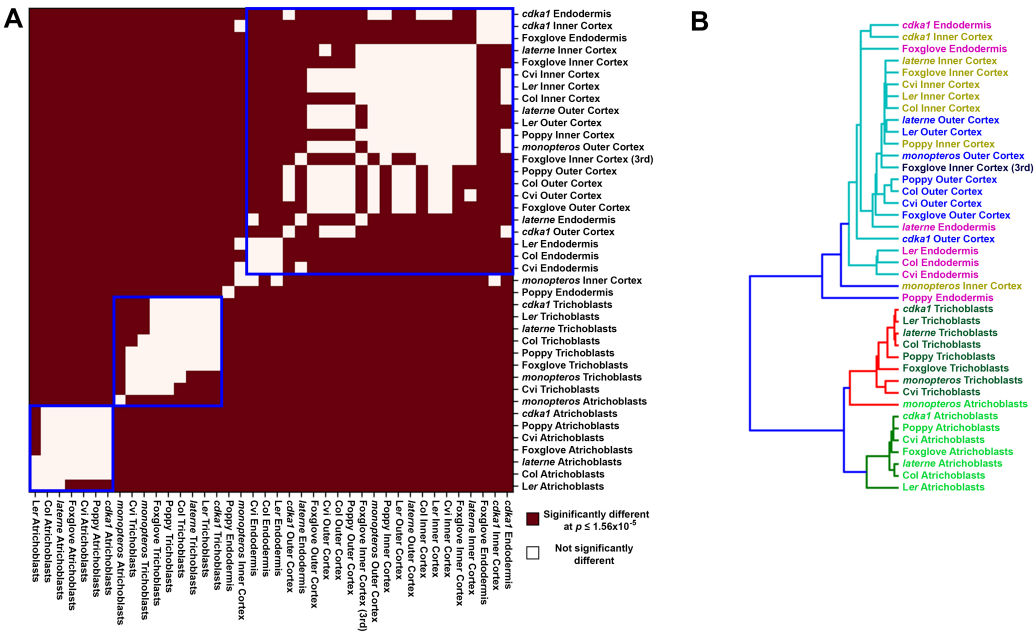


Figure 4.17. Similarities between degree distributions in diverse hypocotyls.
(A) A matrix of pairwise χ^2-tests between degree distributions of all cell types in all hypocotyls topologically analysed. A red square denotes statistical significance between two distributions at the $p \leq 0.05$ level ($p \leq 1.56\times10^{-5}$ after Bonferroni correction for 3200 distribution comparisons in the study). Blue boxes represent clustering of distributions, which were chosen to minimise within-group variability. (B) A dendrogram showing degree distribution clustering. Cyan, red and green branches represent distributions that are clustered together, while blue branches end with distributions that were not clustered. Figure reproduced from Jackson et al., 2017, *eLife.*

The higher-order organisational properties of cell types in each different ecotype, species and mutant hypocotyl were compared by calculating pair-wise distances between all BC distributions (Figure 4.18A). Again, three clusters were identified, with little variation in BC distribution in each group. Trichoblasts across wild-type hypocotyls clustered together, except for the BC distributions of poppy trichoblasts, which remained outside of any group due to its dissimilarity to BC distributions of other cell types and species (Figure 4.18B). This reflects earlier results, where poppy had a distinct lower path length present in trichoblast cells than atrichoblast cells, not seen in any other hypocotyls analysed (Figure 4.10E). The clustering of atrichoblast BC distributions however is far less constrained, where atrichoblasts cluster differently depending on the ecotype or species (Figure 4.18B). *A. thaliana* Cvi and foxglove atrichoblast path lengths are similar, while path lengths in poppy and *A. thaliana* Col atrichoblasts are each distinct. The BC distribution of the *A. thaliana* L*er* ecotype atrichoblasts clusters with outer cortex and endodermal cell types. This is indicative of high phenotypic plasticity in global patterning across atrichoblast cell arrangements from different genetically distinct plants. Wild-type inner cortex BC distributions were put into a distinct cluster, demonstrating the unique global cell patterning features of this cell type, while the BC distributions of the outer cortex and the endodermis in wild-type hypocotyls were clustered together.

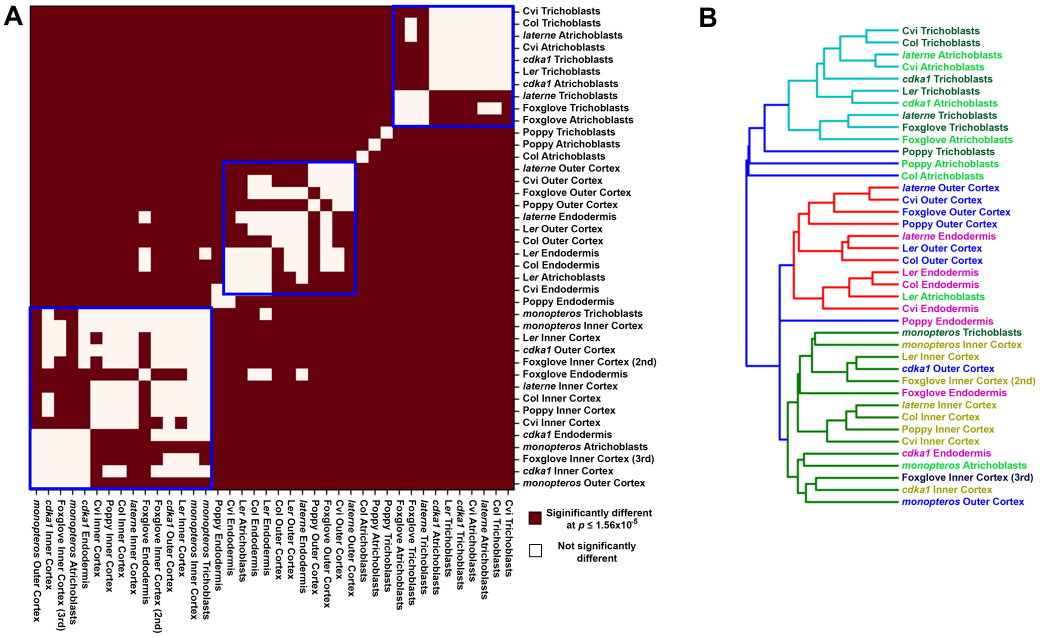


Figure 4.18. Similarities in betweenness centrality distributions in diverse hypocotyls. (A) A matrix of pairwise Kolmogorov-Smirnov tests between degree distributions of all cell types in all hypocotyls topologically analysed. A red square denotes statistical significance between two distributions at the $p \leq 0.05$ level ($p \leq 1.56\times10^{-5}$ after Bonferroni correction for 3200 distribution comparisons in the study). Blue boxes represent clustering of distributions, which were chosen to minimise within-group variability. (B) A dendrogram showing betweenness centrality distribution clustering. Cyan, red and green branches represent distributions that are clustered together, while blue branches end with distributions that were not clustered. Figure reproduced from Jackson et al., 2017, *eLife.*

These results suggest that different cell types have unique organisational properties, which can be measured using topological analysis. Quantifying and comparing patterning across diverse hypocotyls has revealed multicellular design principles used in the structuring of this organ. The structure of the hypocotyl is related to its function in transport, where the movement of molecules is mediated by cells that fall on short paths through the hypocotyl (Figure 4.9). The identification of these short paths shows that topological measurement can be used to predict where optimised

transport and intercellular communication is taking place within an organ, both of which are fundamental processes in plant growth and development.

4.3 Discussion

Previous research into cellular patterning has largely focused on how arrangements of cells arise from division rules (Gibson et al., 2006), and how deviations from these rules, like asymmetric division, alter the cellular organisation of tissues (Di Laurenzio et al., 1996). Less work has focused on how the structure of these cellular patterns relate to the function of an organ. Using the abstraction of cell arrangements into networks, this relationship can be investigated (Jackson et al., 2017a).

Representing the hypocotyl as a cellular interaction network has allowed quantification of cell organisation at both local and global scales. Network analysis has revealed how individual cells in the hypocotyl form an integrated transport system, which has non-intuitive emergent features. The use of betweenness centrality to measure global cell connectivity, in a cell-type specific manner, revealed previously unknown optimised transport conduits along the hypocotyl epidermis of some *Arabidopsis thaliana* ecotypes.

The optimised transport routes identified have a functional significance for longitudinal bulk transport of molecules in the hypocotyl, shown by the tracking of fluorescein through the hypocotyl epidermis (Figure 4.9). Betweenness centrality

predicted the flow of fluorescein through atrichoblast cell files in the *A. thaliana* ecotypes Colombia and Landsberg *erecta*.

While these transport 'shortcuts' were identified in replicate samples of *A. thaliana* Col and L*er*, they were not present in the Cape Verdi Islands ecotype, or in the other species examined, poppy and foxglove. This suggests that there is plasticity in this epidermal cell-patterning feature, possibly making this particular cellular arrangement advantageous for successful growth in some, but not all, environments that plants populate. It is also possible that this epidermal organisation specialised for epidermal transport in the hypocotyl is a recent innovation, which is not yet adopted across a large amount of the plant kingdom.

Though global measurements of cell organisation identified functional short paths, the arrangement of cells themselves may constitute an efficient template on which to mediate transport. Plants may further increase the efficiency of transport in these short paths by increasing the number of active transport processes between cells (Park et al., 2017), or increasing the number of plasmodesmata (Brunkard et al., 2015), in cells with the positional predisposition to topologically mediate cellular communication and organ-wide transport.

The discovery of a bulk-flow transport process in the epidermis of the hypocotyl may additionally provide insight into roles of cellular patterning in the root, where similar cell arrangements are observed (Lin and Schiefelbein, 2001). In the root epidermis, trichoblasts have the capacity to develop root hairs, and their role is to absorb water

and nutrients from the soil. The efflux of these nutrients to atrichoblast cells, positioned for efficient longitudinal transport, could allow the trichoblasts to maintain a favourable concentration gradient for further absorption from the soil. This represents a possible division of labour in the root epidermis, with a function made possible by the global organisation of trichoblast and atrichoblast patterning.

Quantifying cellular organisation at a global scale has allowed measurement of the direct contribution of genes to cell patterning. *CDKA1;1* has a role in reducing atrichoblast path length, whilst overall global connectivity in the hypocotyl epidermis is reduced by the *MONOPTEROS* transcription factor, and is limited in the *laterne* mutant background. Additionally, *MONOPTEROS* may have a role in contributing to robustness in path lengths across individual hypocotyls, where lack of this gene resulted in quantitatively variable patterning phenotypes. The *monopteros* mutant also highlighted the topological robustness within genetic backgrounds, despite the observed plasticity across them. Using topological analysis to capture organisation in cell patterning mutants provides additional levels of detail over traditional qualitative comparisons, which can then be used to more precisely link gene function to organ structure.

CHAPTER FIVE: TOPOLOGICAL ORDER IN THE SHOOT APICAL MERISTEM

5.1 Introduction

Plant organ and tissue development is driven by a combination of cell expansion, division and differentiation. Complex cell organisation in tissues is formed and maintained by careful control of these processes, and it has been previously suggested that this is mediated by communication between neighbouring cells (Gibson et al., 2011). In plants, organogenesis is also mediated by these cellular interactions (Lucas et al., 1995) (Di Laurenzio et al., 1996), though the movement of small molecules, RNAs and even large proteins between cells (Brunkard et al., 2015). Through cell communication, self-organisation has been observed at the cellular level, generating specific organ patterning (Sasai, 2013).

In plants, the shoot apical meristem (SAM) is the stem cell niche from which all above ground organs are formed. At a gross morphological level, the SAM consists of a dome of cells, which is surrounded by organ primordia, arising at regular intervals (Reinhardt et al., 2003) (Figure 5.1A). As the primordial organs increase in size, clear boundary zones are established between the growing primordia and the meristem centre, known as boundary zones, consisting of many highly anisotropic cells (Louveaux et al., 2016). The centre of the meristem, or the central zone, is the site of the more isotropic pluripotent stem cells (Bowman and Eshed, 2000). Cells in the central zone continually divide, and subsequent cell growth pushes cells towards the periphery of the meristem, where they begin to differentiate (Traas and Vernoux, 2002). The rate of cell growth and division must be controlled to ensure that a pool of stem cells is maintained, whilst providing enough differentiating cells for organ growth. The distinct regions of the meristem are determined by strict gene regulation

and interactions, primarily between WUSCHEL and CLAVATA genes, detailed in Section 1.4.

The meristem dome itself has three distinct layers of cells, termed L1, L2 and L3 (Laufs et al., 1998) (Figure 5.1B). In order to maintain this layered structure, all cells in the epidermal L1 layer, along with cells in the L2 and the vast majority of cells in the L3, divide anticlinally, perpendicular to the meristem dome surface (Satina et al., 1940). Below the L3, where the meristem dome is connected to the plant stem, the layered structure begins to break down, as division orientation is less constrained.

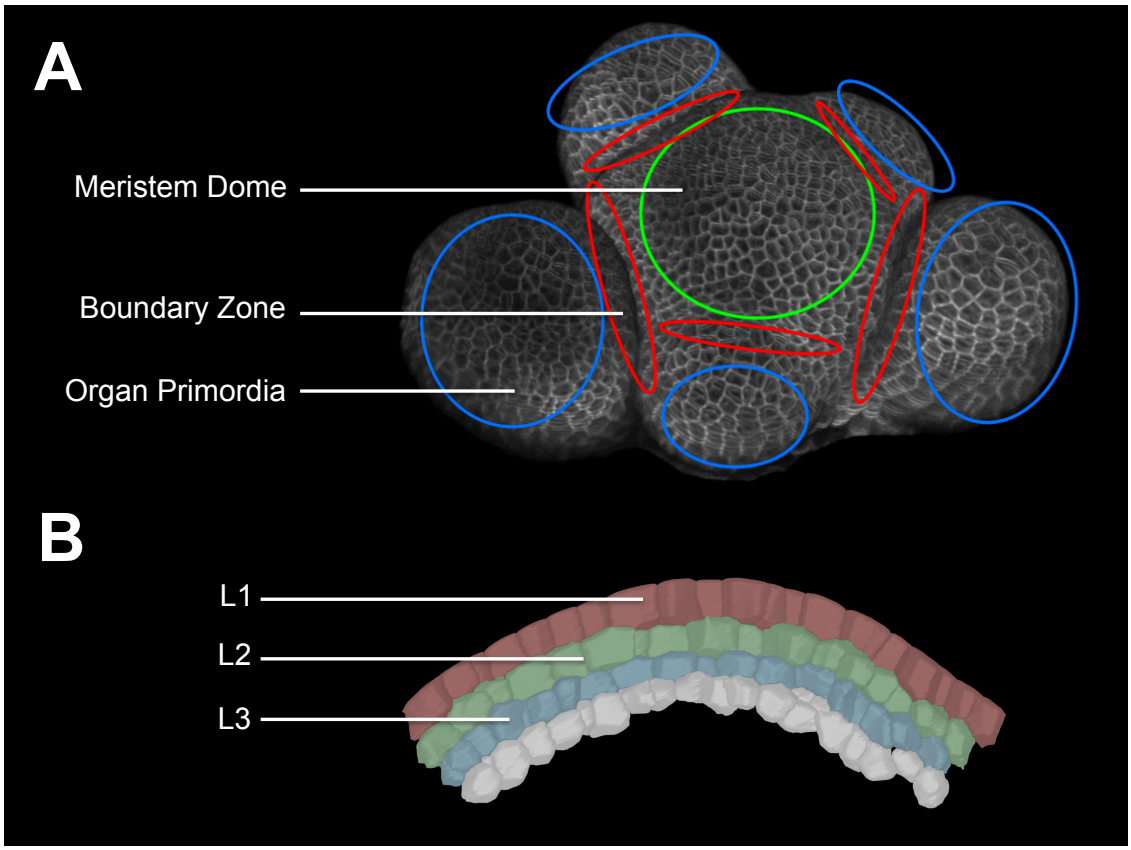


Figure 5.1. Structure of the shoot apical meristem.
(A) A 3D, top-down confocal image of the SAM, showing the locations of the meristem dome containing the stem cell niche, the organ primordia that develop into above ground plane organs, and the boundary zones that connect the meristem dome to the primordia. (B) A cross-section of the meristem dome, showing the epithelial L1 layer, and the underlying L2 and L3 layers. Below the L3, the meristem done is connected to the plant stem.

Because, unlike many animal cells, plant cells lack motility, neighbouring cells that share a cell wall will continue to be adjacent to each other irrespective of cell growth. This feature means that proper timing and orientation of cell division in the SAM is essential for the generation of cellular patterns, which are in turn fundamental to normal organogenesis (Dupuy et al., 2010) (Besson and Dumais, 2011) (Shapiro et al., 2015).

The regulatory mechanisms of cellular homeostasis within the SAM have been the subject of intensive investigation. Classical experiments in unicellular yeast have shown that both cell size and cell cycle length are linked to the onset of cell division (Fantes and Nurse, 1977) (Fantes, 1977). Similar control of the cell-cycle was also observed in bacterial systems, primarily driven by cell-size driven mitosis (Robert et al., 2014). In contrast, in the multicellular SAM, cells do not reliably divide when they reach a particular size, or following a set amount of time after they previously divided, yet both of these features seem to contribute somewhat to the induction of mitosis (Willis et al., 2016). In fact, computational models of the developing SAM are able to more accurately represent features of real tissues when some randomness in division timing is incorporated (Roeder, 2012). These studies suggest that cell

divisions in the multicellular SAM may be controlled by more complex rules and interactions.

In addition to the timing of cell division, the orientation of the cleavage plane during mitosis also contributes to cell patterning in the SAM. When a complete plant cell division occurs, this results in the deposition of a new cell wall. Models to explain the positions of new walls in plant cell divisions have existed since 1863, when Wilhelm Hofmeister noted that plant cells divide using a plane normal to the principle axis of elongation (Hofmeister, 1863) (Figure 5.2A). In 1886, Léo Errera extended this definition, observing that plant cells tend to divide using the shortest possible wall, in a similar manner to soap bubbles (Errera, 1886) (Figure 5.2B). These classical rules, while serving as general rules in many cases, fail to accurately describe many observed plant cell divisions (Kwiatkowska, 2004).

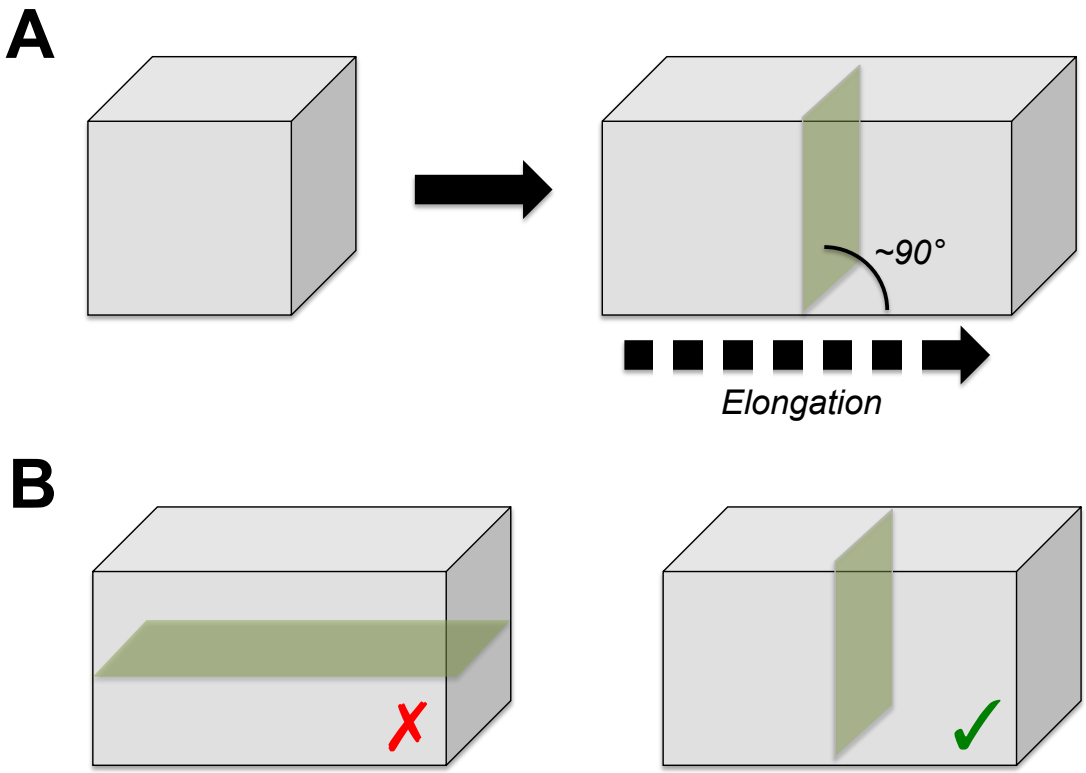


Figure 5.2. Classical meristem cell division observations.
(A) Schematic illustrating Hofmeister's observations of division plane orientation, where the new cell wall is placed perpendicular to the primary axis of elongation. (B) Schematic illustrating Errera's rule of division plane placement, where the wall with the smallest cell wall area, passing through the centre of the cell, is most often used.

More modern models of plant cell division have extended these classical rules. The addition of a stochastic element in division plane selection can account for cleavage planes that are not satisfied by Errera's rule (Besson and Dumais, 2011). Here, it is suggested that cell division in the SAM is not a deterministic process, and that cells in fact divide using a wall that satisfies one of several feasible 'short' walls, rather than the shortest wall. According to the proposed stochastic model, division planes with non-minimal wall area are possible, but wall length is inversely related to the probability of their observation.

Another more recent, data-driven study uses a combination of several geometric factors to generate predictions of cell wall placement in mitosis (Shapiro et al., 2015). Different geometric heuristics were incorporated into a model, specifically equality in daughter cell size, wall deviation from passing through the exact cell centre, and deviation from the shortest wall through the cell. Parameter space was searched to identify which heuristics most successfully replicated observed divisions, and mostly, division planes were best modelled using the shortest wall that passed close to the centre of the cell, very similar to Errera's original observations (Errera, 1886).

Each of these more recent, purely geometric approaches cannot be used to describe all of the diverse division planes observed in the SAM. Wall placement in cell division appears to have stochastic elements (Besson and Dumais, 2011), yet curiously the sum of these cell divisions results in highly conserved plant organ shapes and sizes.

Mechanical forces between adjacent cells in these immobilized cellular networks can also exert influence over their neighbours (Hamant et al., 2008), which can influence the orientation of the placement of cell division planes (Louveaux et al., 2016) (Lintilhac and Vesecky, 1984), and subsequently change the properties of cellular organisation. Other studies of animal and plant epithelia have shown that a cell's number of direct neighbours influences division plane placement (Gibson et al., 2011). It has been shown that cells are more likely to divide with a wall intersecting an adjacent cell with few neighbouring cells, or low degree. It is proposed that following cell division, due to the increase in degree of the neighbouring cells, the

overall distribution of local cellular connections across the SAM is preserved (Gibson et al., 2006) (Gibson et al., 2011). This provides evidence that complex order in proliferating tissues can be driven by local topology. However, whether changes in global topological properties can enable feedback, informing local changes in tissue organisation, is not known. This provides an opportunity to examine whether divisions are coordinated by global cellular topological context within an organ.

The global interactions between cells within the SAM are quantified using the extraction of cellular connectivity and network science algorithms, to identify the higher order properties of organisation within this stem cell niche. The potential for a global regulatory mechanism that works in parallel with the local regulatory features described previously is explored, as well as whether this can integrate cell cycle control in a global context.

5.2 Results

Four *Arabidopsis thaliana* and four tomato (*Solanum lycopersicum)* shoot apical meristems were live-imaged in 3D at three time points, referred to as T0, T1 and T2, each separated by 11 hour periods (Section 2.1.3). At each time point, images were computationally segmented and converted into a mesh format, and cellular connectivity networks were extracted (Section 2.2). Cells in L1-L4 were manually labelled by computationally stripping away progressive layers from the surface of the SAM, and using parent labelling (Section 2.2.6). Both cell division and growth of cells

between time points was tracked, using manual co-segmentation in MorphoGraphX (Section 2.2.8).

5.2.1 Topological buffering of the SAM

In the shoot apical meristem, only the central dome, down to the L4, was imaged at high enough resolution for accurate segmentation. This resulted in edges of the dome that should be connected to the primordia through the boundary regions, as well as the L4 that should be connected to lower layers and the plant stem, being artificially disconnected from the rest of the plant. To reduce the effect of these artificial network edges on subsequent network analysis, topological buffering was used (Section 2.4.7).

A region of cells in the centre of the SAM, whose topological properties, such as RWC, were deemed to be unaffected by edge effects was chosen (Figure 5.3A). Including cells at the edge of the meristem in the network, but not reporting on them, meant that cells with artificially low topological measurements could be excluded from further analysis.

The inclusion of cells in the L4 layer in the network, and their exclusion in further analysis, resulted in accurate reflection of local connectivity in the L3, while preventing the misrepresentation of degree in the L4 (Figure 5.3B). Ensuring that local connectivity was properly represented in L1-L3 resulted in changes in the global topological measurements, log BC and RWC (Figure 5.3C and D). In all subsequent

analyses, the L4 layer was not reported on, but included in the extracted cellular connectivity networks.

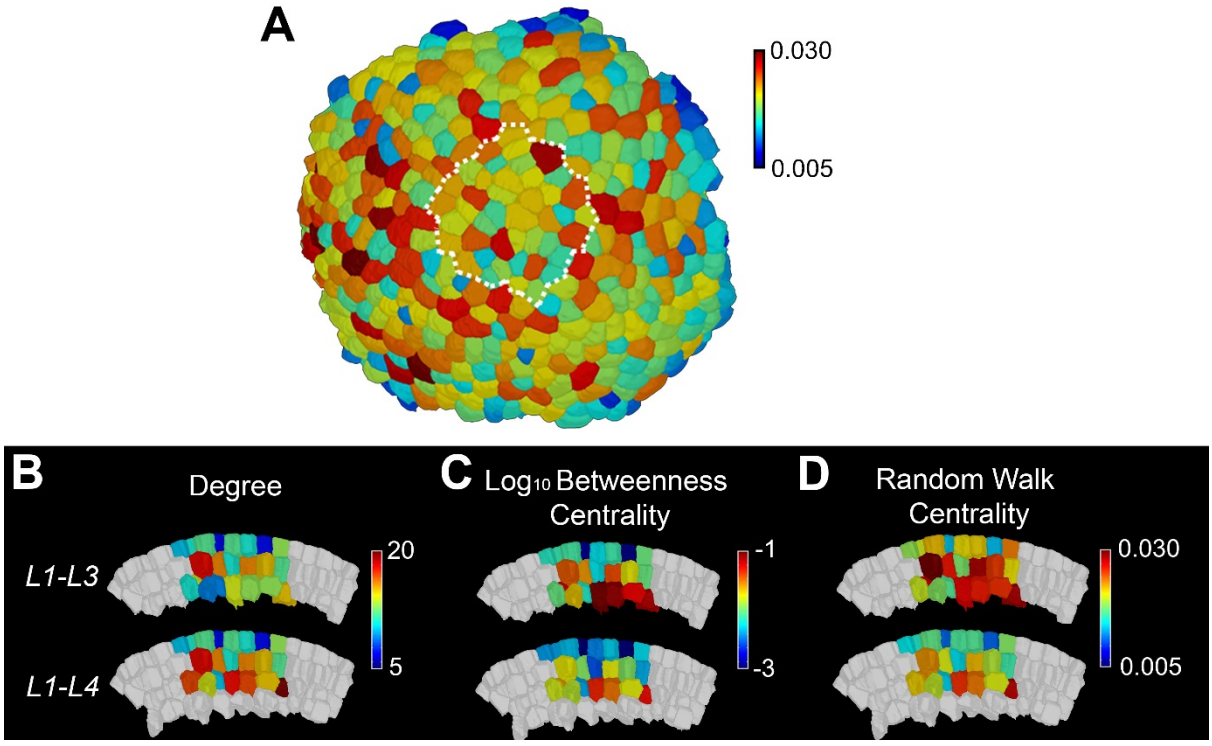


Figure 5.3. Topological buffering of the shoot apical meristem.
(A) A top-down view of the *A. thaliana* shoot apical meristem, false coloured with random walk centrality. The white dashed line encloses the cells that were reported on, while cells on the outside of the dashed line formed the topological buffer region. (B) Cross sections of the *A. thaliana* shoot apical meristem mesh, false coloured with degree. The L4 cell layer is added to the cellular connectivity network before degree is calculated. (C) The *A. thaliana* meristem mesh, false coloured with $\log_{10}$ betweenness centrality. (D) The *A. thaliana* meristem mesh, false coloured with random walk centrality. Figure reproduced from Jackson et al., 2019, *Cell Systems.*

5.2.2 Geometry and topology of the SAM

Though geometry of cells in the SAM has been extensively studied (Grandjean et al., 2004) (Kierzkowski et al., 2012) (Willis et al., 2016), the ability to measure topological properties of the SAM cellular connectivity network provides an opportunity to study both geometry and quantified cell organisation in tandem.

Cells in the *A. thaliana* and tomato SAMs differ in terms of their geometric properties. Overall tomato SAM cells are generally two to four times larger than cells in the *Arabidopsis* meristem (Figure 5.4A and B) The largest cells in the tomato SAM are found in the uppermost L1 layer, while in contrast cells are largest in the *A. thaliana* SAM L2 and L3.

In terms of local topological properties, despite the differences in cell area and volume, the degree of cells in the *Arabidopsis* and tomato meristems are similar across layers (Figure 5.4C). Cells in the L1 have the lowest degree, due to their position at the organ epithelia, and therefore a real edge of the network. Whilst most cells are entirely surrounded on all sides by other cells, making many physical cellular connections, the L1 cells have a surface exposed to the environment.

The distributions of RWC were fairly similar across species (Figure 5.4E), but when measured with log BC, differences in global topological properties were identified (Figure 5.4D). L2 and L3 layers in *A. thaliana* and tomato share similar log BC distributions, while the log BC in *A. thaliana* L1 is generally lower. This is an indication that the global organisation of cells in the SAMs of both species is not

identical. It is important to note that while normalisations for network size have been applied to the calculation of global topological measurements (Section 2.4.3), due to the larger size of the tomato SAM networks, these comparisons may be biased (Section 3.2.1).

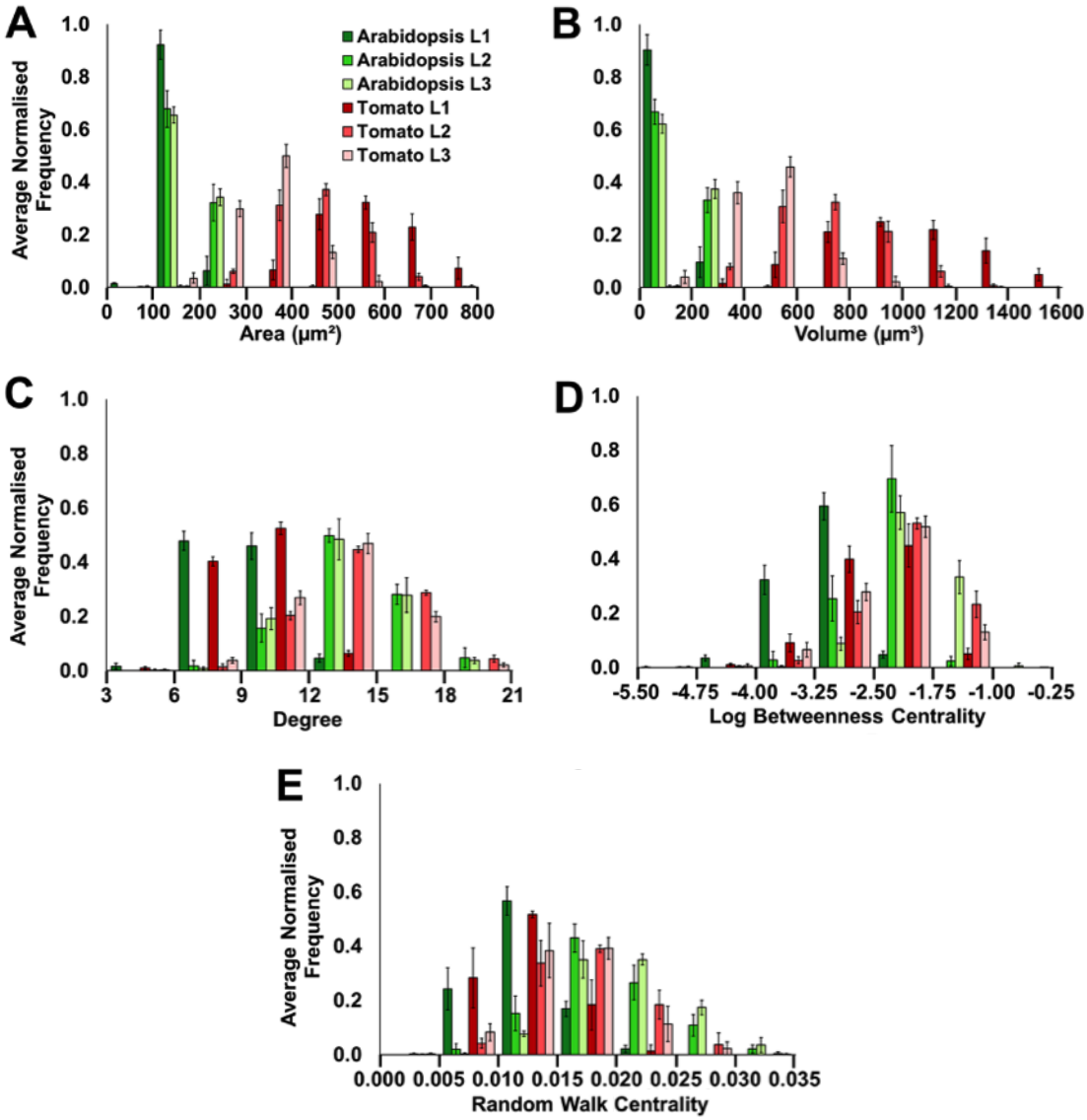


Figure 5.4. Distribution of geometric and topological properties in the *Arabidopsis* and tomato T0 SAMs.
(A) Area (µm²) of cells in the *Arabidopsis thaliana* SAM L1, L2 and L3, and tomato SAM L1, L2 and L3. (B) Volume (µm³) of cells. (C) Cell degree. (D) Cell $\log_{10}$ betweenness centrality. (E) Cell random walk betweenness centrality. Error bars

represent the standard deviation within a frequency bin, from four biological replicates per species. Figure adapted from Jackson et al., 2019, *Cell Systems.*

To examine the spatial distribution of geometric and topological properties in the SAM, measurements from T0 meristems were visualised using heat maps in MorphoGraphX (Section 2.7.1) (Figures 5.5 and 5.6). Cells that were identified as dividing between T0 and T1 were also highlighted for comparison (Figures 5.5D and 5.6D). Both geometric and topological properties were unevenly distributed across the *A. thaliana* SAM (Figure 5.5) and tomato SAM (Figure 5.6), between and across layers.

In the visualised T0 sample, cell size was both largest and more variable in the *Arabidopsis* thaliana SAM L2 and L3. Growth appeared to be particularly sporadic across the meristem, where the size of most cells was relatively invariant, while few cells grew up to 1.3 times their size in T0 (Figure 5.5C). Whilst visually, in the *Arabidopsis* SAM, volume, area and growth appear to be higher in cells that will divide, supporting previous research (Willis et al., 2016), this is by no means a simple relationship (Figure 5.5A - D). Some cells that are large, or that grow the most between time points, undergo division, whilst some do not.

Qualitatively, there are some similarities between geometric and topological properties in the *A. thaliana* SAM (Figure 5.5). Across layers in this sample, geometric, local and global topological measures tend to be lowest in the L1, the edge of the cellular connectivity network. There is no discernable pattern of topological properties within each SAM layer (Figure 5.5E, F and G). However,

particularly in degree and RWC, there is some visual relationship between high local or global connectivity, and cell division (Figure 5.5D).

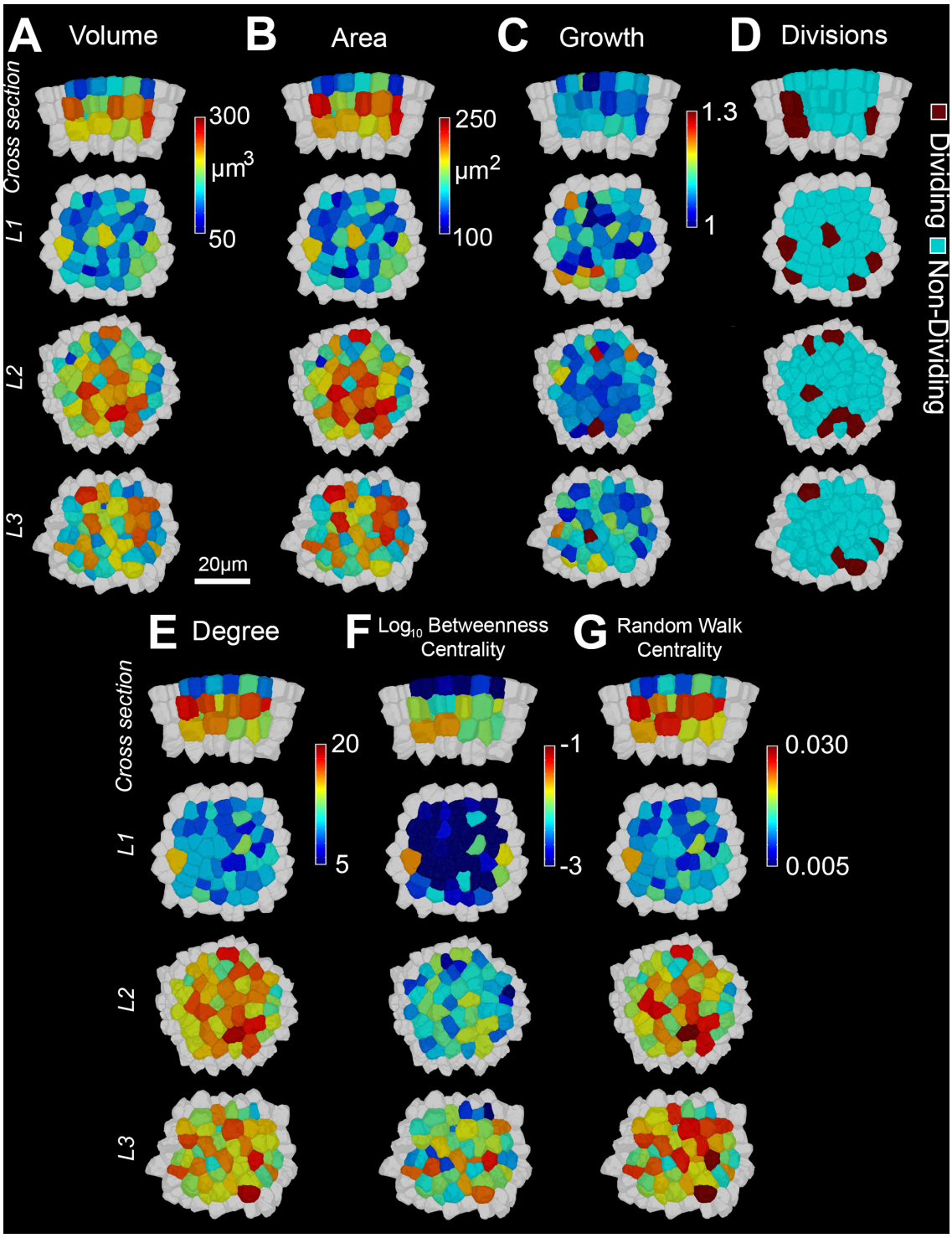


Figure 5.5. Spatial distribution of geometric and topological properties in the *Arabidopsis* SAM.
(A) A heat map of cell volume overlaid on an *A. thaliana* SAM cross-section mesh, and meshes of L1, L2 and L3. (B) Cell area. (C) Cell growth between the T0 and T1 time points. (D) Cell divisions between T0 and T1 time points. (E) Cell degree. (F) Cell $\log_{10}$ betweenness centrality. (G) Cell random walk centrality. Figure reproduced from Jackson et al., 2019, *Cell Systems.*

As well as having larger cells, the tomato meristem dome also contains more cells than the *Arabidopsis thaliana* SAM (Figure 5.5 and 5.6). Both the rate of growth, and the rate of division, is substantially higher in the tomato meristem (Figure 5.6C and D) (Table 5.2). Visualisation of geometric cell properties shows that cell size tends to be largest in the tomato SAM L1, and smallest in the L3 (Figure 5.6A and B). In contrast to the *Arabidopsis* meristem, there appears to be a bias towards the presence of larger cells in the centre of the meristem dome, particularly at the SAM epidermis. Cell growth is fairly consistent in L1 and L2, where many cells double in size, while cell growth is much more sporadic in the tomato SAM L3, with cells distant from the centre of the layer growing fastest (Figure 5.6C). Visually, in this tomato meristem, there is no clear relationship between cell division and any geometric property (Figure 5.6A – D).

There is not an obvious relationship between topological and geometric properties in the tomato SAM layers, in contrast to in *A. thaliana* (Figure 5.5 and 5.6). Whilst cells size is largest in the L1, cell degree in the epithelia is lowest, as is RWC (Figure 5.6E and G). The global topological property of $\log_{10}$ BC is distributed more evenly across the meristem layers (Figure 5.6F). In terms of a relationship between T0 cell local

and global connectivity, and cell division at T1, there is no clear link using purely qualitative assessment (Figure 5.6D – G).

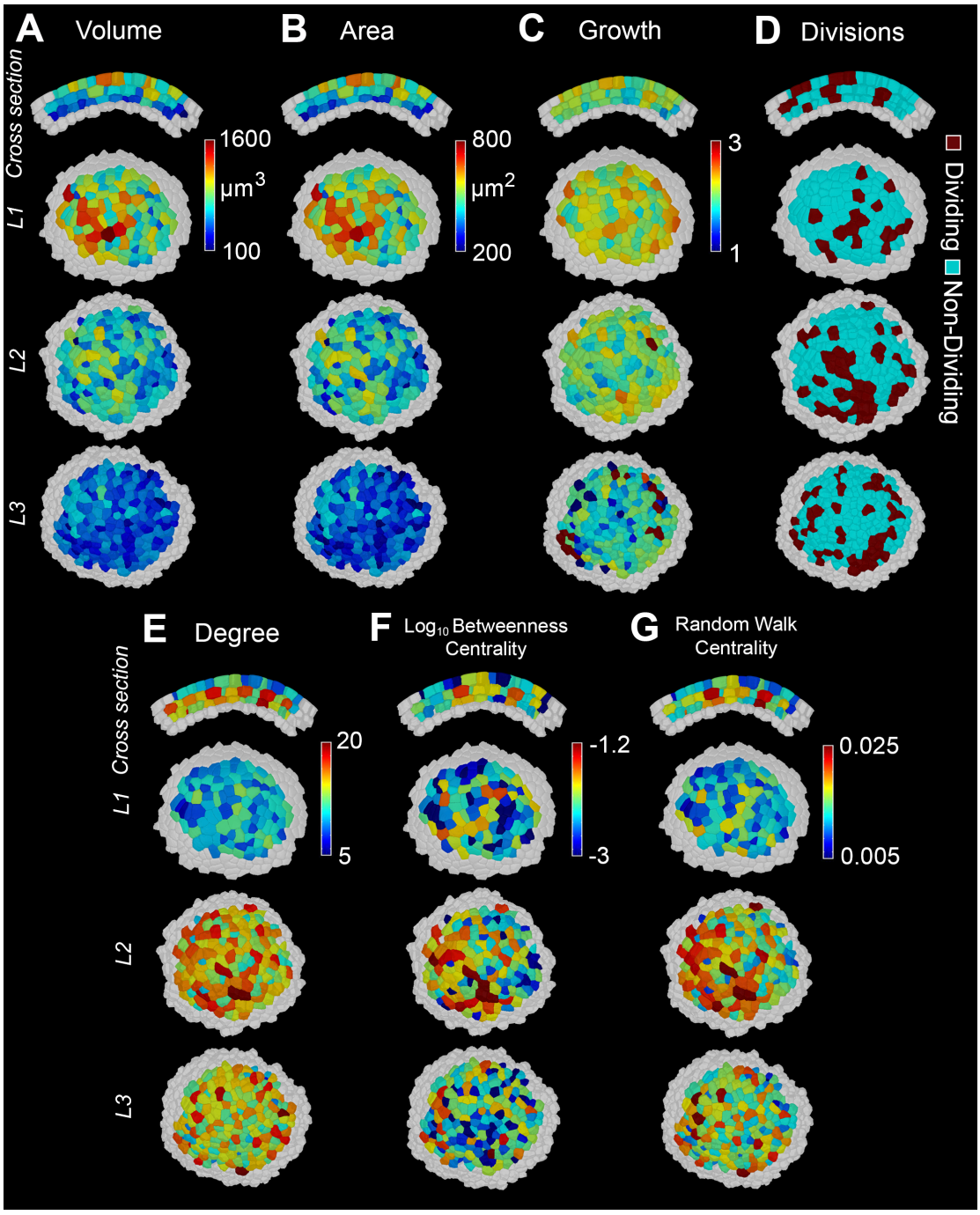


Figure 5.6. Spatial distribution of geometric and topological properties in the tomato SAM.
(A) A heat map of cell volume overlaid on a tomato SAM cross-section mesh, and meshes of L1, L2 and L3. (B) Cell area. (C) Cell growth between the T0 and T1 time

points. (D) Cell divisions between T0 and T1 time points. (E) Cell degree. (F) Cell $\log_{10}$ betweenness centrality. (G) Cell random walk centrality.

Table 5.1. Cell division rates in the *Arabidopsis* SAM.

Cell division between the T0 and T1 time points in the *Arabidopsis thaliana* SAM. Error shown is ± the standard error of the mean, calculated with four biological replicate meristems.

Layer	Average % of Cells Dividing Over 11 Hours (T0 - T1)
L1	**3.1** ± 0.6
L2	**7.7** ± 2.5
L3	**5.4** ± 1.8

Table 5.2. Cell division rates in the tomato SAM.

Cell division between the T0 and T1 time points in the tomato SAM. Error shown is ± the standard error of the mean, calculated with four biological replicate meristems.

Layer	Average % of Cells Dividing Over 11 Hours (T0 - T1)
L1	**19.6** ± 3.0
L2	**23.3** ± 3.0
L3	**29.3** ± 2.2

5.2.3 Dynamics of geometric and topological cell properties in the SAM

The relationship between cell size and division has been previously detailed, and is a contributing factor to a cell's decision to divide (Willis et al., 2016). Whether cell organisation, or more specifically the local or global topological state of a cell, also has an effect on the induction of the cell cycle is not known. To further explore this, a quantitative approach was used.

To examine how cell size and cell connectivity influenced the induction of division in the *Arabidopsis* SAM, firstly cells in the first time point (T0) were split into non-dividing and dividing cells, based on their observed fate in the second time point image (T1). Properties of these cells were then compared to the recently divided cells in the T1 time point (Figure 5.7A). The fold change between non-dividing (T0) and dividing (T0) cells was calculated, as well as the fold change between cells before and after division. Significant differences were present in the geometric measurements of area and volume, in agreement with previous research (Willis et al., 2016). Intuitively, cell size was reduced when cells divided. Divisions also reduced cell degree, as well as tending to increase path length in the resulting daughter cells. Strikingly, as well as in geometric features, there were large reductions in degree, $\log_{10}$ BC and RWC.

Whether there was a role for neighbouring cell connectivity in the timing of cell division was also assessed, using a predictive interpretation of the Gibson division rule, where the neighbouring cell with the lowest degree was used to score cells in the T0 and T1 time points. There was no significant difference between non-dividing

(T0) and dividing (T0), or dividing (T0) and divided (T1) cells using this measurement (Figure 5.7A), indicating that neighbouring cell connectivity is unlikely to play a role in the induction of mitosis in the *Arabidopsis* SAM.

Because the dynamics of cell size and cell centrality suggested that both geometry and topology could be used to distinguish non-dividing and dividing cells, the predictive capacities of these features were measured using logistic regression (Section 2.6.6). Logistic regression was used to build a predictive model that would identify the most useful features at T0, for determining cell division at T1. When all geometric and topological measurements were included in the model, area and volume were singled out as statistically the best measurements for predicting cell division in the *Arabidopsis thaliana* SAM, whilst other factors in the model were not deemed necessary for successful predictions (Figure 5.7B) (Table 5.3). The likelihood ratio is an estimate of how useful any given measurement is in determining the fate of the cell. Because separately degree, $\log_{10}$ BC and RWC could distinguish non-dividing and dividing cells (Figure 5.7A), their low likelihood ratio in the logistic regression model is an indication that there is some correlation or overlap between the information that geometric and topological measurements provide, in *A. thaliana*.

To further elucidate the predictive capacities of these measurements, logistic regression models with differing inclusion of terms were used to identify T1 cell divisions from T0 cell properties (Section 2.6.6) (Figure 5.7C). Logistic regression was used to classify non-dividing and dividing cells using both geometric and topological factors measured previously, indicating their role in influencing cell

division in the shoot apical meristem. Because around 5% of cells divided across the four *A. thaliana* biological replicates, a simple model assuming that no cells divided resulted in around 95% prediction accuracy. To validate the logistic regression approach, cells were randomly assigned “divided” status, and the identification of true positive and negative cases was as expected from a dataset with 5% divisions. Though the small proportion of dividing cells across the samples made large improvements on overall accuracy difficult, adding geometric and topological measurements to the model resulted in improvements the rate of true positive division identification. In *Arabidopsis*, including solely volume, or area, volume and RWC to the model resulted in just as much improvement to the true positive rate as including all measurements in the model. However, as the proportion of correctly identified dividing cells never exceeded 30%, irrespective of terms added, there is limited evidence that any geometric or topological factors analysed have powerful predictive capacities.

The similarities between the topological cycling observed in both geometric and topological features as cells grow and divide (Figure 3.7A), and the similarly restricted logistic regression model predictions using each measurement (Figure 3.7B and C), hint that there may be relationships present across the cell variables measured. Pairwise linear regression was used to identify whether simple linear correlation existed between features of each cell, measured using R^2, where a value of 1 indicates a perfect linear relationship, and a value of 0 means two variables are completely linearly unrelated (Figure 5.7D). Acting as a benchmark, the correlation between area and volume of cells, two highly related features, was 0.98. Similarly, in

the *Arabidopsis* SAMs there were strong relationships between the local feature of cell degree, and the global features of $\log_{10}$ BC and RWC, ranging from $R^2 = 0.8$ to $R^2 = 0.88$. Between geometric and topological features, moderate linear relationships were present, with R^2 between 0.45 and 0.59. The exception to these observations was the very low correlation between the Gibson rule and all other variables, indicating that the degree of neighbouring cells was not related to cell size or topology.

Together, these results provide evidence that the volume of a cell is a good determinant of whether it will divide, and that this geometric property is linked to both local cell connectivity, and the broader, global cell context. Though topological features can be used to differentiate between non-dividing and dividing cells, there is no evidence to suggest that position in the *Arabidopsis* SAM cell connectivity network has any function in induction of the cell cycle, due to their relationship with cell area and volume. Correlations between these properties likely result from the simple embedding of similarly shaped cells in 3D space, where larger cells often have more direct cell-cell connections. This feature then propagates to the global topological scale, where cells with more neighbours are more likely to lie on short paths between pairs of cells in the calculation of BC and RWC.

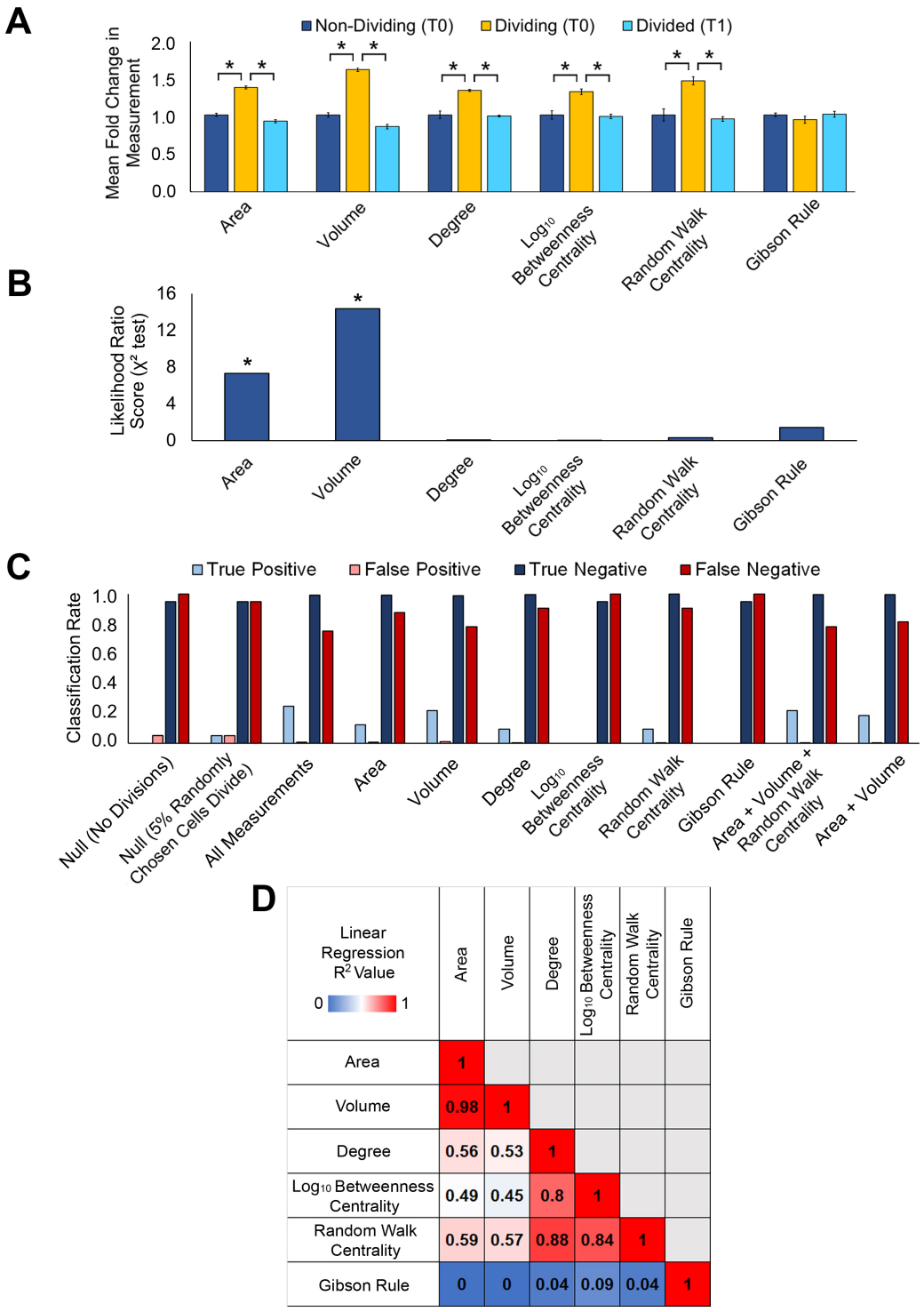


Figure 5.7. Dynamics of geometric and topological properties in the *Arabidopsis thaliana* SAM.
(A) Normalised mean fold change in geometric and topological properties between non-dividing (T0), dividing (T0) and divided cells (T1). Error bars are ± the standard error of the mean. A * denotes significance between classes of cells at the $p \leq 0.05$ level (*t*-test). (B) Likelihood ratio of each parameter incorporated into a logistic regression model, to classify non-dividing and dividing cells in T0. A * represents a

statistically significant contribution to classification (Type II ANOVA, $p \leq 0.05$) (C) Classification rates of logistic regression models with different incorporation of variables, split into true positive, false positive, true negative and false negative rates. (D) A matrix of pairwise linear regressions between measurements, with a heat map for the coefficient of determination (R^2) between each pair. Figure reproduced from Jackson et al., 2019, *Cell Systems.*

Table 5.3. Type II ANOVA test on a logistic regression model with geometric and topological measurements in *Arabidopsis thaliana*.

A logistic regression model was used to classify non-dividing and dividing cells in the T0 *Arabidopsis thaliana* SAM. All measurements were included in the model, and their effectiveness in classification was measured using a Type II ANOVA test, which specifically does not bias model terms based on the order of introduction. A high likelihood ratio (LR χ^2) indicates that a measurement was effective in differentiating dividing and non-dividing cells.

Measurement	LR χ^2	Degrees of Freedom	p(>Chi^2)
Volume	14.4	1	1.50×10^{-4}
Area	7.29	1	6.92×10^{-3}
Gibson Rule	1.42	1	0.232
Random Walk Centrality	0.294	1	0.588
Degree	0.0640	1	0.800
Log_{10} Betweenness Centrality	0.0318	1	0.858

Division Prediction Accuracy	0.944

In the tomato SAM, the same cycling of geometric and topological properties is observed as in *Arabidopsis*, though fold changes across all measurements are

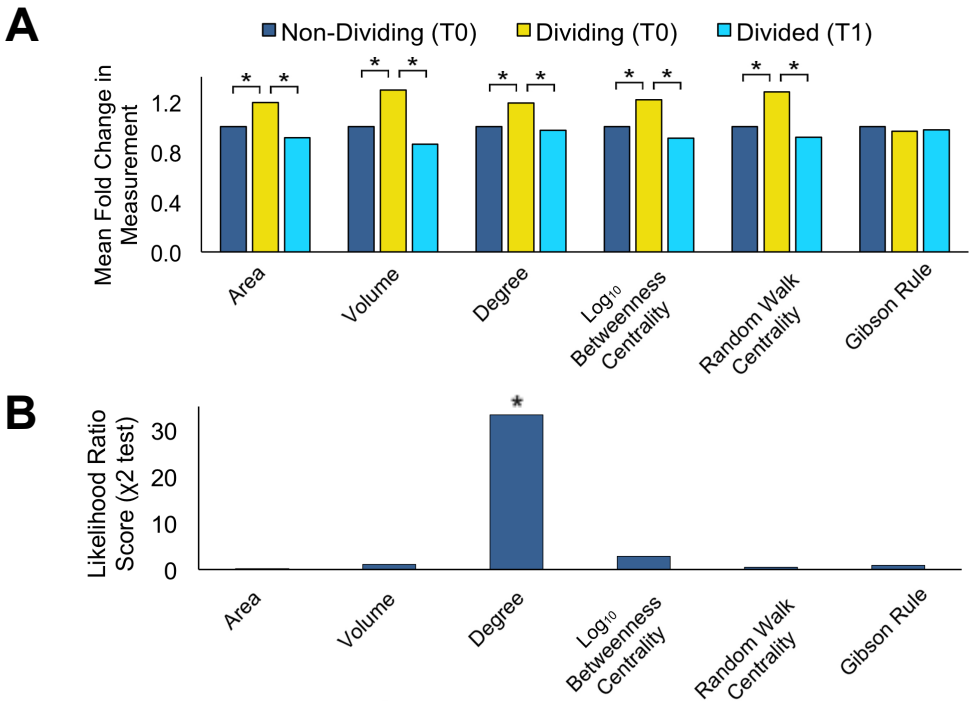
smaller (Figure 5.8A). Cells in the T0 time point that go on to divide within the next 11 hours are on average significantly larger, have more local cell-cell interactions, and fall on more short paths. As in the *Arabidopsis* meristem, after division, tomato SAM cells are smaller and have lower degree, $\log_{10}$ BC and RWC.

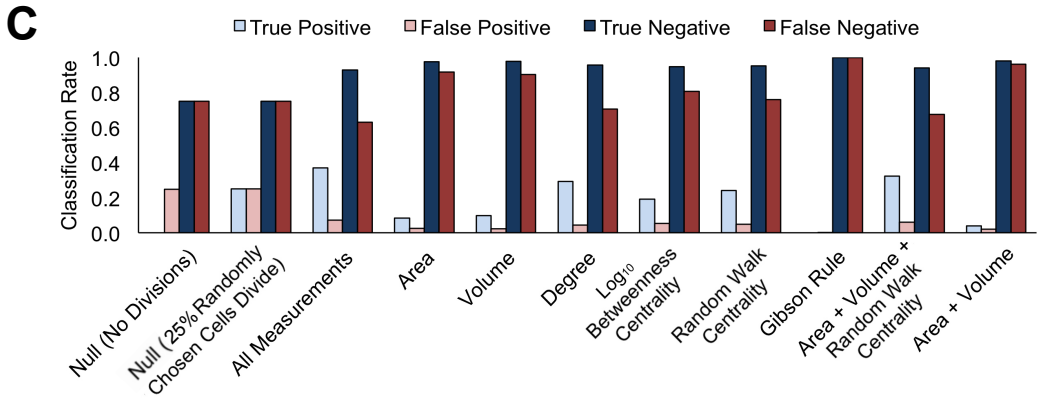
However, in tomato, when all features were incorporated into a logistic regression model, cell degree was the only measurement that significantly contributed to the classification of non-dividing and dividing cells (Figure 5.8B) (Table 5.4). This represents a clear difference in what measurements can be used to identify dividing cells in SAMs of individual plant species, and may indicate a difference in the control of cell organisation in *Arabidopsis thaliana* and tomato.

Another clear difference in the two species examined was their rate of cell division, where around 25% of cells divided in the tomato SAM over 11 hours, five times the rate of cells in the *Arabidopsis* SAM (Table 5.1 and 5.2). With this increased number of divisions in the tomato SAM, assuming that no cells divided resulted in around 75% prediction accuracy (Figure 5.8C). However, though degree was identified as a significant contributor to cell classification, including all features in the model resulted in just a 4% increase in successful division prediction, over the null case of assuming no divisions (Table 5.4). In terms of increasing the identification of true positive cases, using only degree, only RWC, and a combination of area, volume and RWC were most successful, resulting in a 0.3 to 0.4 true positive classification rate (Figure 5.8C). This is in contrast to models used in *A. thaliana*, where mostly, geometric features seem to be the major contributors to successful predictions (Figure 5.7C).

Like in *Arabidopsis*, the combination of significant changes between non-dividing and dividing cells, and the logistic regression results indicate that there may be some relationships between measurements in the tomato SAM. Cells in the tomato meristem still showed strong relationships between area and volume, and moderately strong relationships between local and global topological features (Figure 5.8D). However, in contrast to *A. thaliana*, there were only weak relationships between geometric and topological properties in tomato SAM cells, with R^2 ranging from 0 to only 0.11. This decoupling of cell size and cell organisational properties may again suggest a difference in control and development of stem cells in the tomato stem cell niche.

These analyses have revealed substantial differences in the organisation of cells in the *Arabidopsis* and tomato SAMs, and the relationships of topological cell properties to the well-studied feature of cell size. It is possible that increased control of cell size and shape in the tomato meristem may help to avoid the emergent organisational properties of a 'default' configuration of cells embedded in 3D space as seen in *Arabidopsis*, and allow the generation of specific cellular patterning.





D

Linear Regression R^2 Value

0 — 1

	Area	Volume	Degree	Log_{10} Betweenness Centrality	Random Walk Centrality	Gibson Rule
Area	1					
Volume	0.98	1				
Degree	0	0	1			
Log_{10} Betweenness Centrality	0.11	0.09	0.53	1		
Random Walk Centrality	0.06	0.05	0.75	0.66	1	
Gibson Rule	0.06	0.06	0.01	0.01	0.02	1

Figure 5.8. Dynamics of geometric and topological properties in the tomato SAM. (A) Normalised mean fold change in geometric and topological properties between non-dividing (T0), dividing (T0) and divided cells (T1). Error bars are ± the standard error of the mean. A * denotes significance between classes of cells at the $p \leq 0.05$ level (*t*-test). (B) Likelihood ratio of each parameter incorporated into a logistic regression model, to classify non-dividing and dividing cells in T0. A * represents a statistically significant contribution to classification (Type II ANOVA, $p \leq 0.05$) (C) Classification rates of logistic regression models with different incorporation of variables, split into true positive, false positive, true negative and false negative rates. (D) A matrix of pairwise linear regressions between measurements, with a heat map for the coefficient of determination (R^2) between each pair.

Table 5.4. Type II ANOVA test on a logistic regression model with geometric and topological measurements in tomato.

A logistic regression model was used to classify non-dividing and dividing cells in the T0 tomato SAM. All measurements were included in the model, and their effectiveness in classification was measured using a Type II ANOVA test, which specifically does not bias model terms based on the order of introduction. A high likelihood ratio (LR χ^2) indicates that a measurement had high classification power.

Measurement	LR χ^2	Degrees of Freedom	$p(>Chi^2)$
Degree	33.2	1	8.48×10^{-9}
Log_{10} Betweenness Centrality	2.81	1	0.0935
Volume	1.05	1	0.306
Gibson Rule	0.916	1	0.338
Random Walk Centrality	0.493	1	0.482
Area	0.152	1	0.696

Division Prediction Accuracy	0.790

5.2.4 Predicting division plane orientation in the *A. thaliana* SAM

Whilst the control of division timing in the SAM has an effect on cell organisation, the placement of the division plane during mitosis also has direct consequences for tissue patterning. Depending on cell wall placement, the daughter cells resulting from cell division can have different local cell-cell interactions, and by extension, different global connectivity properties. As plant cells are immotile, the change in cell configuration after cell division is both unchangeable and irreversible, so it is likely that the specific position of cell wall deposition is highly controlled. By computationally simulating cell divisions according to different rules (Section 2.8), whether there is a role for cell topology in cell wall placement can be determined.

To simulate divisions, data from four biological replicate *Arabidopsis* meristems, at the T0, T1 and T2 time points were used. In total, there were 112 cell divisions over all *A. thaliana* meristems imaged. Cells were fused in the T1 time point mesh to identically replicate the cellular topology of the T0 time point, and in the T2 time point mesh to match the topology of the T1 time point before cells were computationally divided (Section 2.8.1). This ensured that division rules did not have to account for cell growth in a plane prediction.

Four different cell division rules were simulated in the fused meshes, in the sites of each of the 112 identified cell divisions. Errera's rule, also referred to as the shortest wall rule, found the plane that bisects the cell using the smallest cell wall area possible (Errera, 1886), relying solely on geometric properties of the cell to make a wall placement prediction. The minimum degree rule found the wall that minimises

the number of neighbours for each daughter cell after division, using local cell connectivity information. Using global topological information, the minimum random walk rule identified the division plane that minimised the RWC of the daughter cells. Finally, the Gibson rule simulated a cell division plane that bisected the connecting cell wall of the neighbouring cell with the lowest degree (Gibson et al., 2011). For every rule, all planes were constrained to be perpendicular to the SAM surface, as well as passing no more than 0.2 μm away from the cell centre, based on observations of SAM cell division in previous studies (Shapiro et al., 2015). For all rules incorporating topological properties, in the case where multiple division planes satisfied a rule, plane with the smallest wall area was chosen.

It is important to note that every cell division causes a change in the local and global topology of the SAM cellular connectivity network, meaning that subsequent division simulations that take topology into account are affected. In addition, the order of cell divisions was unknown between time point images. The large number of cell divisions between tomato samples meant that determining the role of topology in division plane choice would be difficult (Figure 5.6D), as the order of divisions would have a drastic effect on topological plane prediction. Due to the lower number of cell divisions between time points in *A. thaliana* than in tomato (Tables 5.1 and 5.2), all simulations were carried out in *A. thaliana*, restricting the effects of the unknown division order. To further reduce the potential bias resulting from the unknown division order, division simulations in each *Arabidopsis* meristem were carried out three separate times, each with a randomly sampled division order (Section 2.8.3).

Comparisons between simulated and observed division planes were made by calculating the angle between the plane normals (Figure 5.9A) (Section 2.8.4).

Qualitatively, some division planes were captured by every rule, whilst in some cases rules made errors (Figure 5.9B). This may be a consequence of the relatedness between most measurements in the *Arabidopsis* SAM (Figure 5.7D). Using a more quantitative approach with the comparison of plane normal angles, the shortest wall rule and the minimum random walk rule predicted the localisation of a new cell wall closest to the real cleavage plane (Figure 5.9C). Both the shortest wall rule and the random walk minimisation rule significantly outperformed the degree minimisation rule, and notably the Gibson rule. All rules identified planes that were closer to the observed cell division wall than a randomly selected plane, including the Gibson rule, in agreement with previous research (Gibson et al., 2011). This shows that geometric properties, as well as local and global topological information, all have some power in terms of cleavage plane orientation prediction.

There were many examples of identical planes being predicted by both Errera's rule and the minimum random walk rule (Figure 5.9B). Comparing the angles between the simulated shortest wall and simulated minimum random walk rule planes showed that they are more similar to each other than random division planes (Figure 5.9D). This suggests the presence of a link between the global topological properties of a cell, and cell geometry, as previously demonstrated in Figure 5.7D.

Because many observed planes also minimised the random walk centrality of daughter cells, the contribution of individual observed plane angles to this minimisation was explored. In all divisions tested, small deviations, of up to 10 degrees deviation from the real division plane had no effect on local topology, and therefore no effect on the RWC of daughter cells. At angles of between 10 and 20 degrees deviation, 16.2% of daughter cells experienced altered RWC.

To further establish which division rules made the closest predictions, along with which rules made identically close predictions, a Venn diagram of best planes was plotted, using the average counts of closest planes from all three division order permutations (Figure 5.9F) (Section 2.8.3). In a limited number of cases, all rules were able to make the best prediction, while others could not. In particular, the Gibson rule was fairly successful at identifying close division planes when other rules were ineffective (Figure 5.9F). The majority of closest division planes were predicted by the shortest wall and minimum random walk rules. Quantitative and qualitative examination of closest predicted planes in individual layers of the *Arabidopsis* SAM indicated a similar trend (Figures 5.10 and 5.11). In terms of absolute number of planes most closely predicted by each rule, the minimum random walk rule had the most, followed by the shortest wall rule, the minimum degree rule, and lastly the Gibson rule (Figure 5.9G).

The links between plane placement using both Errera's shortest wall rule and the minimisation of daughter cell RWC, show that following simple local geometric rules can lead to emergence of a complex global organisational property. The shape and

size of a cell is used to determine the position of the shortest wall, and as a consequence maximises the path length in daughter cells, resulting in less efficient meristem-wide information transfer through them.

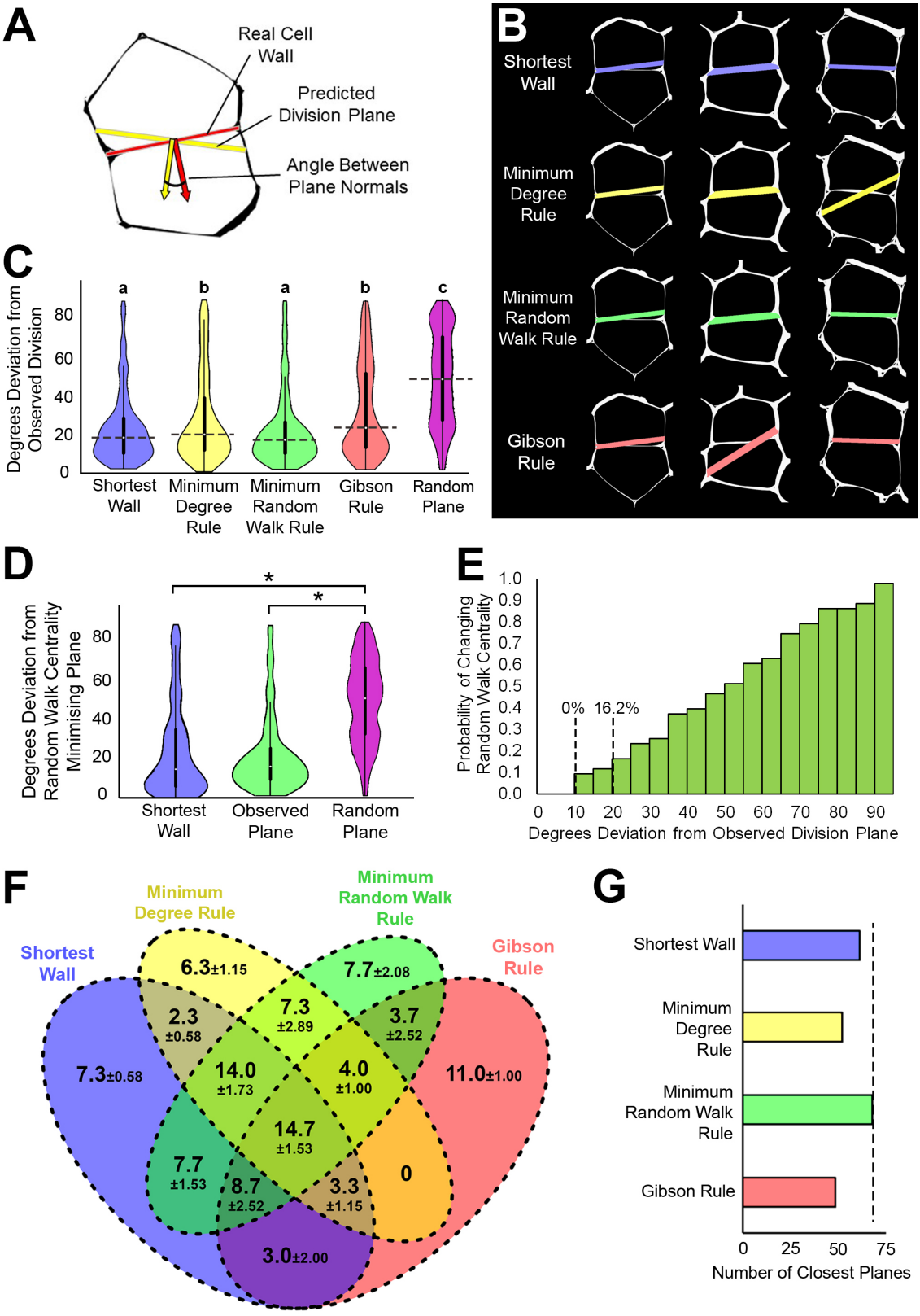


Figure 5.9. Prediction of division plane placement in *A. thaliana* using geometric and topological features.

(A) A schematic of the comparison of real and simulated division planes. The black outline represents a cross section of a cell mesh that has been computationally divided. (B) Examples of predicted division planes using different rules (in colour) overlaid on a cross section of the real daughter cell meshes, with the real division plane (white). (C) Violin plots showing the distribution of degrees deviation of the predicted planes from the real division planes. The dashed line indicates the mean degrees deviation for each rule. Different letters above violins denote significant differences between means (ANOVA with post-hoc Tukey tests, $p \leq 0.05$). (D) Violin plots of degrees deviation from the predicted random walk minimisation plane. A * denotes a significant difference in means (*t*-test, $p \leq 0.05$) (E) Distribution of angle deviations that cause a change in the random walk centrality of the daughter cells, compared to the real division. Dashed lines show the percentage of random walk centrality altered daughter cells at less than 10 degrees deviation, and less than 20 degrees deviation. (F) A Venn diagram of division rules that predicted the closest division plane to the observed real division plane. Predicted planes that were within ± 1 degree were treated as equally close. Error shown is ± one standard deviation, where three random division order permutations were carried out, generating some variance in predictions. (G) Number of planes closest to the observed division that were predicted by each division rule. Figure adapted from Jackson et al., 2019, *Cell Systems.*

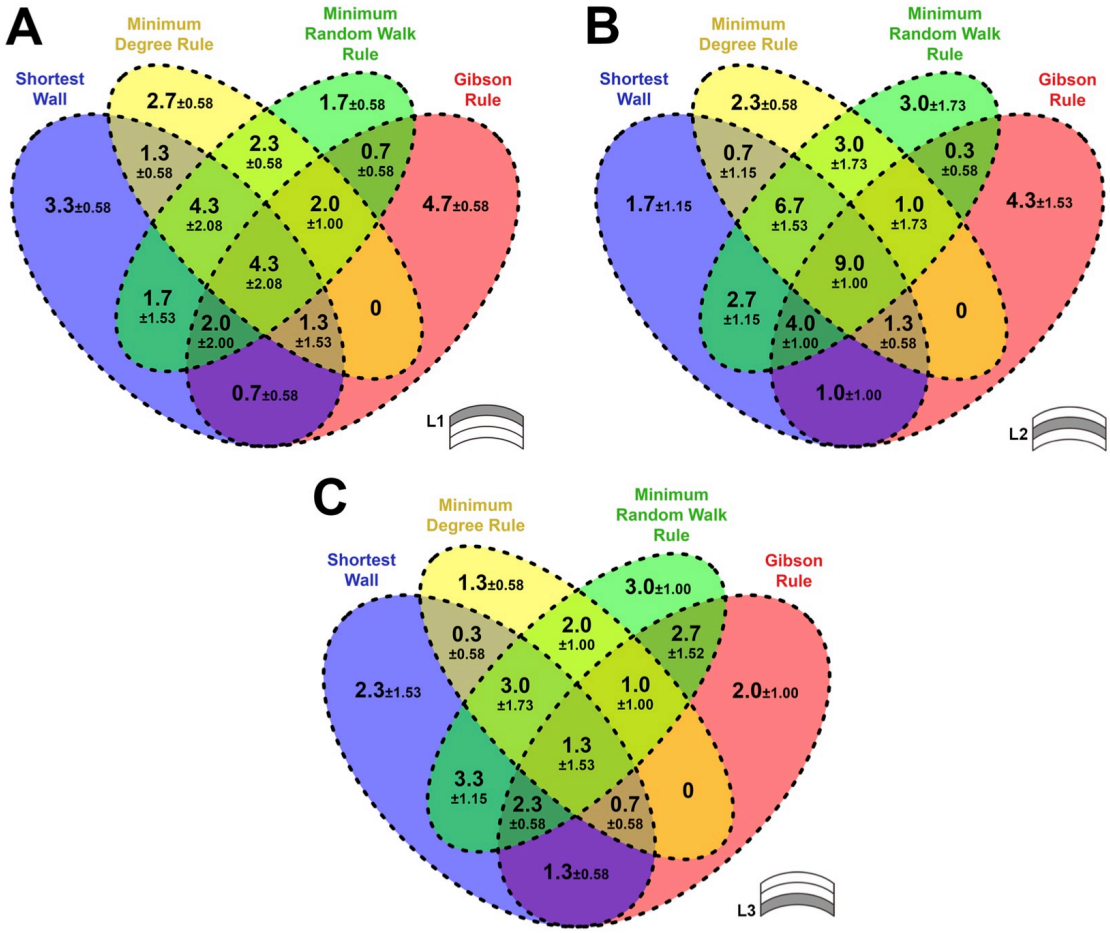


Figure 5.10. Closest plane predictions in individual *A. thaliana* SAM layers.
(A) A Venn diagram of division rules that predicted the closest division plane to the observed real division plane, in L1 only. Predicted planes that were within ± 1 degree were treated as equally close. Error shown is ± one standard deviation, where three random division order permutations were carried out, generating some variance in predictions. (B) Closest division rules in L2 only. (C) Closest division rules in L3 only. Figure reproduced from Jackson et al., 2019, *Cell Systems.*

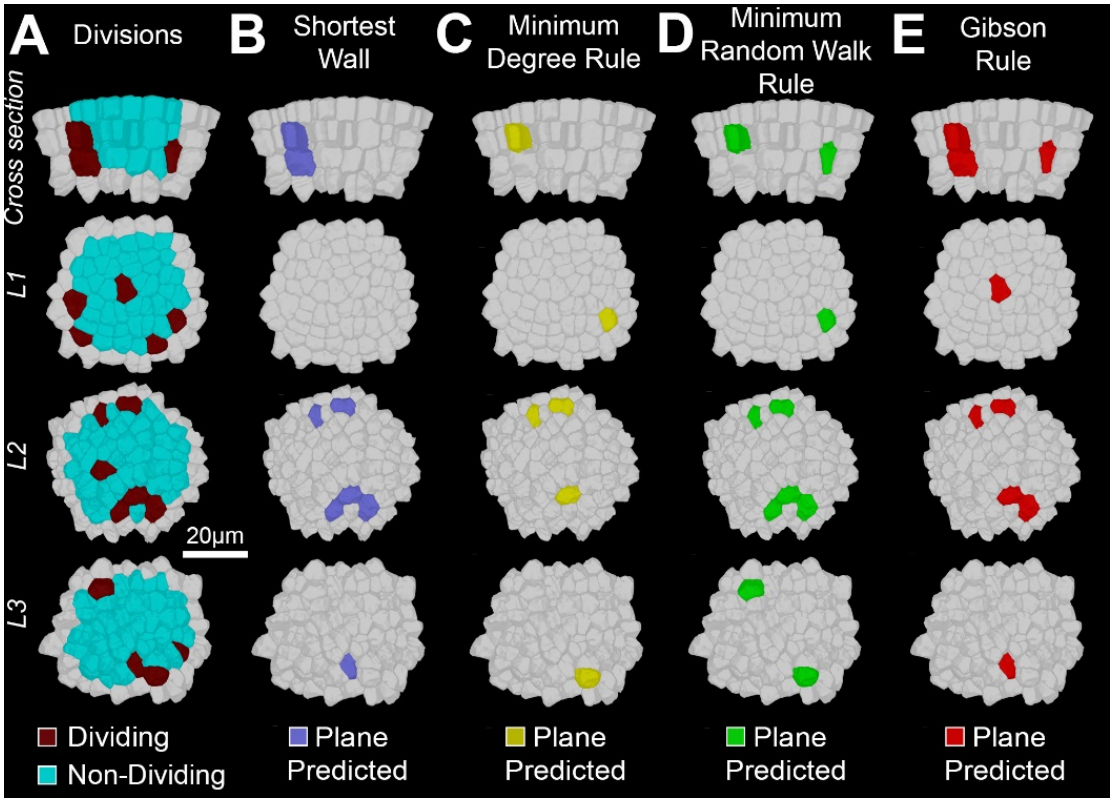


Figure 5.11. Spatial distribution of divisions predicted by different rules.
(A) Cell divisions overlaid on a cross-section of a mesh of the *Arabidopsis thaliana* SAM, and the L1, L2 and L3 layers. (B) Cells where the closest plane predictions were made with the shortest wall rule (in blue). (C) Cells where the closest plane predictions were made with the minimum degree rule (in yellow). (D) Cells where the closest plane predictions were made with the minimum random walk rule (in green). (E) Cells where the closest plane predictions were made with the Gibson rule (in red). Figure reproduced from Jackson et al., 2019, *Cell Systems.*

5.2.5 Organisational consequences of cell divisions in the *A. thaliana* SAM

If cells are continually dividing in the SAM, resulting in minimisation of RWC in daughter cells, this may have organisational consequences for the meristem connectivity network as a whole. Using the whole *Arabidopsis* meristem samples as a template, divisions were continuously simulated using both geometric and topological division rules, until all cells had divided twice. The shortest wall, Gibson,

and minimum degree rules were tested for their ability to preserve meristem cell arrangement, and compared to random division plane placement. Visually, all rules generated cellular architectures that appeared to be patterned in a similar manner to the original *Arabidopsis* SAM (Figure 5.12A – D), while random divisions did not seem to preserve this property (Figure 5.12E).

Both global and local topological effects of continuous division were quantified, as a more robust measure of SAM organisation. After all cells had divided, because the number of cells had quadrupled, each divided sample meristem cellular connectivity network was subsampled from centre outwards until the number of nodes before and after simulated divisions was equal. This preserved overall network size, removing the bias introduced by comparing the global properties of different sized networks (Section 3.2.1).

There were subtle changes in meristem organisation in each meristem sample, depending on what rules were used to divide cells (Figure 5.13). Distributions of degree and RWC were compared with topological distributions of the original meristem templates, in order to examine what division rules were sufficient to preserve the organisational properties of the meristem (Figure 5.12F – G). To compare distributions, the earth-mover's distance was calculated between property distributions to quantitatively measure the deviation from the original template (Section 2.6.2).

Using the shortest wall and minimum degree rules resulted in the least RWC distribution differences, across the four meristems that were continuously divided (Figure 5.12F). Using both of these rules, the earth-mover's distance between the RWC distributions of divided meristems and the original template was significantly less than the distance between the randomly divided meristem and the original. Using the Gibson rule to continuously divide cells in the SAM resulted a poorer conservation of RWC distributions, similar to using random division planes. These results show that minimising wall area, or minimising number of neighbours in the daughter cells, preserves global topological SAM organisation more successfully than using the Gibson rule, or random divisions. This again links the control of path length across the meristem to the geometrically motivated Errera's rule, and additionally shows a link between the control of local topology through degree minimisation, and the global property of RWC.

In terms of preserving local organisational properties, there was a large amount of variance between earth-mover's distances comparing degree distributions (Figure 5.12G). No division rules used to continually divide the meristem were significantly better at preserving local cell connectivity distributions than random division planes. Whilst there are relationships between local and global topological properties in the SAM cellular connectivity network, it is possible that at the whole-meristem scale, degree is not as sensitive to perturbation as RWC, due to constraints of cells packing in 3D space.

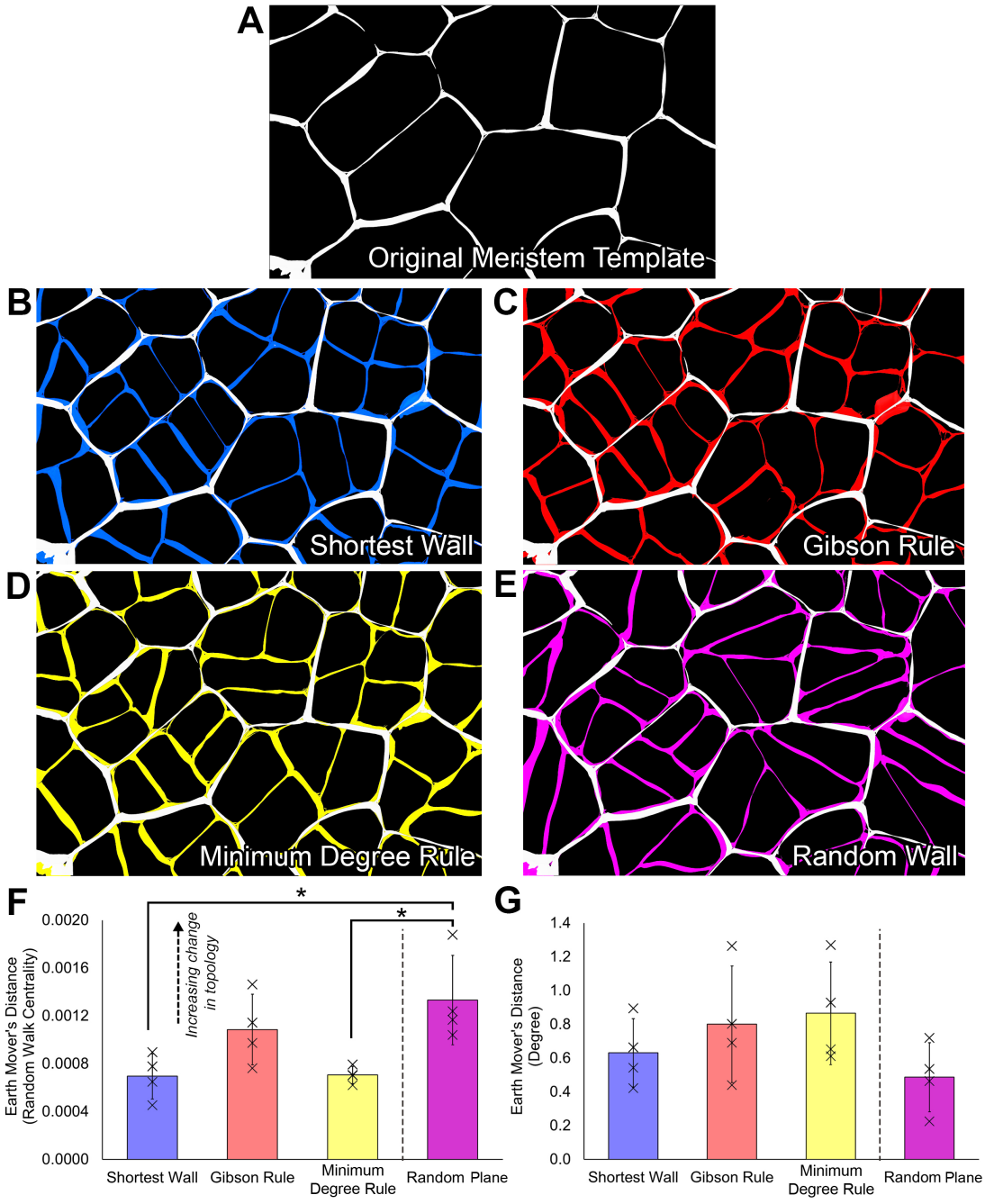


Figure 5.12. Simulating repeated divisions across the entire *Arabidopsis* SAM. (A) A cross-section of cells in the original *A. thaliana* SAM mesh, before simulated divisions. (B) Simulated cell divisions in the SAM mesh, using the shortest wall rule to divide all cells twice. (C) Simulated cell divisions using the Gibson rule. (D) Simulated cell divisions using the minimum degree rule. (E) Simulated divisions using random division planes. (F) Earth-mover's distance between random walk centrality distributions of the computationally divided meristem templates, and the original templates. (G) Earth-mover's distance between degree distributions. Each cross represents an individual comparison. Error bars are ± the standard deviation of the mean. A * represents a significant difference in median earth-mover's distances

(Mann-Whitney U test, $p \leq 0.05$). Figure reproduced from Jackson et al., 2019, *Cell Systems.*

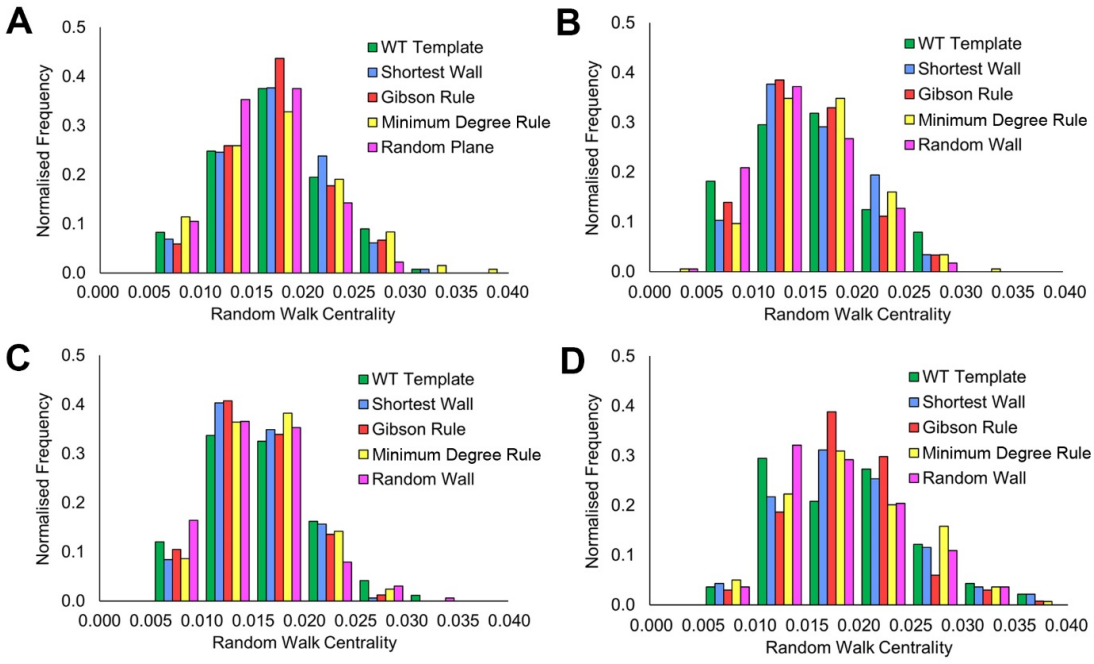


Figure 5.13. Random walk centrality before and after simulated divisions in individual *Arabidopsis* meristem samples.
(A) Distribution of random walk centrality in the first *A. thaliana* SAM sample in the original SAM template, and after all cells have been computationally divided twice, using different rules. (B) Random walk centrality before and after simulated divisions in the second meristem sample. (C) Random walk centrality before and after simulated divisions in the third meristem sample. (D) Random walk centrality before and after simulated divisions in the fourth meristem sample. Figure reproduced from Jackson et al., 2019, *Cell Systems.*

5.2.6 Influences of cell shape and topology on the emergence of organisation

Division plane placement has been shown to influence the global topological properties of the SAM, generating various cellular organisations. Using Errera's rule,

control of cell geometry has been linked to the emergent property of RWC minimisation, constraining SAM cell organisational properties at a global scale. Previously, the distribution of the local property of degree in epithelial tissues was shown to be a consequence of cell divisions in 2D (Gibson et al., 2006) Similarly, topologically similar models of the *Arabidopsis* SAM were used to establish whether the emergence of global order is simply consequence of dividing cells embedded within 3D space. To determine this, firstly models that shared both local and global topological properties were required. Different models were created *in silico* using Voronoi tessellation with varying parameters (Section 2.3.2).

Previously, random points in 2D space were Voronoi tessellated to generate model epithelia, before their centres were extracted and Voronoi tessellation was performed again (Escudero et al., 2011). This process was repeated iteratively to create a set of models referred to as the Centroidal Voronoi Tessellation Path (CVT Path). These models were successful in capturing the local topological properties of many epithelial tissues. The first class of models created in an attempt to recapitulate the cellular organisation in the *Arabidopsis* SAM was based on the CVT Path, extended into three-dimensional space (Figure 5.14). To create meristem models, Voronoi tessellation was first used with centroids with fixed z coordinates, creating four distinct layers representing L1-L4 in the SAM, whilst the x and y coordinates were randomly sampled. Centres of cells were extracted and tessellated iteratively, to generate steps 1, 2 and 5 of the CVT Path (Figure 5.14A, B and C).

Visually, cells in the CVT Path models shared features with *Arabidopsis* SAM cells (Figure 5.5 and Figure 5.14). Geometric and topological properties of models were compared to those of the real *Arabidopsis* SAM, by comparing distributions (Section 2.6.2). Volume was normalised within all models and samples before comparison to account for differences in model and imaged samples relative cell sizes, so that the largest cell in each model had a normalised volume of 1. In terms of geometry, there were significant differences between all models in the CVT Path and the *Arabidopsis* SAM (Figure 5.14D). Each step on the CVT Path reduced the breadth of the normalised volume distributions, though none were similar to the slightly left-shifted distribution of normalised cell volume in the real meristems. Similarly, there were significant differences between cell degree and RWC distributions in CVT Path models and *Arabidopsis* SAMs (Figure 5.14E and F). Again, though not necessarily related to the normalised volume, distributions of degree and RWC in the models fail to capture the left-shifted nature of the real meristems' distributions, and each CVT Path step taken results in further shifting of these properties to higher values, with less variance. This indicates that models created with the CVT Path do not suitably capture the local and global cellular organisation of the *Arabidopsis* meristem.

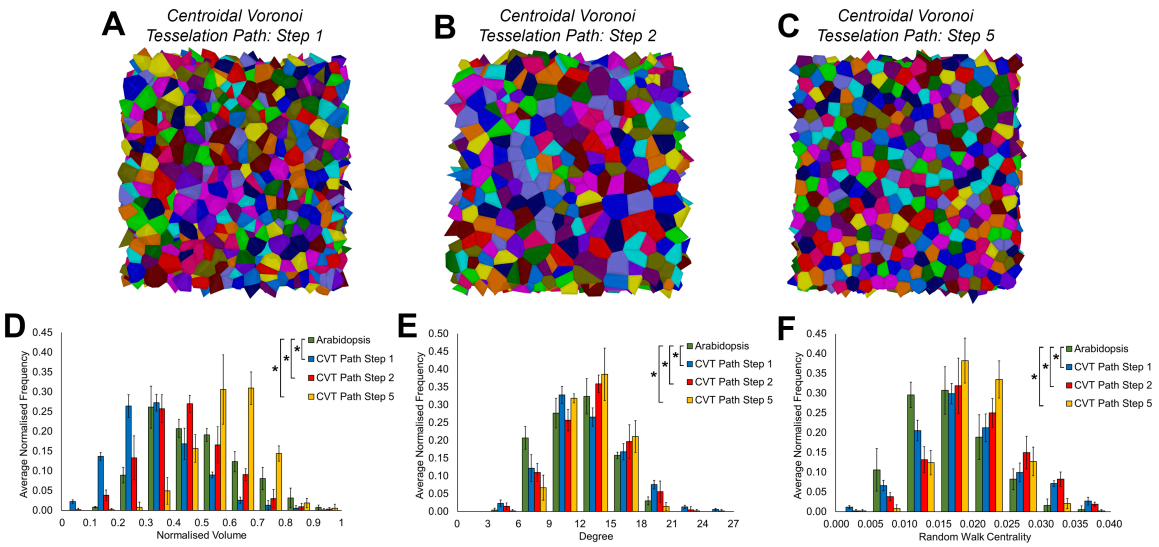


Figure 5.14. SAM models constructed using the Centroidal Voronoi Tessellation Path.
(A) A 3D, 4-layered meristem model created by randomly sampling centroids for subsequent Voronoi tessellation, representing Step 1 of the CVT Path. (B) A model created using Voronoi tessellation of the cell centres in the Step 1 model, representing Step 2 of the CVT Path. (C) A model created with 5 iterations of repeated Voronoi tessellation of cell centres, representing Step 5 of the CVT Path. (D) Normalised cell volume in the *A. thaliana* SAM and CVT Path models. (E) Degree in the *A. thaliana* SAM and CVT Path models. (F) Random walk centrality in the *A. thaliana* SAM and CVT Path models. Error bars represent the standard deviation within a frequency bin from 4 replicate samples of each model and the *Arabidopsis* SAM. A * denotes a significant difference between distributions of the *Arabidopsis* SAM and a model (normalised volume and random walk centrality: Kolmogorov-Smirnov test, $p \leq 0.05$, degree: χ^2-test, $p \leq 0.05$). Figure reproduced from Jackson et al., 2019, *Cell Systems.*

Because the CVT Path models were not sufficient to capture organisation in the *A. thaliana* SAM, another set of models was constructed. To generate another class of models, uniformly spaced centroids in a 4-layered structure were subjected to increased amounts of uniformly sampled random movement, or noise, in the x and y directions, and Voronoi tessellated (similarly to Section 3.2.2) (Figure 5.15A – D). Qualitatively, this increase applied centroid noise resulted in increasingly diverse cell shapes in the models.

As with the earlier CVT Path models, adding any amount of uniformly distributed noise to centroids before Voronoi tessellation was not sufficient to recapitulate the geometric, or topological properties of the *Arabidopsis* SAM, and distributions of normalised volume, degree and RWC differed significantly in all of these models (Figure 5.15E, F and G).

Adding noise sampled from uniform distributions to centroids before Voronoi tessellation did not generate models with similar organisational features to the *Arabidopsis* meristem, but other methods for sampling noise are possible. Before, tessellation, equally spaced centroids were moved using noise sampled from both Gaussian (normal) and Pareto (Hosking and Wallis, 1987) distributions (Figure 5.15H, I and J). Again, the geometric and topological properties of these models were significantly different from those of the *A. thaliana* SAM, and had a less similar cellular organisation to the real meristem than models using uniform noise sampling (Figure 5.15E, F and G). Therefore, increasing the randomness of centroid positions in Voronoi tessellation, despite in many cases generating qualitatively similar structures to the *Arabidopsis* SAM, did not generate topologically similar models in a quantitative sense, using a diverse range of centroid position sampling methods.

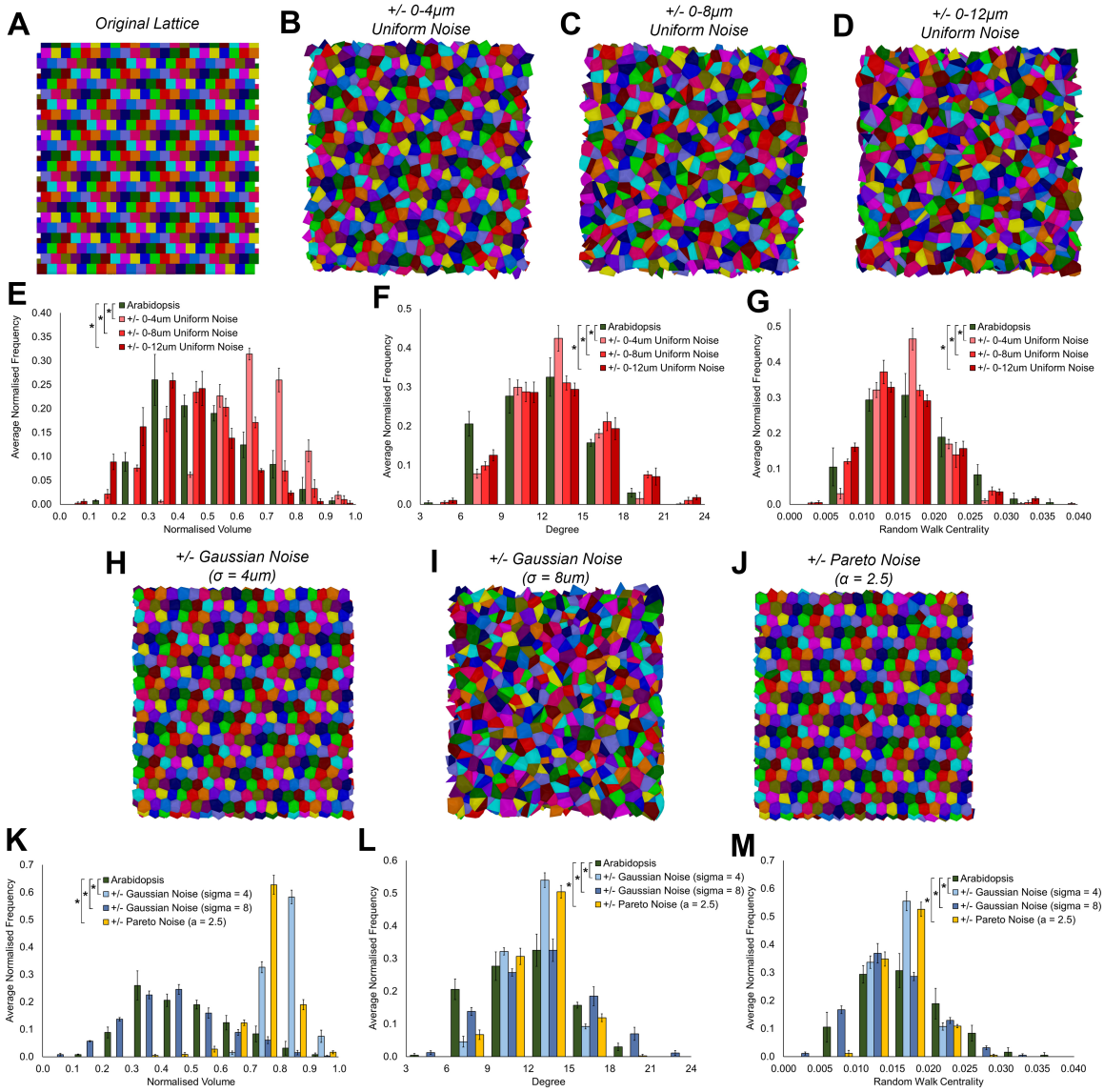


Figure 5.15. SAM models constructed using equidistant centroids, with the addition of random noise before Voronoi tessellation.
(A) A 3D, 4-layered lattice of cubes, where cell centres are equidistant from one another. (B) A 3D, 4-layered meristem model created by Voronoi tessellation of equidistant centroids from a lattice, each moved by a random amount from a uniform distribution between 0 and 4 μm in the x and y directions. (C) A meristem model created with Voronoi tessellation of centroids, randomly moved between 0 and 8 μm, sampled from a uniform distribution. (D) A meristem model created with Voronoi tessellation of centroids, randomly moved between 0 and 12 μm, sampled from a uniform distribution. (E) Normalised cell volume in the *A. thaliana* SAM and uniform centroid noise models. (F) Degree in the *A. thaliana* SAM and uniform centroid noise models. (G) Random walk centrality in the *A. thaliana* SAM and uniform centroid noise models. (H) A meristem model created with Voronoi tessellation of centroids, randomly moved between 0 and 4 μm, sampled from a Gaussian distribution. (I) A meristem model created with Voronoi tessellation of centroids, randomly moved between 0 and 8 μm, sampled from a Gaussian distribution. (J) A meristem model

created with Voronoi tessellation of centroids, randomly moved between values sampled from a Pareto distribution, with α = 2.5. (K) Normalised cell volume in the *A. thaliana* SAM and Gaussian and Pareto centroid noise models. (L) Degree in the *A. thaliana* SAM and Gaussian and Pareto centroid noise models. (M) Random walk centrality in the *A. thaliana* SAM and Gaussian and Pareto centroid noise models. Error bars represent the standard deviation within a frequency bin from 4 replicate samples of each model and the *Arabidopsis* SAM. A * denotes a significant difference between distributions of the *Arabidopsis* SAM and a model (normalised volume and random walk centrality: Kolmogorov-Smirnov test, $p \leq 0.05$, degree: χ^2-test, $p \leq 0.05$). Figure reproduced from Jackson et al., 2019, *Cell Systems.*

In all previous models, that did not reflect the topological properties of the *Arabidopsis* meristem, Voronoi tessellation was used, in which all cells expand starting from centroid positions, until all free space has been filled, and cells completely tessellate (Section 2.3.2). In normal Voronoi tessellation, the rate of cell expansion from each centroid position is constant in all directions. Using a variant of the Voronoi process, anisotropic Voronoi tessellation (Du and Wang, 2005), directions of growth, and the rate of growth in these directions, can be specified. This results in different cell shapes, and different tessellation of cells.

A series of models was generated using anisotropic Voronoi tessellation, where centroids were sampled from a lattice with equidistant ordered cell positions (Figure 5.16A). Three primary directions of growth were randomised for each cell centroid, and the rate of growth in each of these directions (the magnitude) was randomly varied (Figure 5.16A – D). Using this method, though the centroid positions were invariant in each model, the shape and size of resulting cells was variable.

Qualitatively, there was little difference between anisotropic Voronoi models with different magnitudes of directional growth (Figure 5.16B, C and D). As in all previous models, normalised cell volume was significantly different in anisotropic Voronoi tessellation models, compared to real *Arabidopsis* SAM cell size (Figure 5.16E). In all models, irrespective of allowed growth magnitude, there were many more small cells than were present in the *A. thaliana* meristem. However, in terms of both local and global topological measurements, there were no significant differences between distributions of degree or random walk centrality in any anisotropic Voronoi models and the real *Arabidopsis* SAM. This suggests that anisotropic Voronoi tessellation of ordered centroids is not necessarily a valid to reproduce cell geometry in the SAM, but can be used to recapitulate organisational properties of the *Arabidopsis* meristem. As the distributions of degree and RWC were similar in all anisotropic Voronoi models, the earth-mover's distance was calculated, quantitatively comparing distributions of these models to the topological distributions of *A. thaliana*, and determining which model was organisationally the most similar (Figure 5.16H and I). Earth-mover's distance between degree and RWC distributions of models using magnitudes of direction growth between 1 and 3 were most similar to those in the *Arabidopsis* SAM, indicating that this was the most suitable model. Additionally, the relationships between measurements of cells in this anisotropic Voronoi model are similar to relationships in the *Arabidopsis* SAM (Figure 5.7 and 5.17) As in *A. thaliana*, the strongest linear correlations are seen between are and volume, and between the topological properties of degree, $\log_{10}$ betweenness centrality and random walk centrality, while moderate relationships are present between geometric and topological features (Figure 5.17).

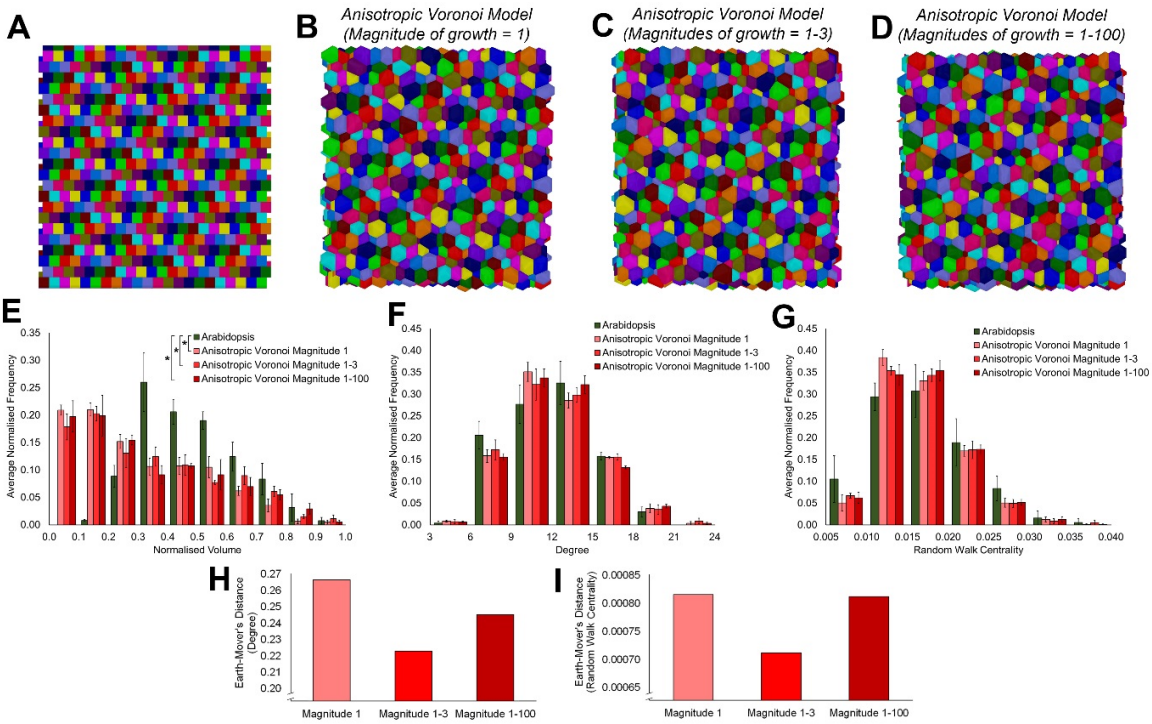


Figure 5.16. SAM models constructed using anisotropic Voronoi tessellation. (A) A 3D, 4-layered lattice of cubes, where cell centres are equidistant from one another. (B) A 3D, 4-layered meristem model created by anisotropic Voronoi tessellation of equidistant centroids in a lattice, where directions of expansion are randomised, and the magnitude of growth in each direction is uniform. (C) A meristem model created with anisotropic Voronoi tessellation, where the magnitude of growth in each direction is randomly chosen, between 1 and 3. (D) A meristem model created with anisotropic Voronoi tessellation, where the magnitude of growth in each direction is randomly chosen, between 1 and 100. (E) Normalised cell volume in the *A. thaliana* SAM and anisotropic Voronoi models. (F) Degree in the *A. thaliana* SAM and anisotropic Voronoi models. (G) Random walk centrality in the *A. thaliana* SAM and anisotropic Voronoi models. (H) Earth-mover's distance between the degree distributions of anisotropic Voronoi models and the *A. thaliana* SAM. (I) Earth-mover's distance between the random walk centrality distributions of anisotropic Voronoi models and the *A. thaliana* SAM. Error bars represent the standard deviation within a frequency bin from 4 replicate samples of each model and the *Arabidopsis* SAM. A * denotes a significant difference between distributions of the *Arabidopsis* SAM and a model (normalised volume and random walk centrality: Kolmogorov-Smirnov test, $p \leq 0.05$, degree: χ^2-test, $p \leq 0.05$). Figure reproduced from Jackson et al., 2019, *Cell Systems.*

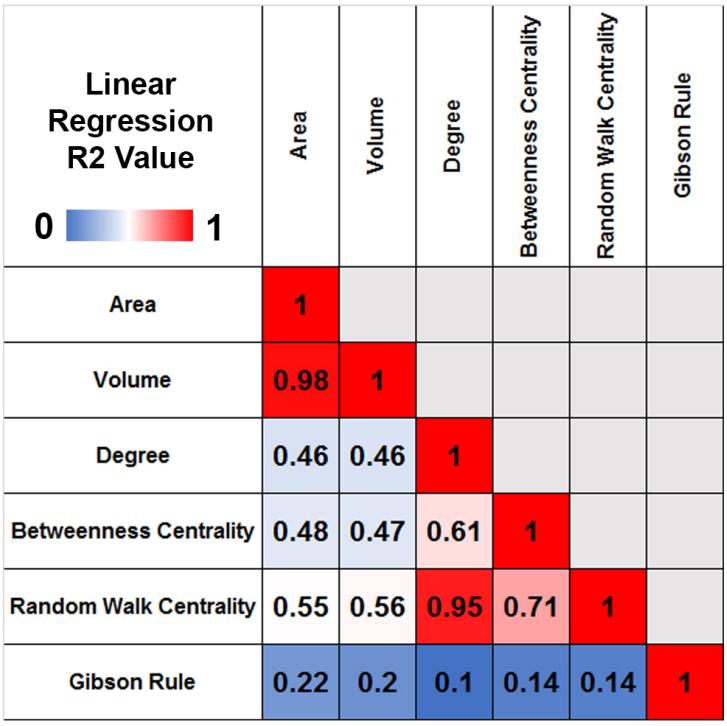


Figure 5.17. Pairwise linear regressions between cell measurements in the anisotropic Voronoi tessellation models with magnitudes 1-3.
A heat map shows the coefficient of determination (R^2) between each pair of variables. Figure reproduced from Jackson et al., 2019, *Cell Systems.*

The purpose of constructing a topologically similar model of the A. thaliana SAM was to determine whether the effect of random walk minimisation from a geometric division rule was purely an emergent property of any cells packing into 3D Euclidean space. This can now be addressed with the topologically equivalent anisotropic Voronoi *Arabidopsis* SAM model.

As with the real *A. thaliana* meristem meshes, model meristems were divided computationally using the shortest wall rule, the Gibson rule and the minimum degree rule, until all cells had divided twice. However, in contrast to results from continuously dividing the *A. thaliana* samples, dividing cells using the shortest wall, or any other rules, was not significantly better at preserving the random walk centrality distribution in the meristem model than using random division planes (Figure 5.18A). Whereas in *Arabidopsis* meristems, dividing all cells with the shortest wall rule generated a global topology more similar to the original templates than when using random cell walls (Figure 5.12F), using Errera's rule in the model meristem was insufficient to maintain global cellular topology in the system. This suggests that particular, pre-existing geometric factors in the *Arabidopsis* SAM are necessary for the emergent property of random walk centrality regulation, arising from a local geometric division rule.

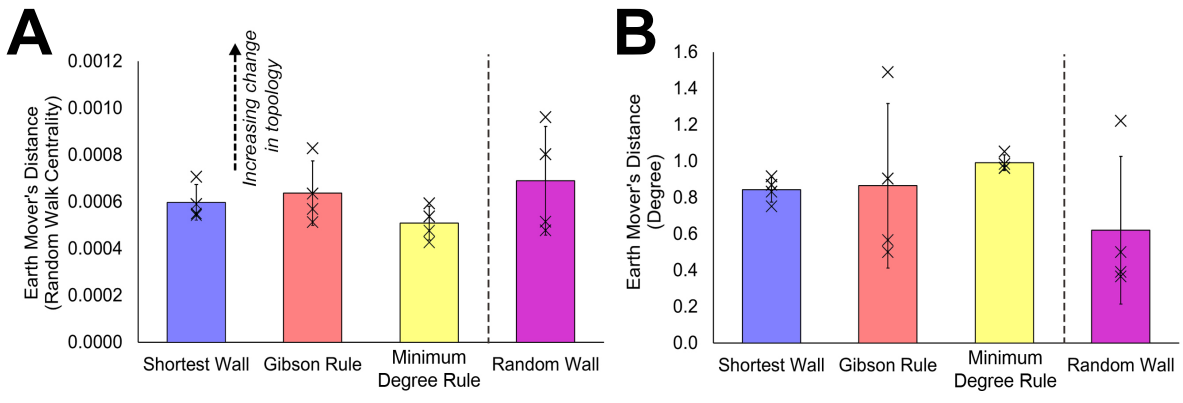


Figure 5.18. The effect of simulating repeated divisions in a model SAM.
(A) Earth-mover's distance between random walk centrality distributions of the computationally divided meristem model, and the original model. (G) Earth-mover's distance between degree distributions. Each cross represents an individual comparison. Error bars are ± the standard deviation of the mean. A * represents a

significant difference in median earth-mover's distances (Mann-Whitney U test, $p \leq 0.05$). Figure adapted from Jackson et al., 2019, *Cell Systems.*

5.2.7 The effect of mechanical cell interactions on SAM organisation

Cell shape in plants is largely controlled by the mechanical interactions between cells in tissues (Hamant et al., 2008). Having explored the role of cell shape on the emergence of cellular organisation in the SAM through a geometric division rule, using topological meristem models, the role of mechanically determined cell shape in maintaining organisation in the real SAM system remains to be established.

To examine the effects of mechanical cell interactions on SAM topology and organisation the *Arabidopsis* mutant *katanin1* (*ktn1*) was used, which lacks the *KATANIN1* gene, responsible for the severing of microtubules in the cell (Bichet et al., 2001) (Luptovčiak et al., 2017). Microtubules have been demonstrated to influence intercellular mechanical interactions, which in turn coordinate cell shape (Uyttewaal et al., 2012). *ktn1* mutant cells are defective in their ability to sense neighbouring cells through microtubules, preventing the mechanical feedbacks from controlling cell shape.

Imaging of the *katanin1* mutant, and qualitative comparison of cell patterning with that of wild-type *Arabidopsis* shows that cell shape, along with the overall tessellation of cells in the SAM, differed (Figure 5.19A and B). Irrespective of this, the relationships between geometric and topological properties in the *ktn1* mutant meristem remained similar to the correlations between properties in wild-type

Arabidopsis thaliana (Figures 5.7D and 5.20). Though average cell size was not significantly different between the wild-type and mutant SAMs, cell shape, measured using anisotropy (Section 2.5.3), was more elongated in the *katanin1* mutant, quantitatively confirming the role of microtubules in controlling this aspect of cell shape (Figure 5.19C and D). As well as cell shape, both average degree and random walk centrality were significantly different from wild-type *Arabidopsis* in the *ktn1* mutant (Figure 5.19E and F), suggesting that some control of local and global organisation is lost when microtubule severing is not fully functional. In particular, the average RWC increased in the *ktn1* mutant, indicating that the loss of normal cell shape control may be impacting the random walk minimising effect of cell division using the shortest wall.

These results suggest that the loss of normal cell shape in the *ktn1* mutant is linked to a loss of cellular organisation in the SAM at both the local and global scales.
This result, using genetic perturbation, reflects the trends observed using model SAMs, where native cell shape at a local scale in *A. thaliana* is required in order to ensure minimisation of the emergent global order property of RWC across the meristem.

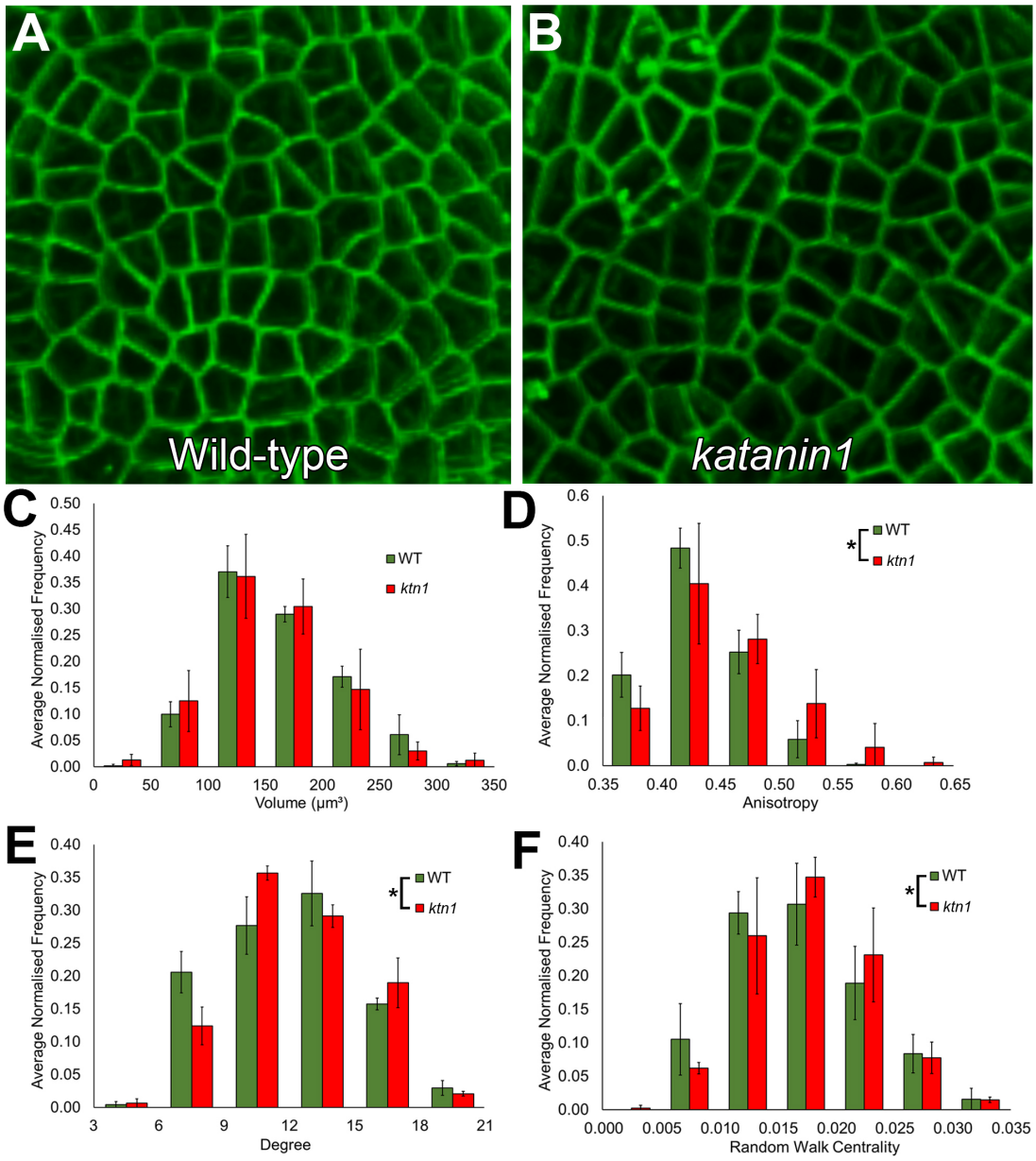


Figure 5.19. Geometric and topological properties of the *ktn1* mutant SAM.
(A) A top-down confocal image cross-section of cells in the wild-type *Arabidopsis thaliana* SAM. (B) Cells in the *ktn1* mutant. (C) Distributions of volume in wild-type *Arabidopsis* and the *ktn1* mutant SAMs. (D) Cell anisotropy in wild-type and *ktn1* SAMs. (E) Cell degree in wild-type and *ktn1* SAMs. (F) Random walk centrality in wild-type and *ktn1* SAMs. Error bars are ± the standard deviation within a frequency bin from 4 replicate samples of each wild-type *Arabidopsis* and *ktn1* SAM. A * denotes a significant difference between means (*t*-test, $p \leq 0.05$). Figure adapted from Jackson et al., 2019, *Cell Systems.*

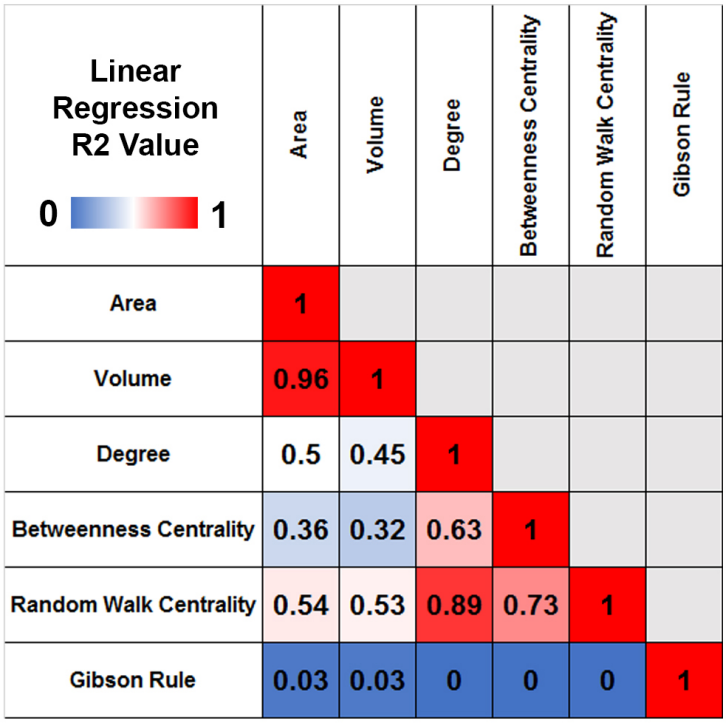


Figure 5.20. Pairwise linear regressions between measurements in the *ktn1* SAM. A heat map shows the coefficient of determination (R^2) between each pair of variables. Figure reproduced from Jackson et al., 2019, *Cell Systems.*

5.3 Discussion

Using organ-wide 3D imaging of meristem development, and representation of the tissue as cellular interaction networks, the impacts of local processes on global cell organisation have been elucidated. This has shown that the induction of mitosis is related, though not necessarily controlled, to the topological properties of individuals within cellular communities. In addition, evidence is presented for a counter-optimised global organising property within the SAM, working to maximise path length through geometric cell division control.

The timing of division appeared to be controlled differently in the tomato SAM than in *A. thaliana*, and was influenced by the local topological property of cell degree. However, these results may have been influenced by the large number of cell divisions between tomato SAM time points, compared to a lower rate of division in *Arabidopsis*. This may have had large consequences for comparisons made between non-dividing and dividing cells, and the data included in logistic regression models. Each division affects the local and global topology of other cells, and the order of divisions was unknown. For the same reason, the *Arabidopsis* SAM was more suitable for the later analysis of division planes.

For more precise study of the impact of cell topology on division timing in both species, knowing the sequence of cell divisions, and therefore enabling the construction of cellular connectivity networks between every cell division, would allow much stronger claims to be made. Though intensive in terms of initial image acquisition, higher temporal resolution could be achieved with much shorter time steps between the acquisitions of developing meristem images.

A striking difference between the organisation of the SAM in *Arabidopsis* and tomato is the different relationships between geometric and topological properties, identified using linear regression (Figure 5.7D and 5.8D). There was a decoupling of topology and geometry in tomato SAM cells, potentially allowing increased control of biological processes that are mediated by either trait.

The emergence of RWC minimisation through cell division across the meristem likely stems from the local behaviour of individual cells, as many observed division planes minimised both cell wall area and RWC. The specific layout of cells in the SAM, and subsequent timing of divisions and their division planes, is conducive to maximising reductions in daughter cell RWC.

The significance of minimising RWC, which is essentially a measure of global connectivity, may lie in a structure-function relationship in the cellular organisation of the SAM. Cells within organs are influenced by their cellular context, not only by their immediate neighbours, but also their wider cellular community (Hamant, 2017). Looking further into higher order properties of tissue organisation allows us to build an understanding of how cells work together to make a complex, functional system.

The calculation of RWC uses random walkers to traverse the network, similarly to a diffusive process (Codling et al., 2008) (Jackson et al., 2017a) (Newman, 2018), common throughout many biological systems (Othmer et al., 1988). This makes the measure suitable for identifying organisational features were the specific function of cell patterning is unknown. Here, RWC was used to model the routes of potential information flow across the SAM cellular network. This revealed that some cells, based on their topological context, are more likely to facilitate the movement of information.

In the *Arabidopsis* SAM, there is a noticeable absence of cells that are positioned on particularly short paths, which could potentially facilitate transport throughout the organ. Instead, the topological analysis carried out suggests that information follows no optimised route in the meristem. In a system where RWC is continually constrained and minimised through cell division, there is no subset of cells that are crucial for the transport of agents. The consequence of this topology is that it ensures robust transport of information across the SAM, at the cost of efficiency.

Whilst the organisation of cells in the SAM results in low efficiency, there are advantages to not relying on a subset of cells for transport of information throughout the system. In nature, due to its exposed apical position in many plants (Sussex and Kerk, 2001), the SAM is susceptible to herbivory, and with this the damage and loss of cells. The robust arrangement of cells in the SAM ensures that the loss of any given cell in the meristem is unlikely to affect transport within the organ.

Cell shape plays a role in SAM organisation, revealed by the perturbed mechanical forces in the *KATANIN1* mutant, where the meristem's ability to minimise RWC in dividing cells appears to be compromised. The shapes of individual cells at the local level are of utmost importance to the global SAM organisation, and its ability to develop a robust cellular architecture.

It is not trivial to explain, or create a model, of how a cell could perceive its own centrality in any given cellular organisation. In turn, there is little evidence to suggest that top-down organisation could influence the construction of patterning in organs. In

the SAM, the emergence of RWC minimisation from local, bottom-up division rules provides a biologically plausible explanation of how a tissue could minimise a global organisational property. This represents a feature that could be positively selected for. Using only a simple set of local rules to generate a complex topological phenotype with high robustness is likely to be an advantage for a species.

CHAPTER SIX: GENERAL DISCUSSION

6.1 Overview

This work has established a method and pipeline for the quantification of cellular patterning and organisation in multicellular 3D tissues. Exploration of how cells tessellate in 3D space, using appropriate local and system-wide topological measurements, has revealed how different cellular architectures can contribute to organisational properties of an organ. Using high-resolution 3D image datasets, networks of cellular interactions in a diverse range of hypocotyls and shoot apical meristems were generated. The topological analysis of these networks revealed previously undescribed links between cellular structures at a global scale, and various organ functions.

6.2 Organisational optimisation in the hypocotyl and SAM

In the hypocotyls of some ecotypes of *Arabidopsis thaliana*, cellular network analysis using betweenness centrality identified the presence of a topological 'shortcut' through the epidermis, which was subsequently confirmed to have a role in the longitudinal, non-specific bulk-flow of molecules (Jackson et al., 2017b). This organisational property, as with all patterning in plant tissues, is a result of coordinated cell division and expansion, decreasing the length of paths specifically through atrichoblast cells.

Though also controlled by cell division and growth, the opposite organisational phenomenon is observed in the shoot apical meristem. In the meristem, cells divide using the cell wall with smallest area, which tends to maximise path length through

the daughter cells. This reduces the capacity for any specific set of cells to be preferentially involved in transport processes across the SAM.

Whilst the hypocotyl epidermis is optimised for global transport efficiency, the shoot apical meristem is counter-optimised for this organ-wide property, and highly inefficient. This is however not without benefits, as a reduction in the transport efficiency of a network generally increases robustness of the system to damage (Latora and Marchiori, 2001) (Boccaletti et al., 2006). These two opposite organisational strategies are features that have advantages for specific organ function. The hypocotyl, as the embryonic stem, has increased transport capacity to move resources throughout the plant, while the meristem, situated close to the top of the plant and at high risk of herbivory, is notably fault-tolerant.

6.3 Exploring cellular organisation in other plant tissues

It stands to reason that if novel structure-function relationships can be identified in the hypocotyl and meristem using analysis of cellular networks, that this approach could uncover interesting properties in other plant organs. Other organs may also employ a similar strategy of using bottom-up rules to generate cellular architectures with useful global features. Amongst others, the leaf and the root meristem are two organs in which the analysis of cellular organisation may be of interest.

In the leaf epidermis, cell shape and size is highly irregular, and similar to ‘puzzle-pieces’ in appearance (Zhang et al., 2011) (Jacques et al., 2014). This cell geometry is controlled in *Arabidopsis* by genes containing the Arp2/3 complex, allowing

protrusion of cell wall lobes (Li et al., 2003). During development of the leaf, continual asymmetric divisions in epidermal cells result in unequally sized daughter cells, driving variability in cell size (Jakoby and Schnittger, 2004). Additionally, stomata are interspersed between cells at regular intervals, arising from further asymmetric cell division of pavement cells, controlled by the gene *TOO MANY MOUTHS* (Nadeau and Sack, 2002).

Whilst the interlocking protrusions in pavement cells are thought to enhance mechanical stability of the leaf as a whole (Jacques et al., 2014), there is no clear understanding of how leaf cell organisation affects leaf function. It is possible that features of cell patterning in this organ, as in the hypocotyl and meristem, may be advantageous for the leaf's role in the capture of light and localised generation of sugars (Smith et al., 1997). Imaging this tissue in 3D at cellular resolution, and extraction and analysis of the cellular connectivity network may reveal links between the highly specific nature of leaf structure, and its function. Analysing the leaf epidermis in its native 3D context could also uncover organisational relationships between the epidermal layer and underlying cells.

While the shoot apical meristem is the source of all above ground tissue plants, the root meristem is responsible for continued below ground root growth (Dolan et al., 1993). The root meristem consists of one initial cell for every cell file, which divides to produce a daughter cell undergoes further divisions before differentiation and elongation, along with a daughter cell to replace itself, and its meristematic activity (Ioio et al., 2008). Signalling from the quiescent centre, near the tip of the root, acts

to maintain this activity by repressing differentiation in meristem cells (van den Berg et al., 1997).

Gradients of auxins (Grieneisen et al., 2007), cytokinins (Werner et al., 2001) and gibberellins (Ubeda-Tomás et al., 2009) each determine the size and structure of the root tip and meristem, whilst simultaneously inducing and suppressing root growth. The patterns of cells on which these plant hormones operate are likely to influence their behaviour, and extraction of cellular interaction networks, along with network analysis, may reveal unknown organisational properties of root cells that contribute to their regulatory function. As in the shoot apical meristem, this type of analysis may shed light on the enduring question of how cell division and cell differentiation is balanced in the root to ensure continued growth (Fisher and Sozzani, 2016) (Di Mambro and Sabatini, 2018).

6.4 Functional annotation of cellular connectivity networks

Analysis throughout this work has focused mainly on purely structural cellular connectivity networks. In cases where more information is available about nodes or edges, for example the size of connecting cell wall area representing a cellular interaction, it is possible to annotate a network. This constitutes a weighted network, and results in bias for edges with high values during the calculation of some measures, including betweenness centrality and random walk centrality (Newman, 2018). Though annotating network edges with shared cell wall area to generate weighted networks did not aid in analysis of the hypocotyl (Section 4.2.4), other types of network annotation may prove more useful.

Molecules, including chemical signals, can move through cells using the symplastic pathway, which is essentially an interconnected network of cell cytoplasm through gaps in cell walls, or plasmodesmata (Roberts and Oparka, 2003). Since cellular networks can be used to model the potential paths that molecules might take through a multicellular system (Figure 4.9) (Jackson et al., 2017a), if data on localisation of plasmodesmata between cells in tissues was available, this would represent a valid network annotation. Plasmodesmata at particular cell-cell interfaces can be identified using confocal microscopy of samples, with propidium iodide to stain cell walls, along with fluorescent-labelled members of the Plasmodesmata-located Protein 1 gene family (Bayer et al., 2008) (Fitzgibbon et al., 2013). This approach can be used to count plasmodesmata at cell interfaces, which could be added as a weighting to cellular connectivity network edges.

Plasmodesmata in the context of modelling processes in cellular connectivity networks are of particular interest, as their distributions across physically connected cells in tissues are not uniform (Fitzgibbon et al., 2013). Development of plasmodesmata occurs in two stages, where primary plasmodesmata formed during cytokinesis, acting as a bridge between cytoplasm in the daughter cells, while secondary plasmodesmata are formed between specific pre-existing cells (Ehlers and Kollmann, 2001). Graph-theoretic measurements of possible symplastic molecular flow through plasmodesmata using annotated networks would therefore be biased towards cellular interactions with high numbers of cytosolic bridges,

potentially revealing additional features of cellular organisation in tissues than using cellular connectivity alone.

Additionally, plants have the ability to up- or down-regulate symplastic flow, using the reversible deposition of callose at plasmodesmata junctions, which regulates their permeability (Zavaliev et al., 2011). This dynamic opening and closing of plasmodesmata, provides the opportunity to study the capacity for signal transduction control in plant cellular networks (Liu et al., 2011). The effect of allowing and disallowing information transport through certain paths on the whole multicellular system could be examined using variably weighted cellular connectivity networks. Through this process, the potential capacity for control in plant tissues is enormous, theoretically allowing multicellular plant systems to perform complex computations with chemical agents.

Though of key importance, the capacity for regulation of cytoplasmic flow is not limited to the functions of plasmodesmata. In many examples, membrane-spanning proteins that link adjacent cells can transport specific molecules between cells.

Of particular interest is the flow of auxin throughout plant tissues, controlled by a class of proteins known as the PIN family (Petrášek and Friml, 2009). PINs are responsible for the directional flux of auxin, and are often situated between specific polar cell-cell interfaces (Wiśniewska et al., 2006). Through their highly controlled positioning, PIN proteins play roles in controlling many auxin-mediated developmental processes in various organs (Benková et al., 2003) (Blilou et al.,

2005). By using cell wall staining and tagged PINs to identify cellular localisation in confocal microscopy (Wiśniewska et al., 2006), a directional cellular network weighted with relative numbers of transporters between adjacent cells could be constructed. This directional network could be used to model identify paths of auxin transport throughout tissues at cellular resolution, potentially highlighting how global cellular organisation contributes to this process.

6.5 Normalisation of topological measurements of cellular connectivity

Some graph theory measurements are more suited to applications in cellular connectivity networks than others. There are limitations to be aware of when using network science algorithms, even in the relatively simple centrality measurements that were used to explore plant tissues in this work. In both betweenness centrality and random walk centrality, a standard normalisation was applied, which accounts for the size of the network, specifically multiplying the number of paths each node lies on by the number of node pairs in the system (Brandes, 2001) (Hagberg et al., 2008) (Section 2.4.3). Analysis of 3D organ models showed that increasing the number of cells in an organ influenced the averages and the variability of these measures (Section 3.2.1), indicating that this normalisation is not appropriate for spatially embedded 3D systems. Because of this observation, in the case of further cellular connectivity networks used, the analysis of real tissues was constrained to networks with similar numbers of nodes. However, this theoretically restricts the comparison of organs with drastically different sizes, perhaps preventing further insights into cellular structure and function relationships.

Though theoretically, any graph can be made using nodes embedded in 3D Euclidean space, the size and shape restrictions of cells do not allow for certain archetypal network layouts. One such common network structure reported repeatedly across diverse fields is the scale-free network, defined by the presence of few nodes with many edges, known as hubs, along with most nodes having few edges (Barabási and Albert, 1999). The discovery of the scale-free network architecture across diverse systems was in part responsible for the explosion of network science as a field (Barabási, 2009), and it is possible that many network science analysis algorithms were developed with this type of network in mind, making them less suitable in other network layouts (Broido and Clauset, 2018). Constraints on cell shape and size in tissues do not allow for realistic cellular connectivity networks with scale-free properties, possibly making certain analyses less powerful, or less suitable, when used to explore organ-wide cellular organisation. Looking forward, it may be possible to develop a more suitable global centrality normalisation, for the exclusive purpose of measuring connectivity in 3D spatially embedded cellular systems. This normalisation would have to take the topological consequences of cells tessellating in 3D space into account.

6.6 Inspirations for further cellular network analysis

As well as in the biological sciences, particularly in neuroscience and genomics, interdisciplinary research involving network science have resulted in advancements in the fields of sociology, urban planning and computer science, amongst others (Lazer et al., 2009) (Derrible and Kennedy, 2011) (Sharma and Singh, 2018). Any system that can be described using the interaction of multiple entities can potentially

be explored using graph theoretic approaches, whether these entities are molecules, people or vehicles, or something else entirely. Due of the level of abstraction involved in representing a system of interacting components into a network, many algorithms used to analyse networks in diverse fields of study may be applicable to cellular connectivity networks. Similarly to how betweenness and random walk centrality identified novel features of the hypocotyl and shoot apical meristem, other network measurements have the potential to reveal organisational properties in multicellular tissues.

Network science is a fast-moving field, and new algorithms for identifying interesting features and key components of complex networks are published regularly. One algorithm that may be of interest for analysis of cellular connectivity networks is ‘transmission centrality’ (Zhang et al., 2018). This centrality identifies highly influential nodes, likely to make significant contributions to the spread of a transmissible element across a network. The algorithm uses an adaptation of the classic SIR model employed in epidemiology, which is used to predict spread of disease in a population, where individuals are susceptible (S), before becoming infected (I), and subsequently recovered or removed (R) with variable rates (Kermack and Mckendrick, 1927) (Hethcote, 2000). In transmission centrality, this processes is simulated in a network by selecting random starting nodes that become infected, and with certain probability, infect their neighbours, spreading the infected status throughout the graph.

The transmission centrality algorithm shares similarities with random walk centrality, whereby spreading of both random walkers and disease is a stochastic process that does not require prior knowledge of the network. However, in contrast to random walk centrality, the recovered or removed state of nodes after infection prevents backtracking of agents in transmission centrality, resulting in different graph-traversal dynamics. Transmission centrality may be a good alternative model for potential diffusive processes across a cellular connectivity network, and useful for the identification of cells with a large influence over spreading of information in the system. Whether this measure provides additional analytical capacity over random walk centrality, and other network measurements, can be established by determining the extent of correlation between topological measurements in cells within the same cellular network, as carried out in this work (Sections 4.2.8 and 5.2.2).

Another potentially relevant measure of global topology is navigation centrality, used to explore connectivity between regions of the brain, in coarse-grained MRI-generated networks (Seguin et al., 2018). Navigation centrality was developed to examine how similar shortest paths between nodes, with minimal node traversal, are to geometrically determined paths.

To calculate navigation centrality, as in other global centrality measurements, paths are identified between all pairs of cells in a network. These paths are determined using only local geometric information about neighbouring cells, where on the route from one cell to another, the closest node to the target node in 3D space is traversed repeatedly, until the target node is reached. Paths between some pairs of cells are

never identified, if during the path-identifying algorithm, no neighbouring node is closer to the target than itself. Navigation centrality for every node in a network is defined as the number of times a node is traversed in these geometrically determined paths.

In coarse-grained brain networks, though navigation centrality uses only local cell information, it shares similar features with betweenness centrality, which requires global knowledge of the network layout in its calculation (Seguin et al., 2018). As it is difficult to propose a biologically plausible mechanism by which betweenness centrality can be calculated by cells in tissues, navigation centrality may represent a more suitable algorithm than betweenness centrality for identifying paths through a cellular network, especially when geometric distance between cells is a relevant feature of the process being modelled.

As well as measurements of centrality, other network science methods can be used to identify interesting features of a given graph. In the fields of electronic engineering, ecology and biochemistry, distributions of network motifs are often identified to gain a deeper understanding of network structure (Shen-Orr et al., 2002). Motifs are common repeated units, seen repeatedly within and across networks, and can be identified by extracting subsamples of a network with different numbers of nodes, while counting the recurrence of observed patterns.

Cellular connectivity networks each have particular organisations, potentially linked to their biological function. Identification of motifs in cellular networks could be used to

understand how design principles in small subsections of a tissue or organ contribute to the organisation of the system as a whole (Smoly et al., 2017). Though not suitable for large networks, due to the computational time taken to iteratively sample a network to find repeated patterns, algorithms for this process are becoming faster and more efficient, and would be sufficient to identify motifs in small cellular connectivity networks of around 1000 nodes in the order of days, on a modern computer (Lin et al., 2017).

6.7 Applications to animal tissues

With results indicating that that the organisation of cells within tissues may contribute to organ function in plant systems (Section 4.2), it is possible that the same is true in animal systems. However, it is worth noting that unlike in plant organs, the focus of this work, cells in animal systems can move, using the continuous rearrangement of intracellular cytoskeletal elements to traverse their environment (Pollard, 2003). This means that in animal organs, adjacency between cells can vary throughout development, even without cell division and growth (Wallingford et al., 2002). To abstract cellular connectivity across an animal tissue, rather than an invariant structural network, it may be more appropriate to represent cellular interactions over time as a temporal network.

In a temporal network, edges between nodes can be temporary, and contain information about the time in which they took place (Holme, 2015). Though most frequently used in social sciences to model human proximity in social situations, temporal networks have been used in the biological sciences to link regions of brain

activity over time using fMRI scanning (Cole et al., 2014). Using live confocal microscopy imaging of animal organs (Marques et al., 2015), and recent developments in computer vision (Weinzaepfel et al., 2015) (Murata et al., 2018) to formulate a protocol to map temporal cell interactions, will enable the construction of temporal cellular interaction networks.

The availability of data sets incorporating temporal information has historically been low, though this availability is increasing, driven by more recent advances in the technologies enabling their capture and storage (Santoro et al., 2011) (Wu et al., 2017). Because of this, algorithms for the analysis of temporal networks are at a fairly early stage in comparison to methods available for the analysis of static, structural networks (Holme, 2015). However, methods exist to measure aspects of network evolution over time, which would enable the quantification of cellular organisation during different stages of development (Holme, 2015). It is also possible to measure the stochasticity of interactions made over time by calculating the entropy of a temporal network (Takaguchi et al., 2011). In terms of cellular connectivity over time, monitoring network entropy would allow deterministic natures of particular developmental organisational processes to be quantified.

6.8 Potential for optimal organ design

Small-scale models of 3D organs, named organoids, have recently been developed to allow previously technically challenging *in vitro* human organ research (Fatehullah et al., 2016). These organoids have similar properties to the organs they are modelled on, and in some cases can even be used in transplantation to replace

human tissues (Shamir and Ewald, 2014). Additionally, the capacity to fabricate 3D organs with the use of what is essentially a cellular 3D printer is an emerging technology (Mironov et al., 2003) (Mironov et al., 2011), enabling the construction of increasingly complex biological tissues in a high-throughput manner.

Applying the knowledge that the structure of these tissues affects their function, going forward it may be possible to construct biological tissues that are improved in specific functions, or even entirely new organ functions, by controlling cell organisation. As synthetic biology advances as a field, the notion that particular cell arrangements can give rise to global tissue properties may help to inform the design of multicellular tissues with desired functionality (Markson and Elowitz, 2014) (Black et al., 2017).

A theoretical morphospace for synthetic organ design has been postulated, suggesting that much of what is possible with a multicellular tissue is not represented by the myriad of forms observed in the natural world (Ollé-Vila et al., 2016). Areas identified where the full range of organ possibilities is yet to be explored include developmental complexity of a system, along with its capacity for the control of information flow. These features can be quantified using a network science framework for exploring the functional outputs of cell organisation. Network analysis could be used to address the possible reasons why certain multicellular designs are not naturally present, or alternatively to guide the creation of models and real synthetic tissues with previously unobserved properties.

6.9 Concluding remarks

The work undertaken in this thesis represents a fundamental step towards understanding the links between organ structure and function at the cellular level. Future advancements in imaging, network science theory, and computational power, will enable further analysis of this relationship, through high-quality, data-rich microscopy, and increasingly powerful, appropriate analysis algorithms.

APPENDICIES

Appendix 1 – Synopsis and contributions to incorporated elements from the paper:

JACKSON, M. D. B., DURAN-NEBREDA, S., BASSEL, G. W. (2017). Network-based approaches to quantify multicellular development. *Journal of The Royal Society Interface,* 14, 20170484.

Synopsis

In this review article, the multicellular structures of diverse organs are discussed, along with the functional properties conferred by these structures. Though there are many examples of how local cell signalling is involved in the development of these multicellular structures, less is known about organ-wide cell patterning and its formation. Less still is understood about how global organisational properties of tissues play a role in organ function.

To uncover links between structure and function at an organ-wide scale, a conceptual framework for the quantification of global cellular patterning is suggested. Through abstraction of cell interactions across a tissue into a network, and subsequent network analyses, cellular organisation can be discretised, enabling comparisons between patterning across different organs, species and models.

The thorough framework to quantify multicellular patterning outlined in this review allows a more nuanced understanding of higher-order organisational properties in organs. This in turn provides the opportunity to explore constraints on the evolution of

cellular organisation, potentially guiding the design of novel organ and tissue structures with specific functions.

Contributions relating to the thesis

M. D. B. J created figures 3.1, 3.2 and 3.3, which were reproduced from this review article.

Appendix 2 – Synopsis and contributions to incorporated elements from the paper:

JACKSON, M. D., XU, H., DURAN-NEBREDA, S., STAMM, P. & BASSEL, G. W. (2017). Topological analysis of multicellular complexity in the plant hypocotyl. *Elife,* 6, e26023.

Synopsis

In this research article, the structure-function relationships of cell organisation in the hypocotyls of diverse plant species and genetic backgrounds are explored. This is achieved using a network science framework, through which cellular connectivity in the hypocotyl is abstracted into a network, allowing the organisational properties of the multicellular organ to be quantified.

A key feature of this article is the discovery of transport conduits along the *Arabidopsis thaliana* hypocotyl epidermis. Network analysis, using a global measure of cell connectivity, identified paths likely to be involved in transport processes along atrichoblast cell files, in some *A. thaliana* ecotypes. This functional prediction suing structural network properties was confirmed to play a role in the bulk transport of molecules through the hypocotyl epidermis. Variations in this global organisational property between ecotypes were reflected by differential compartmentalisation of bulk transport along epidermal cell files.

Using the quantification of mutant cell organisation, the contribution of gene activity to particular hypocotyl cell patterning features was identified. This has implications for the understanding of cell organisation control at higher-order scale, allowing organ-wide principles of tissue construction to be established.

Contributions relating to the thesis

M. D. B. J created figures 4.2 – 4.18 (excluding figure 4.9), which were reproduced from this article.

Creation of figure 4.9 was a collaborative effort from M. D. B. J., S. D.-N., and G. W. B., and data for this figure was collected by S. D.-N.

Appendix 3 – Synopsis and contributions to incorporated elements from the paper:

JACKSON, M. D. B., DURAN-NEBREDA, S., KIERZKOWSKI, D., STRAUSS, S., XU, H., LANDREIN, B., HAMANT, O., SMITH, R. S., JOHNSTON, I. G. & BASSEL, G., W. 2018. Global Topological Order Emerges through Local Mechanical Control of Cell Divisions in the *Arabidopsis* Shoot Apical Meristem. *Cell Systems*, 8, 1-13.

Synopsis

In this research article, the role of cell position and division in establishing shoot apical meristem (SAM) organisation is examined. Through a combination of time-lapse 3D imaging and computational analyses, cellular networks of the developing *A. thaliana* meristem are captured.

Topological and geometric analysis of these networks is used to determine factors that influence cell division, both in terms of the onset of mitosis and the subsequent division plane between daughter cells. While results show that geometric factors are more effective at predicting when a cell would divide, both geometric and topological features can be used to determine the location of division planes, given the context of a cell pre-division. A key finding is that new division planes of the minimum possible size (Errera's rule) also minimise the random walk centrality of the resulting daughter cells.

This is evidence for local division rules coordinating the tissue-scale organisation of the *A. thaliana* SAM, which in the context of cellular communication, is particularly robust to perturbations through cell damage. Further to this, analysis of the *KATANIN* mutant shows how a breakdown in mechanical cell interactions has consequences

for cell geometry, which influences the SAMs ability to maintain the same global cell architecture.

Contributions relating to the thesis

M. D. B. J created figures 5.3 – 5.5, 5.7 and 5.9 – 5.20, which were reproduced and adapted from this article.

LIST OF REFERENCES

ADAMOWSKI, M. & FRIML, J. 2015. PIN-dependent auxin transport: action, regulation, and evolution. *The Plant Cell*, tpc. 114.134874.

AIDA, M., BEIS, D., HEIDSTRA, R., WILLEMSEN, V., BLILOU, I., GALINHA, C., NUSSAUME, L., NOH, Y.-S., AMASINO, R. & SCHERES, B. 2004. The PLETHORA Genes Mediate Patterning of the Arabidopsis Root Stem Cell Niche. *Cell,* 119**,** 109-120.

ALIVISATOS, A. P., CHUN, M., CHURCH, G. M., GREENSPAN, R. J., ROUKES, M. L. & YUSTE, R. 2012. The brain activity map project and the challenge of functional connectomics. *Neuron,* 74**,** 970-974.

APLIN, A. E., HOWE, A. K. & JULIANO, R. L. 1999. Cell adhesion molecules, signal transduction and cell growth. *Current opinion in cell biology,* 11**,** 737-744.

ARENDT, D., HAUSEN, H. & PURSCHKE, G. 2009. The 'division of labour' model of eye evolution. *Philosophical Transactions of the Royal Society B: Biological Sciences,* 364**,** 2809-2817.

ARNOLD, S. J. & ROBERTSON, E. J. 2009. Making a commitment: cell lineage allocation and axis patterning in the early mouse embryo. *Nature reviews Molecular cell biology,* 10**,** 91.

BAKER, D. & SALI, A. 2001. Protein structure prediction and structural genomics. *Science,* 294**,** 93-96.

BALL, P. 2013. In retrospect: On Growth and Form. *Nature,* 494**,** 32.

BARABÁSI, A.-L. 2009. Scale-free networks: a decade and beyond. *science,* 325**,** 412-413.

BARABÁSI, A.-L. 2016. *Network science*, Cambridge university press.

BARABÁSI, A.-L. & ALBERT, R. 1999. Emergence of scaling in random networks. *science,* 286**,** 509-512.

BASCOMPTE, J. 2007. Networks in ecology. *Basic and Applied Ecology,* 8**,** 485-490.

BASSEL, G. W., STAMM, P., MOSCA, G., DE REUILLE, P. B., GIBBS, D. J., WINTER, R., JANKA, A., HOLDSWORTH, M. J. & SMITH, R. S. 2014. Mechanical constraints imposed by 3D cellular geometry and arrangement modulate growth patterns in the Arabidopsis embryo. *Proceedings of the National Academy of Sciences*, 201404616.

BAYER, E., THOMAS, C. & MAULE, A. 2008. Symplastic domains in the Arabidopsis shoot apical meristem correlate with PDLP1 expression patterns. *Plant Signaling & Behavior,* 3**,** 853-855.

BEAN, G. J., MARKS, M. D., HÜLSKAMP, M., CLAYTON, M. & CROXDALE, J. L. 2002. Tissue patterning of Arabidopsis cotyledons. *New Phytologist,* 153**,** 461-467.

BECKER, J. & WITTMANN, C. 2018. From systems biology to metabolically engineered cells—an omics perspective on the development of industrial microbes. *Current opinion in microbiology,* 45**,** 180-188.

BELL, G., HEY, T. & SZALAY, A. 2009. Beyond the data deluge. *Science,* 323**,** 1297-1298.

BENKOVÁ, E., MICHNIEWICZ, M., SAUER, M., TEICHMANN, T., SEIFERTOVÁ, D., JÜRGENS, G. & FRIML, J. 2003. Local, efflux-dependent auxin gradients as a common module for plant organ formation. *Cell,* 115**,** 591-602.

BERGMANN, D. C. & SACK, F. D. 2007. Stomatal development. *Annu. Rev. Plant Biol.,* 58**,** 163-181.

BESSON, S. & DUMAIS, J. 2011. Universal rule for the symmetric division of plant cells. *Proceedings of the National Academy of Sciences,* 108**,** 6294-6299.

BICHET, A., DESNOS, T., TURNER, S., GRANDJEAN, O. & HÖFTE, H. 2001. BOTERO1 is required for normal orientation of cortical microtubules and anisotropic cell expansion in Arabidopsis. *The Plant Journal,* 25**,** 137-148.

BISHOPP, A., LEHESRANTA, S., VATÉN, A., HELP, H., EL-SHOWK, S., SCHERES, B., HELARIUTTA, K., MÄHÖNEN, A. P., SAKAKIBARA, H. & HELARIUTTA, Y. 2011. Phloem-transported cytokinin regulates polar auxin transport and maintains vascular pattern in the root meristem. *Current Biology,* 21**,** 927-932.

BLACK, J. B., PEREZ-PINERA, P. & GERSBACH, C. A. 2017. Mammalian synthetic biology: engineering biological systems. *Annual review of biomedical engineering,* 19**,** 249-277.

BLILOU, I., XU, J., WILDWATER, M., WILLEMSEN, V., PAPONOV, I., FRIML, J., HEIDSTRA, R., AIDA, M., PALME, K. & SCHERES, B. 2005. The PIN auxin efflux facilitator network controls growth and patterning in Arabidopsis roots. *Nature,* 433**,** 39.

BOCCALETTI, S., LATORA, V., MORENO, Y., CHAVEZ, M. & HWANG, D.-U. 2006. Complex networks: Structure and dynamics. *Physics reports,* 424**,** 175-308.

BOWMAN, J. L. & ESHED, Y. 2000. Formation and maintenance of the shoot apical meristem. *Trends in plant science,* 5**,** 110-115.

BRAND, U., FLETCHER, J. C., HOBE, M., MEYEROWITZ, E. M. & SIMON, R. 2000. Dependence of stem cell fate in Arabidopsis on a feedback loop regulated by CLV3 activity. *Science,* 289**,** 617-619.

BRANDES, U. 2001. A faster algorithm for betweenness centrality. *Journal of mathematical sociology,* 25**,** 163-177.

BREDE, M. 2010. Coordinated and uncoordinated optimization of networks. *Physical Review E,* 81**,** 066104.

BREZNY, R. & GREEN, D. J. 1990. The effect of cell size on the mechanical behavior of cellular materials. *Acta metallurgica et materialia,* 38**,** 2517-2526.

BRODAL, P. 2004. *The central nervous system: structure and function*, Oxford University Press.

BROHEE, S. & VAN HELDEN, J. 2006. Evaluation of clustering algorithms for protein-protein interaction networks. *BMC bioinformatics,* 7**,** 488.

BROIDO, A. D. & CLAUSET, A. 2018. Scale-free networks are rare. *arXiv preprint arXiv:1801.03400*.

BROSNAN, C. A. & VOINNET, O. 2011. Cell-to-cell and long-distance siRNA movement in plants: mechanisms and biological implications. *Current opinion in plant biology,* 14**,** 580-587.

BRUEX, A., KAINKARYAM, R. M., WIECKOWSKI, Y., KANG, Y. H., BERNHARDT, C., XIA, Y., ZHENG, X., WANG, J. Y., LEE, M. M. & BENFEY, P. 2012. A gene regulatory network for root epidermis cell differentiation in Arabidopsis. *PLoS genetics,* 8**,** e1002446.

BRUNKARD, J. O., RUNKEL, A. M. & ZAMBRYSKI, P. C. 2015. The cytosol must flow: intercellular transport through plasmodesmata. *Current opinion in cell biology,* 35**,** 13-20.

BULLMORE, E. & SPORNS, O. 2009. Complex brain networks: graph theoretical analysis of structural and functional systems. *Nature Reviews Neuroscience,* 10**,** 186.

BULLMORE, E. T. & BASSETT, D. S. 2011. Brain graphs: graphical models of the human brain connectome. *Annual review of clinical psychology,* 7**,** 113-140.

BURCH-SMITH, T. M., STONEBLOOM, S., XU, M. & ZAMBRYSKI, P. C. 2011. Plasmodesmata during development: re-examination of the importance of primary, secondary, and branched plasmodesmata structure versus function. *Protoplasma,* 248**,** 61-74.

BUSKE, P., GALLE, J., BARKER, N., AUST, G., CLEVERS, H. & LOEFFLER, M. 2011. A comprehensive model of the spatio-temporal stem cell and tissue organisation in the intestinal crypt. *PLoS computational biology,* 7**,** e1001045.

BUSS, L. W. 2014. *The evolution of individuality*, Princeton University Press.

BUTTERY, N. J., ROZEN, D. E., WOLF, J. B. & THOMPSON, C. R. 2009. Quantification of social behavior in D. discoideum reveals complex fixed and facultative strategies. *Current Biology,* 19**,** 1373-1377.

BYRNE, M. E., BARLEY, R., CURTIS, M., ARROYO, J. M., DUNHAM, M., HUDSON, A. & MARTIENSSEN, R. A. 2000. Asymmetric leaves1 mediates leaf patterning and stem cell function in Arabidopsis. *Nature,* 408**,** 967.

CANALES, J., HENRIQUEZ-VALENCIA, C. & BRAUCHI, S. 2018. The integration of electrical signals originating in the root of vascular plants. *Frontiers in plant science,* 8**,** 2173.

CARROLL, S. B. 2000. Endless forms: the evolution of gene regulation and morphological diversity. *Cell,* 101**,** 577-580.

CARROLL, S. B. 2001. Chance and necessity: the evolution of morphological complexity and diversity. *Nature,* 409**,** 1102.

CHALFIE, M., SULSTON, J. E., WHITE, J. G., SOUTHGATE, E., THOMSON, J. N. & BRENNER, S. 1985. The neural circuit for touch sensitivity in Caenorhabditis elegans. *Journal of Neuroscience,* 5**,** 956-964.

CHIANG, A.-S., LIN, C.-Y., CHUANG, C.-C., CHANG, H.-M., HSIEH, C.-H., YEH, C.-W., SHIH, C.-T., WU, J.-J., WANG, G.-T. & CHEN, Y.-C. 2011. Three-dimensional reconstruction of brain-wide wiring networks in Drosophila at single-cell resolution. *Current Biology,* 21**,** 1-11.

CHO, H., DANG, T. V. T. & HWANG, I. 2017. Emergence of plant vascular system: roles of hormonal and non-hormonal regulatory networks. *Current opinion in plant biology,* 35**,** 91-97.

CHOI, W.-G., TOYOTA, M., KIM, S.-H., HILLEARY, R. & GILROY, S. 2014. Salt stress-induced Ca2+ waves are associated with rapid, long-distance root-to-shoot signaling in plants. *Proceedings of the National Academy of Sciences,* 111**,** 6497-6502.

CHOI, W. G., MILLER, G., WALLACE, I., HARPER, J., MITTLER, R. & GILROY, S. 2017. Orchestrating rapid long‐distance signaling in plants with Ca2+, ROS and electrical signals. *The Plant Journal,* 90**,** 698-707.

CHUANG, H.-Y., HOFREE, M. & IDEKER, T. 2010. A decade of systems biology. *Annual review of cell and developmental biology,* 26**,** 721-744.

CHUANG, H. Y., LEE, E., LIU, Y. T., LEE, D. & IDEKER, T. 2007. Network‐based classification of breast cancer metastasis. *Molecular systems biology,* 3**,** 140.

COCK, J. M., STERCK, L., ROUZÉ, P., SCORNET, D., ALLEN, A. E., AMOUTZIAS, G., ANTHOUARD, V., ARTIGUENAVE, F., AURY, J.-M. & BADGER, J. H. 2010. The Ectocarpus genome and the independent evolution of multicellularity in brown algae. *Nature,* 465**,** 617.

CODLING, E. A., PLANK, M. J. & BENHAMOU, S. 2008. Random walk models in biology. *Journal of the Royal Society Interface,* 5**,** 813-834.

COLE, M. W., BASSETT, D. S., POWER, J. D., BRAVER, T. S. & PETERSEN, S. E. 2014. Intrinsic and task-evoked network architectures of the human brain. *Neuron,* 83**,** 238-251.

COOPER, G. A. & WEST, S. A. 2018. Division of labour and the evolution of extreme specialization. *Nature ecology & evolution***,** 1.

COUSO, J. P., BISHOP, S. A. & ARIAS, A. M. 1994. The wingless signalling pathway and the patterning of the wing margin in Drosophila. *Development,* 120**,** 621-636.

DE BOER, A. & VOLKOV, V. 2003. Logistics of water and salt transport through the plant: structure and functioning of the xylem. *Plant, Cell & Environment,* 26**,** 87-101.

DE LAS RIVAS, J. & FONTANILLO, C. 2010. Protein–Protein Interactions Essentials: Key Concepts to Building and Analyzing Interactome Networks. *PLoS Computational Biology,* 6**,** e1000807.

DE REUILLE, P. B., ROUTIER-KIERZKOWSKA, A.-L., KIERZKOWSKI, D., BASSEL, G. W., SCHÜPBACH, T., TAURIELLO, G., BAJPAI, N., STRAUSS, S., WEBER, A. & KISS, A. 2015. MorphoGraphX: a platform for quantifying morphogenesis in 4D. *Elife,* 4**,** e05864.

DE ROBERTIS, E. 2008. Evo-devo: variations on ancestral themes. *Cell,* 132**,** 185-195.

DE RYBEL, B., ADIBI, M., BREDA, A. S., WENDRICH, J. R., SMIT, M. E., NOVÁK, O., YAMAGUCHI, N., YOSHIDA, S., VAN ISTERDAEL, G. & PALOVAARA, J. 2014. Integration of growth and patterning during vascular tissue formation in Arabidopsis. *Science,* 345**,** 1255215.

DEL BENE, F., TESSMAR-RAIBLE, K. & WITTBRODT, J. 2004. Direct interaction of geminin and Six3 in eye development. *Nature,* 427**,** 745.

DERRIBLE, S. & KENNEDY, C. 2011. Applications of graph theory and network science to transit network design. *Transport reviews,* 31**,** 495-519.

DI LAURENZIO, L., WYSOCKA-DILLER, J., MALAMY, J. E., PYSH, L., HELARIUTTA, Y., FRESHOUR, G., HAHN, M. G., FELDMANN, K. A. & BENFEY, P. N. 1996. The SCARECROW gene regulates an asymmetric cell division that is essential for generating the radial organization of the Arabidopsis root. *Cell,* 86**,** 423-433.

DI MAMBRO, R. & SABATINI, S. 2018. Developmental Analysis of Arabidopsis Root Meristem. *Root Development.* Springer.

DISSMEYER, N., WEIMER, A. K., PUSCH, S., DE SCHUTTER, K., KAMEI, C. L. A., NOWACK, M. K., NOVAK, B., DUAN, G.-L., ZHU, Y.-G. & DE VEYLDER, L. 2009. Control of cell proliferation, organ growth, and DNA damage response operate independently of dephosphorylation of the Arabidopsis Cdk1 homolog CDKA; 1. *The Plant Cell,* 21**,** 3641-3654.

DOLAN, L. & DAVIES, J. 2004. Cell expansion in roots. *Current opinion in plant biology,* 7**,** 33-39.

DOLAN, L., JANMAAT, K., WILLEMSEN, V., LINSTEAD, P., POETHIG, S., ROBERTS, K. & SCHERES, B. 1993. Cellular organisation of the Arabidopsis thaliana root. *Development,* 119**,** 71-84.

DU, Q., KAWABE, Y., SCHILDE, C., CHEN, Z.-H. & SCHAAP, P. 2015. The evolution of aggregative multicellularity and cell–cell communication in the Dictyostelia. *Journal of molecular biology,* 427**,** 3722-3733.

DU, Q. & WANG, D. 2003. Tetrahedral mesh generation and optimization based on centroidal Voronoi tessellations. *International journal for numerical methods in engineering,* 56**,** 1355-1373.

DU, Q. & WANG, D. 2005. Anisotropic centroidal Voronoi tessellations and their applications. *SIAM Journal on Scientific Computing,* 26**,** 737-761.

DUNCAN, M. W. 2007. Omics and its 15 minutes. SAGE Publications.

DUNN, O. J. 1961. Multiple comparisons among means. *Journal of the American statistical association,* 56**,** 52-64.

DUNNE, J. A., WILLIAMS, R. J. & MARTINEZ, N. D. 2002. Network structure and biodiversity loss in food webs: robustness increases with connectance. *Ecology letters,* 5**,** 558-567.

DUPUY, L., MACKENZIE, J. & HASELOFF, J. 2010. Coordination of plant cell division and expansion in a simple morphogenetic system. *Proceedings of the National Academy of Sciences,* 107**,** 2711-2716.

DURAN-NEBREDA, S. & BASSEL, G. W. 2017a. Bridging scales in plant biology using network science. *Trends in plant science,* 22**,** 1001-1003.

DURAN-NEBREDA, S. & BASSEL, G. W. 2017b. Fluorescein Transport Assay to Assess Bulk Flow of Molecules Through the Hypocotyl in Arabidopsis thaliana. *eLIFE*.

DURAN-NEBREDA, S. & SOLÉ, R. 2015. Emergence of multicellularity in a model of cell growth, death and aggregation under size-dependent selection. *Journal of The Royal Society Interface,* 12**,** 20140982.

EHLERS, K. & KOLLMANN, R. 2001. Primary and secondary plasmodesmata: structure, origin, and functioning. *Protoplasma,* 216**,** 1.

ELLSON, J., GANSNER, E., KOUTSOFIOS, L., NORTH, S. C. & WOODHULL, G. Graphviz—open source graph drawing tools. International Symposium on Graph Drawing, 2001. Springer, 483-484.

EMMONS, S. W. 2015. The beginning of connectomics: a commentary on White et al.(1986)'The structure of the nervous system of the nematode Caenorhabditis elegans'. *Phil. Trans. R. Soc. B,* 370**,** 20140309.

ENGEL JR, J., THOMPSON, P. M., STERN, J. M., STABA, R. J., BRAGIN, A. & MODY, I. 2013. Connectomics and epilepsy. *Current opinion in neurology,* 26**,** 186.

ERDOS, P. & RÉNYI, A. 1960. On the evolution of random graphs. *Publ. Math. Inst. Hung. Acad. Sci,* 5**,** 17-60.

ERICKSON, R. O. 1986. Symplastic growth and symplasmic transport. *Plant Physiology,* 82**,** 1153-1153.

ERRERA, L. 1886. *Sur une condition fondamentale d'équilibre des cellules vivantes*.

ESCUDERO, L. M., COSTA, L. D. F., KICHEVA, A., BRISCOE, J., FREEMAN, M. & BABU, M. M. 2011. Epithelial organisation revealed by a network of cellular contacts. *Nature communications,* 2**,** 526.

EVANS, M. J., CHOI, W.-G., GILROY, S. & MORRIS, R. J. 2016. A ROS-assisted calcium wave dependent on the AtRBOHD NADPH oxidase and TPC1 cation channel propagates the systemic response to salt stress. *Plant Physiology,* 171**,** 1771-1784.

FANTES, P. 1977. Control of cell size and cycle time in Schizosaccharomyces pombe. *Journal of cell science,* 24**,** 51-67.

FANTES, P. & NURSE, P. 1977. Control of cell size at division in fission yeast by a growth-modulated size control over nuclear division. *Experimental cell research,* 107**,** 377-386.

FATEHULLAH, A., TAN, S. H. & BARKER, N. 2016. Organoids as an in vitro model of human development and disease. *Nature cell biology,* 18**,** 246.

FAULKNER, C., AKMAN, O. E., BELL, K., JEFFREE, C. & OPARKA, K. 2008. Peeking into pit fields: a multiple twinning model of secondary plasmodesmata formation in tobacco. *The Plant Cell,* 20**,** 1504-1518.

FAULKNER, C. & ROBATZEK, S. 2012. Plants and pathogens: putting infection strategies and defence mechanisms on the map. *Current opinion in plant biology,* 15**,** 699-707.

FELLE, H., HERRMANN, A., HÜCKELHOVEN, R. & KOGEL, K.-H. 2005. Root-to-shoot signalling: apoplastic alkalinization, a general stress response and defence factor in barley (Hordeum vulgare). *Protoplasma,* 227**,** 17-24.

FILIPPI, M., VAN DEN HEUVEL, M. P., FORNITO, A., HE, Y., POL, H. E. H., AGOSTA, F., COMI, G. & ROCCA, M. A. 2013. Assessment of system dysfunction in the brain through MRI-based connectomics. *The Lancet Neurology,* 12**,** 1189-1199.

FINLAY, B. L., DARLINGTON, R. B. & NICASTRO, N. 2001. Developmental structure in brain evolution. *Behavioral and Brain Sciences,* 24**,** 263-278.

FISHER, A. P. & SOZZANI, R. 2016. Uncovering the networks involved in stem cell maintenance and asymmetric cell division in the Arabidopsis root. *Current opinion in plant biology,* 29**,** 38-43.

FITZGIBBON, J., BECK, M., ZHOU, J., FAULKNER, C., ROBATZEK, S. & OPARKA, K. 2013. A Developmental Framework for Complex Plasmodesmata Formation Revealed by Large-Scale Imaging of the Arabidopsis Leaf Epidermis. *The Plant Cell Online*.

FLAGEL, L. E. & WENDEL, J. F. 2009. Gene duplication and evolutionary novelty in plants. *New Phytologist,* 183**,** 557-564.

FLEMING, A. J., MANZARA, T., GRUISSEM, W. & KUHLEMEIER, C. 1996. Fluorescent imaging of GUS activity and RT‐PCR analysis of gene expression in the shoot apical meristem. *The Plant Journal,* 10**,** 745-754.

FORGACS, G. & NEWMAN, S. A. 2005. *Biological physics of the developing embryo*, Cambridge University Press.

FORTUNE, S. 1995. Voronoi diagrams and Delaunay triangulations. *Computing in Euclidean geometry.* World Scientific.

FOX, J., WEISBERG, S., ADLER, D., BATES, D., BAUD-BOVY, G., ELLISON, S., FIRTH, D., FRIENDLY, M., GORJANC, G. & GRAVES, S. 2012. Package 'car'. *Vienna: R Foundation for Statistical Computing*.

FREEMAN, L. C. 1977. A set of measures of centrality based on betweenness. *Sociometry***,** 35-41.

GAN, X., STEGLE, O., BEHR, J., STEFFEN, J. G., DREWE, P., HILDEBRAND, K. L., LYNGSOE, R., SCHULTHEISS, S. J., OSBORNE, E. J. & SREEDHARAN, V. T. 2011. Multiple reference genomes and transcriptomes for Arabidopsis thaliana. *Nature,* 477**,** 419.

GANSEL, X., MUNOS, S., TILLARD, P. & GOJON, A. 2001. Differential regulation of the NO3- and NH4+ transporter genes AtNrt2.1 and AtAmt1.1 in Arabidopsis: relation with long-distance and local controls by N status of the plant. *Plant J,* 26**,** 143-55.

GEILFUS, C.-M. & MÜHLING, K. H. 2011. Real-time imaging of leaf apoplastic pH dynamics in response to NaCl stress. *Frontiers in Plant Science,* 2**,** 13.

GHILDIYAL, M. & ZAMORE, P. D. 2009. Small silencing RNAs: an expanding universe. *Nature Reviews Genetics,* 10**,** 94.

GIBSON, M. C., PATEL, A. B., NAGPAL, R. & PERRIMON, N. 2006. The emergence of geometric order in proliferating metazoan epithelia. *Nature,* 442**,** 1038.

GIBSON, W. T., VELDHUIS, J. H., RUBINSTEIN, B., CARTWRIGHT, H. N., PERRIMON, N., BRODLAND, G. W., NAGPAL, R. & GIBSON, M. C. 2011. Control of the mitotic cleavage plane by local epithelial topology. *Cell,* 144**,** 427-438.

GILROY, S. & JONES, D. L. 2000. Through form to function: root hair development and nutrient uptake. *Trends in plant science,* 5**,** 56-60.

GOGGIN, F. L. 2007. Plant–aphid interactions: molecular and ecological perspectives. *Current opinion in plant biology,* 10**,** 399-408.

GOMEZ-CABRERO, D., ABUGESSAISA, I., MAIER, D., TESCHENDORFF, A., MERKENSCHLAGER, M., GISEL, A., BALLESTAR, E., BONGCAM-RUDLOFF, E., CONESA, A. & TEGNÉR, J. 2014. Data integration in the era of omics: current and future challenges. BioMed Central.

GORELICK, F. S., PANDOL, S. & JAMIESON, J. D. 2018. Structure-function relationships in the pancreatic acinar cell. *Physiology of the Gastrointestinal Tract (Sixth Edition).* Elsevier.

GRANDJEAN, O., VERNOUX, T., LAUFS, P., BELCRAM, K., MIZUKAMI, Y. & TRAAS, J. 2004. In vivo analysis of cell division, cell growth, and differentiation at the shoot apical meristem in Arabidopsis. *The Plant Cell,* 16**,** 74-87.

GRIENEISEN, V. A., XU, J., MARÉE, A. F., HOGEWEG, P. & SCHERES, B. 2007. Auxin transport is sufficient to generate a maximum and gradient guiding root growth. *Nature,* 449**,** 1008.

GUNAWARDENA, A. H. 2007. Programmed cell death and tissue remodelling in plants. *Journal of experimental botany,* 59**,** 445-451.

GURDON, J. & BOURILLOT, P.-Y. 2001. Morphogen gradient interpretation. *Nature,* 413**,** 797.

HACKE, U. G. & SPERRY, J. S. 2001. Functional and ecological xylem anatomy. *Perspectives in plant ecology, evolution and systematics,* 4**,** 97-115.

HAGBERG, A., SWART, P. & S CHULT, D. 2008. Exploring network structure, dynamics, and function using NetworkX. Los Alamos National Lab.(LANL), Los Alamos, NM (United States).

HAGMANN, P., CAMMOUN, L., GIGANDET, X., MEULI, R., HONEY, C. J., WEDEEN, V. J. & SPORNS, O. 2008. Mapping the structural core of human cerebral cortex. *PLoS biology,* 6**,** e159.

HAGMANN, P., THIRAN, J.-P., JONASSON, L., VANDERGHEYNST, P., CLARKE, S., MAEDER, P. & MEULI, R. 2003. DTI mapping of human brain connectivity: statistical fibre tracking and virtual dissection. *Neuroimage,* 19**,** 545-554.

HAMANT, O. 2017. Mechano-devo. *Mechanisms of development,* 145**,** 2-9.

HAMANT, O., HEISLER, M. G., JONSSON, H., KRUPINSKI, P., UYTTEWAAL, M., BOKOV, P., CORSON, F., SAHLIN, P., BOUDAOUD, A., MEYEROWITZ, E. M., COUDER, Y. & TRAAS, J. 2008. Developmental Patterning by Mechanical Signals in Arabidopsis. *Science,* 322**,** 1650-1655.

HAMMERSCHMIDT, K., ROSE, C. J., KERR, B. & RAINEY, P. B. 2014. Life cycles, fitness decoupling and the evolution of multicellularity. *Nature,* 515**,** 75.

HARDTKE, C. S. & BERLETH, T. 1998. The Arabidopsis gene MONOPTEROS encodes a transcription factor mediating embryo axis formation and vascular development. *The EMBO journal,* 17**,** 1405-1411.

HARRISON, C. J. 2017. Development and genetics in the evolution of land plant body plans. *Phil. Trans. R. Soc. B,* 372**,** 20150490.

HASTIE, T., TIBSHIRANI, R. & FRIEDMAN, J. 2009. Unsupervised learning. *The elements of statistical learning.* Springer.

HAYTHORNTHWAITE, C. 1996. Social network analysis: An approach and technique for the study of information exchange. *Library & information science research,* 18**,** 323-342.

HELARIUTTA, Y., FUKAKI, H., WYSOCKA-DILLER, J., NAKAJIMA, K., JUNG, J., SENA, G., HAUSER, M.-T. & BENFEY, P. N. 2000. The SHORT-ROOT gene controls radial patterning of the Arabidopsis root through radial signaling. *Cell,* 101**,** 555-567.

HELMSTAEDTER, M. 2013. Cellular-resolution connectomics: challenges of dense neural circuit reconstruction. *Nature methods,* 10**,** 501.

HEPLER, P. 1982. Endoplasmic reticulum in the formation of the cell plate and plasmodesmata. *Protoplasma,* 111**,** 121-133.

HETHCOTE, H. W. 2000. The mathematics of infectious diseases. *SIAM review,* 42**,** 599-653.

HILLEARY, R. & GILROY, S. 2018. Systemic signaling in response to wounding and pathogens. *Current opinion in plant biology,* 43**,** 57-62.

HOCHBERG, M. E., RANKIN, D. J. & TABORSKY, M. 2008. The coevolution of cooperation and dispersal in social groups and its implications for the emergence of multicellularity. *BMC Evolutionary Biology,* 8**,** 238.

HOFMEISTER, W. 1863. Zusatze und Berichtigungen zu den 1851 veroffentlichen Untersuchungen der Entwicklung hoherer Kryptogamen. *Jahrb. Wiss. Bot.,* 3**,** 259-193.

HOLME, P. 2015. Modern temporal network theory: a colloquium. *The European Physical Journal B,* 88**,** 234.

HOSKING, J. R. & WALLIS, J. R. 1987. Parameter and quantile estimation for the generalized Pareto distribution. *Technometrics,* 29**,** 339-349.

HUTTLIN, E. L., TING, L., BRUCKNER, R. J., GEBREAB, F., GYGI, M. P., SZPYT, J., TAM, S., ZARRAGA, G., COLBY, G. & BALTIER, K. 2015. The BioPlex network: a systematic exploration of the human interactome. *Cell,* 162**,** 425-440.

IBANEZ, L., SCHROEDER, W., NG, L. & CATES, J. 2005. The ITK software guide.

INGBER, D. E. 1998. The architecture of life. *Scientific American,* 278**,** 48-57.

IOIO, R. D., NAKAMURA, K., MOUBAYIDIN, L., PERILLI, S., TANIGUCHI, M., MORITA, M. T., AOYAMA, T., COSTANTINO, P. & SABATINI, S. 2008. A Genetic Framework for the Control of Cell Division and Differentiation in the Root Meristem. *Science,* 322**,** 1380-1384.

ISPOLATOV, I., ACKERMANN, M. & DOEBELI, M. 2011. Division of labour and the evolution of multicellularity. *Proceedings of the Royal Society B: Biological Sciences*.

JACKSON, M. D., DURAN-NEBREDA, S. & BASSEL, G. W. 2017a. Network-based approaches to quantify multicellular development. *Journal of The Royal Society Interface,* 14**,** 20170484.

JACKSON, M. D., XU, H., DURAN-NEBREDA, S., STAMM, P. & BASSEL, G. W. 2017b. Topological analysis of multicellular complexity in the plant hypocotyl. *Elife,* 6**,** e26023.

JACQUES, E., VERBELEN, J.-P. & VISSENBERG, K. 2014. Review on shape formation in epidermal pavement cells of the Arabidopsis leaf. *Functional Plant Biology,* 41**,** 914-921.

JAIN, R. K. 2005. Normalization of tumor vasculature: an emerging concept in antiangiogenic therapy. *Science,* 307**,** 58-62.

JAKOBY, M. & SCHNITTGER, A. 2004. Cell cycle and differentiation. *Current Opinion in Plant Biology,* 7**,** 661-669.

JENSEN, K. H. 2018. Phloem physics: mechanisms, constraints, and perspectives. *Current opinion in plant biology,* 43**,** 96-100.

JENSEN, P. J., HANGARTER, R. P. & ESTELLE, M. 1998. Auxin transport is required for hypocotyl elongation in light-grown but not dark-grown Arabidopsis. *Plant Physiology,* 116**,** 455-462.

JONES, E., OLIPHANT, T. & PETERSON, P. 2001. SciPy. *Open source scientific tools for Python*.

JÖNSSON, H., HEISLER, M. G., SHAPIRO, B. E., MEYEROWITZ, E. M. & MJOLSNESS, E. 2006. An auxin-driven polarized transport model for phyllotaxis. *Proceedings of the National Academy of Sciences,* 103**,** 1633-1638.

JORDÁN, F. & SCHEURING, I. 2004. Network ecology: topological constraints on ecosystem dynamics. *Physics of Life Reviews,* 1**,** 139-172.

KANDEL, E. R., SCHWARTZ, J. H., JESSELL, T. M., BIOCHEMISTRY, D. O., JESSELL, M. B. T., SIEGELBAUM, S. & HUDSPETH, A. 2000. *Principles of neural science*, McGraw-hill New York.

KANG, J., HWANG, J.-U., LEE, M., KIM, Y.-Y., ASSMANN, S. M., MARTINOIA, E. & LEE, Y. 2010. PDR-type ABC transporter mediates cellular uptake of the phytohormone abscisic acid. *Proceedings of the National Academy of sciences,* 107**,** 2355-2360.

KATRITCH, V., CHEREZOV, V. & STEVENS, R. C. 2013. Structure-function of the G protein–coupled receptor superfamily. *Annual review of pharmacology and toxicology,* 53**,** 531-556.

KERMACK, W. & MCKENDRICK, A. 1927. A contribution to the mathematical theory of epidemics. *Proceedings of the Royal Society of London. Series A,* 115**,** 700.

KIERZKOWSKI, D., LENHARD, M., SMITH, R. & KUHLEMEIER, C. 2013. Interaction between meristem tissue layers controls phyllotaxis. *Developmental cell,* 26**,** 616-628.

KIERZKOWSKI, D., NAKAYAMA, N., ROUTIER-KIERZKOWSKA, A.-L., WEBER, A., BAYER, E., SCHORDERET, M., REINHARDT, D., KUHLEMEIER, C. & SMITH, R. S. 2012. Elastic domains regulate growth and organogenesis in the plant shoot apical meristem. *Science,* 335**,** 1096-1099.

KITANO, H. 2002. Computational systems biology. *Nature,* 420**,** 206.

KOBAYASHI, K. & ZAMBRYSKI, P. 2007. RNA silencing and its cell‐to‐cell spread during Arabidopsis embryogenesis. *The Plant Journal,* 50**,** 597-604.

KOCH, A. & MEINHARDT, H. 1994. Biological pattern formation: from basic mechanisms to complex structures. *Reviews of modern physics,* 66**,** 1481.

KOLMOGOROV, A. 1933. Sulla determinazione empirica di una lgge di distribuzione. *Inst. Ital. Attuari, Giorn.,* 4**,** 83-91.

KROUK, G., CRAWFORD, N. M., CORUZZI, G. M. & TSAY, Y.-F. 2010. Nitrate signaling: adaptation to fluctuating environments. *Current Opinion in Plant Biology,* 13**,** 265-272.

KRUSKAL, W. H. 1957. Historical notes on the Wilcoxon unpaired two-sample test. *Journal of the American Statistical Association,* 52**,** 356-360.

KUROMORI, T., SUGIMOTO, E. & SHINOZAKI, K. 2014. Inter-tissue signal transfer of abscisic acid from vascular cells to guard cells. *Plant Physiology***,** pp. 114.235556.

KWAK, S.-H. & SCHIEFELBEIN, J. 2007. The role of the SCRAMBLED receptor-like kinase in patterning the Arabidopsis root epidermis. *Developmental biology,* 302**,** 118-131.

KWIATKOWSKA, D. 2004. Structural integration at the shoot apical meristem: models, measurements, and experiments. *American journal of botany,* 91**,** 1277-1293.

LAI, E. C. 2004. Notch signaling: control of cell communication and cell fate. *Development,* 131**,** 965-973.

LATORA, V. & MARCHIORI, M. 2001. Efficient behavior of small-world networks. *Physical review letters,* 87**,** 198701.

LAUFS, P., GRANDJEAN, O., JONAK, C., KIÊU, K. & TRAAS, J. 1998. Cellular parameters of the shoot apical meristem in Arabidopsis. *The Plant Cell,* 10**,** 1375-1389.

LAZER, D., PENTLAND, A. S., ADAMIC, L., ARAL, S., BARABASI, A. L., BREWER, D., CHRISTAKIS, N., CONTRACTOR, N., FOWLER, J. & GUTMANN, M. 2009. Life in the network: the coming age of computational social science. *Science (New York, NY),* 323**,** 721.

LECUIT, T. & LENNE, P.-F. 2007. Cell surface mechanics and the control of cell shape, tissue patterns and morphogenesis. *Nature reviews Molecular cell biology,* 8**,** 633.

LEE, J.-Y. & LU, H. 2011. Plasmodesmata: the battleground against intruders. *Trends in plant science,* 16**,** 201-210.

LEE, M. M. & SCHIEFELBEIN, J. 1999. WEREWOLF, a MYB-related protein in Arabidopsis, is a position-dependent regulator of epidermal cell patterning. *Cell,* 99**,** 473-483.

LEMESHOW, S. & HOSMER JR, D. W. 1982. A review of goodness of fit statistics for use in the development of logistic regression models. *American journal of epidemiology,* 115**,** 92-106.

LEVIN, M. 2012. Morphogenetic fields in embryogenesis, regeneration, and cancer: non-local control of complex patterning. *Biosystems,* 109**,** 243-261.

LI, S., BLANCHOIN, L., YANG, Z. & LORD, E. M. 2003. The Putative Arabidopsis Arp2/3 Complex Controls Leaf Cell Morphogenesis. *Plant Physiology,* 132**,** 2034-2044.

LIBAULT, M., PINGAULT, L., ZOGLI, P. & SCHIEFELBEIN, J. 2017. Plant systems biology at the single-cell level. *Trends in plant science*.

LIN, W., XIAO, X., XIE, X. & LI, X.-L. 2017. Network motif discovery: A GPU approach. *IEEE Transactions on Knowledge and Data Engineering,* 29**,** 513-528.

LIN, Y. & SCHIEFELBEIN, J. 2001. Embryonic control of epidermal cell patterning in the root and hypocotyl of Arabidopsis. *Development,* 128**,** 3697-3705.

LINDSAY, M. R., WEBB, R. I., STROUS, M., JETTEN, M. S., BUTLER, M. K., FORDE, R. J. & FUERST, J. A. 2001. Cell compartmentalisation in planctomycetes: novel types of structural organisation for the bacterial cell. *Archives of Microbiology,* 175**,** 413-429.

LINKERT, M., RUEDEN, C. T., ALLAN, C., BUREL, J.-M., MOORE, W., PATTERSON, A., LORANGER, B., MOORE, J., NEVES, C. & MACDONALD, D. 2010. Metadata matters: access to image data in the real world. *The Journal of cell biology,* 189**,** 777-782.

LINTILHAC, P. M. & VESECKY, T. B. 1984. Stress-induced alignment of division plane in plant tissues grown in vitro.

LIU, Y.-Y., SLOTINE, J.-J. & BARABÁSI, A.-L. 2011. Controllability of complex networks. *Nature,* 473**,** 167.

LOH, K. M., VAN AMERONGEN, R. & NUSSE, R. 2016. Generating cellular diversity and spatial form: Wnt signaling and the evolution of multicellular animals. *Developmental cell,* 38**,** 643-655.

LOHMANN, J. U. & WEIGEL, D. 2002. Building beauty: the genetic control of floral patterning. *Developmental cell,* 2**,** 135-142.

LONG, Y., SCHERES, B. & BLILOU, I. 2015. The logic of communication: roles for mobile transcription factors in plants. *Journal of experimental botany,* 66**,** 1133-1144.

LÓPEZ-MUÑOZ, F., BOYA, J. & ALAMO, C. 2006. Neuron theory, the cornerstone of neuroscience, on the centenary of the Nobel Prize award to Santiago Ramón y Cajal. *Brain research bulletin,* 70**,** 391-405.

LORI, N., AKBUDAK, E., SHIMONY, J., CULL, T., SNYDER, A., GUILLORY, R. & CONTURO, T. 2002. Diffusion tensor fiber tracking of human brain connectivity: aquisition methods, reliability analysis and biological results. *NMR in Biomedicine,* 15**,** 494-515.

LOUVEAUX, M., JULIEN, J.-D., MIRABET, V., BOUDAOUD, A. & HAMANT, O. 2016. Cell division plane orientation based on tensile stress in Arabidopsis thaliana. *Proceedings of the National Academy of Sciences,* 113**,** E4294-E4303.

LUCAS, W. J., BOUCHÉ-PILLON, S., JACKSON, D. P., NGUYEN, L., BAKER, L., DING, B. & HAKE, S. 1995. Selective trafficking of KNOTTED1 homeodomain protein and its mRNA through plasmodesmata. *Science,* 270**,** 1980-1983.

LUCAS, W. J., DING, B. & VAN DER SCHOOT, C. 1993. Plasmodesmata and the supracellular nature of plants. *New Phytologist,* 125**,** 435-476.

LUCAS, W. J., GROOVER, A., LICHTENBERGER, R., FURUTA, K., YADAV, S. R., HELARIUTTA, Y., HE, X. Q., FUKUDA, H., KANG, J. & BRADY, S. M. 2013. The plant vascular system: evolution, development and functions F. *Journal of integrative plant biology,* 55**,** 294-388.

LUPTOVČIAK, I., KOMIS, G., TAKÁČ, T., OVEČKA, M. & ŠAMAJ, J. 2017. Katanin: a sword cutting microtubules for cellular, developmental, and physiological purposes. *Frontiers in plant science,* 8**,** 1982.

LÜRLING, M. & VAN DONK, E. 2000. Grazer-induced colony formation in Scenedesmus: are there costs to being colonial? *Oikos,* 88**,** 111-118.

MARÉE, A. F. & HOGEWEG, P. 2001. How amoeboids self-organize into a fruiting body: multicellular coordination in Dictyostelium discoideum. *Proceedings of the National Academy of Sciences,* 98**,** 3879-3883.

MARKSON, J. S. & ELOWITZ, M. B. 2014. Synthetic biology of multicellular systems: new platforms and applications for animal cells and organisms. ACS Publications.

MARQUES, P. E., ANTUNES, M. M., DAVID, B. A., PEREIRA, R. V., TEIXEIRA, M. M. & MENEZES, G. B. 2015. Imaging liver biology in vivo using conventional confocal microscopy. *nature protocols,* 10**,** 258.

MARSCHNER, I. C. 2011. glm2: Fitting generalized linear models with convergence problems. *The R journal,* 3**,** 12-15.

MARTENS, L. & VIZCAÍNO, J. A. 2017. A golden age for working with public proteomics data. *Trends in biochemical sciences,* 42**,** 333-341.

MARTH, J. D. 2008. A unified vision of the building blocks of life. *Nature cell biology,* 10**,** 1015.

MARTÍNEZ‐VILALTA, J., MENCUCCINI, M., ÁLVAREZ, X., CAMACHO, J., LOEPFE, L. & PIÑOL, J. 2012. Spatial distribution and packing of xylem conduits. *American Journal of Botany,* 99**,** 1189-1196.

MATTHEWS, P. M. & HAMPSHIRE, A. 2016. Clinical concepts emerging from fMRI functional connectomics. *Neuron,* 91**,** 511-528.

MAULE, A. J. 2008. Plasmodesmata: structure, function and biogenesis. *Current opinion in plant biology,* 11**,** 680-686.

MCCOURT, R. M., DELWICHE, C. F. & KAROL, K. G. 2004. Charophyte algae and land plant origins. *Trends in Ecology & Evolution,* 19**,** 661-666.

MCLEAN, B. G., HEMPEL, F. D. & ZAMBRYSKI, P. C. 1997. Plant intercellular communication via plasmodesmata. *The Plant Cell,* 9**,** 1043.

MCQUIN, C., GOODMAN, A., CHERNYSHEV, V., KAMENTSKY, L., CIMINI, B. A., KARHOHS, K. W., DOAN, M., DING, L., RAFELSKI, S. M. & THIRSTRUP, D. 2018. CellProfiler 3.0: Next-generation image processing for biology. *PLoS biology,* 16**,** e2005970.

MEURER, A., SMITH, C. P., PAPROCKI, M., ČERTÍK, O., KIRPICHEV, S. B., ROCKLIN, M., KUMAR, A., IVANOV, S., MOORE, J. K. & SINGH, S. 2017. SymPy: symbolic computing in Python. *PeerJ Computer Science,* 3**,** e103.

MICHOD, R. E. 2005. On the transfer of fitness from the cell to the multicellular organism. *Biology and Philosophy,* 20**,** 967-987.

MICHOD, R. E. & ROZE, D. 2001. Cooperation and conflict in the evolution of multicellularity. *Heredity,* 86**,** 1.

MILES, K. & WILLIAMS, R. 2008. Warburg revisited: imaging tumour blood flow and metabolism. *Cancer Imaging,* 8**,** 81.

MIRONOV, V., BOLAND, T., TRUSK, T., FORGACS, G. & MARKWALD, R. R. 2003. Organ printing: computer-aided jet-based 3D tissue engineering. *TRENDS in Biotechnology,* 21**,** 157-161.

MIRONOV, V., KASYANOV, V. & MARKWALD, R. R. 2011. Organ printing: from bioprinter to organ biofabrication line. *Current Opinion in Biotechnology,* 22**,** 667-673.

MIŠIĆ, B., BETZEL, R. F., DE REUS, M. A., VAN DEN HEUVEL, M. P., BERMAN, M. G., MCINTOSH, A. R. & SPORNS, O. 2016. Network-level structure-function relationships in human neocortex. *Cerebral Cortex,* 26**,** 3285-3296.

MOLNAR, A., MELNYK, C. W., BASSETT, A., HARDCASTLE, T. J., DUNN, R. & BAULCOMBE, D. C. 2010. Small silencing RNAs in plants are mobile and direct epigenetic modification in recipient cells. *science,* 328**,** 872-875.

MONTENEGRO-JOHNSON, T. D., STAMM, P., STRAUSS, S., TOPHAM, A. T., TSAGRIS, M., WOOD, A. T., SMITH, R. S. & BASSEL, G. W. 2015. Digital single-cell analysis of plant organ development using 3DCellAtlas. *The Plant Cell***,** tpc. 15.00175.

MOOR, A. E. & ITZKOVITZ, S. 2017. Spatial transcriptomics: paving the way for tissue-level systems biology. *Current opinion in biotechnology,* 46**,** 126-133.

MOORE, D., WALKER, S. I. & LEVIN, M. 2017. Cancer as a disorder of patterning information: computational and biophysical perspectives on the cancer problem. *Convergent Science Physical Oncology,* 3**,** 043001.

MORGAN, J. L. & LICHTMAN, J. W. 2013. Why not connectomics? *Nature methods,* 10**,** 494.

MÜLLER, G. B. 2007. Evo–devo: extending the evolutionary synthesis. *Nature reviews genetics,* 8**,** 943.

MURATA, T., HOTTA, K., IMANISHI, A., MATSUDA, M. & TERAI, K. 2018. Segmentation of Cell Membrane and Nucleus using Branches with Different Roles in Deep Neural Network.

MURPHY, S. V. & ATALA, A. 2014. 3D bioprinting of tissues and organs. *Nature biotechnology,* 32**,** 773.

NADEAU, J. A. & SACK, F. D. 2002. Control of Stomatal Distribution on the Arabidopsis Leaf Surface. *Science,* 296**,** 1697-1700.

NAGANATHAN, S. R. & OATES, A. C. 2017. Mechanochemical coupling and developmental pattern formation. *Current Opinion in Systems Biology*.

NEWMAN, M. 2018. *Networks*, Oxford university press.

NEWMAN, M. E. 2005. A measure of betweenness centrality based on random walks. *Social networks,* 27**,** 39-54.

NIELSEN, J. 2017. Systems biology of metabolism: a driver for developing personalized and precision medicine. *Cell metabolism,* 25**,** 572-579.

NIKLAS, K. J. 2009. Deducing plant function from organic form: challenges and pitfalls. *Form and function in developmental evolution***,** 47-82.

NIKLAS, K. J. & NEWMAN, S. A. 2013. The origins of multicellular organisms. *Evolution & Development,* 15**,** 41-52.

NOH, J. D. & RIEGER, H. 2004. Random walks on complex networks. *Physical review letters,* 92**,** 118701.

NOWACK, M. K., HARASHIMA, H., DISSMEYER, N., ZHAO, X. A., BOUYER, D., WEIMER, A. K., DE WINTER, F., YANG, F. & SCHNITTGER, A. 2012. Genetic framework of cyclin-dependent kinase function in Arabidopsis. *Developmental cell,* 22**,** 1030-1040.

OKADA, K., UEDA, J., KOMAKI, M. K., BELL, C. J. & SHIMURA, Y. 1991. Requirement of the auxin polar transport system in early stages of Arabidopsis floral bud formation. *The Plant Cell,* 3**,** 677-684.

OLESEN, J. M. & JORDANO, P. 2002. Geographic patterns in plant–pollinator mutualistic networks. *Ecology,* 83**,** 2416-2424.

OLLÉ-VILA, A., DURAN-NEBREDA, S., CONDE-PUEYO, N., MONTAÑEZ, R. & SOLÉ, R. 2016. A morphospace for synthetic organs and organoids: the possible and the actual. *Integrative Biology,* 8**,** 485-503.

OTHMER, H. G., DUNBAR, S. R. & ALT, W. 1988. Models of dispersal in biological systems. *Journal of mathematical biology,* 26**,** 263-298.

PAINE, R. T. 1966. Food web complexity and species diversity. *The American Naturalist,* 100**,** 65-75.

PANZICA, D. A., FINDLAY, A. S., LADESTEIJN, R. & COLLINSON, J. M. 2017. The core planar cell polarity gene, Vangl2, maintains apical-basal organisation of the corneal epithelium. *Journal of Anatomy,* 0.

PARK, J., LEE, Y., MARTINOIA, E. & GEISLER, M. 2017. Plant hormone transporters: what we know and what we would like to know. *BMC biology,* 15**,** 93.

PEARSON, K. 1900. X. On the criterion that a given system of deviations from the probable in the case of a correlated system of variables is such that it can be reasonably supposed to have arisen from random sampling. *The London, Edinburgh, and Dublin Philosophical Magazine and Journal of Science,* 50**,** 157-175.

PEDREGOSA, F., VAROQUAUX, G., GRAMFORT, A., MICHEL, V., THIRION, B., GRISEL, O., BLONDEL, M., PRETTENHOFER, P., WEISS, R. & DUBOURG, V. 2011. Scikit-learn: Machine learning in Python. *Journal of machine learning research,* 12**,** 2825-2830.

PEREZ-RIVEROL, Y., BAI, M., DA VEIGA LEPREVOST, F., SQUIZZATO, S., PARK, Y. M., HAUG, K., CARROLL, A. J., SPALDING, D., PASCHALL, J. & WANG, M. 2017. Discovering and linking public omics data sets using the Omics Discovery Index. *Nature biotechnology,* 35**,** 406.

PETRÁŠEK, J. & FRIML, J. 2009. Auxin transport routes in plant development. *Development,* 136**,** 2675-2688.

POLLARD, T. D. 2003. The cytoskeleton, cellular motility and the reductionist agenda. *Nature,* 422**,** 741.

POWER, R. M. & HUISKEN, J. 2017. A guide to light-sheet fluorescence microscopy for multiscale imaging. *Nature methods,* 14**,** 360.

PROULX, S. R., PROMISLOW, D. E. & PHILLIPS, P. C. 2005. Network thinking in ecology and evolution. *Trends in ecology & evolution,* 20**,** 345-353.

QU, Z., GARFINKEL, A., WEISS, J. N. & NIVALA, M. 2011. Multi-scale modeling in biology: how to bridge the gaps between scales? *Progress in biophysics and molecular biology,* 107**,** 21-31.

RAHME, L. G., STEVENS, E. J., WOLFORT, S. F., SHAO, J., TOMPKINS, R. G. & AUSUBEL, F. M. 1995. Common virulence factors for bacterial pathogenicity in plants and animals. *Science,* 268**,** 1899-1902.

RAJAGOPALA, S. V., SIKORSKI, P., KUMAR, A., MOSCA, R., VLASBLOM, J., ARNOLD, R., FRANCA-KOH, J., PAKALA, S. B., PHANSE, S. & CEOL, A. 2014. The binary protein-protein interaction landscape of Escherichia coli. *Nature biotechnology,* 32**,** 285.

RAPER, K. B. 1940. Pseudoplasmodium formation and organization in Dictyostelium discoideum. *Journal of the Elisha Mitchell Scientific Society,* 56**,** 241-282.

RATCLIFF, W. C., DENISON, R. F., BORRELLO, M. & TRAVISANO, M. 2012. Experimental evolution of multicellularity. *Proceedings of the National Academy of Sciences,* 109**,** 1595-1600.

REINHARDT, D., PESCE, E.-R., STIEGER, P., MANDEL, T., BALTENSPERGER, K., BENNETT, M., TRAAS, J., FRIML, J. & KUHLEMEIER, C. 2003. Regulation of phyllotaxis by polar auxin transport. *Nature,* 426**,** 255.

RINNE, P. L. H., KAIKURANTA, P. M. & VAN DER SCHOOT, C. 2001. The shoot apical meristem restores its symplasmic organization during chilling-induced release from dormancy. *The Plant Journal,* 26**,** 249-264.

ROBERT, L., HOFFMANN, M., KRELL, N., AYMERICH, S., ROBERT, J. & DOUMIC, M. 2014. Division in Escherichia coliis triggered by a size-sensing rather than a timing mechanism. *BMC Biology,* 12**,** 17.

ROBERTS, A. G. & OPARKA, K. J. 2003. Plasmodesmata and the control of symplastic transport. *Plant, Cell & Environment,* 26**,** 103-124.

ROEDER, A. H. 2012. When and where plant cells divide: a perspective from computational modeling. *Current opinion in plant biology,* 15**,** 638-644.

ROKAS, A. 2008. The origins of multicellularity and the early history of the genetic toolkit for animal development. *Annual review of genetics,* 42**,** 235-251.

ROSENBERG, A. 2008. *Darwinian reductionism: Or, how to stop worrying and love molecular biology*, University of Chicago Press.

RUBIN, H. 1985. Cancer as a dynamic developmental disorder. *Cancer research,* 45**,** 2935-2942.

RUBINOV, M. & SPORNS, O. 2010. Complex network measures of brain connectivity: uses and interpretations. *Neuroimage,* 52**,** 1059-1069.

RUBNER, Y., TOMASI, C. & GUIBAS, L. J. A metric for distributions with applications to image databases. Computer Vision, 1998. Sixth International Conference on, 1998. IEEE, 59-66.

RUNIONS, A., TSIANTIS, M. & PRUSINKIEWICZ, P. 2017. A common developmental program can produce diverse leaf shapes. *New Phytologist,* 216**,** 401-418.

SÁNCHEZ‐GUTIÉRREZ, D., TOZLUOGLU, M., BARRY, J. D., PASCUAL, A., MAO, Y. & ESCUDERO, L. M. 2015. Fundamental physical cellular constraints drive self‐organization of tissues. *The EMBO journal***,** e201592374.

SANTORO, N., QUATTROCIOCCHI, W., FLOCCHINI, P., CASTEIGTS, A. & AMBLARD, F. 2011. Time-varying graphs and social network analysis: Temporal indicators and metrics. *arXiv preprint arXiv:1102.0629*.

SASAI, Y. 2013. Cytosystems dynamics in self-organization of tissue architecture. *Nature,* 493**,** 318.

SASAKI, N., PARK, J.-W., MAULE, A. J. & NELSON, R. S. 2006. The cysteine–histidine-rich region of the movement protein of Cucumber mosaic virus contributes to plasmodesmal targeting, zinc binding and pathogenesis. *Virology,* 349**,** 396-408.

SATGÉ, D. 2001. Analysis of somatic mutations in cancer tissues challenges the somatic mutation theory of cancer. *eLS*.

SATINA, S., BLAKESLEE, A. F. & AVERY, A. G. 1940. Demonstration of the three germ layers in the shoot apex of Datura by means of induced polyploidy in periclinal chimeras. *American Journal of Botany,* 27**,** 895-905.

SCHIEFELBEIN, J. 2003. Cell-fate specification in the epidermis: a common patterning mechanism in the root and shoot. *Current opinion in plant biology,* 6**,** 74-78.

SCHIEFELBEIN, J., ZHENG, X. & HUANG, L. 2014. Regulation of epidermal cell fate in Arabidopsis roots: the importance of multiple feedback loops. *Frontiers in plant science,* 5**,** 47.

SCHINDELIN, J., ARGANDA-CARRERAS, I., FRISE, E., KAYNIG, V., LONGAIR, M., PIETZSCH, T., PREIBISCH, S., RUEDEN, C., SAALFELD, S. & SCHMID, B. 2012. Fiji: an open-source platform for biological-image analysis. *Nature methods,* 9**,** 676.

SCHLERETH, A., MÖLLER, B., LIU, W., KIENTZ, M., FLIPSE, J., RADEMACHER, E. H., SCHMID, M., JÜRGENS, G. & WEIJERS, D. 2010. MONOPTEROS controls embryonic root initiation by regulating a mobile transcription factor. *Nature,* 464**,** 913.

SCHOOF, H., LENHARD, M., HAECKER, A., MAYER, K. F., JÜRGENS, G. & LAUX, T. 2000. The stem cell population of Arabidopsis shoot meristems is maintained by a regulatory loop between the CLAVATA and WUSCHEL genes. *Cell,* 100**,** 635-644.

SCHRÖTER, M., PAULSEN, O. & BULLMORE, E. T. 2017. Micro-connectomics: probing the organization of neuronal networks at the cellular scale. *Nature Reviews Neuroscience,* 18**,** 131.

SCHWANN, T. 1847. *Microscopical Researches into the Accordance in the Structure and Growth of Animals and Plants*, Рипол Классик.

SEARLS, D. T. 1964. The utilization of a known coefficient of variation in the estimation procedure. *Journal of the American Statistical Association,* 59**,** 1225-1226.

SEBÉ-PEDRÓS, A., DEGNAN, B. M. & RUIZ-TRILLO, I. 2017. The origin of Metazoa: a unicellular perspective. *Nature Reviews Genetics,* 18**,** 498.

SEGUIN, C., VAN DEN HEUVEL, M. P. & ZALESKY, A. 2018. Navigation of brain networks. *Proceedings of the National Academy of Sciences***,** 201801351.

SHAMIR, E. R. & EWALD, A. J. 2014. Three-dimensional organotypic culture: experimental models of mammalian biology and disease. *Nature Reviews Molecular Cell Biology,* 15**,** 647.

SHAPIRO, B. E., TOBIN, C., MJOLSNESS, E. & MEYEROWITZ, E. M. 2015. Analysis of cell division patterns in the Arabidopsis shoot apical meristem. *Proceedings of the National Academy of Sciences,* 112**,** 4815-4820.

SHARMA, S. & SINGH, A. K. 2018. An election algorithm to ensure the high availability of leader in large mobile ad hoc networks. *International Journal of Parallel, Emergent and Distributed Systems,* 33**,** 172-196.

SHEN-ORR, S. S., MILO, R., MANGAN, S. & ALON, U. 2002. Network motifs in the transcriptional regulation network of Escherichia coli. *Nature genetics,* 31**,** 64.

SHIH, C.-T., SPORNS, O., YUAN, S.-L., SU, T.-S., LIN, Y.-J., CHUANG, C.-C., WANG, T.-Y., LO, C.-C., GREENSPAN, R. J. & CHIANG, A.-S. 2015. Connectomics-based analysis of information flow in the Drosophila brain. *Current Biology,* 25**,** 1249-1258.

SHIMAMURA, M. 2015. Marchantia polymorpha: taxonomy, phylogeny and morphology of a model system. *Plant and Cell Physiology,* 57**,** 230-256.

SHPAK, E. D., MCABEE, J. M., PILLITTERI, L. J. & TORII, K. U. 2005. Stomatal Patterning and Differentiation by Synergistic Interactions of Receptor Kinases. *Science,* 309**,** 290-293.

SIMÓ, C., CIFUENTES, A. & GARCÍA-CAÑAS, V. 2014. *Fundamentals of advanced omics technologies: from genes to metabolites*, Newnes.

SIMPSON, C. 2011. The evolutionary history of division of labour. *Proceedings of the Royal Society B: Biological Sciences*.

SING, T., SANDER, O., BEERENWINKEL, N. & LENGAUER, T. 2005. ROCR: visualizing classifier performance in R. *Bioinformatics,* 21**,** 3940-3941.

SMITH, S. M., VIDAURRE, D., BECKMANN, C. F., GLASSER, M. F., JENKINSON, M., MILLER, K. L., NICHOLS, T. E., ROBINSON, E. C., SALIMI-KHORSHIDI, G. & WOOLRICH, M. W. 2013. Functional connectomics from resting-state fMRI. *Trends in cognitive sciences,* 17**,** 666-682.

SMITH, W. K., VOGELMANN, T. C., DELUCIA, E. H., BELL, D. T. & SHEPHERD, K. A. 1997. Leaf Form and Photosynthesis. *BioScience,* 47**,** 785-793.

SMOLY, I. Y., LERMAN, E., ZIV-UKELSON, M. & YEGER-LOTEM, E. 2017. MotifNet: a web-server for network motif analysis. *Bioinformatics,* 33**,** 1907-1909.

SOLÉ, R., OLLÉ-VILA, A., VIDIELLA, B., DURAN-NEBREDA, S. & CONDE-PUEYO, N. 2018. The road to synthetic multicellularity. *Current Opinion in Systems Biology,* 7**,** 60-67.

SOTO, A. M. & SONNENSCHEIN, C. 2011. The tissue organization field theory of cancer: a testable replacement for the somatic mutation theory. *Bioessays,* 33**,** 332-340.

SPECK, T. & BURGERT, I. 2011. Plant stems: functional design and mechanics. *Annual Review of Materials Research,* 41**,** 169-193.

SPERRY, J. S. 2003. Evolution of water transport and xylem structure. *International Journal of Plant Sciences,* 164**,** S115-S127.

SPORNS, O. & BASSETT, D. S. 2018. Editorial: New Trends in Connectomics. *Network Neuroscience,* 2**,** 125-127.

ST JOHNSTON, D. & NÜSSLEIN-VOLHARD, C. 1992. The origin of pattern and polarity in the Drosophila embryo. *Cell,* 68**,** 201-219.

STAEHELIN, L. A. & HEPLER, P. K. 1996. Cytokinesis in higher plants. *Cell,* 84**,** 821-824.

STAMM, P., TOPHAM, A. T., MUKHTAR, N. K., JACKSON, M. D. B., TOMÉ, D. F. A., BEYNON, J. L. & BASSEL, G. W. 2017. The Transcription Factor ATHB5 Affects GA-Mediated Plasticity in Hypocotyl Cell Growth during Seed Germination. *Plant Physiology,* 173**,** 907-917.

STEUDLE, E. & PETERSON, C. A. 1998. How does water get through roots? *Journal of experimental Botany,* 49**,** 775-788.

STRASSMANN, J. E., ZHU, Y. & QUELLER, D. C. 2000. Altruism and social cheating in the social amoeba Dictyostelium discoideum. *Nature,* 408**,** 965.

SUSSEX, I. M. & KERK, N. M. 2001. The evolution of plant architecture. *Current opinion in plant biology,* 4**,** 33-37.

SZKLARCZYK, D., FRANCESCHINI, A., WYDER, S., FORSLUND, K., HELLER, D., HUERTA-CEPAS, J., SIMONOVIC, M., ROTH, A., SANTOS, A. & TSAFOU, K. P. 2014. STRING v10: protein–protein interaction networks, integrated over the tree of life. *Nucleic acids research,* 43**,** D447-D452.

TABATA, T. & KORNBERG, T. B. 1994. Hedgehog is a signaling protein with a key role in patterning Drosophila imaginal discs. *Cell,* 76**,** 89-102.

TAKAGUCHI, T., NAKAMURA, M., SATO, N., YANO, K. & MASUDA, N. 2011. Predictability of conversation partners. *Physical Review X,* 1**,** 011008.

TAKIZAWA, T., MATSUKAWA, S., HIGUCHI, Y., NAKAMURA, S., NAKANISHI, Y. & FUKUDA, R. 1993. Induction of programmed cell death (apoptosis) by influenza virus infection in tissue culture cells. *Journal of General Virology,* 74**,** 2347-2355.

TAYLOR, I. W., LINDING, R., WARDE-FARLEY, D., LIU, Y., PESQUITA, C., FARIA, D., BULL, S., PAWSON, T., MORRIS, Q. & WRANA, J. L. 2009. Dynamic modularity in protein interaction networks predicts breast cancer outcome. *Nature biotechnology,* 27**,** 199.

THEOCHARIDIS, A., VAN DONGEN, S., ENRIGHT, A. J. & FREEMAN, T. C. 2009. Network visualization and analysis of gene expression data using BioLayout Express 3D. *Nature protocols,* 4**,** 1535.

THOMAS, C. L., SCHMIDT, D., BAYER, E. M., DREOS, R. & MAULE, A. J. 2009. Arabidopsis plant homeodomain finger proteins operate downstream of auxin accumulation in specifying the vasculature and primary root meristem. *The Plant Journal,* 59**,** 426-436.

THOMPSON, D. W. 1942. On growth and form. *On growth and form.*

TRAAS, J. & VERNOUX, T. 2002. The shoot apical meristem: the dynamics of a stable structure. *Philosophical Transactions of the Royal Society of London B: Biological Sciences,* 357**,** 737-747.

TREML, B. S., WINDERL, S., RADYKEWICZ, R., HERZ, M., SCHWEIZER, G., HUTZLER, P., GLAWISCHNIG, E. & RUIZ, R. A. T. 2005. The gene ENHANCER OF PINOID controls cotyledon development in the Arabidopsis embryo. *Development,* 132**,** 4063-4074.

TRUERNIT, E., BAUBY, H., DUBREUCQ, B., GRANDJEAN, O., RUNIONS, J., BARTHÉLÉMY, J. & PALAUQUI, J.-C. 2008. High-resolution whole-mount imaging of three-dimensional tissue organization and gene expression enables the study of phloem development and structure in Arabidopsis. *The Plant Cell,* 20**,** 1494-1503.

TUKEY, J. W. 1949. Comparing individual means in the analysis of variance. *Biometrics*, 99-114.

UBEDA-TOMÁS, S., FEDERICI, F., CASIMIRO, I., BEEMSTER, G. T. S., BHALERAO, R., SWARUP, R., DOERNER, P., HASELOFF, J. & BENNETT, M. J. 2009. Gibberellin Signaling in the Endodermis Controls Arabidopsis Root Meristem Size. *Current Biology,* 19**,** 1194-1199.

UVERSKY, V. N. 2016. P53 proteoforms and intrinsic disorder: an illustration of the protein structure–function continuum concept. *International journal of molecular sciences,* 17**,** 1874.

UYTTEWAAL, M., BURIAN, A., ALIM, K., LANDREIN, B., BOROWSKA-WYKRĘT, D., DEDIEU, A., PEAUCELLE, A., LUDYNIA, M., TRAAS, J. & BOUDAOUD, A. 2012. Mechanical stress acts via katanin to amplify differences in growth rate between adjacent cells in Arabidopsis. *Cell,* 149**,** 439-451.

VAN DEN BERG, C., WILLEMSEN, V., HENDRIKS, G., WEISBEEK, P. & SCHERES, B. 1997. Short-range control of cell differentiation in the Arabidopsis root meristem. *Nature,* 390**,** 287.

VAN DEN HEUVEL, M. P. & SPORNS, O. 2013. Network hubs in the human brain. *Trends in cognitive sciences,* 17**,** 683-696.

VAN ESSEN, D. C. & UGURBIL, K. 2012. The future of the human connectome. *Neuroimage,* 62**,** 1299-1310.

VAN REGENMORTEL, M. H. 2004. Reductionism and complexity in molecular biology: Scientists now have the tools to unravel biological complexity and overcome the limitations of reductionism. *EMBO reports,* 5**,** 1016-1020.

VAN WIJK, B. C., STAM, C. J. & DAFFERTSHOFER, A. 2010. Comparing brain networks of different size and connectivity density using graph theory. *PloS one,* 5**,** e13701.

VATÉN, A., DETTMER, J., WU, S., STIERHOF, Y.-D., MIYASHIMA, S., YADAV, S. R., ROBERTS, C. J., CAMPILHO, A., BULONE, V. & LICHTENBERGER, R. 2011. Callose biosynthesis regulates symplastic trafficking during root development. *Developmental cell,* 21**,** 1144-1155.

VODENEEV, V., MUDRILOV, M., AKINCHITS, E., BALALAEVA, I. & SUKHOV, V. 2018. Parameters of electrical signals and photosynthetic responses induced by them in pea seedlings depend on the nature of stimulus. *Functional Plant Biology,* 45**,** 160-170.

WALLINGFORD, J. B., FRASER, S. E. & HARLAND, R. M. 2002. Convergent extension: the molecular control of polarized cell movement during embryonic development. *Developmental cell,* 2**,** 695-706.

WALSBY, A. E. 2005. Archaea with square cells. *Trends in microbiology,* 13**,** 193-195.

WARD JR, J. H. 1963. Hierarchical grouping to optimize an objective function. *Journal of the American statistical association,* 58**,** 236-244.

WASKOM, M. L. & WAGNER, A. D. 2017. Distributed representation of context by intrinsic subnetworks in prefrontal cortex. *Proceedings of the National Academy of Sciences***,** 201615269.

WATSON, J. D. & CRICK, F. H. The structure of DNA. Cold Spring Harbor symposia on quantitative biology, 1953. Cold Spring Harbor Laboratory Press, 123-131.

WATTS, D. J. & STROGATZ, S. H. 1998. Collective dynamics of 'small-world'networks. *nature,* 393**,** 440.

WEIDNER, N. 1999. Tumour vascularity and proliferation: clear evidence of a close relationship. *The Journal of pathology,* 189**,** 297-299.

WEINZAEPFEL, P., HARCHAOUI, Z. & SCHMID, C. Learning to track for spatio-temporal action localization. Proceedings of the IEEE international conference on computer vision, 2015. 3164-3172.

WERNER, T., MOTYKA, V., STRNAD, M. & SCHMÜLLING, T. 2001. Regulation of plant growth by cytokinin. *Proceedings of the National Academy of Sciences,* 98**,** 10487-10492.

WEST, G. B., BROWN, J. H. & ENQUIST, B. J. 1999. A general model for the structure and allometry of plant vascular systems. *Nature,* 400**,** 664.

WEST, S. A. & COOPER, G. A. 2016. Division of labour in microorganisms: an evolutionary perspective. *Nature Reviews Microbiology,* 14**,** 716.

WHITE, J. G., SOUTHGATE, E., THOMSON, J. N. & BRENNER, S. 1986. The structure of the nervous system of the nematode Caenorhabditis elegans. *Philos Trans R Soc Lond B Biol Sci,* 314**,** 1-340.

WILLENSDORFER, M. 2009. On the evolution of differentiated multicellularity. *Evolution: International Journal of Organic Evolution,* 63**,** 306-323.

WILLIAMS, T. C., POOLMAN, M. G., HOWDEN, A. J., SCHWARZLANDER, M., FELL, D. A., RATCLIFFE, R. G. & SWEETLOVE, L. J. 2010. A genome-scale metabolic model accurately predicts fluxes in central carbon metabolism under stress conditions. *Plant physiology***,** pp. 110.158535.

WILLIS, L., REFAHI, Y., WIGHTMAN, R., LANDREIN, B., TELES, J., HUANG, K. C., MEYEROWITZ, E. M. & JÖNSSON, H. 2016. Cell size and growth regulation in the Arabidopsis thaliana apical stem cell niche. *Proceedings of the National Academy of Sciences,* 113**,** E8238-E8246.

WINZELER, E. A. & DAVIS, R. W. 1997. Functional analysis of the yeast genome. *Current opinion in genetics & development,* 7**,** 771-776.

WIŚNIEWSKA, J., XU, J., SEIFERTOVÁ, D., BREWER, P. B., RŮŽIČKA, K., BLILOU, I., ROUQUIÉ, D., BENKOVÁ, E., SCHERES, B. & FRIML, J. 2006. Polar PIN localization directs auxin flow in plants. *Science,* 312**,** 883-883.

WITTEN, D. M. & TIBSHIRANI, R. 2012. Scientific research in the age of omics: the good, the bad, and the sloppy. *Journal of the American Medical Informatics Association,* 20**,** 125-127.

WRIGHT, S. 1921. Correlation and causation. *Journal of agricultural research,* 20**,** 557-585.

WU, H., ZHAO, Y., CHENG, J. & YAN, D. Efficient Processing of Growing Temporal Graphs. International Conference on Database Systems for Advanced Applications, 2017. Springer, 387-403.

XIA, J., BENNER, M. J. & HANCOCK, R. E. 2014. NetworkAnalyst-integrative approaches for protein–protein interaction network analysis and visual exploration. *Nucleic acids research,* 42**,** W167-W174.

Y CAJAL, S. R. 1888. *Estructura de los centros nerviosos de las aves*.

Y CAJAL, S. R. 1894. *Les nouvelles idées sur la structure du système nerveux chez l'homme et chez les vertébrés*, Paris.

YACHDAV, G., KLOPPMANN, E., KAJAN, L., HECHT, M., GOLDBERG, T., HAMP, T., HÖNIGSCHMID, P., SCHAFFERHANS, A., ROOS, M. & BERNHOFER, M. 2014. PredictProtein—an open resource for online prediction of protein structural and functional features. *Nucleic acids research,* 42**,** W337-W343.

YANG, J., YAN, R., ROY, A., XU, D., POISSON, J. & ZHANG, Y. 2015. The I-TASSER Suite: protein structure and function prediction. *Nature methods,* 12**,** 7.

YOSHIDA, S., DE REUILLE, P. B., LANE, B., BASSEL, G. W., PRUSINKIEWICZ, P., SMITH, R. S. & WEIJERS, D. 2014. Genetic control of plant development by overriding a geometric division rule. *Developmental cell,* 29**,** 75-87.

YOUNG, K. D. 2006. The Selective Value of Bacterial Shape. *Microbiology and Molecular Biology Reviews,* 70**,** 660-703.

YURKOVICH, J. T. & PALSSON, B. O. 2018. Quantitative-omic data empowers bottom-up systems biology. *Current opinion in biotechnology,* 51**,** 130-136.

ZAIDI, Z. H. & SMITH, D. L. 1996. *Protein Structure--function Relationship*, Springer.

ZAVALIEV, R., SAGI, G., GERA, A. & EPEL, B. L. 2009. The constitutive expression of Arabidopsis plasmodesmal-associated class 1 reversibly glycosylated polypeptide impairs plant development and virus spread. *Journal of experimental botany,* 61**,** 131-142.

ZAVALIEV, R., UEKI, S., EPEL, B. L. & CITOVSKY, V. 2011. Biology of callose (β-1, 3-glucan) turnover at plasmodesmata. *Protoplasma,* 248**,** 117-130.

ZENG, H. 2018. Mesoscale connectomics. *Current Opinion in Neurobiology,* 50**,** 154-162.

ZHANG, C., HALSEY, L. E. & SZYMANSKI, D. B. 2011. The development and geometry of shape change in Arabidopsis thalianacotyledon pavement cells. *BMC Plant Biology,* 11**,** 27.

ZHANG, Q., KARSAI, M. & VESPIGNANI, A. 2018. Link transmission centrality in large-scale social networks. *arXiv preprint arXiv:1802.05337*.

ZIMMERMANN, M. R., MAISCHAK, H., MITHÖFER, A., BOLAND, W. & FELLE, H. H. 2009. System Potentials, a Novel Electrical Long-Distance Apoplastic Signal in Plants, Induced by Wounding. *Plant Physiology,* 149**,** 1593-1600.